Comparison of afferent inputs to the retrosplenial cortex in healthy and pathological conditions using a mouse model of amyloidopathy

Submitted by
Gabriella Christina Margetts-Smith
to the University of Exeter as a thesis for the degree of
Doctor of Philosophy in Medical Studies
in September 2022

I certify that all material in this thesis which is not my own work has been identified and that any material that has previously been submitted an approved for the award of a degree by this or any other University has been acknowledged.

Signature: 

Abstract

The retrosplenial cortex (RSC) is a cortical area found in rodents, primates and humans, and is thought to be involved in various cognitive functions including spatial navigation and episodic memory. One of the defining characteristics of the RSC is the high interconnectivity it shares with a range of distal brain regions. This connectivity is likely critical to its function, as reciprocal connections have been anatomically identified with other nodes in the extended memory circuit such as the thalamus and the hippocampal formation. The RSC has also been proposed as a site of covert pathology during Alzheimer's disease (AD). It exhibits many pathological changes during the early stages of the disease, and is highly susceptible to deafferentation following damage to distally-connected areas.

The synaptic strength and specificity of inputs into the RSC are still relatively unknown. Here, the anatomical and functional connectivity of afferent projections into the RSC were examined using a combination of viral anatomical tracing and patch clamp electrophysiology in *ex vivo* slices. Optogenetic interrogation of projections from the anterior cingulate cortex, the dorsal subiculum and the anterior thalamic nuclei in C57BL/6J mice revealed synaptic connectivity differences between inputs as well as between the granular and dysgranular subdivisions of the RSC. The results also showed that anatomical connectivity does not necessarily predict functional connectivity in RSC.

I then investigated whether the anterior thalamic nuclei to RSC projection is disrupted in an amyloidogenic mouse model of AD: the PDGF-APPSw,Ind (J20) transgenic line. While J20 mice exhibited RSC amyloid plaque deposition, there was no change in basal neuronal activity or disruption to synaptic responses. These findings were highly unexpected and speak to the complexity of the RSC and its circuitry. Overall, the work presented in this thesis improves our understanding of the RSC and its circuitry in both healthy and AD conditions. This work increases our knowledge of a brain region that is relatively under-represented in research, but plays a critical role in our cognition by integrating information from all over the brain to help form the complex representations necessary for navigating the world.

Table of Contents

Contents

Acknowledgements

First of all I would like to thank my supervisors; in particular Mick Craig and Jon Witton. Mick encouraged me throughout my PhD and pushed me to be the best scientist I can be. More than that, he also encouraged me through the associated stresses, and aimed to get me through with both good data and a somewhat-sound mind. Jon joined my project a little later, but brought a new perspective to my PhD and challenged me to approach my project with a critical mind. I have enjoyed my discussions with both of you immensely. I would also like to thank my other supervisors John Aggleton and Andy Randall, who provided me with invaluable advice and knowledge when designing and analysing my experiments.

Secondly, I would like to thank the members of the Craig Lab; past and present. Erica Brady was great friend and comrade-in-arms, and our “mentoring” sessions helped me a lot. Shivali Kohli always had time to listen and give advice, and I’ve loved our dinners and Bake Off evenings with Ben. I would like to give special thanks to Lilya Andrianova: Lilya supported me like a supervisor, and made me into the patcher I am today. She is a fantastic person and teacher, and always made time for a coffee and chat. It has not been the same in Hatherly without you. I would also like to thank Meg Elley for being a friend and support these last few months, and for helping push me over the finish line.

My family and friends have been a huge source of support for me throughout my PhD, and I wouldn’t be writing this without them. My parents have always encouraged me to reach for the moon and pursue my passions. I am especially thankful to my mum for everything you have done to get and keep me here, and for always believing in me.

To my husband Andy, I am eternally grateful for your love and encouragement. You have been my unwavering support, always there to push me up when I felt like I was drowning. To the moon and back forever.

Finally, I would like express my gratitude to the animals used during the course of this project. Without them, this research would not have been possible.

List of figures

List of tables

List of abbreviations

3m	3 months
3R	3 repeat
4R	4 repeat
6m	6 months
9m	9 months
Aβ	Amyloid-beta
ACC	Anterior cingulate cortex
aCSF	Artificial cerebral spinal fluid
AD	Alzheimer's disease
ADN	Anterodorsal nucleus
AI	Accommodation Index
AICD	APP intracellular domain
AMN	Anteromedial nucleus
AMPA	a-amino-3-hydroxy-5-methyl-4-isoxazolepropionic acid
AMPAR	AMPA receptor
ANOVA	Analysis of Variance
AP	Action potential
A-P	Anterior-posterior
APOE	Apoliprotein E
APP	Amyloid precursor protein
ATN	Anterior thalamic nuclei
AVN	Anteroventral nucleus
BI	Burst index
BS	Burst-spiking
C1	Cluster 1
C2	Cluster 2
C3	Cluster 3
Ca^{2+}	Calcium ion
$CaCl_2$	Calcium chloride
CamKII	Calmodulin-dependent protein kinase II
CB	Cingulum bundle
ChR	Channelrhodopsin
CLA	Claustrum

CNS	Central nervous system
CS	Conditioned stimulus
$CsMeSO_4$	Cesium methanesulfonate
CTF	C-terminal fragment
DAB	3,3'-Diaminobenzidine-tetrahydrochloride
DAPI	4',6-diamidino-2-phenylindole
DIC	Differential interference contrast
DMN	Default mode network
DNQX	6,7-dinitroquinoxaline-2,3-dione
dRSC	Retrosplenial dysgranular region
dSub	Dorsal subiculum
D-V	Dorsal-ventral
dV/dt	First derivative of the membrane potential
EC	Entorhinal cortex
EGTA	Ethylene glycol-bis(2-aminoethylether)-N,N,N',N'-tetraacetic acid
EMC	Extended memory circuit
EOFAD	Early-onset familial Alzheimer's disease
EPSC	Excitatory post-synaptic current
fMRI	Functional magnetic resonance imaging
GABA	Gamma aminobutyric acid
Gabazine	6-Imino-3-(4-methoxyphenyl)-1(6H)-pyridazinebutanoic acid hydrobromide
GPCR	G protein-coupled receptor
gRSC	Retrosplenial granular region
HD	Head direction
HEPES	4-(2-hydroxyethyl)-1-piperazineethanesulfonic acid
HPC	Hippocampus
I	Current
IC	Intracellular
IEG	Immediate early gene
iGluR	Ionotropic glutamate receptor
I_h	Hyperpolarisation-activated cation current
IN	Interneurons
IPI	Inter-pulse interval

IPSC	Inhibitory post-synaptic current
IQR	Interquartile range
ISI	Inter-spike interval
J20	PDGF-APPSw,Ind transgenic line
K^+	Potassium ion
KA	Kainate
K-gluc	Potassium gluconate
L-689,560	trans-2-Carboxy-5,7-dichloro-4-phenylaminocarbonylamino-1,2,3,4-tetrahydroquinoline
LED	Light emitting diode
LJP	Liquid junction potential
LOAD	Late-onset Alzheimer's disease
LS	Late-spiking
LTD	Long term depression
LTP	Long term potentiation
M2	Secondary motor cortex
mAChR	Muscarinic acetylcholine receptor
MANOVA	Multi-factorial Analysis of Variance
max dV/dt	Peak of the first derivative of the membrane potential
MCC	Midcingulate cortex
Mg^{2+}	Magnesium ion
Mg-ATP	Adenosine 5′-triphosphate magnesium salt
mGluR	Metabotropic glutamates receptor
M-L	Medial-lateral
MTL	Medial-temporal lobe
Na^+	Sodium ion
Na_2-GTP	Guanosine 5′-triphosphate sodium salt hydrate
nAChR	Nicotinic acetylcholine receptor
NFT	Neurofibrillary tangles
NGS	Normal goat serum
NMDA	N-methyl-d-aspartate
NMDAR	NMDA receptor
NMDG	N-methyl-d-glucamine
PBS	Phosphate buffered saline

PBST	Phosphate buffered saline with 0.2% Triton X-100
PC	Pyramidal cell
PCC	Posterior cingulate cortex
PFA	Paraformaldehyde
PKA	Protein kinase A
PP1	Protein phosphotase 1
PPD	Paired pulse depression
PPF	Paired pulse facilitation
PPR	Paired pulse ratio
PSEN	Presenilin
QX-314	N-(2,6-Dimethylphenylcarbamoylmethyl)triethylammonium bromide
R	Resistance
R_a	Access resistance
R_i	Input resistance
ROI	Region of interest
RS	Regular-spiking
RSC	Retrosplenial cortex
RT	Room temperature
sAPP	Soluble amyloid precursor protein
SD	Standard deviation
SEM	Standard error of the mean
ssV	Steady state response
SWR	Sharp wave-ripple
tau	Hyperphosphorylated microtubule-associated protein tau
Tg	Transgenic
τ_w	Weighted decay time constant
V	Volt
V1	Primary visual cortex
vGlut	Vesicular glutamate transport
V_H	Holding membrane potential
V_m	Resting membrane potential
WT	Wild-type

1 | Introduction

1.1 | The retrosplenial cortex

1.1.1 | RSC neuroanatomy

1.1.1.1 | Architecture of the RSC

The rodent RSC is located at the midline, dorsal to the corpus callosum and posterior to the midcingulate cortex (MCC), and spans across the anterior-posterior axis in mice (Paxinos and Franklin, 2001). The architecture of the RSC has been described previously in mice and rats (Vogt and Paxinos, 2014; Vogt and Peters, 1981), and follows a standard cortical laminar delineation into six cytoarchitectonically distinct layers. The RSC can also be further subdivided into two distinct sub-regions, the granular (gRSC) and dysgranular (dRSC), which are analogous to Brodman's areas 29 and 30 in humans (Vann et al., 2009). These sub-region and laminar architectonic distinctions are conserved across mammalian brains, and are similarly described within the human retrosplenial cortex (Morris et al., 2000). Of note is the variation in subdivision within the gRSC and dRSC depending on species and author preference; therefore in this thesis the gRSC and dRSC will be referred to as a collective of their subdivisions in accordance with Aggleton et al. (2021).

Anatomical differentiation of the gRSC and dRSC regions is immediately apparent from neuronal or cellular staining; the clearest cytoarchitectonic difference being the cell density in the superficial layers. gRSC layers 2-4 exhibit a much denser organisation than the dRSC, and the internal granular layer (2) is much thicker and more densely populated (see **Figure 1.1**). The external granular layer (4) is also more pronounced in the gRSC, and is negligible in the dRSC. The gRSC and dRSC also exhibit unique long-range circuitry, discussed in **Section 1.1.2**.

Finally, it should be noted that whilst the architecture of the RSC is similar through the anterior-posterior axis there are some differences: in particular, a small increase in thickness of the dRSC layer 4 in the posterior RSC (Vogt and Paxinos, 2014). Topographic organisation of RSC efferents and afferents also occurs along the anterior-posterior axis.

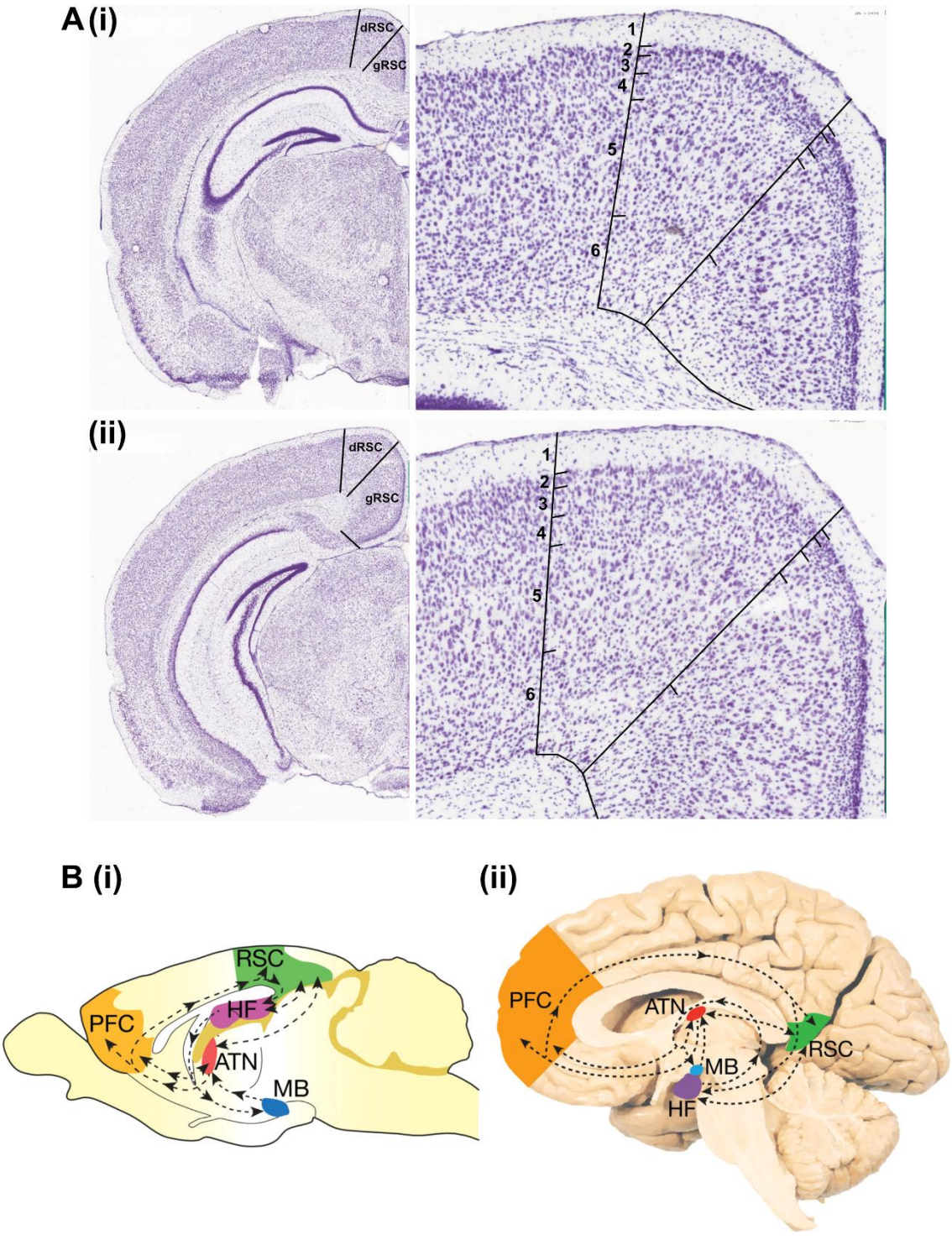

Figure 1.1 | RSC cytoarchitecture and position. **A** Sub-region and laminar distinctions of the **(i)** anterior and **(ii)** posterior RSC in the mouse brain. **B** Position of the RSC in context with other regions of the extended memory circuit in the **(i)** rodent and **(ii)** human brain (ATN: anterior thalamic nuclei; HF: hippocampal formation; MB: mammillary bodies; PFC: prefrontal cortex). Figure adapted from the Allen Brain Atlas (https://mouse.brain-map.org) (**A**) and (Barnett et al., 2018) (**B**).

1.1.1.2 | Pyramidal cell subpopulations in the RSC

Cortical brain regions, like the RSC, typically contain two broad neuron subtypes (Molyneaux et al., 2007): excitatory glutamatergic neurons, of which pyramidal cells (PCs) are the most common type, and inhibitory GABAergic (gamma aminobutyric acid) interneurons (IN). Notably, the RSC exhibits substantial heterogeneity of PC subpopulations within the gRSC region. In rats, the majority of PCs within layers 2 and 3 exhibit a phenotype termed 'late-spiking' (LS). These PCs have small somata, and demonstrate weak hyper-polarisation activated cation currents and increased latency to fire at supra-threshold depolarisation (Kurotani et al., 2013). Similar small PCs are found in the mouse superficial gRSC, and demonstrate a hyperexcitability phenotype compared to regular spiking (RS) PC (Brennan et al., 2020). This phenotype appears specific to the gRSC and perirhinal cortices (Beggs et al., 2000), and is suggested to support synaptic integration and information encoding for larger temporal delays of several hundred milliseconds (Kurotani et al., 2013).

Additionally, a small subset of burst-spiking (BS) PC have been identified in the rat gRSC layer 5 (Yousuf et al., 2020), and were related to RS PC with an unusually pronounced afterdepolarisation. These gRSC PC subpopulations are not present in juvenile rats, suggesting changes in neuronal firing within the RSC that emerge with age and experience. The dRSC also displays some PC heterogeneity, however focus has been on the subpopulations within layer 5 and not superficial PC (Sempere-Ferràndez et al., 2018). Within the dRSC, PCs in layers 2-3 are more hyperpolarised at rest and have a significantly smaller hyperpolarisation-activated current (sag) than PCs in layer 5, while two sub-populations of PCs in layer 5 are distinguished by differences in soma area, input resistance and sag.

1.1.2 | Connectivity of the RSC

One of the hallmark characteristics of the RSC is its high interconnectivity with many other areas of the brain. Neuroanatomical tracing studies in rats have demonstrated reciprocal connections with other cortical regions, including prefrontal cortex (PFC) structures, as well as hippocampal and limbic structures (Groen and Wyss, 2003, 1992, 1990). These connections have mostly been

confirmed in the mouse brain (Aggleton et al., 2021), and are conserved in the primate brain (Kobayashi and Amaral, 2003; Vogt et al., 1987). There is however a lack of information regarding RSC connectivity in the mouse brain, both neuroanatomically and functionally, which is necessary for understanding this area in context of its role in behaviour and within wider brain circuitry.

Whilst the dRSC and gRSC receive comparable density of inputs for many of these pathways, there are some key differences in connectivity between the sub-regions. In the rat brain, the gRSC preferentially receives inputs from the hippocampal formation, such as the CA1 region of the hippocampus (HPC) and the dorsal subiculum (dSub) (Wyss and Van Groen, 1992). These connections are organised along the anterior-posterior axis; the anterior RSC is primarily connected to the anterodorsal HPC and the posterior RSC to the posteroventral HPC. Additionally, the gRSC has denser connections with the anterodorsal nucleus and anteroventral nucleus of the anterior thalamic nuclei (ATN) (Groen and Wyss, 2003, 1990). The dRSC instead receives greater input from the primary visual cortex (V1) and extrastriate visual cortices, as well as the anteromedial nucleus and the lateral dorsal nucleus of the thalamus (Groen and Wyss, 1992).

As well as receiving a wide variety of long-range inputs, the RSC also sends many projections to distal brain regions. Most of these connections are reciprocal in nature and distributed evenly across the RSC sub-regions; however, one noteworthy difference between afferent and efferent connections of the RSC is the relative lack of direct input into the hippocampal formation from the RSC (Sugar et al., 2011). Instead, it is proposed the RSC exerts influence on the hippocampal formation via an indirect pathway through the entorhinal cortex and ATN (Prasad and Chudasama, 2013), highlighting the need to consider the RSC as part of a distributed neuronal circuit when examining its function and connectivity. **Figure 1.2** illustrates the afferent and efferent connectivity of the rodent gRSC and dRSC.

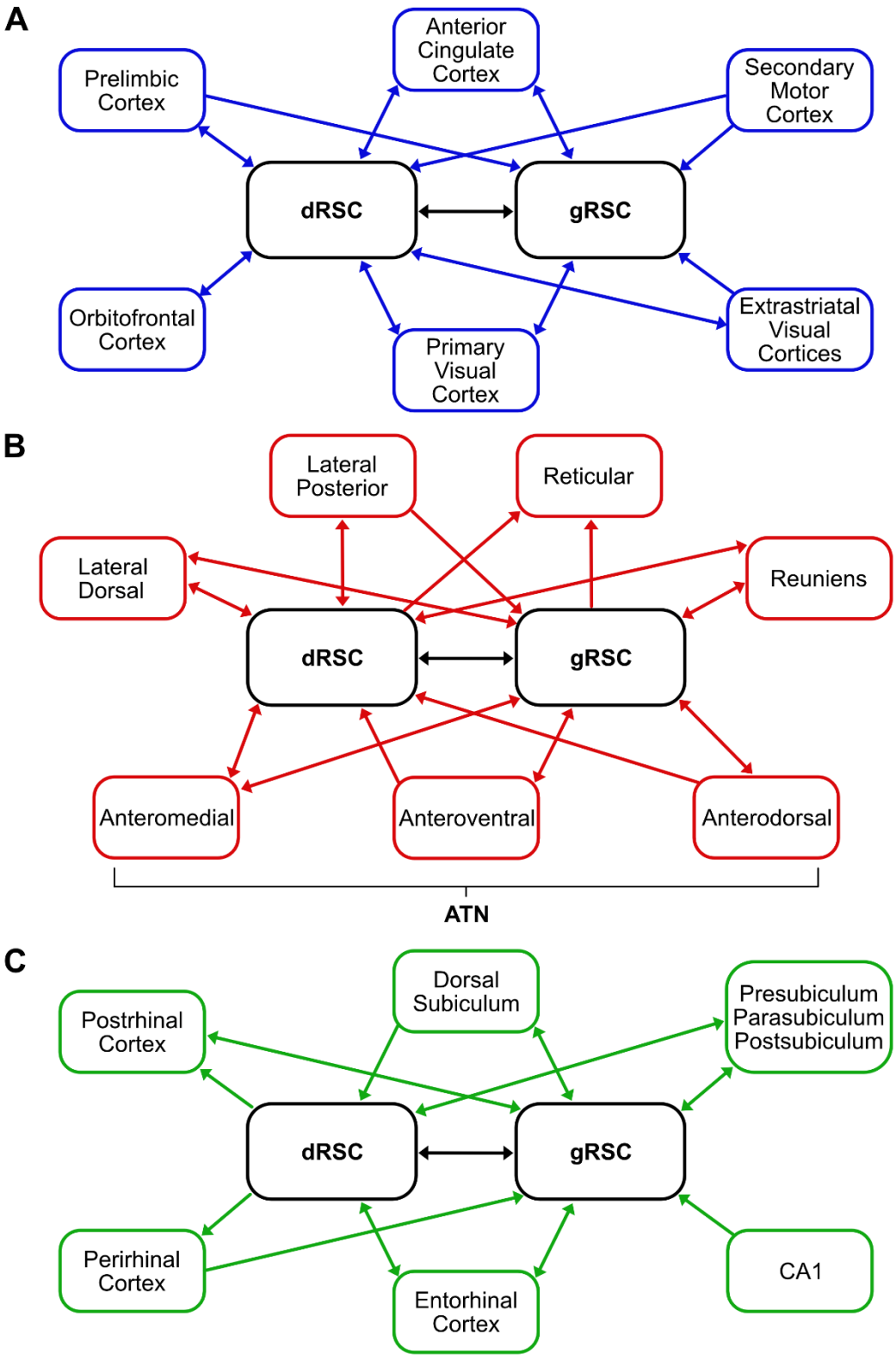

Figure 1.2 | Anatomical connectivity of the rodent gRSC and dRSC. Connectivity diagram indicating afferent and efferent connections with **A** cortical regions, **B** the various nuclei of the thalamus and **C** regions within the medial temporal lobe. Figure is adapted from (Aggleton et al., 2021),

and reflects the non-preferential targeting of the visual cortices and gRSC inputs to the anteromedial thalamic nucleus in the mouse brain.

Currently, an extensive neuroanatomical dissection of the mouse RSC connectivity is lacking; however, a review of the Allen Mouse Brain Connectivity Atlas indicated a lack of input preference for the visual cortices and some minor differences in the RSC to thalamus projections (Aggleton et al., 2021). Therefore, although existing literature on the rat brain is useful for informing hypotheses of the murine RSC, further important differences may come to light in the future.

Long-range inputs into the RSC also show preferential targeting of specific layers within the region. For example, in the gRSC axon terminations from the dSub are found primarily in layer 3 whilst projections from the ATN terminate mainly in layers 1 and 3. In contrast, whilst projections from the claustrum (CLA) and anterior cingulate cortex (ACC) are prominent in layer 1, they also target layer 5 extensively (Brennan et al., 2021). Projections from the secondary motor cortex (M2) preferentially terminate in layers 2-3 in the dRSC (Yamawaki et al., 2016). Further laminar targeting of the RSC by its afferents has been qualitatively described (Wyss and Van Groen, 1992), but its role in circuit function is yet to be fully explored.

Whilst the neuroanatomy of RSC connectivity has been extensively described, particularly in the primate and rat brain, there is limited evidence of the functionality of these connections. The literature indicates excitatory inputs into the gRSC from the dSub, ACC, AD/AV, CLA and M2 (Brennan et al., 2021; Nitzan et al., 2020; Yamawaki et al., 2016). Contrastingly, inputs from the CA1 region of the HPC primarily inhibit the gRSC, and intercept the ATN excitatory inputs (Opalka et al., 2020; Yamawaki et al., 2019b). Afferent inputs from different regions may also be associated with specific synaptic plasticity mechanisms: dSub, ACC and CLA projections into the gRSC exhibit short-term facilitation whereas ATN and CA1 projections are depressing (Brennan et al., 2021; Yamawaki et al., 2019a). Further dissection of these pathways indicates differences in strength or direction of innervation dependent on layer and cell-type (Brennan et al., 2021; Opalka et al., 2020). These afferent projections are also not independent of the rest of the brain; monosynaptic dSub inputs are invariably excitatory however a disynaptic inhibitory circuit has also been

described (Yamawaki et al., 2019a). Understanding the function of these circuits is crucial to dissecting the role the RSC plays in behaviour (see **Section 1.1.3.3**), therefore further research is required. In particular, there has been little to no examination of the function of the afferent connections into the dRSC.

Another approach to examining RSC connectivity is to consider the effects following the disconnection of specific pathways. The RSC is highly sensitive to deafferentation following damage to distally-connected brain regions. Significantly, decreased neuronal activity is observed following lesions in the HPC (Albasser et al., 2007; Jenkins et al., 2006), mammillothalamic tract (Frizzati et al., 2016) and ATN (Jenkins et al., 2004), whilst ATN lesions also cause a loss of synaptic plasticity (Garden et al., 2009) and transcriptional deregulation (Poirier et al., 2008) as well as decreased dendritic spine density (Wolff and Vann, 2019) in the RSC. These findings indicate the importance of RSC connections to its normal functioning, and further support the concept of the RSC as a critical node in an extended circuit.

On a final note, whilst the long-range inputs into the RSC are the focus of this thesis, it is also important to consider the micro-circuitry of the area. Within the RSC, there is evidence of connections between the dRSC and gRSC as well as bi-directional connections along the anterior-posterior axis (Shibata et al., 2009). Interhemispheric connectivity within the RSC is also seen via callosal input into the dRSC and gRSC (Robles et al., 2020; Sempere-Ferràndez et al., 2018), and this micro-circuitry also displays distinct cellular and laminar specificity. In fact, in primates up to 78% of RSC afferent and efferent connections originate and terminate within this area (Kobayashi and Amaral, 2003). Therefore, when discussing any layer or sub-region input specificity we must remain mindful of the extensive cortico-cortical pathways within the RSC itself.

1.1.3 | Behavioural function of the RSC

All behavioural studies discussed in Section 1.1.3 were conducted in rats unless stated otherwise.

1.1.3.1 | Silencing studies

Silencing of the RSC is a useful approach to study the necessity of this brain structure for different behaviours, and silencing methods can be permanent (lesioning) or transient (optogenetic, chemogenetic or pharmacological inactivation). Through these studies we have come to understand the importance of the RSC in spatial memory (see Mitchell et al., 2018 for review). Following lesions in the rodent RSC, impairments in tasks requiring spatial learning and memory were observed: such as the Morris water maze (Vann and Aggleton, 2004, 2002; Whishaw et al., 2001), radial arm maze (Keene and Bucci, 2009; Vann and Aggleton, 2004), matching-to-place (Whishaw et al., 2001) and object-in-place tasks (Parron and Save, 2004). Furthermore, RSC lesioning also leads to deficits in recall of contextually-conditioned fear responses when disrupted both pre- and post-training (Fournier et al., 2019a; Keene and Bucci, 2008a), and impairs performance in associative learning paradigms such as sensory pre-conditioning (Fournier et al., 2020; Keene and Bucci, 2008b; Robinson et al., 2011) and negative patterning discrimination (Fournier et al., 2019b).

The complex role of the RSC in learning and memory is evident in tasks in which RSC disruption leads to little or no perturbation in task performance. For example, the spatial memory deficits correlated with RSC disruption are mostly seen in tasks that require allocentric, not egocentric, spatial processing using distal visual cues (Hindley et al., 2014; Pothuizen et al., 2010; Vann and Aggleton, 2005). However, inactivation of the RSC disrupts navigation in the dark, but not light (Cooper et al., 2001), suggesting that the RSC is not solely concerned with allocentric processing. Disruption of the RSC also affects spatial processing when animals are required to discriminate between relevant and irrelevant cues regardless of whether they are distal or local (Nelson et al., 2015; Wesierska et al., 2009). RSC activity is also necessary for the association of environmental cues and related motor action to drive appropriate action selection for navigation in mice (Franco and Goard, 2021). Therefore, it is suggested that the RSC is crucial for both the integration of allocentric and egocentric information, as well as spatial strategy shifting and decision making (Mitchell et al., 2018). Subtleties within the radial arm maze task also indicate a nuanced role of the RSC; rats with RSC lesions showed increased errors of omission but not commission when a short delay was imposed between arm choices; however, when the delay was

increased errors of commission became evident (Keene and Bucci, 2009). This suggests that while the RSC is important in reference memory (errors of omission), the effect of RSC disruption on spatial working memory (errors of commission) is limited to highly taxing tasks.

Similar specific impairments can also be seen in associative learning paradigms. Whilst RSC lesioning impairs contextual conditioned fear responses, it does not affect fear response to a simple conditioned stimulus (CS) (Keene and Bucci, 2008c). Pavlovian responses to a reward-associated single CS are similarly not affected, however performance impairment is seen in tasks with multiple CS (Keene and Bucci, 2008b) following RSC disruption. This supports another integrative role for the RSC which includes linking separate stimuli and applying value. One of the most striking findings, however, has been that whilst the RSC is not necessary for the acquisition and retrieval of recent simple CS associations, lesioning of the RSC after consolidation significantly reduces fear response to a CS (Todd et al., 2016). Moreover, optogenetic disruption of the mouse RSC prevents retrieval of an associate relationship formed during the latent learning pre-conditioning phase, but later disruption during standard conditioning phases does not affect associative learning (Barros et al., 2021). Therefore, the RSC may be important for storage and retrieval of “remote” associative memories, and this mechanism is driven by N-methyl-d-aspartate (NMDA) receptors in mice (Corcoran et al., 2011). Evidence from a primate RSC lesion study also confirms the role of the RSC in memory retrieval, as bilateral lesioning of the RSC disrupts retrograde, but not anterograde, spatial memory in an object-in-place task paradigm (Buckley and Mitchell, 2016).

There is evidence of topographical organisation of behavioural function in the RSC, as the severity of the behavioural impairments has been shown to be modulated by the extent and placement of lesions along the anterior-posterior axis (Vann and Aggleton, 2004, 2002). Furthermore, silencing of the dRSC and gRSC are associated with distinct deficits: dRSC disruption primarily affects behaviours requiring visual cue information whilst contextual memory is affected following gRSC disruption (Aggleton et al., 2021). However, there is a lack of research directly comparing the two, and the evidence so far also indicates a large overlap in behavioural functions of the two RSC sub-regions.

The majority of knowledge of behavioural outcomes of RSC silencing comes from rodent research, as there is limited literature examining the effect of RSC-specific lesions in humans due to the rarity of localised damage. The data that are available do confirm a role for the RSC in spatial learning and memory, but also suggest a hemispheric lateralisation. Damage to the right RSC results in spatial impairments including navigation and orientation (Hashimoto et al., 2010; Maguire, 2001), whilst damage in the left RSC is associated with anterograde and retrograde episodic memory amnesia (Kim et al., 2007; Maguire, 2001; Valenstein et al., 1987). Furthermore, whilst the extent of cognitive impairment and future prognosis are heavily affected by the size and placement of the damage; prognosis is still generally good even with bilateral RSC lesions (Kim et al., 2007).

1.1.3.2 | Neuronal activity and activation studies

A complementary approach to understanding the function of a particular brain area is to measure the changes in activity during behavioural tasks and infer causality. Histological analysis of markers of neuronal activity, such as the immediate early genes (IEG) *Fos* and *zif268*, indicate increases in RSC activity immediately following a spatial working memory task (Pothuizen et al., 2009). In mice, RSC neuronal activity during memory retrieval is also potentiated after consolidation (1 day vs 30 day post-training), unlike in the hippocampus, suggesting learning and long-term storage are both RSC-dependent (Maviel et al., 2004). Fos protein expression also increases following contextual associative learning and retrieval in mice (Toropova et al., 2020), as well as following instrumental conditioning in rats (Svarnik et al., 2005).

Importantly, the presence of elevated Fos appears a valid indicator of learning and memory in the RSC. Two-photon imaging studies in mice have shown that training in spatial memory tasks recruits specific neuronal ensembles (or engrams) that are then re-instated during retrieval, and that the stability of these engrams are also directly predictive of future performance (Milczarek et al., 2018). Furthermore, optogenetic re-activation of behaviourally-tagged neuronal ensembles in the RSC – using the mouse Fos Tet Tag system – re-instates contextual fear behaviour (Cowansage et al., 2014). Re-activation of contextual

fear ensembles using high-frequency stimulation potentiates consolidation by decreasing time for a recent memory to exhibit remote memory features in mice: such as decreased hippocampal dependence, context generalisation and greater engagement of neocortical regions (de Sousa et al., 2019). Finally, blocking Fos activation in the RSC prevents long term retention of fear memory (Katche and Medina, 2017).

Not only does the RSC present encoding of behavioural neuronal ensembles similar to the HPC, but there is also substantial evidence of complex spatially- and functionally-tuned neurons. Head-direction (HD) cells have long been identified in rats in the dRSC and gRSC (Chen et al., 1994b), however their direction preferences are often modulated by locomotion or visual cue rotation (Chen et al., 1994a) and their firing is anticipatory (Cho and Sharp, 2001; Lozano et al., 2017). Further research has also identified sub-populations of neurons which encode visual landmarks and cues (Fischer et al., 2020; Powell et al., 2020) and locomotor activity in mice (Powell et al., 2020), as well as reward location (Vedder et al., 2017) and spatial border locations (van Wijngaarden et al., 2020) in rats. “Place cells” have also been found in the mouse RSC, however these spatially-tuned cell formations show unique characteristics compared to those found in the HPC as they are experience-dependent and develop gradually over time (Mao et al., 2018). Additionally, the “border cells” found in the rat RSC differ from those in the medial entorhinal cortex as they are less specific, responding to multiple walls and various preferred distances, and are egocentrically tuned (Alexander et al., 2020; van Wijngaarden et al., 2020).

In order to understand the role of the RSC in cognition in humans, functional magnetic resonance imaging (fMRI) has proved a useful tool to measure correlates of neuronal activity during tasks in a non-invasive manner. Research has focused on the role of the RSC in spatial navigation, and this region has been found to be engaged when encoding heading direction (Baumann and Mattingley, 2010), spatial location (Marchette et al., 2014), visual landmarks (Auger et al., 2012), and map-like representations of an environment (Henderson et al., 2011; Wolbers and Büchel, 2005). RSC engagement is also a good predictor of spatial navigation ability with good navigators showing significantly higher BOLD signal in the RSC (Auger et al., 2017, 2012). Moreover, the RSC is highly activated during path integration – which requires knowledge of locomotion, orientation and

location – indicating an integrative function of the RSC similar to that observed in rodents (Sherrill et al., 2013). RSC activity is also associated with both egocentric and allocentric information processing, and EEG data indicates strong RSC engagement during a virtual task requiring translation of egocentric visual flow into an allocentric model of their location (Gramann et al., 2010). As well as spatial processing, meta-analysis of fMRI studies has implicated the RSC in retrieval of recent and remote autobiographical episodic memories (Svoboda et al., 2006) and emotional processing (Maddock, 1999).

1.1.3.3 | RSC connectivity is crucial to its behavioural function

The neuronal silencing and activation studies reviewed in **Sections 1.1.3.1 and 1.1.3.2** indicate that the RSC is a functionally distinct area of the brain necessary to drive behaviours such as spatial processing and memory consolidation and retrieval. However, the RSC is highly interconnected and functional connectivity between the RSC and other brain regions is important in RSC-dependent behaviours. Indeed, the RSC is considered a critical node in two key neural circuits underlying these behaviours: the default mode network (DMN) and extended memory circuit (EMC), formerly known as the Papez circuit (Vann et al., 2009). Brain areas comprising these two circuits are not mutually exclusive, and the RSC is suggested to be a “gateway” between the medial temporal lobe (MTL) – part of the EMC which contains brain regions such as the hippocampus – and the DMN (Kaboodvand et al., 2018). This “gateway” role may underlie the function of the RSC in transforming and integrating egocentric and allocentric information as part of a gain-field circuit, in which neurons conjunctively encode both self-referenced (e.g. body motion) and externally referenced (e.g. environmental) information (Bicanski and Burgess, 2018; Byrne et al., 2007). The complexity of the spatial and mnemonic representations encoded in the RSC supports this theory of a gain-field circuit, as these representations rely on combining multiple sources of information processed in distal brain regions. For example, landmark-encoding cells in the rodent RSC are dependent on integration of visual, motor and spatial information (Fischer et al., 2020). Whilst in humans path integration requires recruitment of the RSC, HPC, medial PFC and parahippocampal cortex (Chrastil et al., 2015). Therefore, disrupting

information flow in or out of the RSC could have significant negative effects on its function.

Models of long-term memory consolidation have posited the HPC as a site of rapid learning which induces changes in the neocortex for stable storage (McClelland et al., 1995), as is suggested by increased activity and cortical reorganisation in the RSC following HPC activity after a spatial memory task in mice (Maviel et al., 2004). Critically, the formation of certain memories within the RSC has been shown to be HPC-dependent. Whilst *Fos* gene expression is necessary for memory formation in both the HPC and RSC at recent and remote time points respectively (Katche et al., 2010; Katche and Medina, 2017), disruption of either area during the critical window for the other prevents maintenance of the memory (Katche et al., 2013). Furthermore, disruption of the HPC is sufficient to abolish the detection of place cells in the mouse RSC (Mao et al., 2018), and conversely inactivation of the RSC reorganises spatial encoding in the HPC itself in rats (Cooper and Mizumori, 2001).

One proposed mechanism for transfer of information from the HPC to the cortex is the propagation of high frequency neural activity patterns, named sharp wave-ripples (SWRs) (Buzsáki, 2015). SWRs are thought to support memory consolidation and retrieval in the HPC (Joo and Frank, 2018), and bursts of oscillatory activity in the ripple frequency band have been observed in the RSC (Khodagholy et al., 2017). SWRs in the HPC are correlated with large peaks in activity in the RSC – measured using a voltage sensitive dye and a glutamate-sensing fluorescent reporter – and this increase in activity was greater than in any other neocortical region in mice (Karimi Abadchi et al., 2020). Moreover, this relationship is bidirectional as RSC activity modulates hippocampal SWR generation; activity increases in the RSC before SWR generation and is suggested to mediate initial information flow in the neocortical-hippocampal-neocortical information loop. Additionally, SWR activity in the RSC is coupled with that in the HPC, and ensembles within the HPC mediate gRSC SWRs via excitatory projections from the subiculum in mice (Nitzan et al., 2020). The mouse RSC also shows anticipatory local disinhibition combined with decreased thalamic input (Chambers et al., 2022) 1-2 seconds before SWR activity, demonstrating that external afferents to the RSC can gate local circuit activity. Other forms of neuronal ensemble encoding are also regulated by different

pathways into the RSC, such as border cell encoding, which relies on input from the medial entorhinal cortex (van Wijngaarden et al., 2020).

Transient silencing of specific pathways in mice has further elucidated the importance of RSC afferents for normal behavioural function. Chemogenetic silencing of the excitatory ATN to RSC pathway attenuates context-induced freezing responses, whilst silencing the inhibitory CA1 to RSC pathway potentiates this behaviour (Yamawaki et al., 2019b). Contrastingly, optogenetic silencing of dorsal HPC (dHPC) projection terminals in the RSC impaired context-induced freezing (Opalka and Wang, 2020). However, in this study viral injections into the dHPC targeted both the CA1 region of the HPC and the dSub; therefore, it is likely behavioural impairment is due to silencing of the excitatory subicular efferents as the RSC receives substantially denser projections from this region. Specific targeting of different cell types in the presynaptic region can also alter behavioural outcome. Input into the RSC from the dSub can be separated into two sub-groups of excitatory projection neurons: those expressing vesicular glutamate transporter 1 (vGlut1) and vGlut2. Optogenetic stimulation of these axons triggers different inhibition and excitation patterns in the RSC, and chemogenetic silencing of vGlut1 projections impairs recent memory retrieval whilst vGlut2 silencing disrupts remote memory (Yamawaki et al., 2019a). Although there is currently limited evidence for the distinct functions of specific pathways in behaviour, it is clear that the RSC relies on – and also significantly modulates – activity in the distal regions it is directly and indirectly connected to in order to drive normal learning and memory processes. Finally, the RSC may allow integration of multiple sources of behaviourally salient information derived from upstream brains areas as well as internally between the gRSC and dRSC (Sigwald et al., 2019).

1.2 | Alzheimer's disease

1.2.1 | Introduction to Alzheimer's disease

Dementia is classified as a syndrome whose symptoms include memory loss, confusion and problems with language and understanding. Alzheimer's disease (AD) is the most common cause of dementia, accounting for between 60-70% of cases. AD is characterised by the deposition of extracellular plaques and

intracellular neurofibrillary tangles (NFT) in the brain, which are formed by aggregation of amyloid-β (Aβ) proteins and hyperphosphorylated microtube-associated protein tau (tau) respectively (Serrano-Pozo et al., 2011). AD is an increasingly prevalent neurodegenerative disorder which leads to gross morphological and synaptic degradation (Knobloch and Mansuy, 2008), and its neuropathological markers are correlated with irreversible and progressive memory loss and decreases in other cognitive functions such as attention and decision making (Duyckaerts et al., 2009).

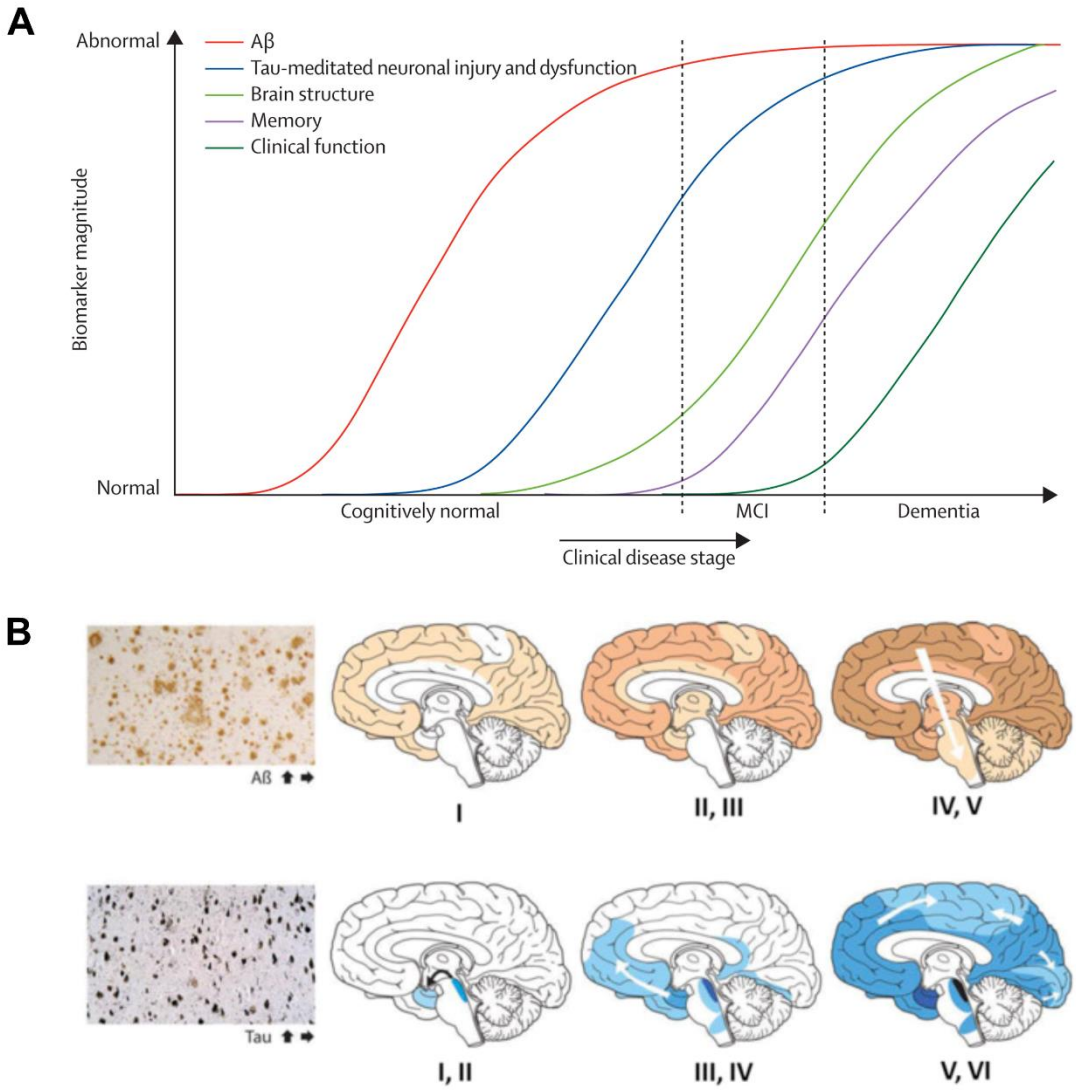

Figure 1.3 | AD neuropathology development. A Schematic illustrating the developmental time-course of pathological biomarkers of AD against the clinical staging of disease. Note that Aβ deposition begins before other neuropathologies or cognitive symptoms. **B** Aβ and tau deposition follow distinct and reliable spatial-temporal patterns in the brain, with the isocortex

expressing amyloidopathy in the prodromal stages. Figure is adapted from Jack et al. (2010) and Jucker and Walker (2011).

AD is typically considered to progress through 3 clinical stages: pre-symptomatic, mild cognitive impairment (MCI) and dementia (Jack et al., 2010). The neuropathological progression of AD has also been extensively described (Braak and Braak, 1991a; Thal et al., 2002) and follows distinct spatial-temporal patterns (**Figure 1.3 B**). When considering the timeline of AD development, the primary neuropathological marker of early-stage – or pre-clinical – AD appears to be amyloidopathy which presents before all other neurodegenerative markers and cognitive decline (Jack et al., 2010) (**Figure 1.3 A**). While amyloidopathy is not the only pathology present at onset of MCI, it is still an essential marker of later prodromal and clinical AD. Understanding how the brain is affected in prodromal AD is important for identifying therapeutic targets to prevent or delay subsequent severe cognitive decline. Functional changes in the RSC in AD patients – such as glucose hypometabolism and hypoactivity – are some of the earliest biomarkers of the disease (Vann et al., 2009), and disrupted functional connectivity of the RSC distinguishes patients with mild AD from normal cognitive aging (Greicius et al., 2004). These functional biomarkers in the RSC coincide with increased amyloid deposition in the region during MCI (Buckner et al., 2005), and the research in this thesis focuses on the effects of amyloidopathy on RSC circuitry.

1.2.2 | Amyloidopathy and the amyloid cascade hypothesis

Amyloid precursor protein (APP) is a transmembrane protein that is converted by proteolytic processing into several fragments, including Aβ (Müller and Zheng, 2012). APP plays a fundamental role in both the developmental and adult central nervous system (CNS), and is necessary for regulating neuronal excitability, synaptic plasticity and learning and memory (S. H. Lee et al., 2020)., however deregulation of its downstream product Aβ is synonymous with AD.

APP undergoes proteolytic cleavage via two principal pathways characterised as either being amyloidogenic (Aβ generating) or non-amyloidogenic (non-Aβ generating), by way of specific protease processing (Chow et al., 2010; Hefter et al., 2020). In the non-Aβ generating pathway, α-secretase cleaves APP to create

soluble APPα (sAPPα) and a C-terminal fragment, CTF83, which is further cleaved by γ-secretase to produce the short peptide p3 and the amino-terminal APP intracellular domain (AICD) (**Figure 1.4 A**). Importantly, cleavage by α-secretase occurs at a site located within the Aβ peptide sequence – thereby preventing Aβ generation through this pathway – whilst sAPPα is neuroprotective in its own right (Mockett et al., 2017). Conversely, β-secretase cleavage of APP occurs at the N-terminus of the Aβ sequence to generate CTF999; subsequent γ-secretase processing of CTF999 results in creation of Aβ peptides as well as the AICD (**Figure 1.4 B**). Aβ fragments can range from 38-43 amino acids in length, and certain forms are considered more pathogenic than others (Chow et al., 2010). Finally, a third APP processing pathway has been recently identified in which η-secretase cleaves APP after the N-terminus of the Aβ sequence, which allows for subsequent α- and β-secretase cleavage (Willem et al., 2015) (**Figure 1.4 C**). Therefore, this pathway can be both amyloidogenic and non-amyloidogenic, and whilst its function is currently unknown there is preliminary evidence of the products being synaptotoxic.

The classic amyloid cascade hypothesis suggests that aggregation of Aβ initiates a pathogenesis cascade in AD, so that neuropathologies such as NFT, cell loss and cognitive decline are a downstream result of Aβ deposition (Hardy and Higgins, 1992). Aβ monomers formed after β-secretase cleavage of APP are prone to aggregate into various forms including soluble oligomers and insoluble fibrils (**Figure 1.4 D**), and the 42 amino acid Aβ42 isoform, in particular, is more likely to aggregate due to its structure and increased hydrophobicity (Chen et al., 2017; Long and Holtzman, 2019). Whilst Aβ plaques are an easily recognisable neuropathological marker of AD, and application of fibrils to *in vitro* cultured cells is highly neurotoxic (Lorenzo and Yankner, 1994), evidence suggests the damaging effects of Aβ *in vivo* are more likely due to the action of Aβ oligomers on the brain (Klein, 2013). Neuronal death, tau hyperphosphorylation and synaptic dysfunction are suggested to be downstream effects of Aβ binding to various neuronal receptors (Chen et al., 2017). Furthermore, Aβ aggregates are suggested to become prion-like, allowing for self-propagation through the brain and intracellular accumulation (Watts and Prusiner, 2018). Acute application of Aβ oligomers, but not monomers, has also been shown to disrupt cognitive function in wild-type animals (Cleary et al., 2005).

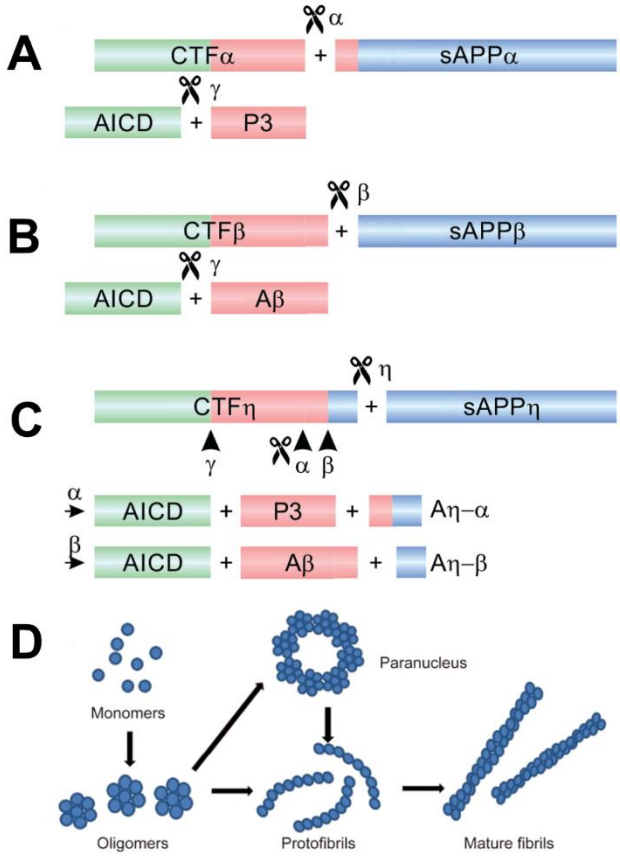

Figure 1.4 | APP cleavage pathways and Aβ aggregation. A-C Cleavage pathways by α-secretase, β-secretase and η-secretase. **D** Aβ monomers formed from γ-secretase cleavage following β-secretase aggregate into various protein species including soluble oligomers and insoluble fibrils. Figure is adapted from Chen et al. (2017) and Hefter et al. (2020).

The amyloid cascade hypothesis is supported by evidence of a genetic component of early-onset familial AD (EOFAD): around 50% of EOFAD patients carry mutations in either the APP gene or the presenilin (PSEN) 1 and 2 genes which encode for subunits of γ-secretase (Wu et al., 2012). There are currently 210 mutations found within these genes that are confirmed or suspected to be pathogenic for AD (ALZFORUM, 2022), and they are generally associated with alterations in Aβ production and processing. Alterations caused by these mutations can include increases in total Aβ, elevated Aβ42/Aβ40 ratio, and increased propensity for Aβ aggregation and fibrilisation (Long and Holtzman, 2019). Furthermore, triplicate copies of the APP gene are associated with AD and increased amyloid burden in people with trisomy of human chromosome 21 (Down's Syndrome) (Salehi et al., 2016). However, EOFAD only accounts for

around 5% of total AD diagnoses, and as few as 13% of those cases are inherited in an autosomal dominant manner for more than 3 generations (Bekris et al., 2010). The most common subtype of AD is late-onset AD (LOAD) which presents much later in life and is often sporadic in occurrence with no dominant genetic cause. Genetic risk factors have been identified for LOAD, such as the apoliproptein E (APOE) ε4 polymorphism which significantly increases the chance of developing AD in later life (Corder et al., 1993). The APOE ε4 allele does not directly affect Aβ production however, but instead disrupts clearance of soluble Aβ allowing increased accumulation in the brain (Castellano et al., 2011). Aβ clearance can occur through a variety of different mechanisms – including transvascular clearance across the blood brain barrier, enzymatic degradation and microglial phagocytosis (Rogers et al., 2002; Yoon and Jo, 2012) – providing multiple potential points of failure in the system. Therefore, for most forms of AD it may be better to consider pathogenesis as arising from a deficiency in clearance of cerebral Aβ rather than over-production (Mawuenyega et al., 2010).

There are problems with the amyloid cascade hypothesis however, suggesting that an update of the model is needed. Genetically modified rodent models expressing EOFAD mutations show Aβ deposition in the brain and behavioural impairments, but not NFT formation or neuronal cell death (Elder et al., 2010). However, this may be due to rodents not possessing humanised tau and therefore missing a crucial step in the cascade. Mice and humans both express tau protein, but their isoform profiles are different (Andorfer et al., 2003). Humans generate 6 isoforms, which are described as either 3 repeat (3R) or 4 repeat (4R) and are found in equal levels in the brain, while mice only generate 4R isoforms. While NFTs found in AD patients contain both 3R and 4R tau (Jellinger and Attems, 2007), NFTs found in brain regions which exhibit early tau depositions predominantly contain 3R (Kitamura et al., 2005). Moreover, when AD-patient-derived pathological tau is injected into a mouse model of amyloidopathy, Aβ aggregates facilitate formation and spread of NFTs (He et al., 2018). Additionally, in a chimeric model of AD, human pluripotent stem cells transplanted into a mouse model of amyloidopathy developed tauopathy and neurodegeneration (Espuny-Camacho et al., 2017). Furthermore, amyloid deposits are found in cognitively normal people (Davis et al., 1999), suggesting that the development of some amyloid pathology is a feature of normal aging. Also, whilst high amyloid

burden is predictive of AD, a small percentage of clinically-probable patients who fulfil other clinical criteria for AD do not show increased amyloid load (Edison et al., 2007) and cognitive impairment better correlates with NFT burden in the neocortex (Nelson et al., 2012). Finally, the amyloid cascade hypothesis posits that Aβ depositions directly cause tauopathy, however the spatial-temporal progression of these two neuropathologies is remarkably different (**Figure 1.3 B**).

A recent alternative to the classical 'amyloid hypothesis' has been proposed called the "cellular phase of AD" hypothesis (De Strooper and Karran, 2016). This theory attempts to reconcile evidence that Aβ has limited predictive validity for AD, and suggests that amyloidopathy and tauopathy evolve separately in a biochemical phase of AD that initially has little symptomatology due to compensatory mechanisms. It is only when the two pathologies interact that AD manifests in a cellular phase, after homeostasis can no longer be maintained due to excessive cellular stress that causes neurodegeneration to occur. This degeneration is a result of multiple factors and feedback loops, including disrupted clearance of Aβ and tau, and eventually leads to breakdown of the cellular homeostasis culminating in the clinical phase of AD in which cognitive impairments appear. Therefore, whilst Aβ pathology plays a crucial role in AD development, it has a more complex relationship with the disease than simply causative. However, it is important to understand the effects of Aβ deposition in the early stages of AD – before tauopathy development and subsequent cellular death – to describe the initial effects of cellular stress on cellular and synaptic function. Identifying these effects could point us towards future preclinical or prodromal AD biomarkers.

1.2.3 | Effects of amyloidopathy on synaptic function

1.2.3.1 | Synaptic loss

The ability of the brain the brain to collect, transfer and store information is enabled by communication between neurons via synaptic transmission, and any disruption or degradation of synaptic transmission through diseases such as AD can have devastating effects on cognitive function. Synaptic impairment is suggested to be the basis of memory loss in prodromal AD, and synapse loss is highly correlated with severity of cognitive symptoms in AD patients (DeKosky

and Scheff, 1990; Terry et al., 1991). Synapse loss also occurs at a significantly higher rate than neuronal loss as the synapse to neuron ratio decreases in AD (Davies et al., 1987).

Although the cellular phase of AD hypothesis describes an interaction of Aβ and tau pathology as necessary for full expression of AD, the effects of amyloidopathy on synaptic dysfunction have been well described particularly in the HPC. Mouse models of amyloidopathy show significant synaptic loss and dendritic abnormalities primarily localised around amyloid plaques (Pozueta et al., 2013). Synaptic loss has also been observed in areas without plaque deposition in mouse models of hAPP overexpression (Mucke et al., 2000) – suggesting soluble Aβ oligomers may be responsible for this synaptic degradation – and prior to plaque formation these soluble Aβ aggregates cluster around synaptic terminals (Klementieva et al., 2017). This theory has been tested directly through application of soluble Aβ oligomers to healthy mouse brain tissue both *in vitro* and *in vivo*, and leads to significant dendritic simplification and spine loss (Arbel-Ornath et al., 2017; Wu et al., 2010). Interestingly, using a controllable APP mouse model under a tTA promoter, it was found that prevention of further Aβ production after initial plaque deposition leads to synaptic recovery which is correlated with improved cognitive function (Fowler et al., 2014).

1.2.3.2 | Synaptic dysfunction

The effect of Aβ is not confined to morphological impairments, but also affects synaptic function. Of interest are the effects of Aβ on synaptic plasticity; mechanisms within the brain which are important for the encoding and consolidation of memory (Takeuchi et al., 2014). Synaptic plasticity describes the process by which the synaptic strength between neurons strengthens or weakens (Citri and Malenka, 2008). This umbrella term typically refers to either long term potentiation (LTP) or long-term depression (LTD), but other forms of short-term plasticity such as facilitation and depression also play a significant role.

In very low concentrations, such as would be found in normal non-AD conditions, Aβ actually facilitates both LTP and learning and memory outcomes (Morley et al., 2008; Puzzo et al., 2011, 2008). Pathological levels of Aβ42 however have very different effects: amyloidopathy mouse models exhibit both a significant

decrease in LTP and increase in LTD (reviewed by Mango et al., 2019). Similar to the morphological changes in synapses, this effect on synaptic function is driven by soluble Aβ oligomers which inhibit LTP and enhance LTD in the hippocampus when acutely applied to either *ex vivo* slices (Li et al., 2009; Shankar et al., 2008; Wang et al., 2002) or *in vivo* (Walsh et al., 2002). However, it should be taken into consideration that the disruptive effect of Aβ oligomers on LTP in hippocampal slices requires the presence and phosphorylation of tau protein (Shipton et al., 2011), indicating an interactive effect of Aβ and tau on synaptic plasticity in AD.

Synaptic plasticity disruption is likely a result of Aβ disruption of glutamatergic signalling (see **Section 1.3.3** for a discussion of the glutamatergic system) both pre- and postsynaptically. Acute application of Aβ oligomers to mouse hippocampal slices depresses excitatory neurotransmission and enhance paired pulse facilitation (PPF) by decreasing presynaptic glutamate release probability (He et al., 2019). Pathologically elevated Aβ levels in APP_{Ind} mice are correlated with significant impairment to basal synaptic transmission in hippocampal slices from 4 weeks old – while, in the postsynaptic compartment, an increased ratio of N-methyl-d-aspartate (NMDA) receptor response to α-amino-3-hydroxy-5-methyl-4-isoxazolepropionic acid (AMPA) receptor response is observed in this mouse model from 8 months (Hsia et al., 1999). In murine organotypic hippocampal slice cultures, inducing overexpression of human Aβ leads to downregulation of AMPA receptors; which may in turn be driven by the observed facilitation of LTD (Hsieh et al., 2006). Overall, the literature suggests amyloidopathy leads to a significant imbalance in synaptic plasticity: decreased ability to strengthen synapses via LTP combined with elevated LTD-driven synaptic weakening. Furthermore, whilst amyloidopathy may supress synaptic transmission, it is also associated with neuronal hyperexcitability in various amyloidopathy mouse models such as in >20-month-old PDAPP mice (Stargardt et al., 2015 (review); Tamagnini et al., 2015). Thus an imbalance between synaptic function and neuronal activity is created which may perpetuate neurodegeneration (Palop and Mucke, 2016).

The mechanisms through which Aβ perturbs synaptic transmission and plasticity are still not completely understood; however, its ability to bind to various neuronal receptors and affect secondary signalling pathways is likely an important factor.

In particular, emphasis has been given to Aβ actions on the NMDA receptor (NMDAR) as acute *in vivo* application of Aβ oligomers to the rat hippocampus significantly enhances NMDAR responses (Molnár et al., 2004). In hippocampal cultures application of Aβ oligomers results in dendritic spine loss modulated via NMDAR signalling pathways following calcium ion (Ca^{2+}) influx (Shankar et al., 2007), as well as demonstrating Aβ-mediated oxidative stress is also NMDAR-dependent (Decker et al., 2010). Aβ-mediated synaptic depression can also be similarly explained through AMPA receptor (AMPAR) endocytosis, which is a mechanism of LTD following NMDAR activation and Ca^{2+} influx (Tu et al., 2014). Indeed, blocking pathological NMDAR signalling using the use-dependent NMDAR channel blocker memantine improves cognitive function in >6-month-old 3xTg-AD mice (Martinez-Coria et al., 2010). Memantine also prevents synaptic loss in neuronal/glial cell cultures (Talantova et al., 2013) and inhibition of LTP in murine hippocampal slices (Martinez-Coria et al., 2010) following application of Aβ oligomers. Similarly, elevated expression of postsynaptic density protein 95 – which is normally significantly reduced in AD – protects neurons in organotypic hippocampal slices from Aβ-mediated toxicity and synaptic depression by downregulating NMDAR signalling (Dore et al., 2021). Aβ also non-directly affects the glutamatergic system by disrupting the astrocytic clearance of extracellular glutamate following acute Aβ oligomer application to *ex vivo* neuronal slices, causing elevated glutamate levels that spread beyond the target synapse (Scimemi et al., 2013). Overall, Aβ toxicity is closely related with the excitotoxic effects of an imbalanced glutamatergic system, leading to synaptic dysfunction and later neuronal damage.

Of course, the glutamatergic system is not the only neurotransmitter system affected in AD. The cholinergic system is also disrupted, with loss of cholinergic neurons as well as muscarinic (mAChR) and nicotinic (nAChR) acetylcholine receptors (Buckingham et al., 2009; Hampel et al., 2019; Yi et al., 2020). nAChR activation in the brain is associated with increased performance on memory tasks in rodents, monkeys and humans (Levin and Simon, 1998), and contributes to synaptic transmission and plasticity (McKay et al., 2007). Interestingly, Aβ effects on nAChRs follow a similar concentration pattern as lower “normal” Aβ peptide levels potentiate nAChR activation in isolated hippocampal and neocortical synaptosomes, but pathological Aβ levels inhibit this receptor activity (Dougherty

et al., 2003). Furthermore, M1 mAChR activation is also associated with the regulation of synaptic plasticity (Shinoe et al., 2005), and there is a significant loss of M1 mAChR protein in the temporal cortex of patients with AD compared to age-matched non-disease controls (Yi et al., 2020). Furthermore, acute application of Aβ oligomers weakens postsynaptic mAChR function in organotypic and *ex vivo* hippocampal slices via aberrated activation of metabotropic glutamatergic receptors, while administration of an mGluR5-negative allosteric modulator restores novel object recognition in 6-month-old 5XFAD mice (Yi et al., 2020). Therefore, dysfunction of glutamatergic synaptic transmission and associated plasticity imbalance in AD may be modulated by other neurochemical systems. This highlights the importance of considering neuronal and brain region impairments within the context of a larger interconnected system.

It is important to be aware that much research on the effects of amyloidopathy on synaptic plasticity have either looked at cultured neurons or focused on the HPC. There is, however, evidence of synaptic depression in the neocortex of APP/PS1 and AβPPPS1-21 mice (Battaglia et al., 2007; Lo et al., 2013), indicating effects beyond the HPC which deserve future attention.

1.2.4 | Looking beyond the medial temporal lobe in AD

Studies focusing on the hippocampus and other structures in the MTL have dominated AD research. However, from examining the spatio-temporal spread of AD pathology, it is clear that other brain areas exhibit pathological alterations – including Aβ deposition – in the early stages of disease (Braak and Braak, 1991a), and are so prime targets for study into preclinical and prodromal AD (Aggleton et al., 2016). Two such areas considered in this thesis are the RSC and the ATN.

1.2.4.1 | RSC and AD

The hypothesis that the RSC is disrupted in AD arises from both its important role in learning and memory (**Section 1.1.3**) and the fact it displays neuropathological changes early in AD development. The RSC is one of the first regions to show glucose hypometabolism in prodromal AD and MCI patients (Minoshima et al., 1997; Nestor et al., 2003; Villain et al., 2008), and this metabolic decline is

correlated with cognitive impairment (Desgranges et al., 2002). The RSC also shows atrophy of grey matter comparable to the HPC (Pengas et al., 2010), and HPC atrophy itself is correlated highly with RSC hypometabolism (Villain et al., 2008). Interestingly, the RSC is often grouped within the posterior cingulate cortex (PCC) for analysis due to the limited anatomical resolution of imaging using in the clinical assessment of AD, but it actually shows distinct functional connectivity patterns in AD progression (Dillen et al., 2016). In prodromal AD, the RSC fails to mediate HPC functional connectivity with other nodes in DMN indicating a breakdown in communication across distributed neural networks involving the RSC (Dillen et al., 2017). These disruptions in function may be due to early accumulation of Aβ and tau in the RSC (Palmqvist et al., 2017; Ziontz et al., 2021), and associated synapse loss (Scheff et al., 2015).

Various mouse models of amyloidopathy confirm RSC Aβ deposition during early stages of pathological progression (Reilly et al., 2003; Whitesell et al., 2019), and these depositions are correlated with behavioural impairment in 4-month-old 5xFAD Tg mice (Kim et al., 2020). Dysfunction of the RSC is observed before Aβ aggregation into plaques in Tg2576 mice, presenting as significantly decreased neuronal activity and increased energy metabolism following exposure to a novel environment (Poirier et al., 2011). Amyloidopathy is also associated with disrupted functional connectivity within the DMN, which includes the RSC, in both developmental and mature-onset amyloidopathy mouse models (Ben-Nejma et al., 2019; Shah et al., 2013). Additionally, disruption in neural activity patterns related to behaviour have been observed; such as impaired PFC-RSC coupling during sleep (Zhurakovskaya et al., 2019). However, it should be qualified that the Aβ accumulation seen in the RSC – and its subsequent functional consequences – are driven by non-endogenous promoters and not an exact recapitulation of AD.

That the functional connectivity of the RSC is altered in AD is not surprising given the evidence that Aβ pathology can disrupt synaptic function and that the RSC's distributed synaptic connectivity underpins its role in learning and memory. Indeed, this interconnectivity may be the root of early neuropathological changes in the RSC, as Aβ propagation into the RSC requires intact synaptic transmission (George et al., 2014). Changes in the RSC in prodromal AD may also be a result of the area being a site of covert pathology. The RSC is highly sensitive to

deafferentation (see **Section 1.1.2**) and its neuronal activity and metabolic pathology could be linked to damage in other afferent-projecting brain regions also known to be involved in early AD such as the PFC, hippocampal formation and various thalamic nuclei.

1.2.4.2 | ATN and AD

The thalamus consists of a range of nuclei, of which the ATN are of particular interest in AD. The ATN can be subdivided into the anterodorsal (ADN), anteroventral (AVN) and anteromedial (AMN) nuclei: these nuclei have a lot of overlap in their function and connectivity but do show some topographical differences in their connectivity to the RSC (**Section 1.1.2**). This introduction, however, considers the ATN as a functional group because, whilst the individual nuclei each contribute to learning and memory, their combined contribution is far greater. Additionally, there is limited literature available which has isolated individual nuclei to assess their distinct behavioural function; therefore, historically this area is considered as a collective brain region.

The diencephalic model of memory proposes that the thalamus – in particular the ATN – plays a crucial role in episodic memory encoding and recall (Aggleton et al., 2011; Aggleton and Brown, 1999). Patients who have sustained damage to the thalamus following infarction present with deficits in long-term episodic memory (Van der Werf et al., 2003), whilst specific lesioning of the ATN in rodents similarly disrupts behavioural measures of memory acquisition and recall (Aggleton and Nelson, 2015). Similar to the RSC, the connectivity of the ATN with other brain regions is critical to their effects on learning and memory. Disruption of the ATN has significant deleterious effects on other nodes in the EMC such as the RSC (Garden et al., 2009; Wolff and Vann, 2019) and subiculum (Frost et al., 2021). Furthermore, disconnection of the ATN-HPC pathway disrupts learning (Henry et al., 2004; Warburton et al., 2001).

The thalamus overall does not present such strong or early neuropathological changes as the RSC in AD patients; but Aβ deposits and tauopathy are observed especially within the ATN (Braak and Braak, 1991a, 1991b). The functional connectivity of the thalamus is also disrupted in MCI and AD patients, with decreased connectivity between the thalamus and the PCC of particular note

(Zhou et al., 2013). Furthermore, in AD patients reduced volume of the thalamus correlates with both impaired cognitive performance and increased cortical amyloid burden (de Jong et al., 2008; Pardilla-Delgado et al., 2021). Interestingly, the effects of ATN-RSC pathway disruption are bidirectional. In patients with RSC damage, hypoactivity is observed in the thalamus (Heilman et al., 1990), and RSC-lesioned rats exhibit cell loss in the ATN (Neave et al., 1994). The function of the ATN and their position in the neural circuitry of learning and memory is yet to be fully understood in regards to AD, but there is evidence that they do play an important role.

1.2.5 | Mouse models of AD

While some non-invasive experimental techniques such as fMRI and positron emission tomography can be used to study AD in those living with dementia, we need animal models of AD to truly understand the precise biological and cellular mechanisms of the disease while maintaining intact neuronal circuitry and the ability to assess cognitive decline. If we consider cognition as a product of activity in neuronal circuits, then cognitive impairment would reflect a malfunction in the circuit; thus, it is imperative AD pathologies are investigated in organisms which model these circuits. Unfortunately, however, AD appears to be a disease almost unique to humans. Whilst chimpanzees, dogs and cats all show age-related amyloidopathy, tauopathy and cognitive decline (Edler et al., 2017; Head, 2013; Sordo et al., 2021), the years to decades-long time course across which AD pathologies develop in these species makes them unsuitable models for preclinical research. Other more commonly used animal models do not spontaneously display AD neuropathological changes, necessitating the development of alternative approaches. One such approach is the genetic modification of mice to generate models that express human transgenes containing EOFAD mutations or altering the animal's homologous gene of interest (Elder et al., 2010). Many of these mouse lines model amyloidopathy via APP or PSEN mutations, including the primary model used in this thesis; the PDGF-APP$_{Sw,Ind}$ transgenic line (J20) (Mucke et al., 2000).

J20 mice express the mutant human APP (hAPP) gene containing the Swedish (KM670/671NL) (Mullan et al., 1992) and Indiana (V717F) (Murrell et al., 1991)

mutations under the platelet-derived growth factor β-chain promotor (Mucke et al., 2000). Both these substitution mutations alone increase Aβ levels in cultured cells; with the Swedish mutation causing increased total Aβ (Citron et al., 1992) and the Indiana mutation increasing Aβ42/Aβ40 ratio (Tamaoka et al., 1994), acting on the β-secretase and γ-secretase pathways respectively. The J20 mouse presents an amyloidogenic phenotype with increased cerebral total Aβ production and Aβ42 ratio by age 2-4 months, and amyloid plaque formation by age 5-7 months (Mucke et al., 2000). This line shows other neuropathological markers of AD such as synaptic loss, neuroinflammation and neuronal loss in the HPC (Hong et al., 2016; Wright et al., 2013), as well as cortical and hippocampal hyperexcitability and inhibition of synaptic transmission and plasticity (Palop et al., 2007; Saganich et al., 2006). The J20 mouse also shows impairments in spatial learning and memory, as well as in short-term recognition memory (Ameen-Ali et al., 2019; Etter et al., 2019; Harris et al., 2010).

The J20 line is relevant for studying RSC postsynaptic dysfunction, as this model preferentially expresses Aβ deposition in the cortex and hippocampus with a much higher plaque load in the RSC than other amyloidopathy models (Whitesell et al., 2019), better correlating with the isocortical deposition in AD than other APP-overexpression models. In addition, the RSC is hypothesised to be important for integrating distal cues in spatial navigation, and the behavioural tasks that require this associative integration of egocentric and allocentric information are reliably impaired in the model (Karl et al., 2012).

1.3 | Synaptic transmission

Communication between neurons is the foundation of cognition and is enabled by synaptic transmission. The average human brain has at least 10^{14} synaptic connections, allowing for a large amount of information to be shuttled around the brain (Kandel et al., 2000). The majority of synaptic transmission occurs via presynaptic neurotransmitter release and postsynaptic receptor activation at the chemical synapse. There is a large variety of neurotransmitters released in the vertebrate brain which can be excitatory, inhibitory or modulatory depending on the mechanisms of action that occur following binding to their receptors. The primary excitation system in the brain relies on glutamate release (Orrego and

Villanueva, 1993) and is the focus in this thesis due to its role in long-range connectivity (Cotman et al., 1987) as well as learning and memory processes (McEntee and Crook, 1993).

1.3.1 | Glutamatergic neurotransmission

Glutamate is by far the most ubiquitous neurotransmitter in the brain; around 90% of all synapses are estimated to involve glutamate, and the glutamatergic system accounts for around 80% of total brain energy expenditure (Andersen et al., 2021). The excitatory nature of this neurotransmitter system however is not due to glutamate itself, but instead is caused by the properties of the receptors that it binds to.

Glutamate receptors are divided into two broad classifications: ionotropic and metabotropic receptors (Niciu et al., 2012). Ionotropic glutamate receptors (iGluR) are ligand-gated cation channels on the cell membrane, and are responsible for fast excitatory synaptic transmission. iGluRs can be further sub-divided by their agonist selectivity to either NMDA, AMPA or kainate (KA). All iGluR have exclusively excitatory effects and are tetrameric structures formed of four large subunits creating a central ion channel pore. Of particular interest to learning and memory are the AMPAR and NMDAR (Peng et al., 2011), which will be discussed in further detail.

Metabotropic glutamate receptors (mGluR) in comparison do not directly gate ion channels, but instead are G protein-coupled receptors (GPCR) which indirectly gate ion channels through secondary messenger cascades. The effect of glutamate binding can therefore be excitatory or inhibitory depending on which GPCR subgroup the mGluR belongs to. Whilst mGluR are crucial to normal function, their slow neurotransmission and modulatory actions are unsuitable to be measured using standard optogenetic pathway interrogation.

1.3.1.1 | AMPA receptors

AMPAR assemblies are built from homo/hetrotetramer combinations of the four main AMPAR subunits (GluA1-4). GluA1-4 are all formed of an extracellular N terminus, an intracellular C terminus and four transmembrane domains (M1-4)

one of which forms a re-entrant loop (M2), and these different subunits alter permeability and action kinetics of the receptors through various mechanisms allowing for a diverse array of AMPARs available in the brain (Greger et al., 2017). The binding of glutamate to the ligand binding domain(s) opens the pore and allows rapid influx of sodium ions (Na^+), as well as an efflux of potassium ions (K^+), creating a fast and robust excitatory postsynaptic current (EPSC) as well as rapid decay and desensitisation. The Ca^{2+} permeability of the AMPAR is dependent on whether it contains the Q/R edited GluA2 subunit: as most of the AMPARs in the mature brain contain this subunit, endogenous AMPARs are generally considered Ca^{2+} impermeable (Isaac et al., 2007). Overall, AMPARs are thought to be responsible for the majority of fast excitatory transmission in the brain and are heavily involved in the mechanisms of synaptic plasticity.

1.3.1.2 | NMDA receptors

The subunits of NMDARs – of which three distinct families have been identified (GluN1-3) – have a homologous structure to AMPAR subunits, and a similar diversity conferred by tetrameter combinations and splicing variations. NMDARs have a higher affinity for glutamate than AMPARs, however their activity is more tightly regulated and require co-agonism (with glycine or D-serine) for activation as well as having many subunit-specific allosteric binding sites which modulate activity (Hansen et al., 2018). Moreover, while AMPAR activity produces EPSCs at resting membrane potential, NMDAR pores are blocked with extracellular magnesium (Mg^{2+}) in a voltage-dependent manner. Sufficient depolarisation of the membrane is required to unblock the ion channel, but when NMDARs are active they are permeable to Na^+, Ca^{2+} and K^+ and mediate a much slower EPSC. As well as facilitating EPSCs, this influx of Ca^{2+} also has longer-term effects by activating various intracellular signalling pathways to regulate synapses (Fan et al., 2014).

While the GluN1 subunit is ubiquitously expressed across the adult CNS and is necessary for NMDA channel function (McBain and Mayer, 1994), channel properties depend upon regulatory GluN2 subunit composition as most native receptors function only as heteromeric assemblies of two GluN1 and two GluN2 subunits (Cull-Candy and Leszkiewicz, 2004). GluN2 receptors are expressed

throughout the brain during early development but are restricted to the forebrain in the adult brain. Additionally, the four GluN2 subunits (A/B/C/D) also have distinct developmental and regional expression patterns, and confer different pharmacological and kinetic properties to the NMDA channel (Monyer et al., 1994). Within the forebrain, GluN2A and GluN2B NMDAR subtypes predominate, however their ratio transforms over development as GluN2A levels increase postnatally. Comparison of GluN2A and GluN2B-containing di-heteromeric NDMARs reveals GluN2A-containing channels exhibit faster kinetics including rise, deactivation and decay times, while GluN1/2A/2B tri-heteromeric channels exhibit intermediate kinetics (Yashiro and Philpot, 2008). Furthermore, GluN2B-containing NMDARs display lower peak currents, but carry more Ca^{2+} per unit of current and have a stronger binding affinity with the CamKII protein downstream signalling pathway. These differences in channel properties indicate distinct roles in synaptic plasticity (Yashiro and Philpot, 2008), and there is evidence of Aβ oligomers selectively disrupting GluN2B-containing NMDARs in the HPC – thereby inhibiting long-term potentiation (Shipton et al., 2011). Thus, identifying postsynaptic NMDAR subunit composition is an important step in understanding the function, and vulnerabilities, of target circuits.

1.3.2 | Glutamate and synaptic plasticity

Whilst postsynaptic plasticity can be mediated by a variety of mechanisms, NMDAR-dependent LTP and LTD are both very important for learning and memory (Lüscher and Malenka, 2012). LTP and LTD are induced by different patterns of activity and mechanisms, however both rely on Ca^{2+} influx postsynaptically (Yang et al., 1999).

During LTP, large releases of glutamate presynaptically strongly activates AMPARs and causes sufficient postsynaptic depolarisation to allow NMDAR channels to open. The subsequent elevated Ca^{2+} influx induces activation of various signalling cascades such as via calmodulin-dependent protein kinase II (CamKII) and protein kinase A (PKA), which in turn leads to phosphorylation of AMPARs already present at the postsynaptic membrane (increasing their probability of opening) and/or AMPAR exocytosis (Baudry et al., 2015; Lisman et al., 2012). These signalling pathways are also involved in further downstream

signalling which is responsible for the maintenance of LTP. There is also evidence of a presynaptic NMDAR-dependent mechanism which increases probability of release of glutamate (McGuinness et al., 2010). On the other hand, LTD induction relies on decreased Ca^{2+} levels leading to AMPAR dephosphorylation and endocytosis via different signalling cascades such as those involving protein phosphatase 1 (PP1) (Collingridge et al., 2010). The ability of the cell to differentiate between LTP- and LTD-inducing stimulation can be explained by the high sensitivity of intracellular Ca^{2+}-sensing systems. Crucially, antagonism of NMDARs by AP5 – a selective NMDAR antagonist – blocks induction of LTP and LTD (Collingridge et al., 1983; Dudek and Bear, 1992); signifying the role of NMDARs in the normal functioning of long term synaptic plasticity.

Whilst it should be kept in mind that I have discussed NMDAR-dependent LTP and LTD in a simplified form here, it is abundantly clear that glutamate and its receptors are essential to long term plasticity within the brain and therefore also to learning and memory. One of the key functions of synaptic plasticity is to strengthen and weaken synapses where appropriate to allow efficient activation of specific neuronal ensembles required for memory encoding and maintenance. Indeed, neurons recruited into these ensembles display alterations in synaptic strength and plasticity, including increased AMPAR-mediated EPSCs (Ryan et al., 2015). Additionally, Fos protein expression – a marker of neuronal activity and ensembles – requires strong and sustained glutamatergic activation and is the product of some of the same Ca^{2+}-associated signalling cascades involved in LTP induction (Chung, 2015). Therefore, deficits in synaptic transmission and plasticity may be visible as alterations in Fos levels, and related to changes in memory encoding and storage.

The glutamatergic system also presents another form of synaptic plasticity: a short-term version which is primarily presynaptically mediated (Zucker and Regehr, 2002). This short-term plasticity can either be facilitatory or depressive, and is a result of changes to the synapse dynamics such as altered neurotransmitter release probability or availability of vesicle pools. Short-term plasticity is thought to be important in synaptic computation, information processing and working memory (Deng and Klyachko, 2011). Due to the

integrative nature of the RSC, it is of no doubt that short-term plasticity plays an important role in its function.

Due to the different roles that afferent inputs into the RSC play in its behavioural function (**Section 1.1.3.3**), it is likely that these neural pathways exhibit different functionality including measures of synaptic plasticity. It is clear that the glutamatergic system is crucial for normal RSC function: indeed, blocking AMPAR-mediated neurotransmission attenuates spatial memory (Czajkowski et al., 2014) and antagonising NMDARs attenuates contextual fear memory formation and prevents activity-dependent gene activation similar to HPC (Baumgärtel et al., 2018). Furthermore, as Aβ has been shown to affect synaptic transmission and plasticity by altering glutamatergic release and receptors (**Section 1.2.3.2**), it is not a great leap to suggest that some of the learning and memory deficits seen in AD are as a result of disruption to these systems. Therefore, identifying which pathways are affected, and when, is a crucial step to understanding the progression of this disease.

1.4 | Hypotheses and Aims

Hypothesis 1 | Afferent projections to the gRSC and dRSC differ in synaptic strength and specificity.

The RSC is a highly connected hub region of the brain, and understanding the properties of RSC afferent projections is crucial to understanding the function of this area. Whilst some research has begun to quantify afferent inputs into the RSC, these studies have focused on the gRSC (Brennan et al., 2021; Yamawaki et al., 2019b). Therefore, I aim to examine inputs into the RSC from three distal areas – the ACC, ATN and dSub – measuring synaptic transmission onto PCs. These areas were chosen as they are all important constituents of the EMC and play different but critical roles in learning and memory (Aggleton et al., 2022). Furthermore, inputs from these areas onto gRSC PCs have previously been described (Brennan et al., 2021). I expect to corroborate differences in the strength and specificity of excitatory input to the superficial and deep layers of the gRSC, as well as describe and compare the pattern of innervation to the dRSC. To do this, I will use optogenetic stimulation of afferent terminals arising from ACC, ATN and dSub, respectively, combined with whole cell patch clamp electrophysiology to measure properties of glutamatergic synaptic transmission.

Hypothesis 2 | RSC basal neuronal activity is altered in a mouse model of amyloidopathy.

The RSC is highly susceptible to deafferentation in AD, therefore any disruption to connected brain regions – or to the synaptic connections arising from these pathways – could alter RSC neuronal activity. The RSC is known to present amyloidopathy in the early stages of AD and is likely affected by the synaptotoxic consequences of pathological Aβ. As Aβ oligomers are known to disrupt glutamatergic signalling at presynaptic and postsynaptic loci, and *Fos* expression is mediated by glutamatergic excitation, I will quantify RSC neuronal activity in the J20 mouse model by assessing basal Fos protein expression in the area. A previous study found decreased RSC Fos expression in mice expressing amyloidopathy following exposure to a novel environment (Poirier et al., 2011), and it is expected that basal neuronal activity will be similarly impaired.

Hypothesis 3 | Synaptic responses will be disrupted in the ATN to RSC pathway in a mouse model of amyloidopathy.

While MTL disruption is a key factor in AD development, a comprehensive understanding of the aetiology of AD requires knowledge of cellular and synaptic dysfunction in areas outside the MTL that also exhibit pronounced pathology. The ATN provides substantial excitatory input to the RSC, and both areas are crucial for learning and memory. The RSC and ATN also both rely heavily on their connectivity to drive mnemonic processes therefore I aim to assess whether this pathway is disrupted in a model of prodromal AD. Since, amyloidopathy is significantly correlated with synaptic dysfunction I will use the J20 mouse model to investigate whether measures of synaptic function are altered at different stages of Aβ deposition.

Overall, these hypotheses aim to elucidate the functional connectivity of the RSC in both normal and pathological states. While the research field involving the RSC is growing, we still lack information about this area; especially compared to other regions of the brain that are significant to cognitive function as the RSC – such as the PFC and HPC. The findings from this thesis can be used in the future to inform further research into this cortical region, and its role in AD and other neuropathological disorders.

2 | Materials and Methods

2.1 | Animals

2.1.1 | Ethics

All animal procedures carried out in this thesis were done in accordance with the UK Animals (Scientific Procedures) Act (ASPA) 1986 and were approved by the University of Exeter Institutional Animal Welfare and Ethical Review Body.

2.1.2 | Housing

All mice were bred in house at the University of Exeter and kept on a 12 hour light-dark cycle with ad libitum access to food and water. Mice were group housed where possible. Both male and female C57BL/6J and PDGF-APPSw,Ind transgenic (J20) (Mucke et al., 2000) mice were used in the experiments described in Sections 3 and 4. Details of the mouse strain and ages used for each study are described in sections **3.2** and **4.2**.

2.2 | Intracerebral viral injection surgery

All surgeries were conducted using aseptic technique. Mice were weighed and handled 3-5 days prior to surgery to check welfare. On the surgical day, the mice were weighed and then anaesthetised using isoflurane (5% induction, 1.2-2.5% maintenance) delivered in a constant flow of oxygen. Their scalp was then shaved and they were placed in a Kopf stereotaxic frame and secured with non-rupture ear bars. Analgesia was provided via a subcutaneous injection of buprenorphine (0.03 mg/kg) at the start of the surgery. Isoflurane concentration was adjusted throughout the surgery as anaesthesia level was monitored by checking pedal reflex and breathing rate (1-2 breaths per second target). Body temperature was maintained at 36-37°C using a feedback probe and heat mat.

Iodine was applied to the scalp and the skull exposed via a vertical incision to the skin. The skull was cleaned and flattened to ensure the z-position of bregma and lamda did not differ by > 0.1 mm. A craniotomy was drilled at the appropriate anterior-posterior and medial-lateral coordinates for the injection site, and a 33 gauge Hamilton needle was lowered to the appropriate dorsal ventral coordinates (see **Figure 2.2.1** for coordinates). Using a syringe and microinjection pump connected to the needle, 0.25 µl of virus was injected at 0.1 µl/min (see **Table 2.4** for details of the viruses used). The needle was left in position for 3 minutes

following the injection, then extracted by 0.1-0.2 µm and left in position for a further 4 minutes. The needle was then slowly removed from the brain, EMLA cream (5%) was applied to the wound edges which were then sutured closed.

Immediately post-surgery, mice were given a subcutaneous injection of carprofen (5 mg/kg) and 0.9% saline (10 ml/kg). They were monitored in heated recovery chamber for 30-60 minutes or until consciousness was fully regained. Mice were given a second injection of carprofen (1 mg/kg) the following day, and during the subsequent 3 days were administered carprofen orally (5-10 mg/kg in strawberry flavoured jelly).

	ACC	ATN	dSub
AP	+1.75	-0.71	-3.79
ML	±0.20	±0.80	±2.25
DV	+1.50	+2.76	+1.80

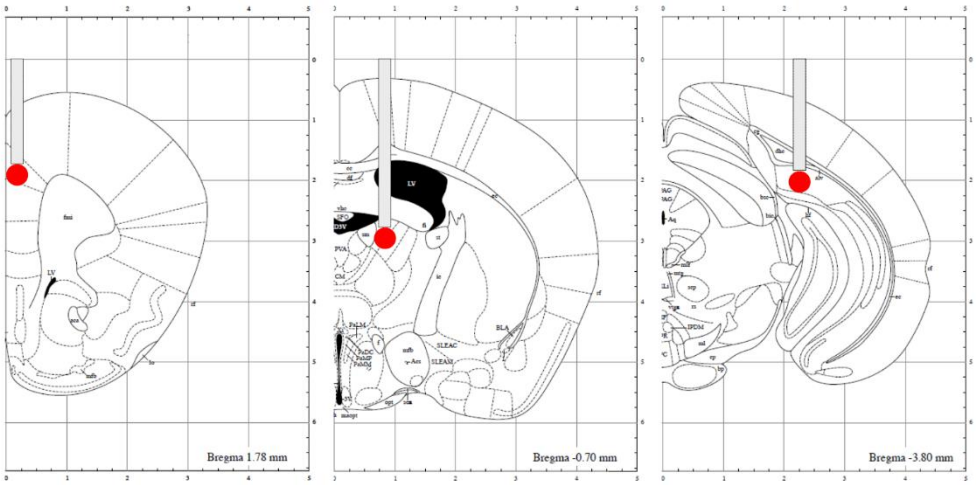

Figure 2.1 | Intracerebral injection target sites. Target injection sites for ACC, ATN and dSub (Paxinos and Franklin, 2001). Coordinates for each site are given above (in mm) with anterior-posterior (A-P) and medial-lateral (M-L) coordinates defined from Bregma = 0, and dorsal-ventral (D-V) coordinates defined from pia.

2.3 | Slice preparation

Mice were anaesthetised with 5% isoflurane and decapitated before the brain was rapidly removed and placed in room temperature (RT) oxygenated N-methyl-

d-glucamine (NMDG) solution (Ting et al., 2014) consisting of (in mM): 135 NMDG, 10 D-Glucose, 1.5 $MgCl_2$, 0.5 $CaCl_2$, 1 KCl, 1.2 KH_2PO_4, 20 Choline bicarbonate. 300 µm coronal slices corresponding to approximately Bregma +2.25 mm to +1.25 mm (for ACC) and -0.5 mm to -4.5 mm (for RSC, ATN and dSub) were sectioned using a Leica VT1200 vibratome. Following sectioning, slices were transferred to a holding chamber containing artificial cerebral spinal fluid (aCSF) perfused with a continuous flow of carbogen (95% O_2, 5% CO_2). The aCSF solution consisted of (in mM): 119 NaCl, 3 KCl, 1 NaH_2PO_4, 26 $NaHCO_3$, 10 D-Glucose, 2.5 $CaCl_2$, 1.3 MgCl (pH 7.4). The slices were then incubated in the holding chamber at 35°C for 30 minutes then for at RT for another 30 minutes to recover before recording. For optogenetic experiments the injection site fluorescence was visually confirmed immediately following slicing, and slices were discarded if viral expression was absent or in an anatomically incorrect location.

2.4 | Electrophysiological recordings

2.4.1 | Whole-cell patch clamp

RSC containing slices were attached to a 0.1% poly-L-lysine coated coverslip and transferred to the recording chamber where they were perfused with carbogen-saturated aCSF (4 ml/min, 32-34°C). Differential interference contrast (DIC) and fluorescent signal imaging was performed using an Olympus BX51W1 microscope and SciCam Pro camera with a CoolLED pE-4000 LED light source.

Borosilicate glass microelectrodes (OD 1.5mm, ID 0.86mm, 3-6 MΩ) were fabricated using a P-97 Flaming Brown micropipette puller and filled with intracellular (IC) solution; detailed in sections 2.4.2 and 2.4.3. Pyramidal cells (PC) were tentatively identified under DIC visualisation, and assigned as being located in the superficial (L2-4) or deep (L5-6) layers of the dRSC or gRSC sub-regions of the RSC. Confirmation of cell-type and location was conducted for a sub-set of cells by visualising cell morphology via *post-hoc* cell recovery (see **section 2.5.4**).

Data were collected with a Multiclamp 700B amplifier combined with a Digidata 1440A analogue-to-digital converter and a standalone computer equipped with pClamp software (Molecular Devices). Signals were digitised at 20 kHz and

lowpass filtered at 8 kHz. Custom MATLAB scripts were used to analyse electrophysiological recordings unless stated otherwise. Electrophysiology traces were inspected using Igor Pro 7 (Wavemetrics) or MATLAB (Mathworks) software. The liquid junction potential (LJP) was calculated using the LJP Calculator available on pClamp software. LJP was -15.7 mV for current clamp recordings and -11.7 mV for voltage clamp recordings, and was not corrected for.

2.4.2 | Current clamp

2.4.2.1 | Current clamp recordings

Whole-cell current clamp recordings were performed using a potassium gluconate (K-gluc) IC solution containing 2 mg/ml biocytin and consisting of (in mM): 135 K-gluc, 3 $MgCl_2$, 0.5 EGTA, 10 HEPES, 0.3 Na_2-GTP, 2 Mg-ATP. Cells were left at their natural resting membrane potential (V_m) for the duration of all recordings. All recordings were made in standard aCSF.

Immediately following entry in cell, a 60 second gap free recording was made of spontaneous activity at rest without injection of any bias current. Rheobase was measured from V_m using a 200 ms square positive current injection protocol: beginning at -5 pA and incrementing in 2 pA steps until an action potential (AP) was induced. All other measures were computed from a 1000 ms square positive current injection protocol. Most cells underwent a standard protocol beginning at -200 pA and incrementing at 50 pA steps until +400 pA; however, this was not appropriate for all recordings and, in some cases, a protocol starting at -100 pA and increasing to +200 pA in 25 pA steps or starting at -400 pA and increasing to 1000 pA was be applied. The 25 pA step protocol was applied if a depolarising block presented by +150 pA during the standard protocol, and the 100 pA step protocol was applied if the cell did not fire by +300 pA during the standard protocol.

2.4.2.2 | Current clamp analysis

Cells were excluded from analysis if they had an access resistance (R_a) > 20 MΩ or V_m > -50 mV.

Passive membrane properties

Methods used to measure passive membrane properties are illustrated in **Figure 2.1**. Resting membrane potential (V_m) was calculated as the average membrane voltage for 100 ms before current injection. Input resistance (R_i) was calculated as mean voltage deflection during the last 200 ms (ΔV) – the steady state response (ssV) – of the first hyperpolarisation current injection sweep divided by the amplitude of the negative current injection (ΔI).

$$Ri = \frac{\Delta V}{\Delta I}$$

20-80% rise time was calculated using a first order exponential curve fitted to the charge curve of the membrane between 20 and 80% of the peak amplitude of voltage deflection.

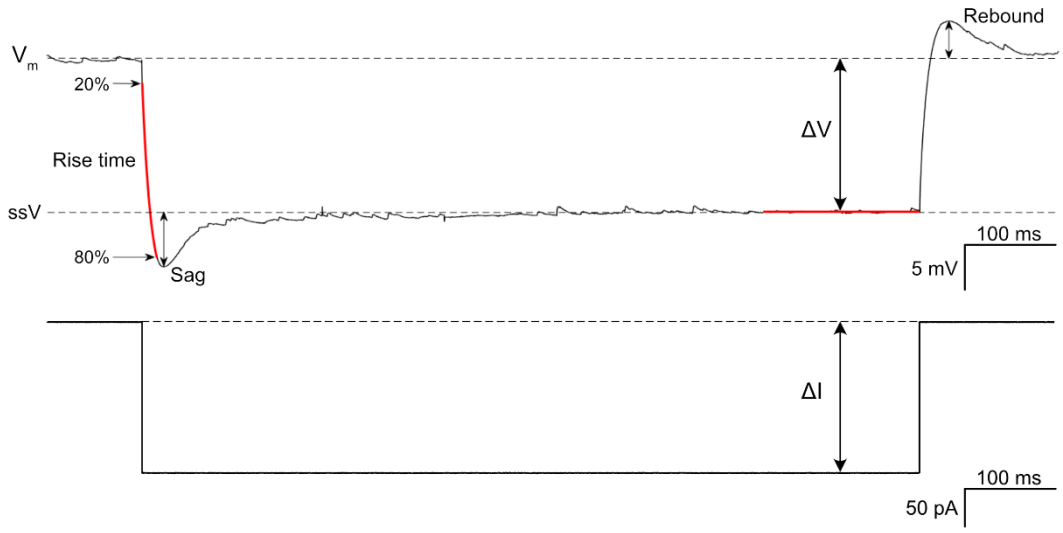

Figure 2.2 | Calculation of passive membrane properties and I_h current. Voltage trace in response to square hyperpolarising current injection. Highlighted in red is the charging curve of the membrane used to calculate rise time (left) and the time point used to calculate the ssV (right). The arrows indicate the voltage deflections and inflections used to calculate ΔV, ΔI, sag and rebound. The dashed lines indicated the mean voltage calculated for V_m and ssV.

AP waveforms and excitability

Rheobase was calculated by manually identifying the depolarising current injection magnitude when an AP was first generated on ClampFit software (Molecular Devices).

The hyperpolarisation-activated cation current (I_h) was measured by calculating the sag and rebound voltages of the first hyperpolarisation sweep. Sag voltage was calculated as percentage of the difference between the maximum negative voltage deflection (V_{min}) and steady state response (ssV) divided by the difference between V_{min} and V_m. Rebound voltage was calculated as the difference between the maximum positive voltage peak following the end of the negative current injection step (V_{max}) and V_m.

Spike characteristics were computed from the first AP of the first spike train to contain ≥4 spikes. AP threshold was calculated as the voltage at which the first derivative of the membrane potential (dV/dt) exceeded 20 mV/ms (**Figure 2.3 B**). Maximal rate of rise (max dV/dt) was calculated as the peak of the first derivative of the membrane potential. AP peak was computed as the absolute maximum voltage of the AP waveform (**Figure 2.3 A**). AP half-width was calculated as the width at half maximal voltage from AP threshold.

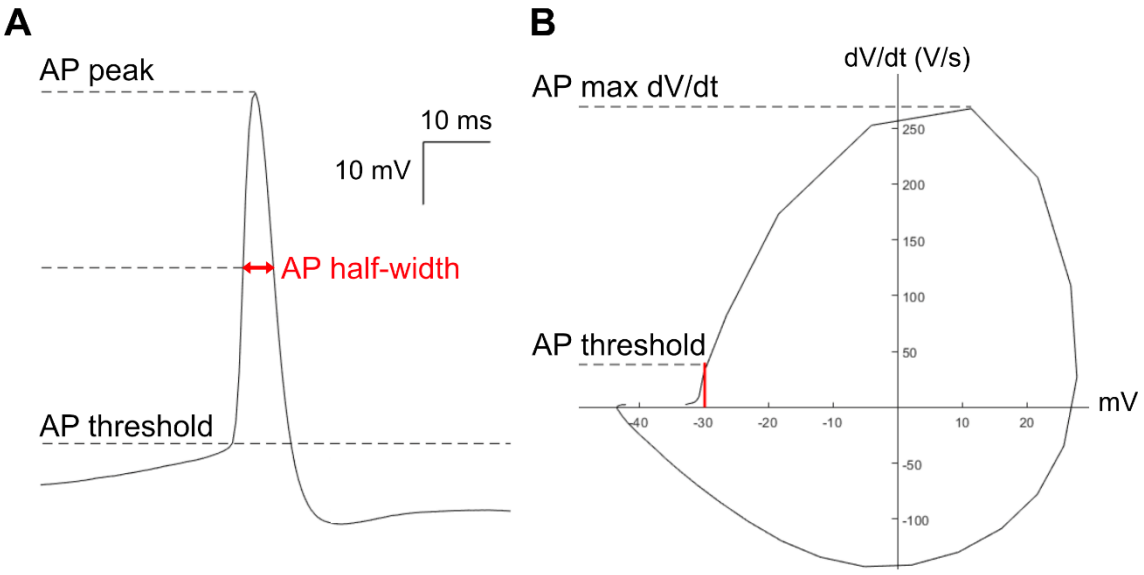

Figure 2.3 | Calculation of AP properties. A Voltage trace of first AP following depolarising current injection (+50 pA). **B** Phase plot of 1st order derivative of AP.

Accommodation index (AI) was calculated as the as the ratio between the first and last inter-spike interval (ISI). Burst index (BI) was calculated as the sum of the inverse of the spike number squared multiplied by the ISI.

2.4.3 | Voltage clamp

2.4.3.2 | Voltage clamp recordings

Whole-cell voltage clamp recordings were performed using a cesium methanesulfonate ($CsMeSO_4$) IC solution containing 2 mg/ml biocytin and consisting of (in mM): 135 $CsMeSO_4$, 8 KCl, 0.5 EGTA, 10 HEPES, 0.5 QX-314, 0.1 Spermine, 0.3 Na_2-GTP, 2 Mg-ATP. Cells were recorded from at a holding membrane potential (V_H) of -70 mV for recordings unless otherwise stated. All recordings were made in standard aCSF unless otherwise stated. All optic stimulation was carried out at a 470 nm wavelength generated by a CoolLED pe-4000 light source at 100% power.

Following entry into the cell, a 60 second gap free recording was made of spontaneous activity at V_H = -70 mV. Two stimulation train protocols at different frequencies were then applied to the cell for 10-20 sweeps each. Both stimulation train protocols consisted of a 500 ms -10 mV square voltage injection followed by five 5 ms optic stimulation pulses at 7 Hz and 40 Hz frequencies. In order to examine paired pulse ratio (PPR) an increasing inter-pulse interval (IPI) protocol was applied, which consisted of: a 500 ms -10 mV square voltage injection followed by two 5 ms optic stimulation pulses at 10, 17, 51, 100, 170, 510 and 1000 ms intervals. Finally AMPAR- and NMDAR-mediated currents were measured using a protocol consisting of a 500 ms -10 mV square voltage injection followed by a single 5 ms optic stimulation pulse. AMPAR-mediated currents were measured at V_H = -70 mV in standard aCSF and NMDAR-mediated currents were measured at V_H = +40 mV in aCSF containing antagonists for $GABA_A$, $GABA_B$ and non-NMDA ionotropic glutamate receptors (standard aCSF containing (in µM): 10 Gabazine, 1 CGP-55845, 10 DNQX).

2.4.3.2 | Voltage clamp analysis

Cells were excluded from analysis if they had R_a > 20 MΩ or displayed a change in R_i (ΔR_i) > 20%. R_i was calculated for each sweep as the mean current deflection during the voltage injection step divided by the amplitude of the negative voltage injection. ΔR_i percentage was computed by subtracting the R_i of the first sweep from the final sweep, then dividing by first sweep R_i. Average R_i was calculated as the mean R_i for all sweeps.

EPSC magnitude and kinetics

EPSC magnitude and kinetics were calculated from the first optogenetic stimulation pulse generated in the 7 Hz stimulation protocol, cells were excluded if < 10 viable sweeps were recorded. Sweeps were averaged and normalised: baseline current was calculated as the mean current for 500 ms following voltage injection, and adjusted to 0 pA. For the C57BL/6J synaptic function characterisation studies detailed in **Section 3**, a binary response rate was calculated and responding cells were further analysed.

Magnitude and kinetic data was calculated for each stimulation pulse. The EPSC magnitude was calculated as either the maximum negative current peak or the current at time of the first EPSC peak; where a multi-peak response generated defined peaks before the maximum. Identification of peaks before maximum was computed by plotting the first order differential of the response and identifying peaks of greater than 4 standard deviations from the differential trace (**Figure 2.4**). Total EPSC charge was calculated as the area under the curve (AUC) between onset and next pulse, or for the last pulse until mean inter-pulse interval (IPI) time had passed. Onset latency was calculated as time to respond following initiation of optogenetic pulse, where time to respond was calculated as the first point when amplitude ≥ 3 SD from mean on a Hilbert transform of the trace. Rise time was calculated as time taken for the first EPSC to rise from 20 to 80% of its peak.

EPSC magnitude and kinetics were analysed for only the first pulse in the stimulation train, however PPR were computed for subsequent pulses compared to the initial response at both 7 and 40 Hz frequencies.

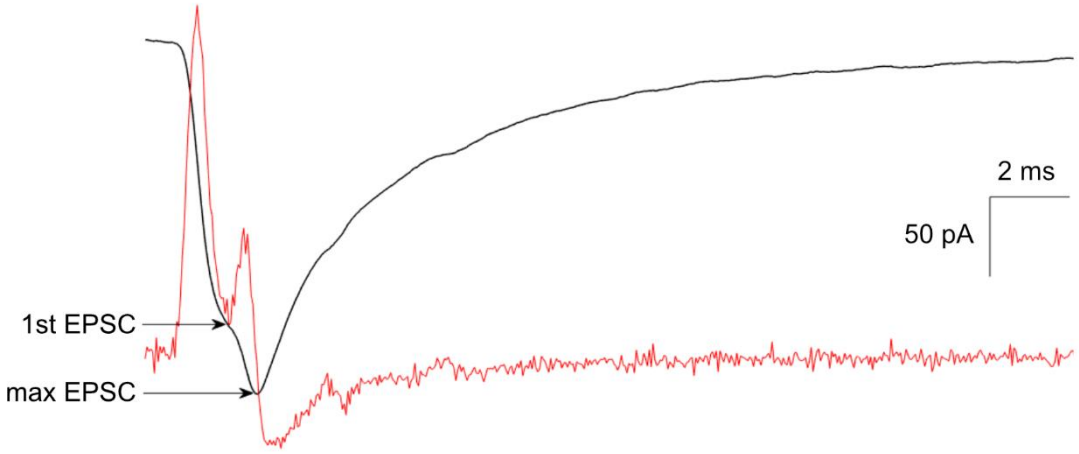

Figure 2.4 | Current trace and differential plot of multi-peak EPSC. In black is current trace of a multi-peak optogenetic stimulation-evoked EPSC. In red is the first differential of the trace plotted against the current trace. 1st and maximum EPSC locations are indicated.

Increasing IPI PPR

Three replicate recordings were made for each cell, and corresponding sweeps were averaged together. R_i calculation and baseline adjustment were computed as described above. EPSC magnitude for each pulse was calculated as the maximum negative current peak, and a PPR ratio was generated for each averaged sweep by dividing the second pulse EPSC by the first pulse EPSC

AMPA-NMDA ratio

Sweeps used to compute AMPAR- and NMDAR-mediated currents were averaged and normalised for each block. R_i and ΔR_i were calculated for the AMPAR-current sweeps only.

AMPAR-mediated EPSC magnitude was calculated as the maximum negative current peak in a 200 ms window following optogenetic stimulation. NMDAR-mediated EPSC magnitude was calculated as the maximum positive current peak in the same time window. AMPA-NMDA ratio was then calculated by dividing NMDAR EPSC by the AMPAR EPSC. Any cells which displayed an AMPAR but not NMDAR were discarded from analysis due to being unable to divide by 0.

Where an NMDAR response was present, the weighted decay time constant (τ_w) was calculated in Clampfit 11.2 (Molecular Devices) by fitting the following double exponential function equation to the average current trace at +40 mV using the least square method (Shipton et al., 2022):

$$I(t) = I_f e^{-t/\tau_f} + I_s e^{-t/\tau_s}$$

where I_f and I_s are the amplitudes of the fast and slow component, t is time, and τ_f and τ_s are the fast and slow time constants. τ_w was computed using these values using the following equation:

$$\tau_w = \tau_f \left(\frac{I_f}{I_f + I_s}\right) + \tau_s \left(\frac{I_s}{I_f + I_s}\right)$$

2.5 | Immunohistochemistry

2.5.1 | Fixed tissue preparation

Mice were taken directly from their home cage and terminally anaesthetised with an intraperitoneal injection of sodium pentobarbital (200 mg/kg) before being transcardially perfused (5 ml/min) with phosphate buffered saline (PBS) for 5 mins followed by 4% paraformaldehyde (PFA) in PBS for 10 mins. The animals were not handled or exposed to any other non-home cage stimulation for 2 hours prior to perfusion in order to capture only basal Fos expression. Following the perfusion, the brains were removed and stored in 4% PFA in PBS for 22 hours at 4°C, then cryoprotected in 30% Sucrose in PBS-(0.02%)Azide (PBS, 0.02% sodium azide) for at least 3 days.

Using a freezing sledge microtome (Leica SM2010R with Physitemp BFS-5MP temperature controller) coronal sections were taken from frozen brains (-20°C). Sections were either directly mounted on Superfrost Plus slides and immediately coverslipped, or stored in either PBS-(0.02%)Azide at 4°C or a cryoprotectant solution (25% glycerol, 30% ethylene glycol, 25% 0.2 M Phosphate buffer, 20% ddH_2O) at -20°C for long-term storage.

2.5.2 | Fos staining

All steps were conducted at RT unless stated otherwise. 30 µm free-floating sections stored in PBS-Azide were washed in PBS (3x 10 minutes), before being incubated in PBS containing 0.09% hydrogen peroxide for 20 minutes to quench endogenous peroxidase. Next, sections were washed in PBS (3x 10 minutes),

then blocked and permeabilised in PBS-(0.2%)Tx (PBS, 0.2% Triton X-100) containing 3% normal goat serum (NGS). The sections were then incubated in 1:800 anti-Fos primary antibody in PBS-(0.2%)Tx with 3% NGS at 4°C overnight.

The following day the sections were washed in PBS (3x 10 minutes), then incubated for 2 hours in 1:600 biotinylated anti-rabbit secondary antibody in PBS-(0.2%)Tx with 1% NGS. Sections were washed in PBS (2x 10 minutes), then incubated in an Avidin-Biotin complex (ABC) solution for 1 hour. After a further three washes in PBS the sections were incubated with 0.04% 3,3'-Diaminobenzidine-tetrahydrochloride (DAB) with 0.04% hydrogen peroxide and 0.05% ammonium nickel(II) sulfate in PBS for approximately 10 minutes. After a final two 10 minute washes in PBS, sections were mounted on Superfrost Plus slides and left to dry overnight. The next day, sections were serially dehydrated in graded ethanol (EtOH) baths (all 2 minutes: 2x ddH_2O, 30% EtOH, 60% EtOH, 90% EtOH, 95% EtOH, 2x 100% EtOH), and then cleared in Histo-Clear II (2x 10 minutes). Slides were then sealed and coverslipped using Histo-Mount mounting medium.

The RSC, CA1 region of the HPC and V1 were visualised using bright-field microscopy and images captured using a 10x objective on a Nikon Eclipse 800 microscope attached to a SPOT RT monochrome camera running SPOT Basic imaging capture software (SPOT Imaging). Four replicates of each ROI were captured for each mouse, taken from the left and right hemispheres of two sections.

Image analysis (**Figure 2.5**) consisted of an automatic count of nuclei expressing high levels of Fos (Fos+) in predefined regions of interest (ROI) (Paxinos and Franklin, 2001) using Fiji software (Schindelin et al., 2012). To perform this count, images were submitted to a fast Fourier transform bandpass filter and colour scale inversion before being run through the 3D object counter plugin with a brightness threshold (set to 1.7) that depended on average pixel brightness of the filtered image (Bolte and Cordelières, 2006). Fos+ cell counts were then normalised to ROI area, described as Fos+/mm^2.

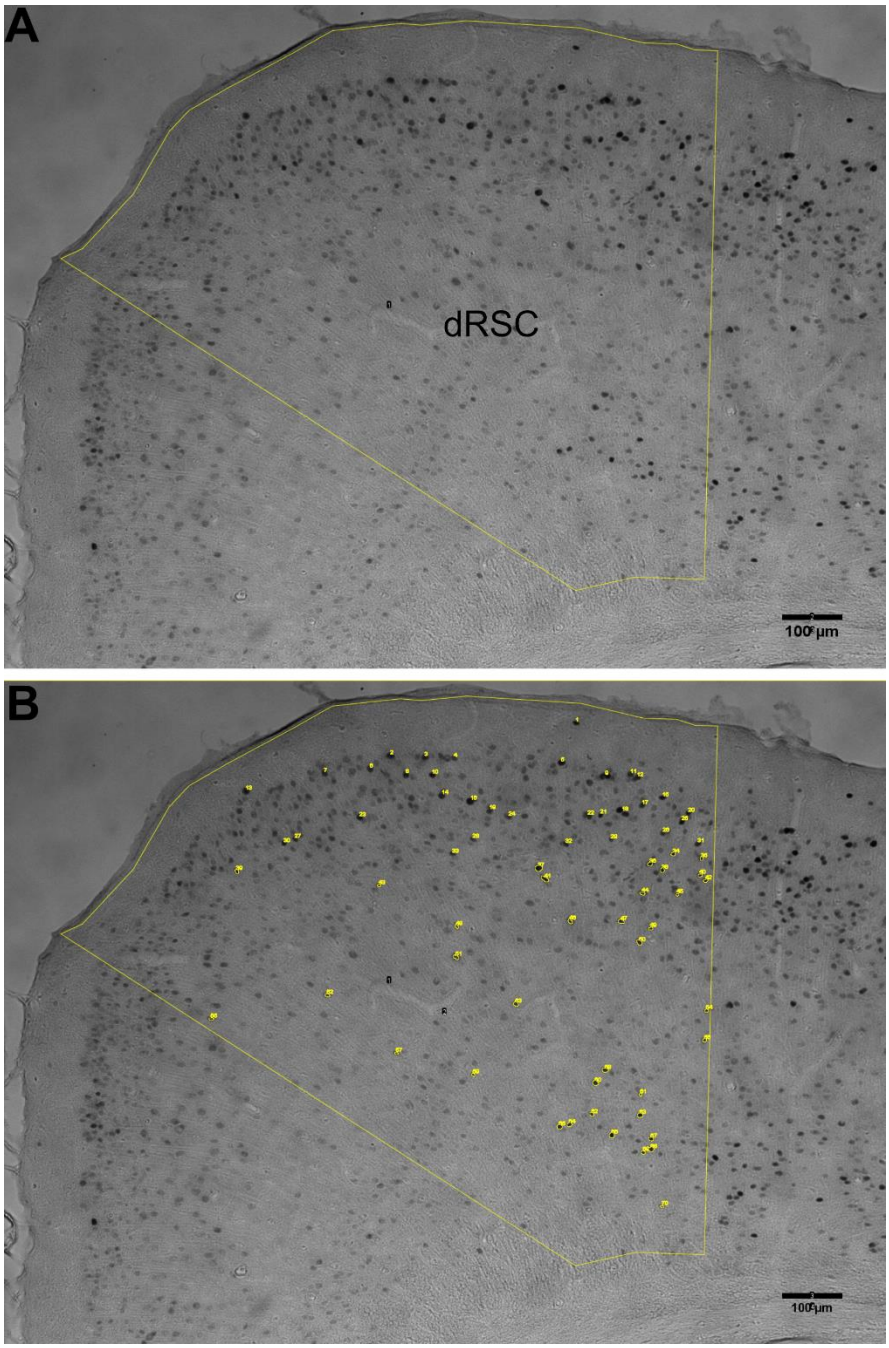

Figure 2.5 | Fos IHC image analysis. A Raw image from a 3 month old wild-type mouse with dRSC ROI overlay. **B** Automated count overlay identifies Fos+ nuclei with 1.7 brightness threshold. Only highly stained Fos+ nuclei were identified. (Scale bar: 100 µm)

2.5.3 | Amyloid plaque staining

30 µm free-floating sections stored in cryoprotectant solution were washed in PBS (3x 10 minutes) before being mounted onto Superfrost Plus slides and left to dry overnight. The following morning a hydrophobic barrier was drawn around the sections and sections were covered in 70% ethanol for 5 minutes before being washed with ddH_2O (2x 2 minutes). Next, sections were incubated in 1:100 Amylo-Glo solution in 0.9% saline for 10 minutes. Sections were then rinsed in 0.9% saline for 5 minutes, followed by PBS washes (3x 10 minutes). Sections were left to dry, then coverslipped with Fluoromount mounting medium.

Aβ plaques in the RSC, HPC and V1 were visualised using epifluorescent microscopy (Nikon Eclipse 800 microscope with CoolLED pE-4000 LED light source) at 365 nm excitation. Images were captured at 4x magnification using a SPOT RT camera running SPOT Basic imaging capture software. Four replicates of each ROI were captured for each mouse.

Image analysis was conducted using Fiji software; amyloid plaques were quantified by measuring the area covered by plaques in predefined brain ROIs. Plaque areas were manually drawn and measured where present (**Figure 2.5.3**), then normalised as a percentage of brain area, described as Plaque/Area (%).

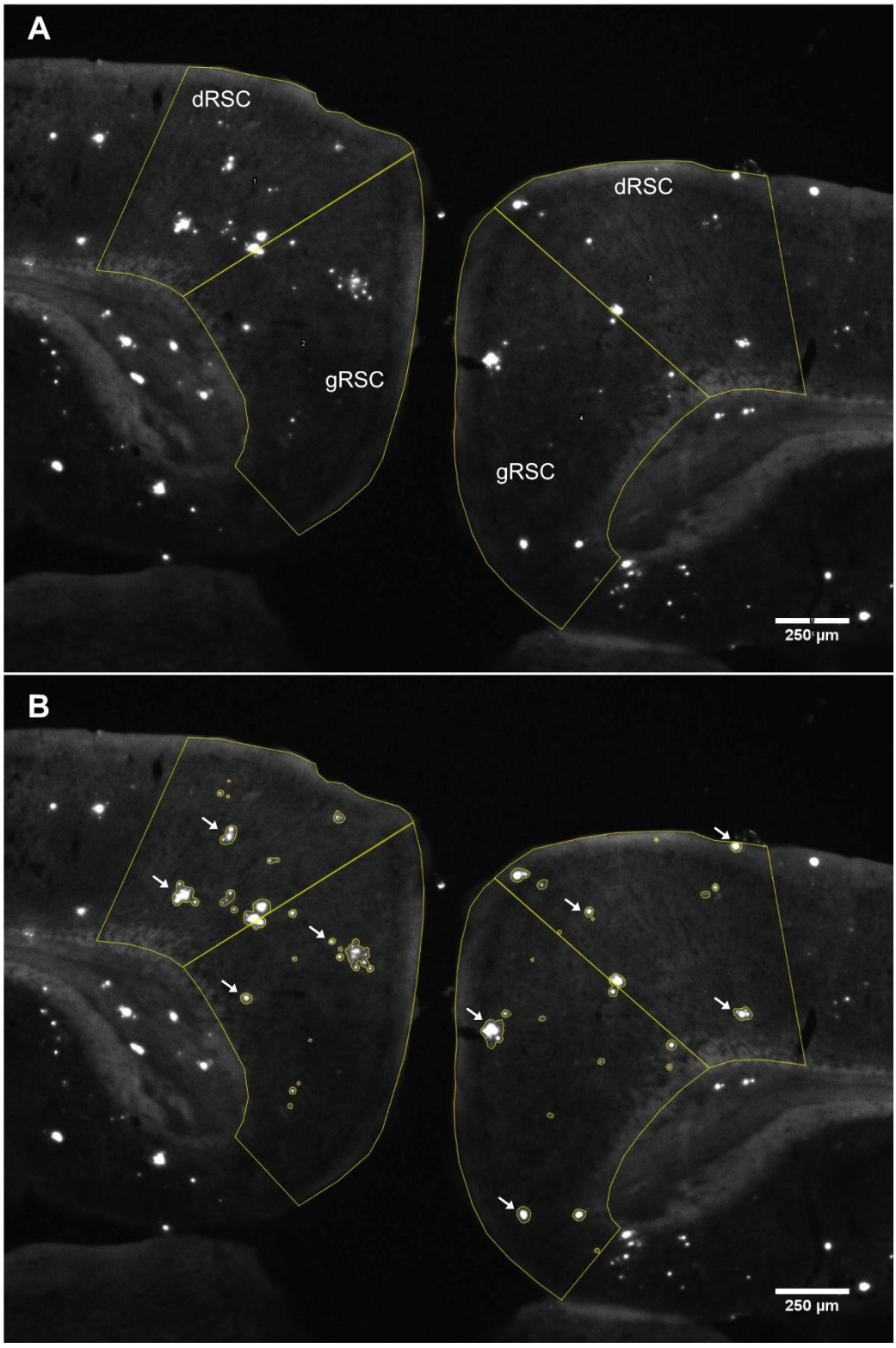

Figure 2.6 | Amyloid plaque image analysis. A Raw image from 9 month transgenic J20 mouse with dRSC and gRSC overlays. **B** Manually drawn ROIs around amyloid plaques including visible processes. Arrows indicate plaques but are not exhaustive. Scale bar: 250 µm.

2.5.4 | Cell recovery

Immediately following electrophysiological recording, slices were transferred into 4% PFA in PBS for 1-3 days, then transferred to PBS-(0.02%)Azide. The free-floating slices were then washed in PBS (3x 10 minutes) then blocked and permeabilised in PBS-(0.5%)Tx with 3% NGS for 1 hour. Slices were then incubated in 1:500 Streptavidin-DyLight 488 or Streptavidin 650 in PBS-(0.5%)Tx with 1% NGS overnight at 4°C. The following day, the slices were washed in PBS (3x 10 minutes) then transferred to 30% sucrose in PBS overnight for cryoprotection.

The 300 µm slices were then re-sectioned at 100 µm on a freezing sledge microtome (Leica SM2010R with Physitemp BFS-5MP temperature controller), mounted on SuperFrost Plus slides and coverslipped with VectaShield Hardset mounting medium containing DAPI.

Sections were first visualised using epifluorescent microscopy (Nikon Eclipse 800 microscope with CoolLED pE-4000 LED light source) at 10x magnification to confirm cell recovery, and cell type and location. Representative images of stained cells were taken on a MLS203 confocal microscope with a Quantalux sCMOS camera (ThorLabs) at 20x magnification.

PC were confirmed by morphology: a rounded pyramidal shaped soma with two distinct dendritic fields emerging from the apex (apical dendrites) and base (basal dendrites) (**Figure 2.7**). In the neocortex these dendritic fields are typically oriented with the apical dendrites ascending towards the superficial layers and the basal dendrite fanning around the soma (Valverde, 1986). Location of soma was confirmed by identifying distinct cortical layers in the DAPI stain using previously described boundaries (Vogt and Paxinos, 2014).

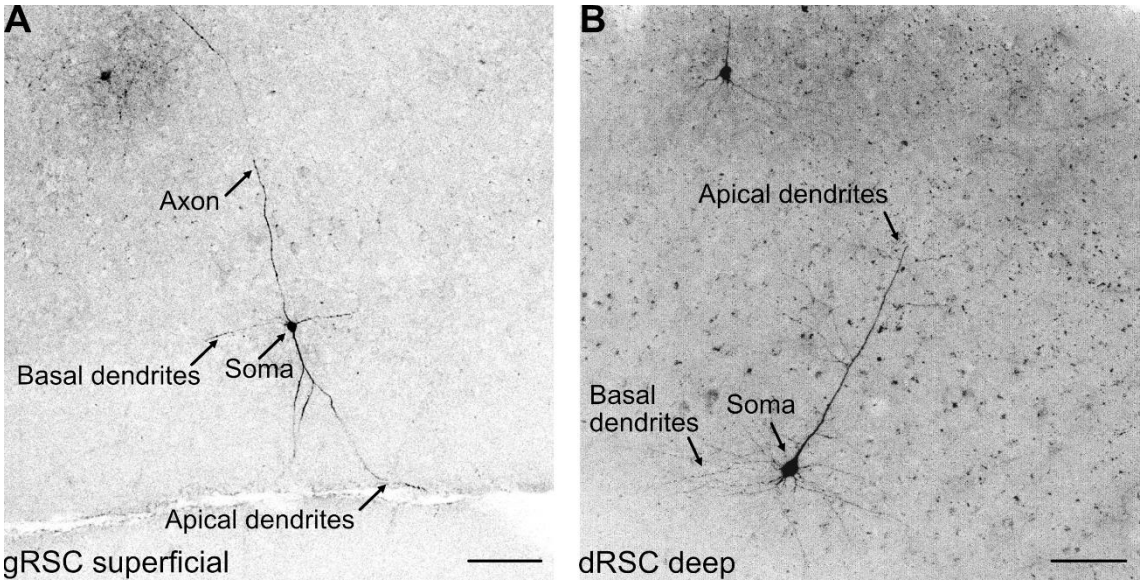

Figure 2.7 | Representative PC reconstruction. A Reconstructed PC in the gRSC superficial layers. **B** Reconstructed PC in the dRSC deep layers. Arrows indicate features used to identify as a PC: rounded pyramidal soma, and distinct apical and basal dendritic fields that are characteristic of the cell type. Scale bar: 100 µm.

2.6 | Statistical analysis

RStudio was used to conduct all statistical analyses and generate all data graphs; all non-standard packages used are listed in **Table 2.7**.

For the intrinsic properties electrophysiological data (**Section 3.3.**1) the variable AI was excluded because many cells has non-constant firing pattern which meant AI was heavily skewed and no longer fully representative of the measure. The remaining intrinsic properties variables were pre-processed by scaling each variable between 0 and 1 to standardise between the measures, before hierarchically clustering using Euclidean distances and Ward's method. The hierarchical cluster was then cut: cluster number was chosen by running multiple iterations of K-means (max 24) and comparing variance explained, cluster plots and other cluster index measures (such as the Hubert and silhouette indices) to identify the likely best number of clusters. Hierarchical clustering bootstrapping (1000 runs) using the Jaccard coefficient (Hennig, 2007) was then used to test cluster stability. The non-standardised variables were then tested for collinearity using Pearson's r correlation coefficient and the correlations were clustered. Due

multiple significant correlations, a multifactorial analysis of variance (MANOVA) was conducted to look for differences between the cell clusters, followed by *post hoc* univariate analysis of variance (ANOVA) and Tukey's HSD tests.

Synaptic response probability (**Section 3.3.3**) was analysed using Pearson's chi-squared test, followed by *post hoc* chi-squared tests where appropriate. For neuroanatomical tracing and synaptic response data (**Sections 3.3.2 & 3.3.3**) – when comparing between presynaptic region inputs – data was tested for normality and parametric and non-parametric tests were used where appropriate. To compare between independent groups one-way ANOVA, Kruskal-Wallis (one-way) or Scheirer-Ray-Hare (two-way) tests were used, followed by *post hoc* Mann-Whitney U comparisons. Two-way mixed ANOVA were used to compare between groups for a repeated measures variable. Aβ plaque deposition and basal Fos expression data (**Sections 4.3.1 & 4.3.2**) were analysed using two-way independent and three-way mixed ANOVA, followed by *post hoc* t-test multiple comparisons.

Mixed effect models were used for synaptic response data when comparing between sub-regions, layers, sex, age and genotype (**Sections 3.3.3 & 4.3.3**). These models included mouse ID as a random effect to control for multiple cells belonging to the same animal within the experimental group (eg. presynaptic region input). For independent measures data, a null model was fitted with just mouse random effect (random slope and intercept), then a linear mixed effect model was fitted by force-entering all independent variables as fixed effects. For repeated measures data (such as PPR) the null model included mouse random effect and the repeated measures data as a fixed effect factor. For the more complex modelling in **Section 4.3.3**, multiple experimental models were evaluated and sub-region and layer were always entered alone in the first model for each outcome. Subsequent models added age, genotype and sex and are detailed more thoroughly in the results. The goodness-of-fit for the null and mixed experimental models was compared using the χ^2-likelihood ratio test and the mixed model was reported when it generated a significant improvement upon the null model or on prior experimental models. Goodness-of-fit was also assessed and reported using Akaike information criterion (AIC): the model with the lowest AIC was deemed better. AIC was used to select the best model instead of the Bayesian information criterion as, while both estimates of goodness-of-fit correct

for number of parameters used, the AIC penalises multiple parameters less harshly (Field, 2013). Also, the AIC is considered the best model selection tool for predictive accuracy and is more appropriate for exploratory analysis and imprecise modelling (Aho et al., 2014). Main fixed effects were calculated using ANOVA, and pairwise comparisons reported as the fixed effect estimate and t-test statistics. Where random effects were found, the contribution to variance was reported.

All *post hoc* analyses were *p*-adjusted using the Benjamini-Hochberg correction to control for false discovery rate, unless specified as Tukey's HSD tests. Mice of both sexes were used in all experiments, but sex was only controlled for in the experiments using J20 mice in **Chapter 4**. Sex was controlled for here since there was theoretical justification as females are known to present with a higher Aβ burden in some AD models (Yang et al., 2018), and the effects of AD on neurophysiology can be modulated by sex (Arsenault et al., 2020).

2.7 | Lists of consumables and equipment

Item	Source	Identifier
Adenosine 5′-triphosphate magnesium salt (Mg-ATP)	Merck Life Sciences	A9187
Biocytin	VWR International	90055
Borosilicate capillary glass pipettes	VWR International	HARV30-0057
Calcium chloride ($CaCl_2$)	Merck Life Sciences	C5080
Cesium methanesulfonate ($CsMeSO_4$)	Merck Life Sciences	C1426
CGP 55845 hydrochloride	Tocris	1248
Choline bicarbonate	Merck Life Sciences	C7519
D-Glucose	Merck Life Sciences	G8270
DNQX	Hello Bio	HB0261
EGTA	Merck Life Sciences	E3889
Gabazine	Hello Bio	HB0901
Guanosine 5′-triphosphate sodium salt hydrate (Na_2-GTP)	Merck Life Sciences	51120
HEPES	Merck Life Sciences	H3375
L-689,560	Tocris	0742
Magnesium Chloride ($MgCl_2$)	Merck Life Sciences	M2670
NMDG	Merck Life Sciences	M2004
Poly-L-Lysine	Merck Life Sciences	P8920
Potassium Chloride (KCl)	Merck Life Sciences	P9333
Potassium D-gluconate (K-gluconate)	Merck Life Sciences	G4500

Potassium dihydrogen phosphate (KH_2PO_4)	Merck Life Sciences	229806
QX-314 chloride	Hello Bio	HB1030
Silver wire	World Precision Instruments	AGT0525
Sodium bicarbonate ($NaHCO_3$)	Merck Life Sciences	S5761
Sodium Chloride (NaCl)	Merck Life Sciences	S9888
Sodium dihydrogen phosphate (NaH_2PO_4)	Merck Life Sciences	S9763
Spermine	Merck Life Sciences	S3256

Table 2.1 | List of consumables and reagents used in electrophysiology experiments

Item	Source	Identifier
Ammonium nickel(II) sulfate	Merck Life Sciences	A1827
Amylo-Glo	2B Scientific	TR-300-AG
DAB tetrachloride	Hello Bio	HB0687
DyLight 488 Streptavidin	2B Scientific	SA-5488
DyLight 649 Streptavidin	2B Scientific	SA-5649
Ethanol	Merck Life Sciences	443611
Ethylene glycol	Merck Life Sciences	324558
Fluoromount	Merck Life Sciences	F4680
Glycerol	Merck Life Sciences	G5516
Goat biotinylated anti-rabbit antibody	2B Scientific	BA-1000
Histo-Clear II	Scientific Laboratory Supplies	NAT1334
Histomount	Scientific Laboratory Supplies	NAT1310
Hydrogen peroxide 30%	Merck Life Sciences	H1009
ImmEdge hydrophobic barrier PAP pen	2B Scientific	H-4000
Normal goat serum	Vector Laboratories	S-1000
Paraformaldehyde	Merck Life Sciences	158127
PBS tablets	VWR International	E404
Rabbit anti-Fos antibody	Cell Signalling Technology	2250
Sodium azide	Merck Life Sciences	S2002
Sodium pentobarbital	Covetrus	N/A
Sucrose	Merck Life Sciences	S0389
Superfrost slides	VWR International	631-0108
Triton X-100	Merck Life Sciences	X100
Vectashield Hard Set Mounting Medium with DAPI	2B Scientific	H-1000
Vectastain ABC-HRP Kit	2B Scientific	PK-4000

Table 2.2 | List of consumables and reagents used in immunohistochemistry experiments

Item	Souce	Identifier
Buprenorphine hydrochloride	Covetrus	N/A
Carprofen (Rimadyl)	Covetrus	N/A
EMLA cream 5% (Aspen)	Covetrus	N/A
Hamilton needle 33g	Fisher Scientific	15162654
Isoflurane	Covetrus	N/A
Prolene sutures 6/0	Medisave	W8005T

Table 2.3 | List of consumables used in surgical procedures

Use	Vector	Titer	Source	Identifier
Excitatory opsin	$AAV_{5/2}$-hSyn1-hChR2(H134R)_mCherry-WPRE-hGHp(A)	7.1 x 10^{12} vg/ml	ETH Zurich Viral Vector Facility	V124-5
Green fluorescent reporter	$AAV_{8/2}$-hSyn1-chI-EGFP-WPRE-SV40p(a)	5.9 x 10^{12} vg/ml	ETH Zurich Viral Vector Facility	V132-8
Red fluorescent reporter	$AAV_{8/2}$-hSyn1-chI-mCherry-WPRE-SV40p(A)	5.6 x 10^{12} vg/ml	ETH Zurich Viral Vector Facility	V133-8

Table 2.4 | List of viral vectors used in the present study

Item	Source
CoolLED -pE4000	CoolLED
Digidata 1440A digitiser	Digidata
Electrode holder 1-HL-U	Molecular Devices
Gibson MiniPuls 3 peristaltic pump	Gilson
Hamilton syringe	Hamilton
Leica SM2010R microtome	Leica
Leica VT1200 vibratome	Leica
Microinjector	World Precision Instruments
Model 940 Small animal stereotaxic instrument	David Kopf Instruments
Moving stage platform with control cube	Scientifica
Multiclamp 700B amplifier	Molecular Devices
Nikon Eclipse 800 microscope	Nikon
Olympus BX51W1 microscope	Olympus
P-97 Flaming Brown micropipette puller	Sutter Instrument Company
PatchStar motorised micromanipulator	Scientifica
Physitemp BFS-5MP temperature controller	Physitemp
SciCam Pro camera	Scientifica
SPOT RT monochrome camera	SPOT
Surgical drill (503598)	World Precision Instruments
Temperature controller with in-line Peltier heater SM-4600	Scientifica

Table 2.5 | List of equipment used in the present study

Software	Source
ClampFit 10.7	Molecular Devices
Fiji	National Institutes for Health (Schindelin et al., 2012)
Igor Pro 7	Wavemetrics
MATLAB	Mathworks
pClamp 10	Molecular Devices
RStudio	RStudio Team (2020)
SPOT Basic Imaging Capture	SPOT

Table 2.6 | List of software used in the present study

R package	Source
afex	https://cran.r-project.org/web/packages/afex/index.html
BBmisc	https://cran.r-project.org/web/packages/BBmisc/index.html
corrplot	https://cran.r-project.org/web/packages/corrplot/index.html
dendextend	https://cran.r-project.org/web/packages/dendextend/index.html
factoextra	https://cran.r-project.org/web/packages/factoextra/index.html
flextable	https://cran.r-project.org/web/packages/flextable/index.html
foreign	https://cran.r-project.org/web/packages/foreign/index.html
fpc	https://cran.r-project.org/web/packages/fpc/index.html
ggplot2	https://cran.r-project.org/web/packages/ggplot2/index.html
ggpubr	https://cran.r-project.org/web/packages/ggpubr/index.html
gridExtra	https://cran.r-project.org/web/packages/gridExtra/index.html
lme4	https://cran.r-project.org/web/packages/lme4/index.html
lmerTest	https://cran.r-project.org/web/packages/lmerTest/index.html
mvnormtest	https://cran.r-project.org/web/packages/mvnormtest/index.html
rcompanion	https://cran.r-project.org/web/packages/rcompanion/index.html
Rmisc	https://cran.r-project.org/web/packages/Rmisc/index.html
rstatix	https://cran.r-project.org/web/packages/rstatix/index.html
SimComp	https://cran.r-project.org/web/packages/SimComp/index.html
sjPlot	https://cran.r-project.org/web/packages/sjPlot/index.html
svglite	https://cran.r-project.org/web/packages/svglite/index.html
tidyverse	https://cran.r-project.org/web/packages/tidyverse/index.html

Table 2.7 | R packages used for statistical analysis and graph generation

3 | The dRSC and gRSC differ in their connectivity with the ACC, dSub and ATN in the C57BL/6J mouse

3.1 | Introduction

The RSC is known to be involved in a variety of cognitive functions (Chrastil, 2018), including learning and memory, yet there is still much we do not know about this brain region. For example, are there unique features in terms of cell-to-cell communication, or neuronal physiological or synaptic properties that contribute to the function of this region?

Characterising the neuronal populations within a brain region can help understand the function of the area. For instance, the structural complexity of PCs is associated with differences in cognitive specialisation between different cortical areas (Elston, 2003). Additionally, within cortical subregions, different PC subtypes display distinct morphology related to intracortical connectivity and differing synaptic response to inhibitory activity (Chagnac-Amitai et al., 1990). Different PC subtypes also show different patterns of synaptic plasticity and mechanisms, indicating fundamental synaptic connectivity differences which may have significant functional implications (Greenhill et al., 2015; Jacob et al., 2012). Therefore, confirming and extending our understanding og PC diversity in the RSC forms part of a larger picture when understanding its connectivity and function. Some studies have identified different PC subtypes in the gRSC, including small hyperexcitable cells in the superficial layers in the mouse (Brennan et al., 2020), PCs with a significantly delayed spike response in the rat (Kurotani et al., 2013), as well as burst-spiking PCs in the rat gRSC deep layers (Yousuf et al., 2020). However, little is known about the intrinsic electrical properties of RSC PCs, particularly compared to other better-studied areas such as the HPC or barrel cortex. So far PCs in the dRSC have not been characterised. This chapter reports an analysis ofPC subtypes in the gRSC and dRSC to establish a framework through which we can understand the function of afferent inputs into both sub-regions.

Neuroanatomical tracing studies have extensively mapped RSC connectivity in the rodent brain (Groen and Wyss, 2003, 1992, 1990), and some studies have identified distinct sub-region targeting (Aggleton et al., 2021), however laminar distribution and synaptic response of these connections is still relatively unknown. The few studies that have characterised the function of excitatory and inhibitory afferent projections into the RSC (**see Section 1.1.3**) have typically focused on

the gRSC region. Therefore, there is a clear gap in the literature regarding synaptic responses to afferent inputs in the dRSC. Additionally, while research by Brennan et al. (2021) and Yamawaki et al. (2019) dissected synaptic responses in individual PCs across different layers in the gRSC, generally only the magnitude and direction of the responses have been reported. Other measures of synaptic function, such as the properties of AMPAR- and NMDAR-mediated EPSCs and short-term plasticity, as well as probability of response, can provide more detailed information about these synaptic connections in the RSC.

The primary aim of the experiments reported in this chapter was to describe and compare the neuroanatomical laminar distribution and synaptic response to afferents in both dRSC and gRSC arising from three presynaptic areas: the ACC, the dSub and the ATN. One very recent study investigated these inputs solely in the gRSC (Brennan et al., 2021). Therefore examining whether and how these inputs differ between RSC sub-regions will provide more information on functional connectivity into the RSC. Experiments were performed using a combination of neuroanatomical tracing and electrophysiological recordings of synaptic responses following optogenetic stimulation of afferent terminals arising from each presynaptic region.

3.2 | Methods and animals

Measurement of intrinsic electrical membrane properties

27 C57BL/6J mice (n_{male} = 12, n_{female} = 15) aged between 3-6 months were used. The age range of all the animals in this chapter was between 3 and 8 months, and included only adult healthy mice to prevent any developmental or excessive ageing-related effects on the results. 163 cells were recorded, of which 35 were excluded as not being viable for analysis (**Section 2.4.2.2)**. Of the 128 cells remaining, 63 were anatomically reconstructed and 3 excluded for presenting non-PC like morphology. Confidence in the remaining cells being PC is high as false positive rate for the reconstructed cells was <5% and the excluded cells had already been highlighted as potential INs pre-reconstruction.

Neuroanatomical viral tracing

20 (n_{male} = 8, n_{female} = 12) C57BL/6J mice aged between 3-5 months were used. Mice were injected in two of the experimental presynaptic brain regions (ACC, dSub, ATN) with either AAV_8-hSyn1-EGFP or AAV_8-hSyn1-mCherry (see **Table 2.4** for viral vector details) and were killed by perfusion fixation 6 weeks post-surgery. 7 mice were excluded due to a failed or misplaced injection in both regions. Of the 11 (n_{male} = 4, n_{female} = 7) remaining mice; 7 mice had one viable injection and 4 mice had two viable injections, leaving 15 viable injections of which 6 were in the ACC, 4 were in the ATN and 5 in the dSub. Two images from the anterior (pre-splenium) and posterior (post-splenium) RSC were taken for each injection. Mean fluorescent intensities were taken per sub-region then per layer and averaged for the anterior and posterior sections. As mean fluorescent intensities were used for analysis, fluorophore was not controlled for.

Optogenetic characterisation of long-range synaptic connectivity

All mice were from the C57BL/6J line and aged between 4 and 8 months at time of recording. Mice were injected with AAV_5-hSyn1-ChR2(H134R)-mCherry (see **Table 2.4**). 24 mice were injected in the ACC; 7 mice were excluded from recording or analysis for missing or misplaced injection sites and 3 mice were excluded because of poor slice quality. 126 cells were recorded overall from 14 mice (n_{male} = 7, n_{female} = 7), and 30 were excluded for not meeting viability criteria (**Section 2.4.3.2**). 21 mice were injected in the dSub; 6 mice were excluded for missing or misplaced injection sites and 5 mice were excluded because poor slice quality. 84 cells were recorded overall from 10 mice (n_{male} = 6, n_{female} = 4), and 19 were excluded for not meeting viability criteria. 16 mice were injected in the ATN; 5 were excluded for missing or misplaced injection site and 2 were excluded because of poor slice quality. 52 cells were recorded overall from 9 mice (n_{male} = 7, n_{female} = 2), and 13 were excluded for not meeting viability criteria. In addition, 2 mice were injected with $AAV_{8/2}$-hSyn1-mCherry in the ATN (n_{male} = 1, n_{female} = 1). 21 cells were recorded and 1 cell was excluded for not meeting viability criteria.

3.3 | Results

3.3.1 | PC heterogeneity in the RSC forms clusters with distinct intrinsic properties

Different features from intrinsic membrane properties (named in **Figure 3.1**) from 125 cells were entered into a hierarchical clustering model and 3 distinct clusters emerged (**Figure 3.1 A-B**): cluster 1 (C1), cluster 2 (C2), and cluster 3 (C3), respectively. The clusters appeared relatively distinct, however there was some overlap between C1 and C3. Additionally, C2 and C3 were relatively disperse and a low Dunn Index value of 0.11 (a measure of clustering validity which calculates the ratio of the smallest inter-cluster distance to the largest intra-cluster distance) indicated probable high intra-cluster variability. Bootstrapping (1000 runs) indicated that C1 was highly stable (> 0.85) and C2 and C3 were moderately stable (> 0.7) (**C1:** *stability* = 0.90, *dissolutions* = 2; **C2:** *stability* = 0.65, *dissolutions* = 42; **C3:** *stability* = 0.76, *dissolutions* = 7). However, the variance explained by 3 clusters was fairly low at 30.0% (increasing from 18.5% for 2 clusters). While variance explained did continue to increase in smaller increments for larger numbers of clusters (k_4=35.1%, k_5=39.6%), cluster plots indicated these extra clusters were highly overlapping and not distinct from each other. When considering how the clusters were separated, it was clear that C2 was separated from C1 and C3 along the principal component 2 (PC2) axis but was dispersed along the principal component 1 (PC1) axis, which separated C1 and C3 (**Figure 3.1 B**). The variable loadings for PC1 and PC2 are presented in **Figure 3.1 C**, and show that that R_i, rise time, rheobase, BI, AP max dV/dt and AP peak had the strongest effects on clustering; which is supported by significant differences between clusters for these measures. These clusters were not solely located to specific RSC sub-regions or layers (**Figure 3.1 E**), indicating some PC diversity within these areas. However superficial cells – especially those in the dRSC – were predominantly sorted in cluster 3; suggesting PCs in layers 2-3 present less heterogeneity than deep layer PCs (see also **Figure 3.4**). A similar number of PCs per sub-region and cortical layer were recorded indicating this was not due to a sampling error (**dRSC superficial:** 30, **dRSC deep:** 31, **gRSC superficial:** 37, **gRSC deep:** 27).

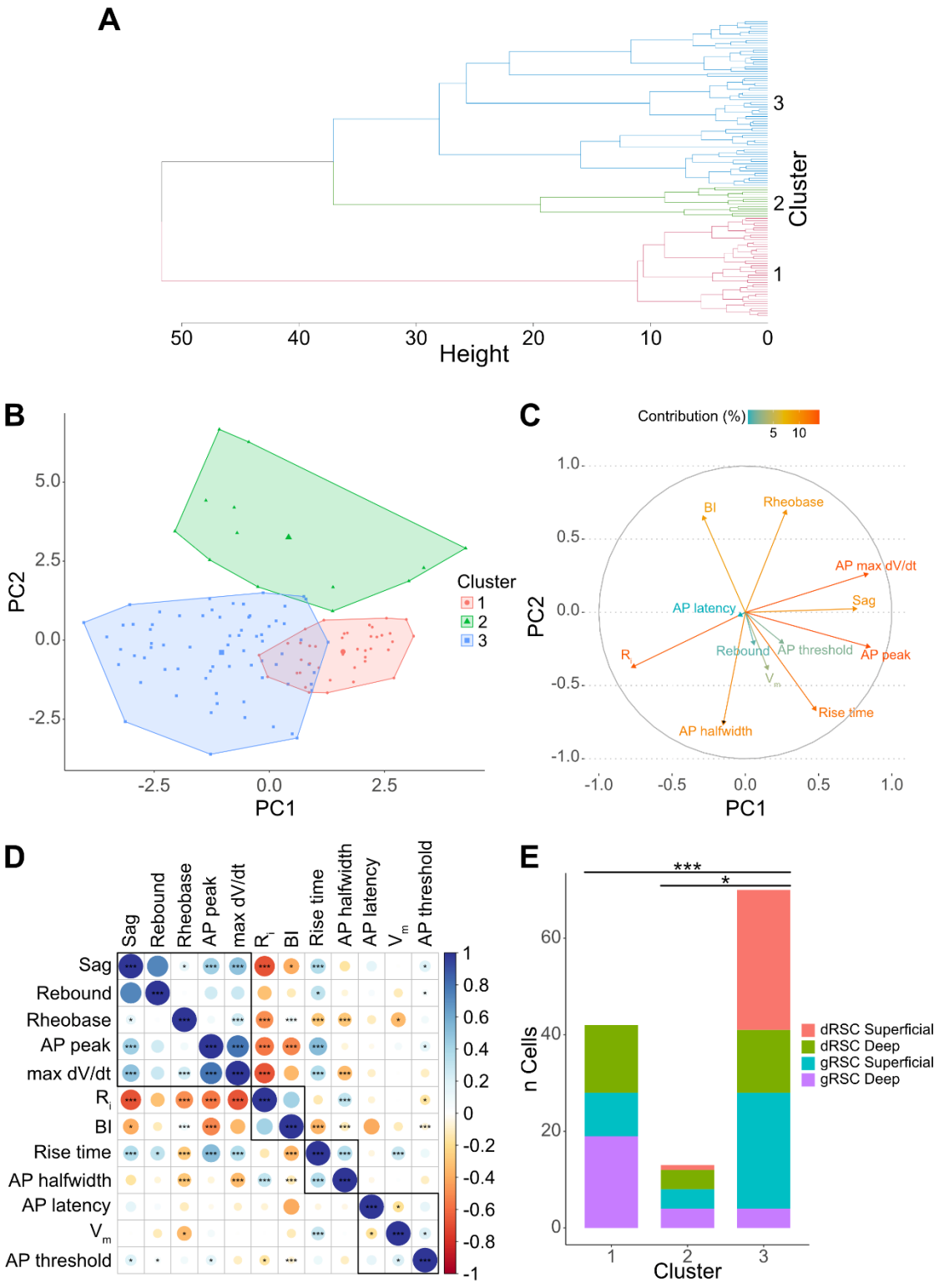

Figure 3.1 | PCs in the RSC are highly heterogeneous. A Dendrogram showing the hierarchical clustering of PCs recorded in the RSC. **B** Scatterplot of principal components 1 (PC1) and (PC2) with hierarchical clusters imposed. **C** Variable loadings onto PC1 and PC2. **D** There was a large amount of correlation between the non-normalised variables, significance values indicated on correlogram. **E** There were significantly

different proportions of PCs from the different sub-regions of the RSC between the clusters ($\chi_2(6) = 43.92$, $p < .001$; Pearson's Chi-Squared test). Chi-squared *post hoc* tests showed that the cell proportions between C1 and C2 did not differ significantly ($p = 0.25$), but did differ between C1 and C3 and C2 and C3. * $p < .05$, *** $p < .001$.

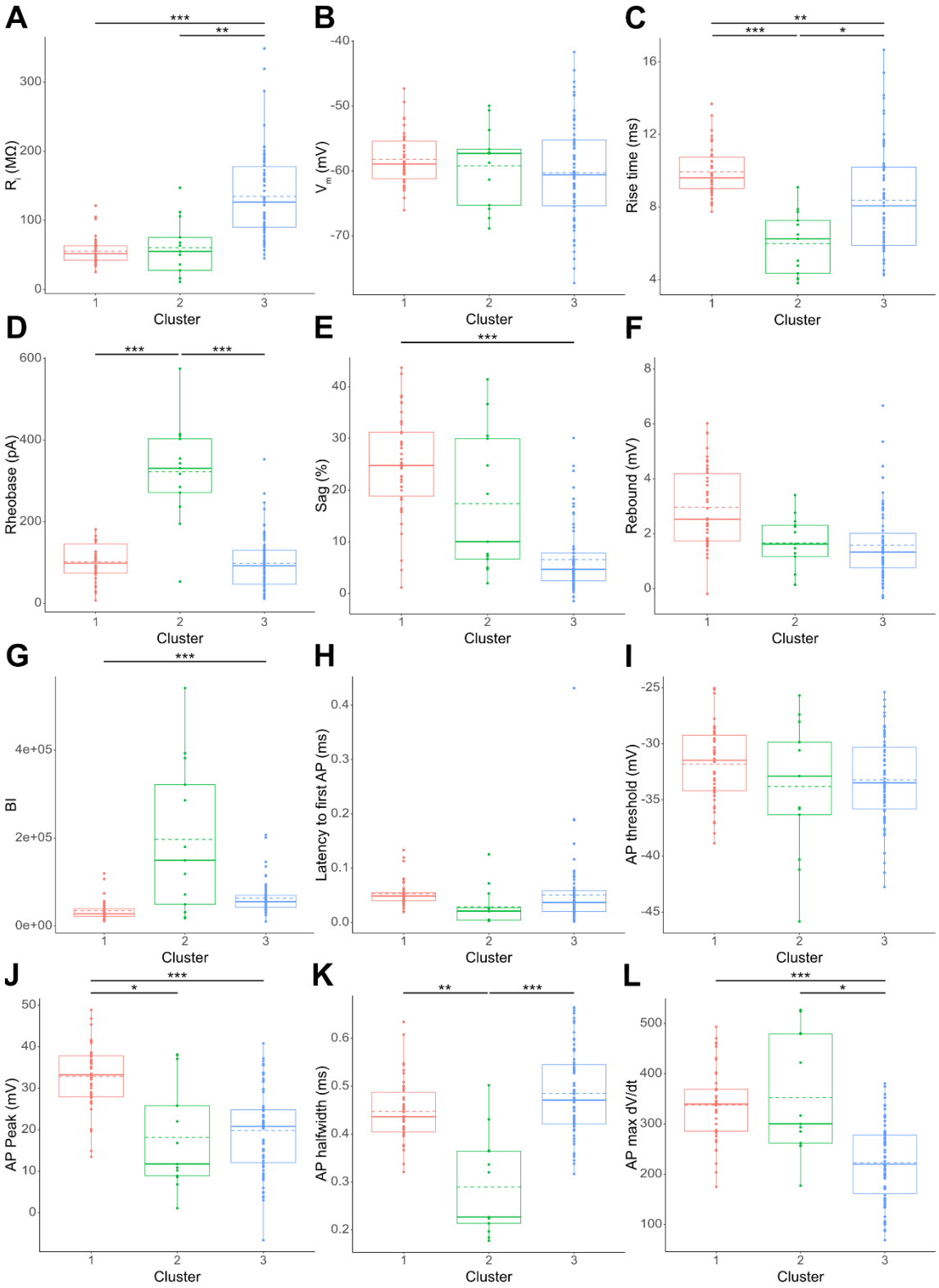

Figure 3.2 | Cell clusters have distinct differences in intrinsic membrane properties. Tukey's HSD tests were conducted and significance values were adjusted for multiple tests. **A** While C1 and C2 showed no significant difference in R_i (p = 1), C3 had a significantly higher R_i than both C1 and C2. **B** There was no significant effect of cluster on V_m. **C** All three clusters showed significant differences in their rise time; C1 had a higher rise time than both C2 and C3, and C2 rise time was lower than C3. **D** While C1 and C3 showed no significant difference in rheobase (p = 1), C2 showed a higher rheobase than both C1 and C3. **E** C1 had a significantly higher sag than C3, however C2 did not differ from C1 (p = .64) and C3 (p = .17). **F** There was no significant effect of cluster on rebound. **G** C1 had a significantly lower burst index than C3, whilst C2 did not differ from C1 (p = .06) and C3 (p = .17). **H** There was no significant effect of cluster on latency to first AP. **I** There was no significant effect of cluster on AP threshold. **J** C1 had a significantly higher AP peak than C2 and C3, but C2 and C3 did not differ (p = 1). **K** While C1 and C3 did not show significantly different AP halfwidths (p = .18), C2 showed a significantly lower AP halfwidth than C1 and C3. **J** C3 showed a significantly lower AP max dV/dt than C1 and C2, while C1 and C2 did not significantly differ (p = 1). Boxplots display median (solid line), mean (dashed line), IQR and range. * *p < .05,* ** *p < .01,* *** *p < .001*

As the non-standardised intrinsic properties variables showed a high collinearity (**Figure 3.1 D**), a MANOVA was conducted and showed that intrinsic properties differed significantly between clusters (Pillai's trace = 1.38, $F(24,224) = 20.64$, $p < .001$). Univariate ANOVA were then conducted to determine which properties showed significant differences between clusters (**Table 3.1**) and *post hoc* tests determined where those differences lay (**Figure 3.2**). Overall, the *post hoc* tests indicated that C1 showed the highest rise time, sag and AP peak as well as the lowest BI. C2 showed the highest rheobase and the lowest rise time and AP halfwidth. C3 showed the highest R_i and the lowest sag and AP max dV/dt. **Table 3.1** shows mean and SD for all measures by cluster and representative traces for each cluster are shown in **Figure 3.3**.

	Cluster 1 (n=42)	Cluster 2 (n=13)	Cluster 3 (n=70)	ANOVA
	Mean	Mean	Mean	
R_i (MΩ)	**55.38 (19.5)**	**60.28 (41.52)**	**134.71 (61.87)**	***F*(2,122) = 38.26, *p* < .001**
V_m (mV)	-58.20 (4.10)	-59.22 (6.13)	-60.27 (7.77)	*F*(2,122) = 1.30, *p* = .30
Rise time (ms)	**9.94 (1.34)**	**5.98 (1.75)**	**8.38 (2.99)**	***F*(2,122) = 14.08, *p* < .001**
Rheobase (pA)	**101.26 (45.38)**	**322.38 (125.32)**	**97.61 (66.33)**	***F*(2,122) = 61.53, *p* < .001**
Sag (%)	**24.47 (9.71)**	**17.13 (13.71)**	**6.31 (6.32)**	***F*(2,122) = 60.73, *p* < .001**
Rebound (mV)	2.97 (1.46)	1.66 (1.01)	3.58 (12.19)	*F*(2,122) = 0.26, *p* = .77
BI	**34575.41 (22276.10)**	**196922.19 171188.86)**	**63144.10 (34082.02)**	***F*(2,122) = 35.70, p < .001**
Latency to first AP (ms)	0.053 (0.024)	0.029 (0.036)	0.050 (0.06)	*F*(2,122) = 1.35, *p* = .30
AP threshold (mV)	-31.81 (3.39)	-33.81 (6.05)	-33.23 (3.91)	*F*(2,122) = 2.08, *p* = 0.17
AP peak (mV)	**32.83 (7.76)**	**18.14 (12.85)**	**19.78 (9.95)**	***F*(2,122) = 26.86, *p* < .001**
AP halfwidth (ms)	**0.45 (0.07)**	**0.29 (0.10)**	**0.48 (0.09)**	***F*(2,122) = 29.47 *p* < .001**
AP max dV/dt	**337.50 (73.37)**	**35227 (117.82)**	**223.27 (76.75)**	***F*(2,122) = 32.98, *p* < .001**

Table 3.1 | Summary of intrinsic membrane properties between clusters. Mean and SD deviation are shown for each cluster, and univariate ANOVA results are presented. Rows in bold indicate significant differences in R_i, rise time, rheobase, sag, BI, AP peak, AP halfwidth and AP max dV/dt, respectively.

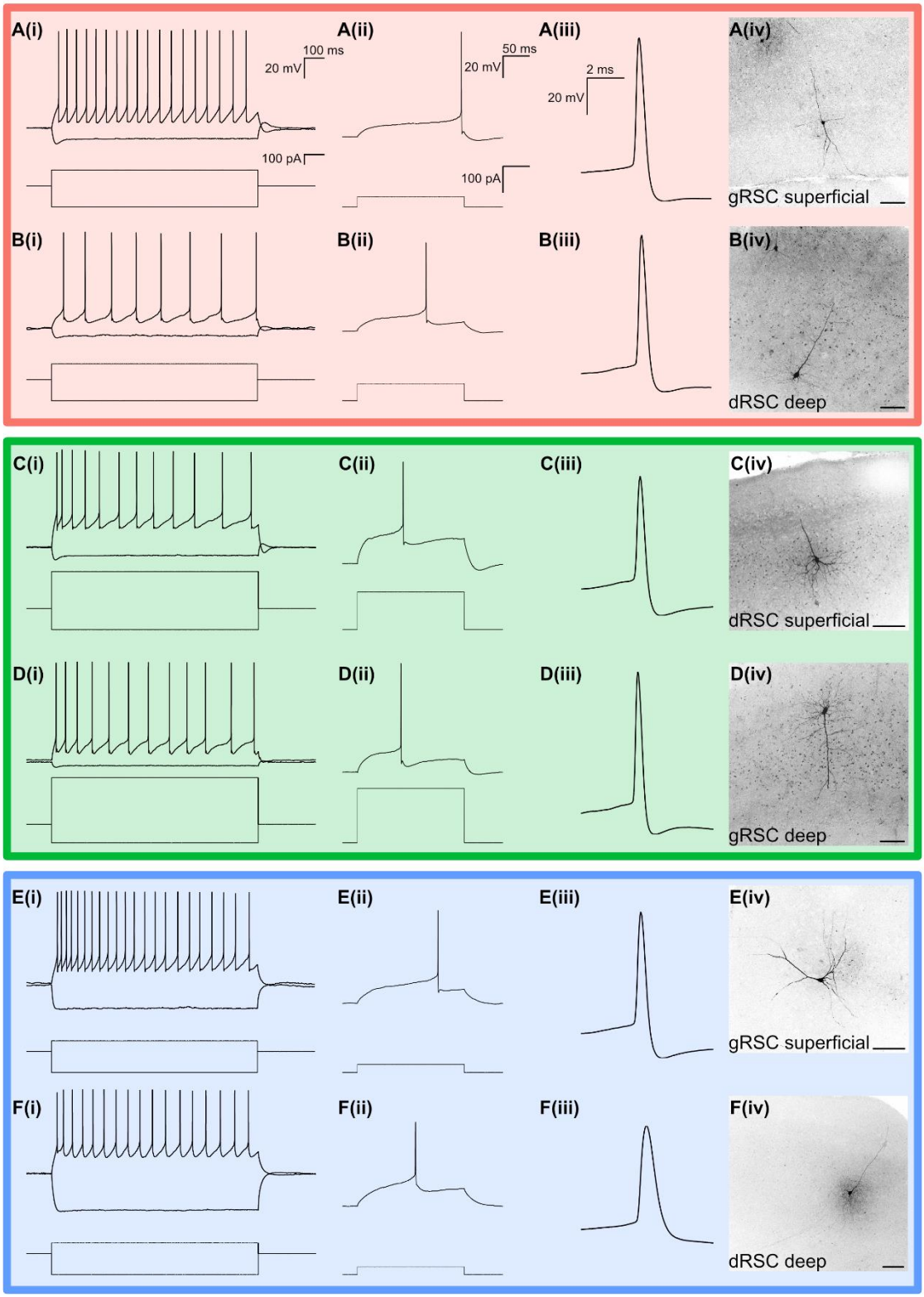

Figure 3.3 | Example electrophysiological recordings and cell reconstructions for each cluster. Traces and cell recoveries are shown for C1 (**A-B**), C2 (**C-D**) and C3 (**E-F**). **A-F(i)** Voltage response (top) to depolarising and hyperpolarising current injections (bottom). The depolarisation step shown was the first to induce a train of ≥4 spikes. **A-F(ii)**

Voltage response (top) to rheobase depolarising current injection (bottom). **A-F(iii)** Zoomed-in view of the first spike in (**i**) trace. Scale bars apply to all recordings. **A-F(iv)** Biocytin-staining showing morphology of cell recorded in (**i-iii**). Scale bar 100 µm.

While the different clusters of PCs were not completely sub-region and layer specific (**Figure 3.1 E**), analysis of the cluster frequency in these areas showed clear patterns of cell subtype location (**Figure 3.4**). The sub-regions of the RSC showed significantly different ratios of each cell cluster type ($\chi_2(6) = 43.92$, $p < .001$; Pearson's Chi-squared test). Chi-squared *post hoc* tests indicated that the dRSC superficial region differed from all other regions (dRSC deep: $p < .001$, gRSC superficial: $p < .01$, gRSC deep: $p < .001$). While the gRSC superficial region differed from the gRSC deep region ($p < .001$) it was not significantly different from the dRSC deep region ($p = .15$), which also did not differ from the gRSC deep region ($p = .09$). The dRSC and gRSC superficial layers predominately contained PCs from C3: cells with a high R_i, a small hyperpolarisation-activated cation current (sag) and the fastest AP maximal rise time. Cells in the dRSC deep layers were more evenly distributed in the groups, while in the gRSC deep layers cells belonged primarily to C1 which had the largest sag, greatest AP magnitude and the lowest BI (see **Figure 3.2**).

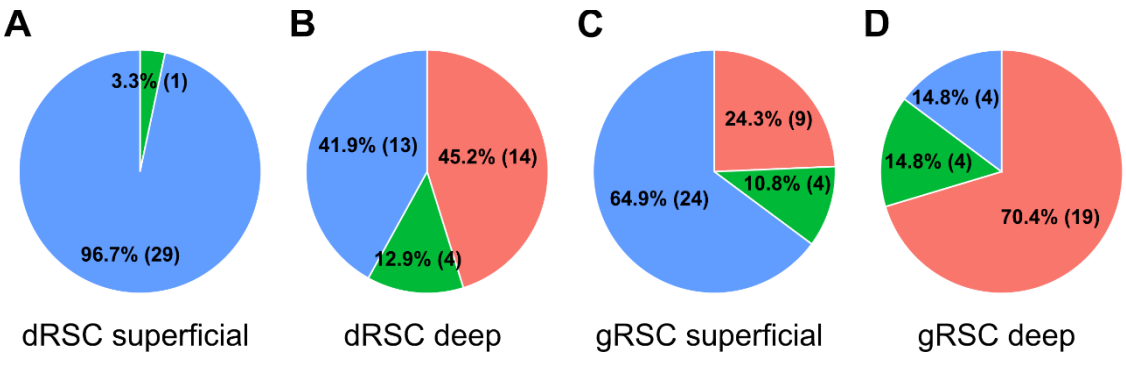

Figure 3.4 | RSC sub-regions contain different ratios of each cell cluster type. A PCs in the dRSC superficial region showed a significant difference in cluster allocation ($\chi_2(2) = 54.20$, $p < .001$). No cells belonged to C1 while the large majority belonged to C3 (96.7%). **B** PCs in the dRSC deep region did not differ significantly in their cluster allocation ($\chi_2(2) = 5.88$,

p = .05). **C** PCs in the gRSC superficial region showed a significant difference in cluster allocation ($\chi_2(2) = 17.57$, $p < .001$). The largest percentage of cells belonged to cluster 3 (64.9%). **D** PCs in the gRSC deep region showed a significant difference in cluster allocation ($\chi_2(2) = 16.67$, $p < .001$) with the highest frequency of cells belonging to cluster 1. Pie charts are annotated with cell percentage and count (in brackets) for each cluster.

3.3.2 | Afferent inputs from different presynaptic regions differentially target RSC sub-regions and layers

Sections containing sites in the ACC, ATN, or dSUB injected with anterograde viral tracer or in the anterior (pre-splenium) or posterior (post-splenium) RSC were imaged and processed for analysis. ACC injections were primarily limited to the ACC however there was some leakage into neighbouring regions, namely the prelimbic (PL) cortex and M2 both of which have connections to the RSC (**Figure 3.5 A**). However, viral spread into the surrounding cortical areas was minor and considered sufficiently negligible in this study. dSub injections were primarily restricted to the target region, although some spreading into the adjacent dentate gyrus (DG) of the HPC was seen (**Figure 3.5 B**). However, the DG does not have direct input into the RSC, so this small level of leakage would not confound the results of the tracing experiment. ATN injections did not spread into neighbouring areas, but the ADN and AVN showed viral expression with little to no expression in the AMN (**Figure 3.5 C**). It is not possible to cleanly inject all ATN in a single injection, and so to prevent virus volume bias the ADN/AVN were targeted. The ADN/AVN were chosen in order to compare our results with previous literature examining the functional connectivity of RSC afferents (Brennan et al., 2021; Yamawaki et al., 2019c). These patterns of injection site expression were consistent across all animals, suggesting low variability in afferent terminal density. The tracing technique used allowed for presynaptic labelling only, therefore postsynaptic targets were not analysed at a cellular level.

In the RSC, fluorescence from afferent terminals was seen only in the ipsilateral RSC for dSub and ATN injections (**Figure 3.5 E-F & H-I**). ACC injections showed the majority of fibres projected to the ipsilateral RSC, with negligible fibre fluorescence in the contralateral RSC (**Figure 3.5 D & G**). Therefore, all analyses

measured fluorescence in the ipsilateral RSC only. Mean fluorescence intensities were calculated for each sub-region and normalised as a percentage of total fluorescence to compare between inputs. Laminar analysis calculated mean fluorescence intensities for each layer, normalised within sub-region to compare the laminar distribution of terminals for the dRSC and gRSC.

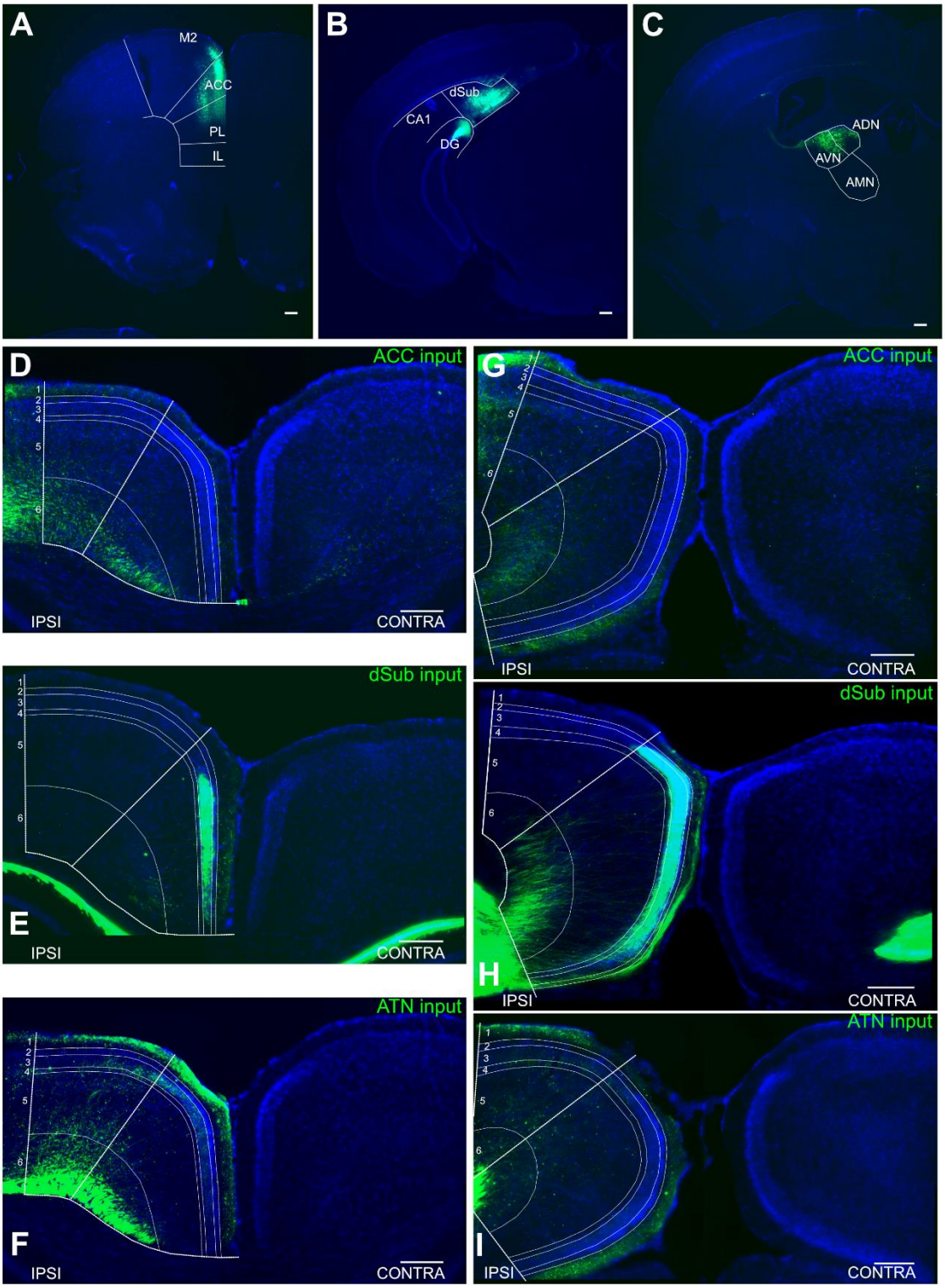

Figure 3.5 | Anterograde viral tracing from the ACC, dSub and ATN shows projections to the anterior and posterior RSC. A-C Representative images of EGFP-labelled injection sites in the ACC (**A**), dSub (**B**) and ATN (**C**). **D-F** Representative images of the anterior RSC showing EGFP-labelled afferent terminals from the ACC (**D**), dSub (**E**) and ATN (**F**) in the ipsilateral cortex. **G-I** Representative images of the posterior RSC showing EGFP-labelled afferent terminals from the ACC (**G**), dSub (**H**) and ATN (**I**) in the ipsilateral cortex. Scale bars: 250 µm.

There was a significant difference in afferent terminal distribution between sub-regions for all inputs (**Figure 3.6 A**). Inputs from the ACC preferentially targeted the dRSC compared to the gRSC, while the opposite was true for inputs from the dSub and ATN, which had increased fibre expression in the gRSC. This pattern of sub-region targeting was maintained along the A-P axis (**Figure 3.6 B**). Fibre density was not directly compared between anterior and posterior slices – but rather the pattern of sub-region targeting within slice was compared – due to the inability to normalise fully because of differing callosal and neighbouring region fluorescence artefacts along the A-P axis.

As there was no interaction between A-P position and sub-region, the anterior and posterior values were combined for laminar distribution analysis. ACC input was different between layers, but the laminar distribution did not differ between sub-regions (**Figure 3.6 C**). Inspection of the fluorescence distribution indicated increased fibre density in layer 6 while layers 1-5 were relatively similar in both the dRSC and gRSC. Fibre density was different between layers for dSub input, and this distribution was modulated by sub-region (**Figure 3.6 D**). Observation of the fluorescence data showed that the gRSC dSub input showed the most density in layer 3, while density was highest in layer 6 for the dRSC. Input from the ATN also showed differences between layer modulated by sub-region (**Figure 3.3.6 E**): the graph shows that both the dRSC and gRSC had highest expression in layer 6, however layer 3 in the gRSC also displayed a smaller increase compared to the dRSC. Overall, the dSub and ATN showed similar patterns of neuroanatomical connections in gRSC and dRSC, but the ACC had a distinct afferent terminal pattern between RSC sub-regions.

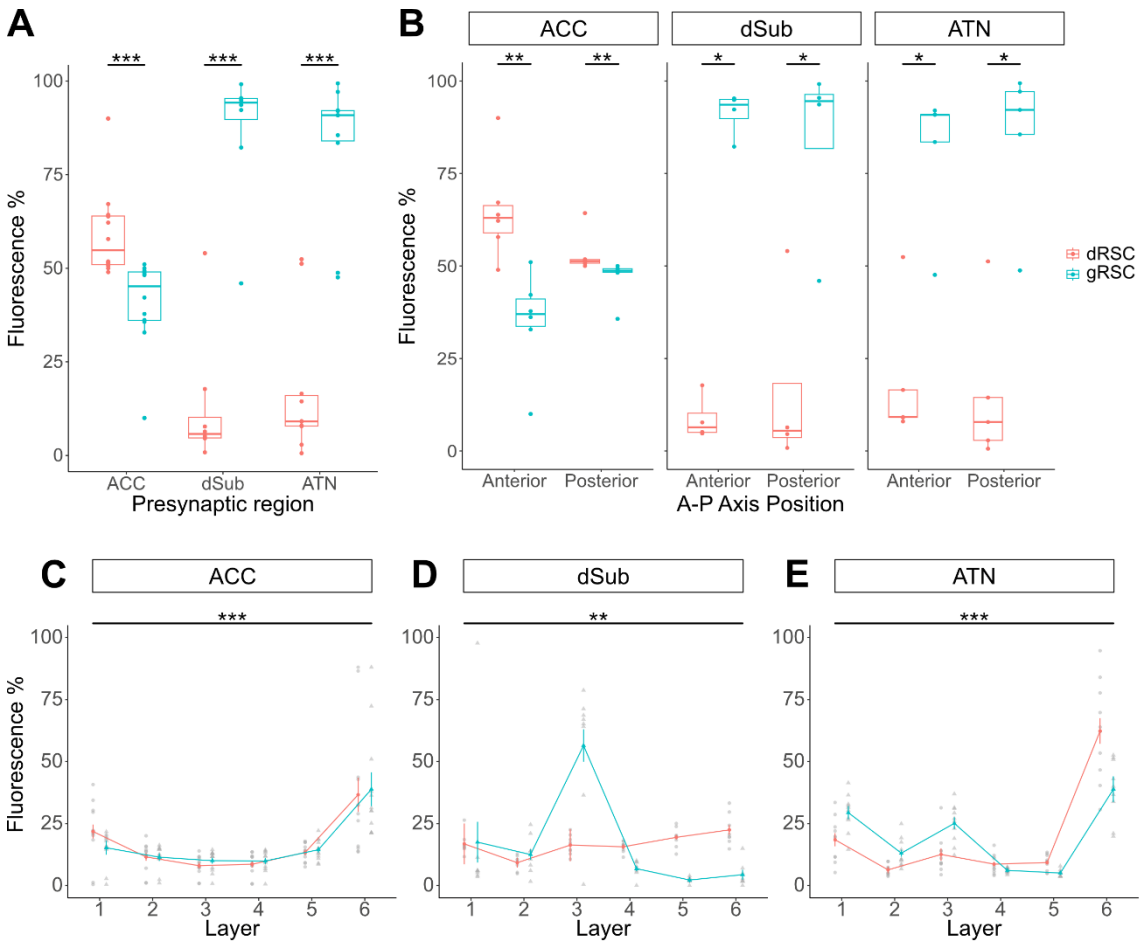

Figure 3.6 | Sub-region and laminar differences in anatomical inputs to the RSC. A Mean fluorescence intensities for the dRSC and gRSC were normalised to the total fluorescence and presented as percentages. There was a main effect of RSC sub-region ($H(1) = 11.02$, $p < .001$; Scheirer-Ray-Hare test), and a significant interaction between sub-region and presynaptic region ($H(2) = 29.73$, $p < .001$). Mann-Whitney U *post hoc* pairwise comparisons revealed significantly higher fluorescent signal in the gRSC compared to dRSC for inputs from the dSub (**dRSC:** 5.75 (4.67 – 10.23), **gRSC:** 94.25 (89.77 – 95.33) %) and ATN (**dRSC:** 9.11 (7.86 – 15.98), **gRSC:** 90.89 (84.02 – 92.14) %), whilst ACC input showed higher fluorescent signal in the dRSC compared to the gRSC (**dRSC:** 54.82 (50.97-63.96), **gRSC:** 50.97, (63.96) %). **B** This input-specific RSC sub-region pattern was maintained along the A-P axis with a significant effect of sub-region for all presynaptic regions. For ACC input there was a significant main effect of ($H(1) = 14.74$, $p < .001$; Scheirer-Ray-Hare test) but no interaction between sub-region and AP position ($H(1) = 1.02$, $p = 0.31$). The dSub and ATN inputs also showed

significant main effects of sub-region ($H(1) = 10.59$, $p < .01$ and $H(1) = 12.09$, $p < .001$ respectively) and no interaction effect with AP position ($H(1) = 0.09$, $p = 0.75$ and $H(1) = 0.69$, $p = .41$). *Post hoc* tests showed significant differences between sub-regions anterior and posterior sections for all sub-regions. **C-E** Mean fluorescence for each cortical layer normalised within sub-region. **C** ACC input showed a significant main effect of layer ($F(5,110) = 19.5$, $p < .001$; 2-way mixed ANOVA with Greenhouse-Geisser correction) but no interaction between sub-region and layer ($F(5,110 = 0.45$, $p = .53$). **D** dSub input showed a significant main effect of layer ($F(5,70) = 8.30$, $p < .01$; 2-way mixed ANOVA with Greenhouse-Geisser correction) and a significant interaction between sub-region and layer ($F(5,70) = 9.69$, $p < .01$). **E** ATN input showed a significant main effect of layer ($F(5,90) = 64.08$, $p < .001$; 2-way mixed ANOVA with Greenhouse-Geisser correction) and interaction between sub-region and layer ($F(5,90) = 10.41$, $p < .01$). Descriptive statistics display median and IQR. Boxplots display median, IQR and range. Line-graphs show mean ±1 SEM. ** $p < .01$, *** $p < .001$

3.3.3 | RSC sub-region and laminar differences in synaptic inputs from different presynaptic regions

Following optogenetic stimulation of afferent terminals in the RSC, cells were classed as either responding (R) or non-responding (NR) depending on whether they showed a change in membrane current time-locked to the light stimulus (**Figure 3.7 A**). All patch recordings were made in voltage-clamp mode with a holding potential of -70 mV, but without presence of any GABAergic antagonists, unless stated otherwise. GABAergic antagonists were omitted from the standard aCSF as ATN stimulation generated epileptiform activity with the antagonists present. **Table 3.2** displays cell counts for all synaptic response measures separated by input, sub-region and layer.

Input	Sub-region	Layer	Respond	Count		
				EPSC measures	NMDA/AMPA	PPR
ACC	*dRSC*	*Superficial*	14 / 29	14	5	7
		Deep	11 / 20	11	5	8
	gRSC	*Superficial*	2 / 27	2	1	2
		Deep	14 / 20	14	7	13
dSub	*dRSC*	*Superficial*	5 / 9	5	0	2
		Deep	4 / 8	4	2	3
	gRSC	*Superficial*	10 / 12	10	5	5
		Deep	28 / 35	28	3	8
ATN	*dRSC*	*Superficial*	12 / 12	12	2	4
		Deep	5 / 5	5	1	5
	gRSC	*Superficial*	11 / 11	11	5	9
		Deep	11 / 11	11	4	8
		Total		**127**	**40**	**74**

Table 3.2 | Recorded cells separated by presynaptic input, RSC sub-region and cortical layer. All putative PCs were first classified as responding or not responding to stimulation of afferent terminals, stated as a fraction. EPSC magnitude was calculated from 127 cells total, NMDA/AMPA ratio from 40 cells, and PPR from 74 cells.

ACC input showed the lowest response probability (**R:** 41/96 cells, **NR:** 55/96 cells) followed by dSub input (**R:** 47/64 cells, **NR:** 17/64 cells), whilst ATN input led to responses in all cells recorded (**R:** 39/39) (**Figure 3.7 B**). Response probability for ACC input also differed by sub-region and layer (**Figure 3.7 C**) but not for dSub input (**Figure 3.7 D**). ATN input sub-analysis was not conducted as 100% of cells responded. All responses recorded were excitatory in nature.

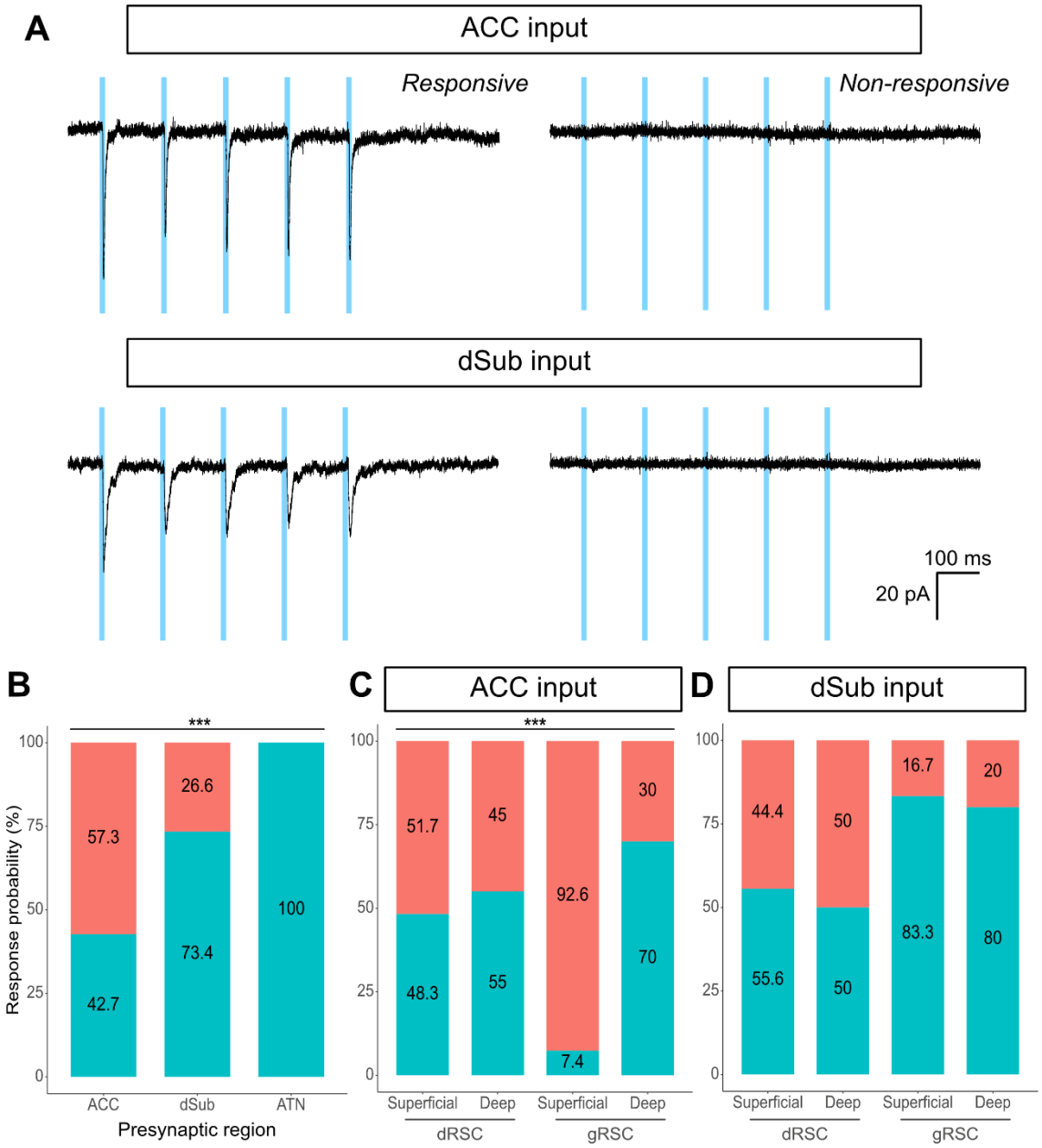

Figure 3.7 | Probability of RSC synaptic response differs between inputs. A Representative voltage-clamp (V_H = -70 mV) traces of responsive and non-responsive PCs: cells recorded in the superficial dRSC following ACC and dSub input stimulation. **B** Probability of PC synaptic response in the RSC significantly differs dependent on presynaptic region ($\chi_2(2) = 43.20$, $p < 0.001$; Pearson's Chi-squared test). Chi-squared *post hoc* tests showed each presynaptic region produced a different response probability in RSC PC (all $p < .001$) with ACC input showing the lowest probability and ATN input the highest. **C-D** Response probabilities for ACC and dSub input analysed by RSC sub-region (dRSC and gRSC) and laminar group (superficial and deep). **C** Probability of PC synaptic response to ACC input

was significantly different dependent on cell location within the RSC ($\chi_2(3) = 21.44$, $p < .001$; Pearson's Chi-squared test). *Post hoc* tests showed that superficial gRSC cells had a significantly lower response probability than those in the deep gRSC ($p < .001$) and both superficial and deep dRSC cells (both $p < .01$). The others groupings did not significantly differ from one another (**dRSC superficial : dRSC deep** $p = .86$; **dRSC superficial : gRSC deep** $p = .37$; **dRSC deep : gRSC deep** $p = .62$;). **D** Cell location did not significantly affect response probability to dSub input ($\chi_2(3) = 5.10$, $p = 0.16$; Pearson's Chi-squared test). *** *p < .001*

Two mice were injected in the ATN with a virus containing only the mCherry-fluorophore in order to confirm that synaptic responses recorded were a result of activity-mediated synaptic transmission following activation of ChR2 receptors presynaptically. The ATN was chosen as the presynaptic region as 100% of PCs in the RSC responded to stimulation of the opsin-expressing afferent terminals (**Figure 3.7 B**). 20 cells were recorded and analysed from the superficial and deep cortical layers of the dRSC and gRSC (**Figure 3.8 A**), and no cells showed any synaptic response to optical stimulation in absence of ChR2 (**dRSC superficial R:** 0/7, **dRSC deep R:** 0/4, **gRSC superficial R:** 0/4, **gRSC deep R:** 0/5) (**Figure 3.8 B**).

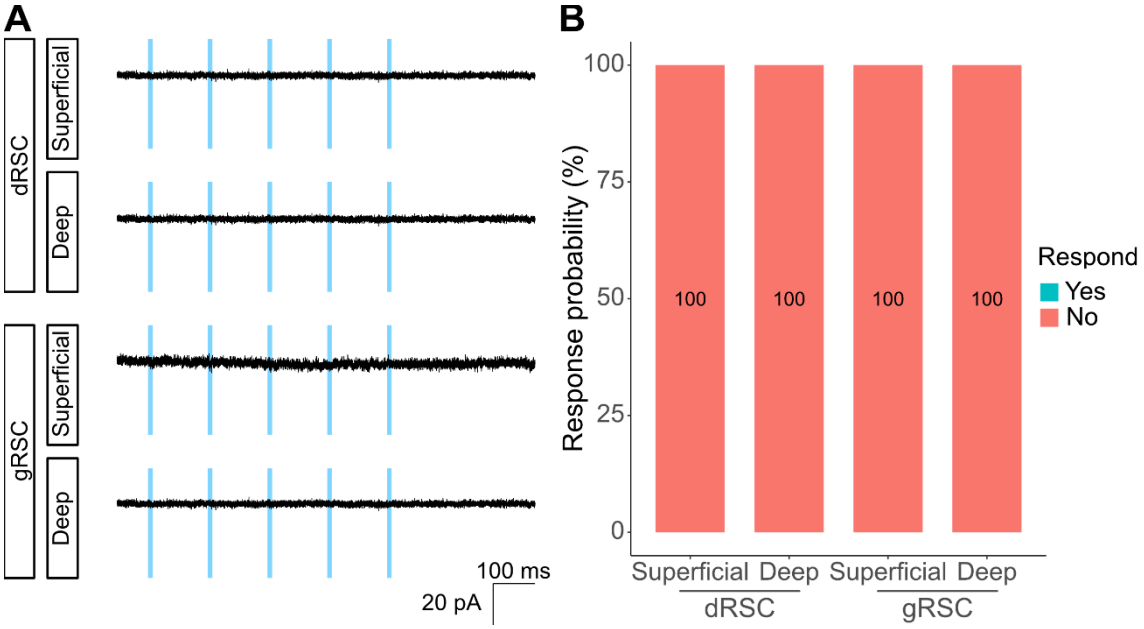

Figure 3.8 | Optical stimulation in absence of presynaptic ChR2 receptors does not generate a synaptic response. A Representative voltage-clamp (V_H = -70 mV) traces of 7 Hz optical stimulation (5 ms

stimulation period indicated by blue boxes). **B** 0% of cells recorded in the RSC responded to optical stimulation of afferent terminals containing the mCherry-fluorophore only.

To understand the general strength – irrespective of cell location – of different afferent inputs into the RSC, measures were first averaged for each presynaptic region combining cells from the all layers of the dRSC and gRSC. ATN input induced larger magnitude EPSCs in the RSC than ACC and dSub input (**Figure 3.9 D**), but the regions did not significantly differ in their NMDA/AMPA ratio (**Figure 3.9 E**) or in the weighted decay time constant (τ_w) of NMDAR responses (**Figure 3.9 F**). PPR increased as IPI time increased for all inputs, but there was no significant difference in average PPR or rate of PPR increase across time between inputs (**Figure 3.9 G**). The average PPR for all inputs remained below 1, indicating paired pulse depression (PPD) was present in all projections. The increasing time intervals relate to distinct neural oscillation frequency bands (negative relationship with IPI and frequency), and PPD was exhibited at all frequencies suggesting consistent short-term synaptic depression in these pathways, which lessens with lower frequency stimulation. Representative traces for EPSC magnitude, NMDA/AMPA ratio and PPR are shown in **Figure 3.9 A-C**.

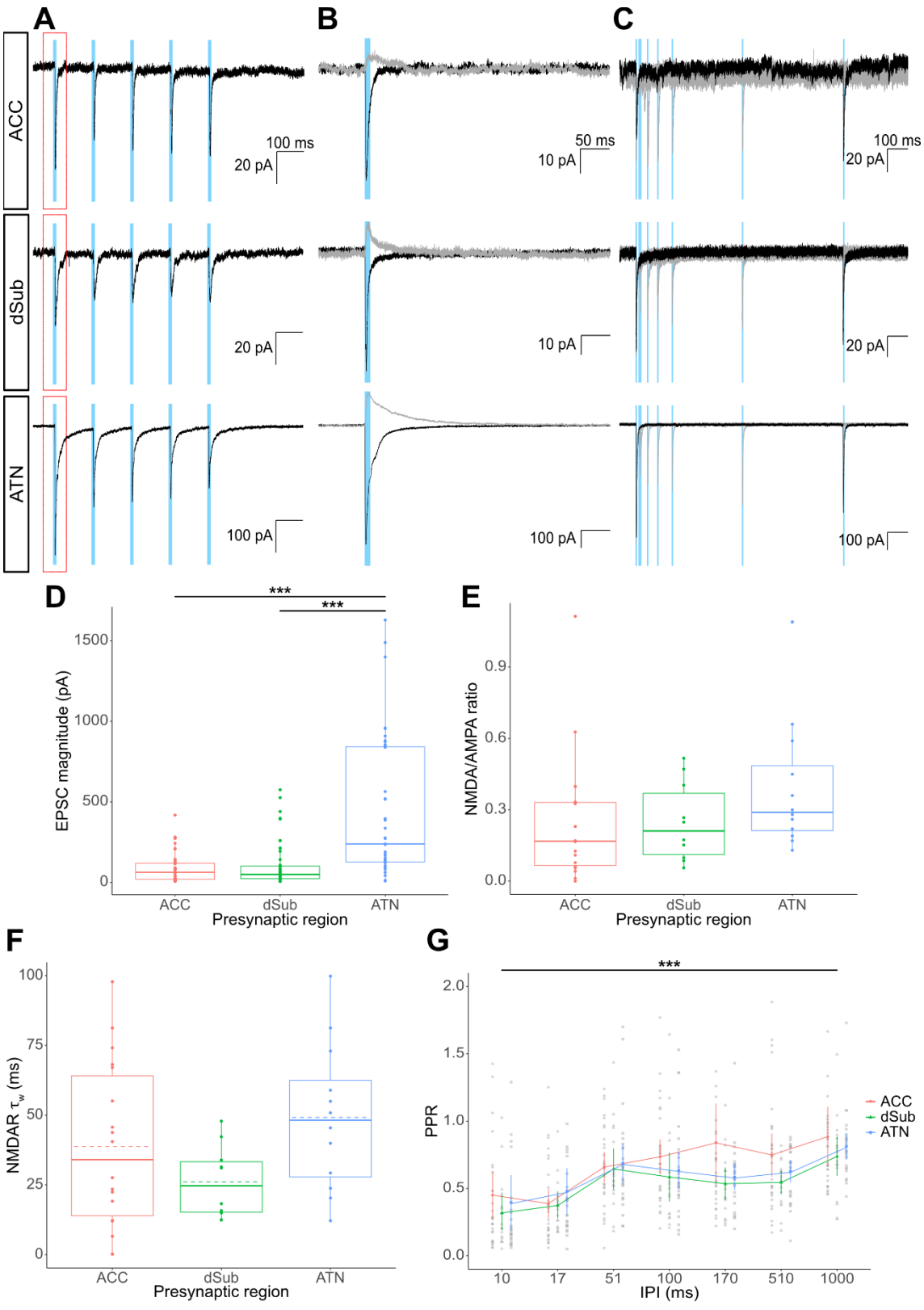

Figure 3.9 | Differences in RSC synaptic response measures between inputs. A Representative voltage-clamp (V_H = -70 mV) traces of EPSCs generated by a 7 Hz stimulation protocol. EPSC magnitude was calculated as the first negative peak during the first stimulation (highlighted in red dashed box). **B** Representative voltage-clamp traces showing AMPAR-

mediated (black) and NMDAR-mediated (grey) EPSCs. AMPAR responses were recorded at V_H = -70 mV (standard aCSF) and NMDAR responses were recorded at V_H = +40 mV (standard aCSF containing (in µM): 10 DNQX, 1 CGP-55845, 10 Gabazine). **C** Representative voltage-clamp (V_H = -70 mV) traces showing EPSCs generated by two stimulations separated by increasing intervals. Each trace displays 7 sweeps with intervals of (grey) 10 ms, 17 ms, 51 ms, 100 ms, 171 ms, 510 ms and (black) 1000 ms. 5 ms optical stimulation periods indicated by blue boxes in all traces and protocols. **D** EPSC magnitude significantly differed between regions of presynaptic innervation ($H(2) = 33.28$, $p < .001$; Kruskal-Wallis test. Mann-Whitney U *post hoc* tests showed that whilst the ACC (61.793 (19.37 – 119.0) pA) and dSub (48.44 (23.13 – 10.98) pA) input EPSCs did not differ in size ($p = .93$), the median EPSC generated from ATN input (443.29 (126.5 – 842.5) pA) was significantly larger than that from both the ACC and dSub. **E** NMDA/AMPA ratio did not differ significantly between presynaptic regions ($H(2) = 4.28$, $p = .12$; Kruskal-Wallis test; **ACC:** 0.17 (0.07 – 0.25), **dSub:** 0.21 (0.11 – 0.37), **ATN:** 0.29 (0.21 – 0.39)). **F** The τ_w of the NMDAR response did not differ significantly between presynaptic regions ($F(2,37) = 2.32$, $p = .12$; 1-way independent ANOVA; **ACC:** 38.76 (29.69) ms, **dSub:** 26.06 (12.96) ms, **ATN:** 50.26 (25.53) ms. **G** There was a significant main effect of IPI on PPR ($F(6,426) = 15.71$, $p < .001$; 2-way mixed ANOVA), with a steady increase in ratio as IPI increased. There was, however, no overall difference between the presynaptic regions ($F(2,71) = 1.57$, $p = .22$) nor an interaction between presynaptic region and IPI ($F(12, 426) = 1.02$, $p = .43$). Descriptive statistics display median and IQR or mean and SD. Boxplots display median (solid line), mean (dashed line), IQR and range. Line graph displays mean ±1 SEM *** $p < .001$

Next, synaptic responses were compared between sub-region and laminar grouping for each presynaptic region. To examine effects of sub-region and layer grouping on synaptic responses, a null model was compared against a mixed effect model including sub-region and layer as fixed effects. For ACC input, the EPSC magnitude ($\chi_2(2) = 3.7$, $p = .16$; $\mathbf{AIC_{null}} = 492.4$, $\mathbf{AIC_{mem}} = 492.7$) and NMDA/AMPA ratio mixed effect models did not significantly improve upon the null model ($\chi_2(2) = 1.2$, $p = .55$; $\mathbf{AIC_{null}} = 9.2$, $\mathbf{AIC_{mem}} = 12$). Additionally, EPSC

magnitude showed a large random effect of mouse, with an additional 15.5% of the variance explained by this random variable, but NMDA/AMPA ratio did not.

The mixed effect model of PPR did not show a significant improvement on the null model ($\chi_2(2) = 0.8$, $p = .69$; $\mathbf{AIC_{null}} = 299.1$, $\mathbf{AIC_{mem}} = 302.3$). However the fitted model indicated that overall IPI had a significant effect on PPR ($F(6, 194) = 4.8$, $p < .001$; ANOVA), and the IPI level effect sizes all show significant increases from PPR at 10 ms except at 17 and 51 ms IPI (**Table 3.3**). There was also a random effect of mouse on PPR, increasing variance explained by the model by 8.3%. Therefore, EPSC magnitude, NMDA/AMPA ratio and PPR did not significantly differ between sub-region and layer grouping for ACC input. Finally, while mouse was a significant random effect for both the EPSC magnitude and PPR models, the intraclass correlation coefficient (ICC) in both models indicate a weak resemblance between different mice (**Table 3.3**). **Figure 3.10** shows a graphical representation of the synaptic response to ACC input.

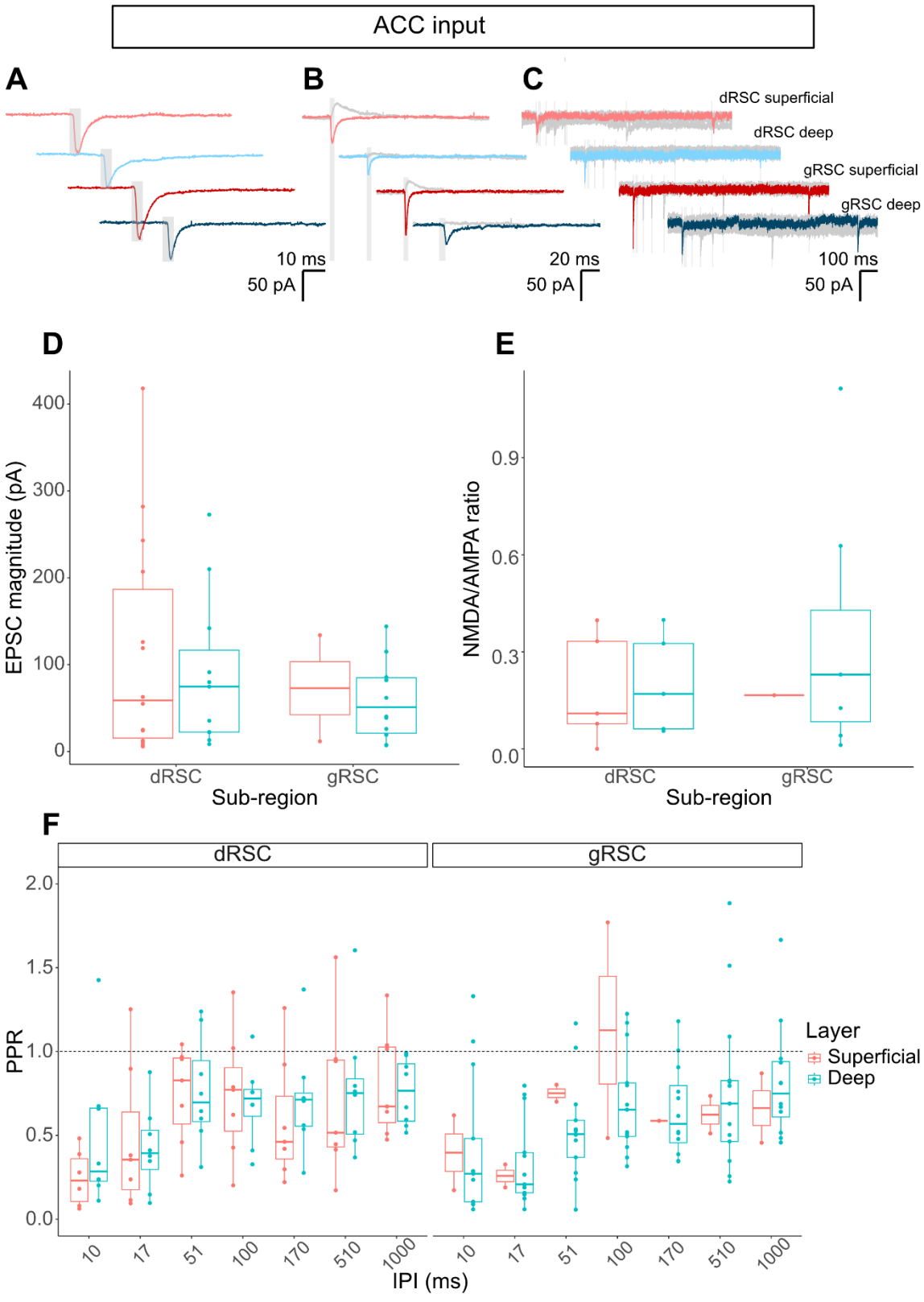

Figure 3.10 | Synaptic response to ACC input separated by cell location. **A** Representative voltage-clamp (V_H = -70 mV) traces showing the first EPSC generated from a 7 Hz stimulation protocol. Grey boxes indicate the 5 ms optical stimulation period (470 nm wavelength). **B** Representative voltage-clamp traces showing AMPAR-mediated (blue/red trace) and NMDAR-

mediated EPSCs (grey trace) generated by optogenetic stimulation (grey box indicates 5 ms optical stimulation period). AMPAR responses were recorded at V_H = -70 mV (standard aCSF) and NMDAR responses were recorded at V_H = +40 mV (standard aCSF containing (in µM): 10 DNQX, 1 CGP-55845, 10 Gabazine). **C** Representative voltage clamp traces (V_H = -70 mV) showing EPSCs generated by two optogenetic stimulations separated by increasing intervals. Each plot displays 7 sweeps with intervals of (grey traces) 10 ms, 17 ms, 51 ms, 100 ms, 170 ms, 510 ms and (red trace) 1000 ms. Optical stimulation periods indicated by pale grey boxes. **D** RSC sub-region or layer grouping did not significantly affect EPSC magnitude. E RSC sub-region or layer did not significantly affect NMDA/AMPA ratio. **F** PPR significantly increased as IPI increased, but there was no significant effect of sub-region or layer on PPR. Boxplots display median, IQR and range. Black dashed line indicates PPR = 1.

	EPSC magnitude			**NMDA/AMPA ratio**			**PPR**		
Predictors	*Estimates*	*t*	*p*	*Estimates*	*t*	*p*	*Estimates*	*t*	*p*
Intercept	112.71 (64.84 – 160.57)	4.78	**<0.001**	0.16 (-0.07 – 0.39)	1.53	0.15	0.44 (0.21 – 0.67)	3.76	**<0.001**
Sub-region: gRSC	-34.05 (-94.42 – 26.31)	-1.14	0.26	0.1 (-0.18 – 0.39)	0.78	0.449	0.06 (-0.08 – 0.20)	0.82	0.412
Layer: Deep	-35.03 (-96.31 – 26.25)	-1.16	0.254	0.06 (-0.24 – 0.36)	0.42	0.679	0 (-0.16 – 0.16)	-0.03	0.976
PPR: 17 ms							-0.06 (-0.30 – 0.18)	-0.52	0.604
PPR: 51 ms							0.21 (-0.03 – 0.45)	1.72	0.087
PPR: 100 ms							0.28 (0.05 – 0.52)	2.34	**0.02**
PPR: 170 ms							0.39 (0.15 – 0.63)	3.2	**0.002**
PPR: 510 ms							0.3 (0.06 – 0.54)	2.46	**0.015**
PPR: 1000 ms							0.43 (0.20 – 0.67)	3.58	**<0.001**
Random Effects									
σ^2	6543.56			0.07			0.22		
τ^2_{mouse}	1358.64			0			0.02		
ICC	0.17						0.09		
N	13			9			8		
Observations	41			18			210		
Marginal R^2 / Conditional R^2	0.096 / 0.251			0.068 / NA			0.114 / 0.197		

Table 3.3 | ACC input mixed model results for EPSC magnitude, NMDA/AMPA ratio and PPR. For fixed effects, table displays effect sizes, confidence intervals, *t* statistic and significance values. For random effects, the table displays residual variance (σ^2), mouse variance (τ^2) and the ICC.

Marginal R^2 refers to variance explained by fixed effects only, while conditional R^2 refers to variance explained by combined fixed and random effects.

For dSub input, the EPSC magnitude mixed effect model significantly improved on the null model ($\chi_2(2) = 6.7$, $p < .05$; $\mathbf{AIC_{null}} = 604.5$, $\mathbf{AIC_{mem}} = 601.7$). ANOVA of the fixed effects showed that while cells in the gRSC differed from dRSC ($F(1,47) = 7.0$, $p < .05$; ANOVA), layer did not affect EPSC magnitude ($F(1,47) = 0.0$, $p = .89$). Overall, the fixed effects explained 13.6% of the variance in data, and there was no random effect of mouse (**Table 3.4**). The NMDA/AMPA ratio mixed model did not improve upon the null model ($\chi_2(2) = 5.9$, $p = .05$; $\mathbf{AIC_{null}} = -2.6$, $\mathbf{AIC_{mem}} = -4.5$), and there was no also no random effect of mouse on the data. However it should be noted that 3 NMDA/AMPA recordings were excluded for not containing an NMDA component, and these were all in the dRSC superficial layer, meaning no data for this group was included in the model. It was not known why these cells did not show an NMDAR-mediated response, but observation of the traces suggested that it may have been a methodological issue. The cells appeared not to return to baseline in time following the preceding voltage step and therefore the NMDAR component could not be measured.

The PPR mixed model also significantly improved on the null model ($\chi_2(2) = 35.2$, $p < .001$; $\mathbf{AIC_{null}} = 35.4$, $\mathbf{AIC_{mem}} = 4.2$). IPI had an overall significant effect on PPR ($F(6, 112.3) = 7.7$, $p < .001$; ANOVA), and the effect estimates (**Table 3.4**) indicate that subsequent IPI levels after the second (17 ms) increased PPR compared to the first (10 ms). Sub-region and layer grouping also significantly affected PPR ($F(1,117) = 30.9$, $p < .001$, and $F(1,111.3) = 14.2$, $p < .001$, respectively; ANOVA). The effect estimates indicate that gRSC cells displayed higher PPR than dRSC cells, and also that cells in the deep layers had higher PPR than in the superficial layers. There was also a random effect of mouse, contributing 13.4% of variance to the total explained by the model, but the ICC score implies a weak resemblance between mice (**Table 3.4**). Overall, cells in the dRSC showed larger EPSC magnitudes and lower PPR than those in the gRSC. Deep layer cells also had a higher PPR than superficial cells. **Figure 3.11** shows a graphical representation of the synaptic response to dSub input data.

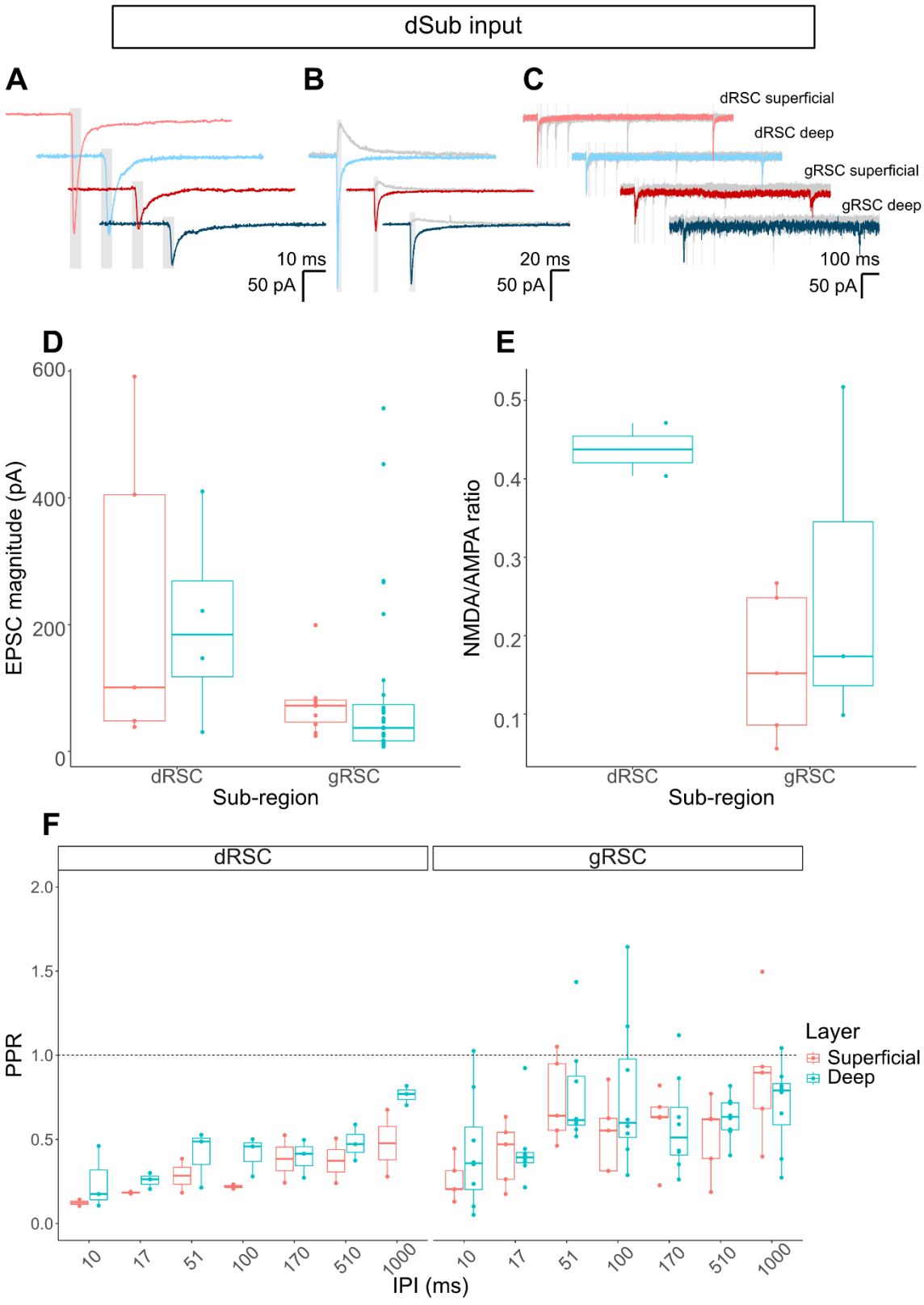

Figure 3.11 | Synaptic response to dSub input separated by cell location. A Representative voltage-clamp (V_H = -70 mV) traces showing the first EPSC generated from a 7 Hz stimulation protocol. Grey boxes indicate the 5 ms optical stimulation period (470 nm wavelength). **B** Representative voltage-clamp traces showing AMPAR-mediated (blue/red

trace) and NMDAR-mediated EPSCs (grey trace) generated by optogenetic stimulation (grey box indicates 5 ms optical stimulation period). AMPAR responses were recorded at V_H = -70 mV (standard aCSF) and NMDAR responses were recorded at V_H = +40 mV (standard aCSF containing (in µM): 10 DNQX, 1 CGP-55845, 10 Gabazine). **C** Representative voltage clamp traces (V_H = -70 mV) showing EPSCs generated by two optogenetic stimulations separated by increasing intervals. Each plot displays 7 sweeps with intervals of (grey traces) 10 ms, 17 ms, 51 ms, 100 ms, 170 ms, 510 ms and (red trace) 1000 ms. Optical stimulation periods indicated by pale grey boxes. **D** EPSC magnitude was significantly higher for cells in the dRSC than in the gRSC, but there was no difference between cells in the deep and superficial layers. **E** No significant effects of sub-region or layer seen on NMDA/AMPA ratio. **F** Overall PPR significantly increased as IPI increased. Both sub-region and layer significantly affected PPR with higher PPR seen in gRSC vs dRSC cells, and deep vs superficial cortical layers. Boxplots display median, IQR and range. Black dashed line indicates PPR = 1.

	EPSC magnitude			**NMDA/AMPA ratio**			**PPR**		
Predictors	*Estimates*	*t*	*p*	*Estimates*	*t*	*p*	*Estimates*	*t*	*p*
Intercept	211.07 (115.03 – 307.11)	4.44	**<0.001**	0.34 (0.03 – 0.64)	2.82	0.037	0.02 (-0.15 – 0.19)	0.23	0.819
Sub-region: gRSC	-132.55 (-233.79 – -31.31)	-2.64	**0.012**	-0.17 (-0.45 – 0.10)	-1.6	0.164	0.27 (0.18 – 0.37)	5.56	**<0.001**
Layer: Deep	5.99 (-79.46 – 91.45)	0.14	0.888	0.1 (-0.12 – 0.32)	1.18	0.29	0.19 (0.09 – 0.30)	3.77	**<0.001**
PPR: 17 ms							0.06 (-0.09 – 0.20)	0.74	0.461
PPR: 51 ms							0.33 (0.18 – 0.47)	4.37	**<0.001**
PPR: 100 ms							0.27 (0.12 – 0.41)	3.58	**0.001**
PPR: 170 ms							0.22 (0.07 – 0.37)	2.91	**0.004**
PPR: 510 ms							0.23 (0.08 – 0.37)	3.04	**0.003**
PPR: 1000 ms							0.42 (0.27 – 0.57)	5.62	**<0.001**
Random Effects									
σ^2	17196.91			0.01			0.05		
τ^2_{mouse}	0			0			0.01		
ICC							0.22		
N	9			7			6		
Observations	47			10			126		
Marginal R^2 / Conditional R^2	0.136 / NA			0.470 / NA			0.401 / 0.535		

Table 3.4 | dSub input mixed model results for EPSC magnitude, NMDA/AMPA ratio and PPR. For fixed effects, the table displays effect sizes, confidence intervals, *t* statistic and significance values. For random

effects, the table displays residual variance (σ^2), mouse variance (τ^2) and the ICC. Marginal R^2 refers to variance explained by fixed effects only, while conditional R^2 refers to variance explained by combined fixed and random effects.

Finally, for ATN input the EPSC magnitude mixed model showed significant improvement from the null model ($\chi_2(2) = 8.2$, $p < .05$; $\mathbf{AIC_{null}} = 590.2$, $\mathbf{AIC_{mem}} = 586.0$). ANOVA of the fixed effects showed that sub-region, but not layer, significantly affected EPSC magnitude ($F(1,33.8) = 7.9$, $p < .01$ and $F(1, 34.1) = 0.8$, $p = 0.39$ respectively). Effect estimates indicate that gRSC cells had a lower EPSC magnitude than dRSC cells (**Table 3.5**). The mixed model for NMDA/AMPA ratio showed no improvement from the null model ($\chi_2(2) = 0.5$, $p < 0.78$; $\mathbf{AIC_{null}} = 7.3$, $\mathbf{AIC_{mem}} = 10.8$). There was a strong random effect of mouse on NMDA/AMPA ratio however, increasing the variance explained by 18.5%. The PPR mixed model also significantly improved on the null model ($\chi_2(2) = 18.1$, $p < .001$; $\mathbf{AIC_{null}} = 141.9$, $\mathbf{AIC_{mem}} = 127.8$). IPI had an overall significant effect on PPR ($F(6, 168.3) = 4.4$, $p < .001$; ANOVA), and the effect estimates (**Table 3.5**) indicate that subsequent IPI levels after the second (17 ms) increased PPR compared to the first (10 ms). Sub-region and layer grouping also significantly affected PPR ($F(1,132.4) = 7.1$, $p < .01$ and $F(1,121.7) = 12.6$, $p < .01$, respectively; ANOVA). The effect estimates indicate that gRSC cells displayed higher PPR than dRSC cells, and also that cells in the deep layers had higher PPR than in the superficial layers. There was also a small random effect of mouse, contributing 1% of variance to the total explained by the model with a very low ICC (**Table 3.5**). Overall, cells in the dRSC had larger EPSC magnitudes and lower PPR than those in the gRSC. Deep layer cells also had a higher PPR than superficial cells. **Figure 3.12** shows a graphical representation of the synaptic response to ATN input data.

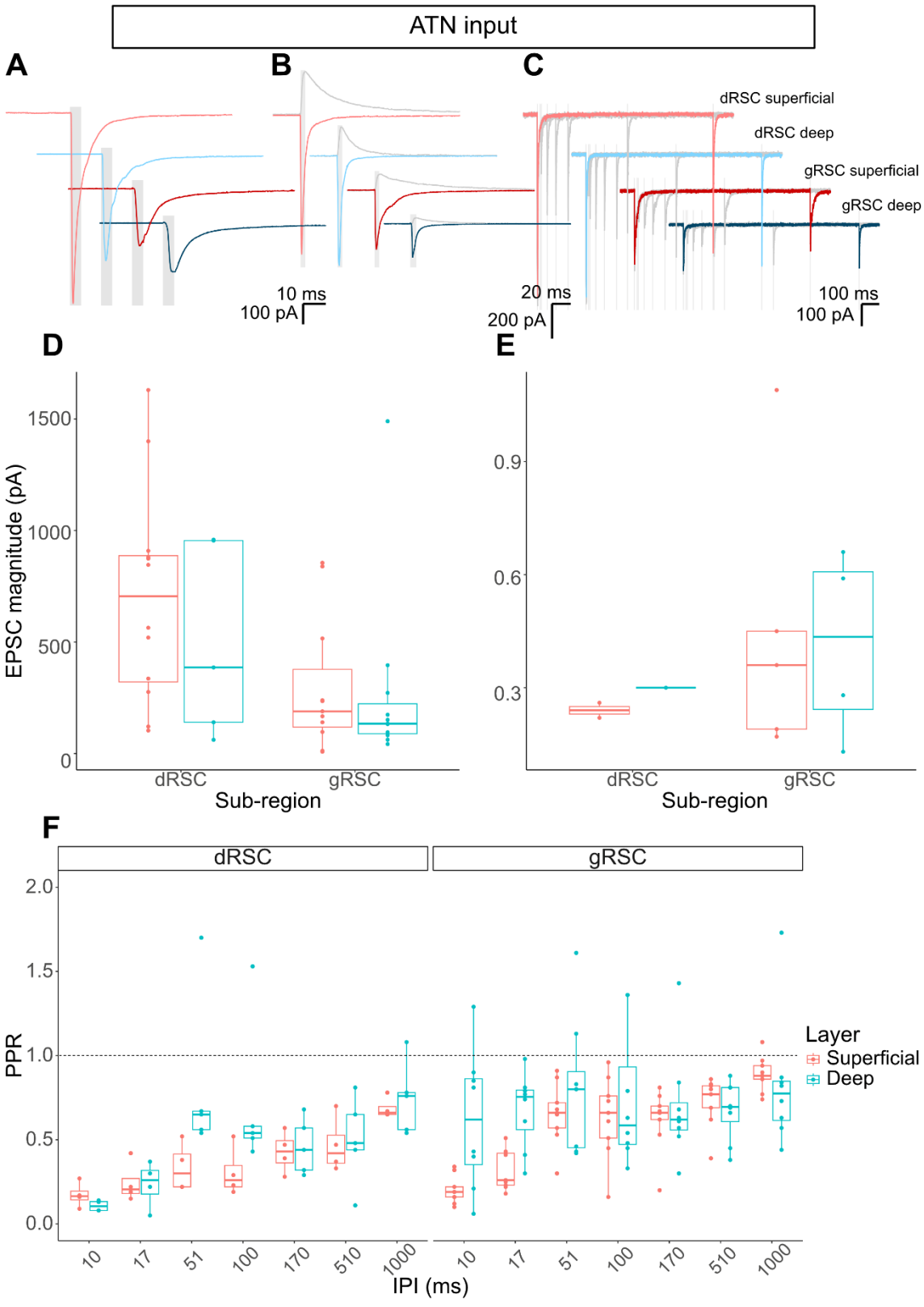

Figure 3.12 | Synaptic response to ATN input separated by cell location. A Representative voltage-clamp (V_H = -70 mV) traces showing the first EPSC generated from a 7 Hz stimulation protocol. Grey boxes indicate the 5 ms optical stimulation period (470 nm wavelength). **B** Representative voltage-clamp traces showing AMPAR-mediated (blue/red

trace) and NMDAR-mediated EPSCs (grey trace) generated by optogenetic stimulation (grey box indicates 5 ms optical stimulation period). AMPAR responses were recorded at V_H = -70 mV (standard aCSF) and NMDAR responses were recorded at V_H = +40 mV (standard aCSF containing (in µM): 10 DNQX, 1 CGP-55845, 10 Gabazine). **C** Representative voltage clamp traces (V_H = -70 mV) showing EPSCs generated by two optogenetic stimulations separated by increasing intervals. Each plot displays 7 sweeps with intervals of (grey traces) 10 ms, 17 ms, 51 ms, 100 ms, 170 ms, 510 ms and (red trace) 1000 ms. Optical stimulation periods indicated by pale grey boxes. **D** EPSC magnitude was significantly higher for cells in the dRSC than in the gRSC, but there was no difference between cells in the deep and superficial layers. **E** No significant effects of sub-region or layer seen on NMDA/AMPA ratio. F Overall PPR significantly increased as IPI increased. Both sub-region and layer significantly affected PPR with higher PPR seen in gRSC vs dRSC cells, and deep vs superficial layers. Boxplots display median, IQR and range. Black dashed line indicates PPR = 1.

	EPSC magnitude			**NMDA/AMPA ratio**			**PPR**		
Predictors	*Estimates*	*t*	*p*	*Estimates*	*t*	*p*	*Estimates*	*t*	*p*
Intercept	684.53 (467.91 – 901.15)	6.42	**<0.001**	0.29 (-0.07 – 0.66)	1.88	0.102	0.21 (0.05 – 0.37)	2.66	**0.009**
Sub-region: gRSC	-351.81 (-606.12 – -97.51)	-2.81	**0.008**	0.13 (-0.28 – 0.53)	0.75	0.476	0.14 (0.04 – 0.25)	2.67	**0.008**
Layer: Deep	-111.06 (-367.43 – 145.30)	-0.88	0.385	0.02 (-0.33 – 0.36)	0.11	0.915	0.18 (0.08 – 0.28)	3.55	**0.001**
PPR: 17 ms							0.08 (-0.10 – 0.26)	0.92	0.361
PPR: 51 ms							0.29 (0.11 – 0.47)	3.18	**0.002**
PPR: 100 ms							0.24 (0.06 – 0.42)	2.61	**0.01**
PPR: 170 ms							0.19 (0.01 – 0.37)	2.08	**0.039**
PPR: 510 ms							0.23 (0.05 – 0.41)	2.54	**0.012**
PPR: 1000 ms							0.42 (0.24 – 0.60)	4.56	**<0.001**
Random Effects									
σ^2	140021.34			0.05			0.11		
τ^2_{mouse}	14039.34			0.01			0		
ICC	0.09			0.19			0.01		
N	9			8			8		
Observations	39			12			182		
Marginal R^2 / Conditional R^2	0.199 / 0.272			0.053 / 0.238			0.200 / 0.210		

Table 3.5 | ATN input mixed model results for EPSC magnitude, NMDA/AMPA ratio and PPR. For fixed effects, the table displays effect

sizes, confidence intervals, *t* statistic and significance values. For random effects, the table displays residual variance (σ^2), mouse variance (τ^2) and the ICC. Marginal R^2 refers to variance explained by fixed effects only, while conditional R^2 refers to variance explained by combined fixed and random effects.

3.4 | Discussion

3.4.1 | Summary

In this chapter I aimed to assess how PCs in the superficial and deep layers of the dRSC and gRSC differed in both their intrinsic electrical membrane properties and in their synaptic responses to afferent inputs from different presynaptic regions. The results showed that PC diversity, and the distribution of different sub-groups of PCs, differed between the sub-regions and layers of RSC. Crucially, these PCs also differed in their synaptic response to three afferent projections. ATN inputs had the strongest connectivity overall; and while the structural connectivity indicated preferential targeting of the gRSC, cells in the dRSC showed the largest synaptic response. Projections from the dSub also displayed a similar discrepancy between structural and functional connectivity, but size of synaptic response to optogenetic activation of ACC axons was similar throughout the RSC. Finally, no evidence was found of pathway-specific differences in NMDA/AMPA ratios, NMDAR decay kinetics or overall PPR, although PPR did differ between sub-region and layer for dSub and ATN input. Therefore, the short-term plasticity of these projections differs dependent on the responding postsynaptic cell.

3.4.2 | PC diversity in the RSC

Cortical PCs are a diverse neuronal population that have generally been divided into two sub-categories characterised by their firing properties: regular spiking (RS) and intrinsic bursting (IB) cells (Connors and Gutnick, 1990). While most experiments examining PC diversity have used rodent models, RS and IB cells are found in similar proportions in the primate and human cortex (Chang and Luebke, 2007; Moradi Chameh et al., 2021; Zaitsev et al., 2012). Findings

presented in this chapter confirm a similar diversity of pyramidal neurons in the retrosplenial cortex: a non-biased hierarchical clustering shows three clusters (C1-C3) with distinct intrinsic passive and active membrane properties. C1 and C3 cells exhibited characteristics similar to RS cells, whilst C2 cells presented with a greater propensity for burst firing. However, other properties identified as significantly different in the C2 cluster are not necessarily associated with IB cells, such as a shorter AP halfwidth, faster 20-80% rise time and increased rheobase (Huggenberger et al., 2009). The relative lack of a hyperpolarisation-activated cation current (sag) shown by C2 cells is similar to that found in PCs in the superficial layers of other cortices (Gottlieb and Keller, 1997), which could explain the high percentage of C2 cells found in the superficial layers of the RSC.

While the clustering of intrinsic properties shows some similarities to previously described PC sub-types, sufficient dissimilarities occur which prevent confident assignment to these sub-types. Furthermore, the three clusters described in the model only explained 30% of the variance. While the current data set could not be partitioned into more clusters without sacrificing cluster distinction, increasing the number of cells in the model could reduce variability and allow for further sub-categories of PCs to emerge within the broader classifications. Additionally, although PC sub-types are often described by their firing properties, other factors such as genetic markers could be used to reliably separate sub-types and to explore the mechanisms underlying their differences (Tasic et al., 2016; Zeisel et al., 2015).

As PC sub-populations have already been described in many other cortical regions and in hippocampal structures, what is the importance of describing these cells in the RSC? Whilst PC properties have been described as homogenous across some different cortical regions in mice (Gilman et al., 2017), it is still important to confirm PC diversity and associated intrinsic properties in different cortical regions of interest due to the role these properties play in connectivity and cognition. For example, PC diversity in the CA1 enables processing of parallel information streams and is theorised to facilitate the regions ability to process and store multiple forms of memory (Soltesz and Losonczy, 2018). In the cortex, PC diversity is often considered in respect to its location in a cortical column, and there is a large amount of research showing afferent and efferent connectivity of these PCs differs significantly (Lübke and Feldmeyer, 2007).

However, PC diversity is not solely associated with its location and many measures of PC diversity are not unique to specific cortical layers (Groh et al., 2010). Within the RSC itself, a small number of studies have characterised properties of PCs in the gRSC (Brennan et al., 2020b; Kurotani et al., 2013), and found that PCs with distinct intrinsic properties exist within the same layer. As briefly discussed in **Section 3.3.1**, the intrinsic properties of a neuron are fundamentally linked to their function. The structural and electrophysiological properties of neurons can determine their activity patterns (Kowalski et al., 2016), and factors such as bursting, adaptation and sag can alter processes such as temporal integration and information encoding (Brennan et al., 2020; Van Welie et al., 2006). These differences in intrinsic membrane properties can consequently impact learning and memory by influencing aspects such as neural coding and oscillatory activity (Marder et al., 1996).

The work presented in this thesis extends upon our knowledge of PC heterogeneity in the RSC by recording from cells in both the gRSC and dRSC. Interestingly, while latency to first AP was an important property for classifying PCs in the rat gRSC superficial layers (Kurotani et al., 2013; Yousuf et al., 2020), this variable was not significant in our model, similar to Brennan et al., 2020b. However, during the analysis no cluster of PCs exhibiting low rheobase (Brennan et al., 2020) emerged either. This may be due to the method of analysis – a hierarchical clustering with no grouping pre-identified – requiring a larger sample size to reliably separate these cells.

3.4.3 | Structural connectivity differences between presynaptic region inputs

The rodent RSC neuroanatomical connectivity has been well mapped and some sub-region specific and laminar differences have been described (Brennan et al., 2021; Groen and Wyss, 2003, 1992, 1990; Sugar et al., 2011; Yamawaki et al., 2019c), however the tracing experiments in this chapter quantified and described pathway-specific laminar distribution of afferent terminals in both the gRSC and dRSC. Additionally, little work has been done to link anatomical and functional connectivity. Furthermore, until now, there has been no detailed study of afferent inputs to the dRSC at the synaptic level.

ACC input preferentially targeted the dRSC over the gRSC, and fibres were most abundant in layer 6 for both sub-regions. Conversely, dSub and ATN input both preferentially targeted the gRSC and showed differences in laminar distribution between the sub-regions. dSub afferent terminals were denser in layer 6 in the dRSC, but in the gRSC this projection targeted layer 3. A similar pattern was found for the ATN afferent terminals; dRSC and gRSC layer 6 had the highest proportion of terminals but there was also an increase in targeting for layer 3 in the gRSC. The lamination is similar to that described in the rat brain (Groen and Wyss, 2003, 1992, 1990), with some differences such as the layer 6 targeting by dSub and ATN. Additionally, no subicular input was found in the rat dRSC, whereas some fibres were observed in this study in the mouse. The experiments in this chapter allowed for quantitative, instead of subjective, comparison between sub-regions and layers.

The sub-region targeting preferences for each input remained consistent in the anterior and posterior RSC, however differences in overall fluorescent intensity along the A-P axis were not measured as sections could not be normalised against each other. However, it is likely that certain pathways may preferentially target the anterior or posterior sections of the RSC as afferent and efferent connections with hippocampal structures have been shown to be different depending on the A-P position within the RSC, but also along the A-P and D-V axes in areas such as the subiculum and CA1 (Wyss and Van Groen, 1992). Thalamocortical projections to the RSC from the ATN also preferentially target the anterior and posterior RSC depending on location of the originating neurons along the A-P and D-V axes (Sripanidkulchai and Wyss, 1986). Furthermore, different information is relayed from the ACC, dSub and ATN to the RSC: for example, HD signals are transmitted from the ATN (Jankowski et al., 2013) while the dSub conveys information about speed, place and trajectory (Kitanishi et al., 2021). In comparison, projections from the ACC to other cortical regions, such as the visual cortex, are responsible for top-down attentional control (Norman et al., 2021). There is evidence that the anterior and posterior areas of the RSC are responsible for different aspects of spatial behaviour: the anterior RSC is suggested to be important for internally-directed navigation, while the posterior RSC is responsible for visually-guided navigation (see Vann et al., 2009 for review). Moreover, the electrophysiological literature suggests that only neurons

in the anterior RSC respond to location, direction and movement stimuli (Vann et al., 2009). Therefore, it is probable that projection pathways conveying dissimilar forms of information will target the A-P axis differently.

3.4.4 | Functional connectivity differences between presynaptic region inputs

The functional connectivity of the afferent inputs from the ACC, dSub and ATN differed in a variety of measures. Firstly, inputs from each presynaptic region had a differing probability of forming an excitatory synaptic connection with PCs in the RSC. Stimulation of afferent terminals from the ATN resulted in EPSCs in every PC recorded, but inputs from the dSub and ACC were more sparsely distributed in the RSC. Around three quarters of cells responded to dSub terminal stimulation, and the proportion was even lower for ACC input, which formed connection with fewer than half of the cells recorded. This specificity of synaptic connection onto RSC PCs was modulated by layer and sub-region for ACC input, with the majority of non-responders being found in the gRSC superficial layer, but not for dSub input. The frequency of connectivity in these results appears unusual; for example, corticocortical contralateral connectivity typically does not exceed 40%, and decreases further with increased physical distance (Goulas et al., 2017). However, a study examining optogenetic stimulation of a thalamocortical projection to V1 layer 4 observed that all PCs responded (Kloc and Maffei, 2014), suggesting the results in this chapter are not anomalous.

This specificity of synaptic connectivity, however, relates only to excitatory synaptic events as only EPSCs were recorded. While excitatory transmission is often the focus of long-range connectivity research, long-range inhibitory neurons have also been identified in cortical and hippocampal regions (Christenson Wick et al., 2019; Tamamaki and Tomioka, 2010). These long-range GABAergic projections are important for regulation of behaviour, and top-down cortical inhibition of the HPC enhances spatial encoding in the CA1 and promotes object exploration (Malik et al., 2022). Additionally, long-range inhibitory input into the RSC has been described (Yamawaki et al., 2019c), originating from the CA1 region of the HPC; therefore the non-responding cells recorded may in fact have received inhibitory input that was not detected. However, as GABA receptor

antagonists were not present in the standard recording aCSF this seems possibly unlikely. Furthermore, the cortical inhibition of the CA1 described by Malik et al. (2022) exclusively targeted INs – augmenting feed-forward inhibition – while only PCs were recorded in these results. Finally, the possibility of postsynaptically silent synapses (Voronin and Cherubini, 2004) can be ruled out, as no EPSC component was seen for any of the non-responding PCs when the cell was held above the voltage threshold for NMDAR magnesium block removal.

The strength of the synaptic connectivity also differed between inputs: inputs from the ATN generated a median EPSC magnitude around 8-fold larger than those from the dSub and ACC. Therefore, the ATN pathway exerts a larger AMPAR-mediated excitatory effect on PCs in the RSC, but it is unknown whether this is due to more synaptic connections and/or an increase in postsynaptic AMPARs. A strong feed-forward drive of HD information from the ATN to RSC is important for HD updating (van der Goes et al., 2022), and a projection pathway with a strong input would allow for transmission of this information with high fidelity.

The NMDA receptor is considered a crucial component of excitatory transmission and long-term plasticity in the brain (Citri and Malenka, 2008) and its activation allows for Ca^{2+} influx into the neuron facilitating slower excitatory currents as well as regulating the synapse through various signalling pathways (Fan et al., 2014). Therefore measuring AMPAR-mediated EPSCs alone does not give a full picture of the functional connectivity and synaptic strength of afferent inputs into the RSC. Firstly, there was no significant difference between presynaptic region input in NMDAR decay kinetics suggesting no observable difference in the ratio of GluN2 subunits. Next, the results showed no difference in the ratio of NMDAR- to AMPAR-mediated responses between inputs, suggesting there is no significant difference in the proportion of NMDAR to AMPAR at the synapses for the different pathways. Studies examining pathways known to be highly plastic, such as CA3-CA1, normally observe NMDA/AMPA ratios between 0.6 and 1 (Schnell and Nicoll, 2001; Shipton et al., 2022). However, a much lower NMDA/AMPA receptor ratio was observed in all RSC afferent pathways examined, which corroborates previous findings that LTP cannot be induced in the RSC following tetanic stimulation (Garden et al., 2009). Moreover, AMPAR- and NMDAR-mediated glutamatergic transmission is not the only mechanism of long-term plasticity, and there is substantial evidence of the role of other

neuromodulators in gating plasticity (Bazzari and Parri, 2019). Thus, whilst NMDA/AMPA ratios may not be different between these pathways, other neuromodulatory systems – such as metabotropic GluRs or cholinergic transmission – may display differences associated with altered plasticity.

Similarly, PPR was analysed as a measure of short-term plasticity; again, inputs from the different presynaptic regions did not differ significantly. On average, all inputs displayed PPD – signified by ratios of < 1 – and showed similar rates of recovery for EPSC magnitude following increased time between stimulations. PPD can be mediated by a variety of mechanisms, but the most basic models suggest potential presynaptic vesicle depletion and postsynaptic receptor desensitisation (Zucker and Regehr, 2002). This could suggest that all RSC input pathways tested in this study showed similar levels of glutamate release and rate of repletion (Brenowitz and Trussell, 2001; Turecek and Trussell, 2000) and/or similar AMPAR desensitisation (Chen et al., 2002). This finding was unexpected as previous interrogation of these pathways in the gRSC showed that only the ATN pathway was depressing and that the ACC and dSub pathways were weakly facilitating (Brennan et al., 2021). However, in this study, PPR was recorded from only a particular subtype of PCs (the LR PCs) and short-term dynamics are known to be cell subtype-specific (Markram et al., 1998; Reyes et al., 1998). Further inspection of the data revealed variability in response with the range of PPR extending > 1, indicating that some cells showed paired pulse facilitation. Short-term plasticity is dynamic *in vivo* and can alter, and is altered by, network activity (Benita et al., 2012). Additionally, synaptic depression can increase rate of information transfer dependent on whether spike-evoked release depresses less than spontaneous release (Salmasi et al., 2019). Future interrogation of these pathways *in vivo* would shed light on the function of the PPD observed.

Differences in synaptic responses were also observed between RSC sub-regions and layers for some of the afferent input pathways. No effect of sub-region or layer was found for ACC input synaptic responses: PCs in the superficial and deep layers of the dRSC and gRSC all responded to ACC presynaptic excitation in a similar manner. However, synaptic strength did differ by sub-region for dSub and ATN inputs: for both pathways, cells in the dRSC displayed stimulus-evoked EPSCs of a greater magnitude than those in the gRSC. Although synaptic strength did not differ for either input between cells in the superficial and deep

cortical layers. Finally, while all pathways showed PPD throughout the RSC, cells in the gRSC had a higher PPR and therefore weaker PPD than cells in the dRSC for both the ATN and dSub pathways. This is likely related to the finding that cells in the gRSC had a smaller synaptic response suggesting presynaptic terminals in the dRSC may have a higher glutamate release probability. Furthermore, deep layer cells also showed a weaker PPD than cells in the superficial layers, but superficial and deep cells did not differ in the strength of their synaptic connections so the mechanism is unknown. It is theorised that extent of synaptic depression is important for determining the neural code between PCs in the cortex (Tsodyks and Markram, 1997), therefore the differences in PPD observed between RSC sub-regions and layers suggests different contributions of firing rates and temporal coherence.

3.4.5 | Conclusions

The primary aim of this chapter was to compare the strength and specificity of afferent inputs onto PCs in the RSC from three major projection areas. Differences in PC diversity, structural and functional connectivity were identified between the two RSC sub-regions and their layers. The results indicate that PCs in the dRSC receive significant input from the ACC, dSub and ATN and therefore future research need to consider the role of this sub-region. The functional implications of the differences between the projections and the strength and specificity of their synaptic connections is unknown and should be explored. Additionally, the effect of these pathways on INs in the RSC was not investigated here and could provide crucial information regarding the function of the projections.

4 | RSC amyloidopathy in J20 mice does not disrupt synaptic responses to the ATN afferent pathway

4.1 | Introduction

One of the pathological hallmarks of AD is the presence of insoluble Aβ plaques in the brain, which are formed from oligomeric Aβ. Biomarkers of Aβ pathology are observed before cognitive symptoms (Jack et al., 2010), and this neuropathology may be a crucial predictor of neurodegeneration in AD. While Aβ pathology does occur in the early stages of AD, not at all brain areas are affected at similar time points. Aβ plaque deposition follows a distinct and consistent spatio-temporal pattern (Braak and Braak, 1991a; Thal et al., 2002), and the RSC expresses neuropathological markers of AD – including plaques – in preclinical and prodromal stages of the disease. In patients, prodromal AD is associated with RSC hypometabolism, atrophy, synapse loss and Aβ accumulation (Palmqvist et al., 2017; Pengas et al., 2010; Scheff et al., 2015; Villain et al., 2008). While in mouse models of amyloidopathy, the RSC exhibits significant Aβ deposition which is concurrent with neuroinflammatory responses as well as cognitive impairment (Kim et al., 2020). The RSC also displays decreased neuronal activity in response to a novel environment at a preclinical stage preceding plaque deposition in Tg2576 mice (Poirier et al., 2011).

The experiments in this chapter use the J20 mouse model of amyloidopathy to investigate RSC disruption in AD. While RSC Aβ deposition has been described in the J20 mouse from 13 months (Whitesell et al., 2019), analysis at younger pre-clinical and prodromal time points is required. In order to contextualise RSC Aβ pathology, plaque deposition was also analysed in the CA1 region of the HPC and the entorhinal cortex (EC). These two brain regions are known to present elevated levels of soluble Aβ at 3 months and Aβ aggregates from 6 months in J20 mice (Harris et al., 2010; Ying et al., 2022). The J20 transgenic mouse was chosen for these experiments, as this model displays more severe amyloidopathy in the RSC than other APP overexpression models (Whitesell et al., 2019). Moreover, significant synaptic deficits have already been described in 3-month-old J20 mice in other brain areas presenting amyloidosis including the HPC (Harris et al., 2010); therefore it is hypothesised that if ATN input postsynaptic cells in the RSC are vulnerable to Aβ then this model will provide sufficient amyloidosis for deficits to be observed.

To determine whether amyloidopathy leads to chronic changes in RSC excitability, baseline neuronal activity was assessed by quantifying basal Fos expression in the region. Previous literature has found aberrant epileptiform activity in J20 mice in the HPC and cortical networks (Palop et al., 2007) as well as increased intrinsic excitability in PCs in the PFC (Zhang et al., 2021). However, quantification of Fos-positive cells – a marker of neuronal activity (Chung, 2015) – found decreased Fos expression in the dentate gyrus region of the HPC (Gulbranson et al., 2021; Palop et al., 2003) that could be a result of abnormal activity in inhibitory circuits. Fos expression has not been examined in the cortex of this model, however an alternate mouse model of amyloidopathy (Tg2576) found fewer Fos expressing cells in the RSC following exposure to a novel environment at 5 months, which could be observed before the onset of plaque deposition at 17 months (Poirier et al., 2011). Additionally, decreased levels of basal and novelty-induced *Fos* mRNA are found in cortical regions such as the PFC in 9-month-old APP/PS1ΔE9 mice (Christensen et al., 2013). Therefore, it is expected that basal Fos expression will be decreased in J20 transgenic mice during early stages of amyloidopathy.

Potential decreases in Fos expression in the RSC could be a product of the region's high interconnectivity with other areas of the brain. The RSC is particularly sensitive to deafferentation in distally connected brain regions including the ATN (Albasser et al., 2007; Jenkins et al., 2004; Poirier et al., 2008), and has been proposed as a site of covert pathology in AD due to neural circuit disruption (Jenkins et al., 2004; Vann et al., 2009). Synaptic dysfunction is thought to underlie the cognitive deficits seen in AD, and soluble Aβ oligomers are believed to be responsible for synaptic degradation (Mucke et al., 2000). Elevated levels of Aβ depress excitatory neurotransmission via both pre-synaptic and post-synaptic mechanisms (He et al., 2019; Hsia et al., 1999). As Fos expression is a result of glutamatergic receptor activation (Lerea and McNamara, 1993; Sonnenberg et al., 1989), neuropathological disruption to RSC inputs should result in decreased Fos expression.

To further explore the effect of amyloidopathy on RSC connectivity, post-synaptic responses of RSC PCs to optogenetic activation of ATN inputs were investigated in J20 mice. Disruption of this pathway could have substantial effects on RSC function due to the large excitatory influence the ATN shows on RSC PCs

(**Section 3.3.3**). While AD is associated with a decline in a range of cognitive functions, deficits in spatial navigation are proposed to be a reliable marker of prodromal stages of the disease (Coughlan 2018). Spatial navigation can be based on egocentric and allocentric cues, and the RSC is considered a "gateway" node that can transform and integrate these cues as part of a gain-field circuit (Bicanski and Burgess, 2018; Byrne et al., 2007). Head direction (HD) cells are an important aspect of spatial navigation and help form spatial representations or 'cognitive maps' in the brain along with other spatially-tuned cells such as place and grid cells (Moser and Moser, 2008). The ATN contain an abundance of HD cells (Taube, 1995), and the normal function of these cells is crucial in navigation (Gibson et al., 2013), while around 10% of neurons in the RSC can also be classified as HD cells (Cho and Sharp, 2001). A hierarchical model of HD signal propagation proposes that these signals are generated sub-cortically in the lateral mammillary bodies, and spread from the thalamus to the cortex (Jankowski et al., 2013; Taube, 2007). Therefore the ATN to RSC pathway may be crucial for HD cells in the RSC. Additionally, the activity of non-directional cells in the ATN has also been suggested as a mechanism by which RSC HD cells are primed (Albo et al., 2003). Interestingly, lesioning of the RSC also impairs HD cell representation in the ATN (Clark et al., 2010), thus HD signals appear to propagate in a reciprocal fashion. However, experiments investigating HD updating suggest that the relationship between the ATN and RSC is primarily a strong thalamocortical feedforward drive (van der Goes et al., 2022). Furthermore, similar to the RSC, the ATN contains spatially-tuned cells beyond HD cells – such as those resembling grid, place and border cells (Aggleton and O'Mara, 2022) – and may be a propagate other spatial information to the RSC. Finally, the ATN are likely not solely responsible for RSC HD cells and other spatially-tuned cells, but are the source of one major input stream that is processed in parallel with other pathways; allowing for HD information of increased complexity to be encoded in the RSC (Brennan et al., 2021).

There is preliminary evidence of HD cell instability in TgF344-AD mice; another amyloidopathy model of AD which also display impaired spatial navigation (Berkowitz et al., 2020, 2018). Similar spatial navigation and learning deficits have been in observed in the J20 mouse from around 3-4 months (Cheng et al., 2007; Higa et al., 2016; Jankowski et al., 2013), and HD cell disruption could be

a potential factor in these behavioural impairments. Therefore, I aimed to investigate whether synaptic responses in the ATN to RSC pathway are disrupted at ages roughly analogous to transitional, prodromal and clinical stages of amyloidopathy in J20 transgenic mice to potentially elucidate one of the mechanisms underlying these deficits. Furthermore, the ATN to RSC pathway is also crucial in conditioned fear retrieval (Yamawaki et al., 2019b), and fear conditioning impairments have been found in J20 mice (Saura et al., 2005); further supporting the argument for possible disruption to this neural pathway in AD.

The primary aim of the experiments reported in this chapter was to investigate neuropathological changes in the RSC of J20 mice during early and late phases of Aβ accumulation. Aβ plaque deposition and Fos expression were analysed at 3, 6 and 9 months. Post-synaptic responses to optogenetic stimulation of afferent terminals from the ATN were analysed to investigate whether amyloidopathy in the RSC disrupts this important circuit.

4.2 | Animals and methods

Immunohistochemical analyses

In total, 49 wild-type (WT) and heterozygous transgenic (Tg) mice were used from an in-house J20 breeding colony at three different age points: 3 months (3m), 6 months (6m) and 9 months (9m). 24 WT and 25 Tg mice were transcardially perfused under deep anaesthesia immediately following removal from the home-cage (**Section 2.5.1**). Mice were genotyped prior to perfusion as part of general animal husbandry practices, and genotype was confirmed from tissue removed from the tail after anaesthesia was applied. 30 µm coronal sections were collected and stained for Fos (**Section 2.5.2**) and Aβ plaques (**Section 2.5.3**), and tissue and staining quality was assessed from Fos-stained sections. Mice were excluded from analysis of Fos and Aβ deposition if sections were highly damaged or if the Fos staining failed (assessed from an absence of staining in the olfactory bulb, piriform cortex, somatosensory cortex and visual cortex). 9 mice were excluded due to low tissue quality, leaving 18 WT (**3m:** n_{male} = 4, n_{female} = 5; **6m:** n_{male} = 1, n_{female} = 3; **9m:** n_{male} = 4, n_{female} = 1) and 22 Tg mice (**3m:** n_{male} = 2, n_{female} = 5; **6m:** n_{male} = 4, n_{female} = 3; **9m:** n_{male} = 5, n_{female} = 3).

Optogenetic interrogation of the ATN to RSC pathway

In total, 107 mice (WT and Tg) from the J20 in-house colony were used and were aged at 3m, 6m or 9m at time of recording. Mice were injected with $AAV_{5/2}$-hSyn1-ChR2(H134R)-mCherry (see **Table 2.4**) in the ATN, and *ex vivo* RSC slices were prepared a minimum of 4 weeks following surgery. 24 mice were excluded from recording and analysis for missing or misplaced injection sites, and 15 mice were excluded because of poor slice quality. Voltage clamp electrophysiological recordings were undertaken in slices from 68 mice: 39 WT (**3m:** n_{male} = 8, n_{female} = 3; **6m:** n_{male} = 7, n_{female} = 9; **9m:** n_{male} = 5, n_{female} = 7) and 29 Tg (**3m:** n_{male} = 4, n_{female} = 4; **6m:** n_{male} = 5, n_{female} = 6; **9m:** n_{male} = 5, n_{female} = 5). Overall, 438 PCs were recorded and 133 cells were excluded for not meeting viability criteria (**Section 2.4.3.2**), **Table 4.1** displays cell count by sub-region, layer, age and genotype. Mice were genotyped prior to surgery as part of general animal husbandry practices, and genotype was confirmed from tail cuttings collected during slice preparation.

4.3 | Results

4.3.1 | Aβ plaque deposition increases with age in Tg J20 mice

Coronal sections containing the RSC were stained with AmyloGlo, a marker of Aβ aggregates, to measure the deposition of Aβ plaques in this brain region in J20 miceat three different age points: 3m, 6m and 9m. No plaques were seen in the WT J20 mice at any age point, indicating no observable Aβ pathology develops in animals without the humanised APP gene (**Figure 4.1 A top**). Plaques were seen in the Tg animals at 6m and 9m, but not at 3m, suggesting amyloid oligomers had not aggregated by 3m (**Figure 4.1 A bottom**). In the Tg animals, RSC area covered by plaques (**Figure 4.1 C**) significantly increased with age. Furthermore, the average size – or surface area – of the individual plaques (**Figure 4.1 B**) increased with age (**Figure 4.1 D**). While plaques were present in some 6m animals, not all animals showed Aβ plaques in the RSC ($n_{plaque+}$ = 3, $n_{plaque-}$ = 4) suggesting significant variability in Aβ deposition at the level of the individual animal. At the 9m age point all animals displayed plaques in RSC, and both percentage area and plaque size measures of amyloid deposition were large enough to be significantly differentiated from earlier age points. Both the

percentage area covered by plaques and the average plaque size were similar between the dRSC and gRSC, therefore the two RSC sub-regions do not differ in their development and presentation of this amyloidopathy marker.

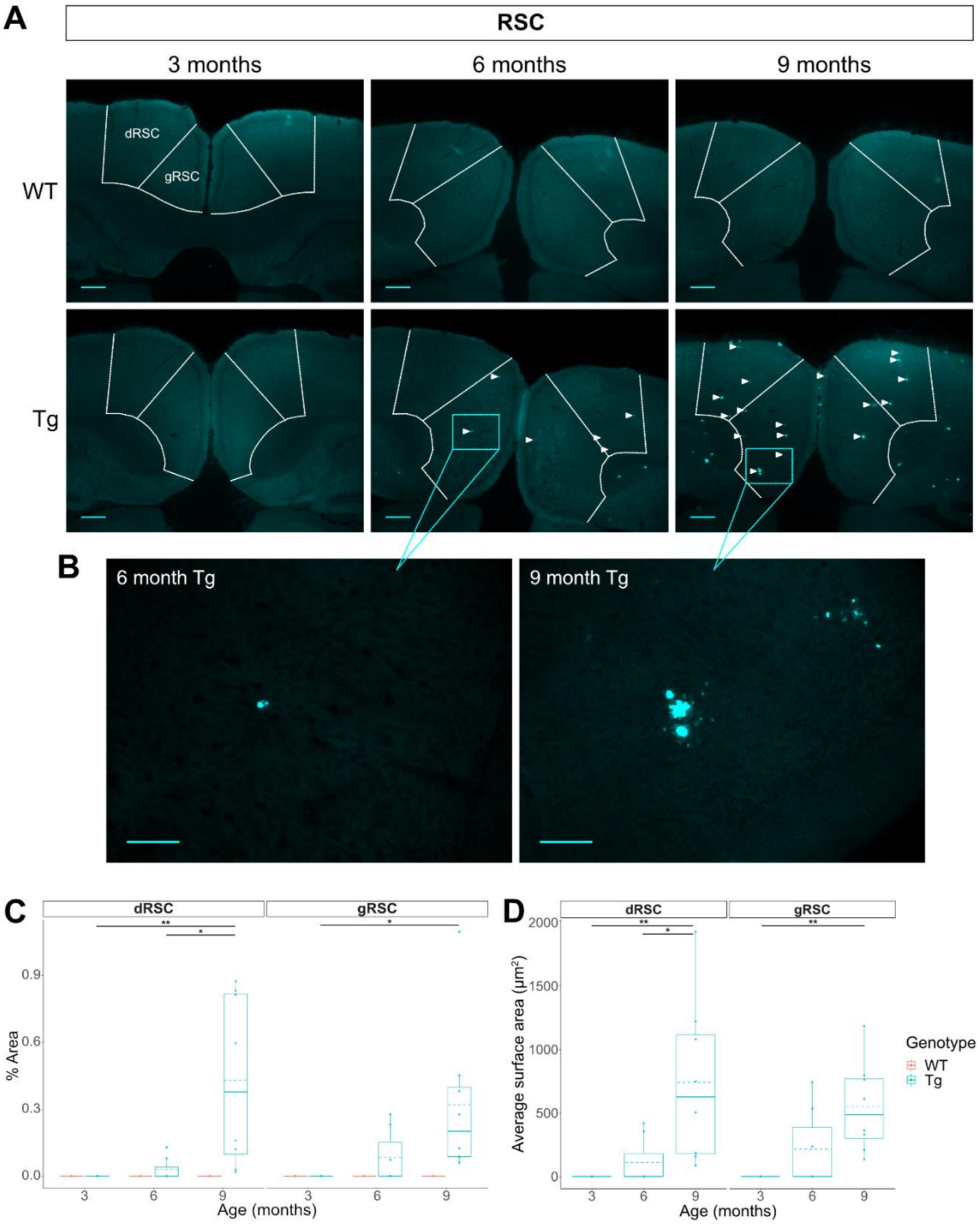

Figure 4.1 | Aβ plaque deposition in the RSC increases with age in J20 Tg mice. A Representative images (4x magnification) of Aβ plaque deposition in the RSC in WT and Tg J20 mice at 3m, 6m and 9m. Arrows indicate plaques at 6m and 9m in Tg mice. Scale bars: 250 µm. **B** 20x

magnification images displaying representative plaques from the 6m and 9m Tg mice sections respectively (white boxes) shown in (**A**). Scale bars: 100 µm. **C** Analysis of dRSC and gRSC surface area covered by plaques found significant main effects of age ($F(2, 34) = 5.44$, $p < .01$; 3-way mixed ANOVA) and genotype ($F(1,34) = 7.86$, $p < .01$), as well as an interaction between the two variables ($F(2,34) = 5.44$, $p < .01$). Tg *post hoc* tests found that the area covered by plaques in the dRSC was significantly higher in the 9m group as compared to 3m and 6m (**3m:** 0 (0); **6m:** 0.03 (0.05); **9m:** 0.43 (0.38) %). Area covered by plaques at 3m and 6m did not significantly differ ($p = .82$). In the gRSC, area covered was only significantly increased in the 9m group compared to 3m (**3m:** 0 (0); **6m:** 0.08 (0.12); **9m:** 0.32 (0.35) %), and neither group differed from 6m (**3m *vs* 6m:** $p = .49$, **6m *vs* 9m:** $p = .08$). There was no main effect of sub-region ($F(1,34) = 0.18$, $p = .68$), or interaction between sub-region and age ($F(2,34) = 1.06$, $p = .36$) or genotype ($F(1,34) = 0.18$, $p = .68$). **D** Analysis of average surface area of plaques in Tg mice showed a significant main effect of age ($F(2,19) = 10.21$, $p < .001$; 2-way mixed ANOVA) but no main effect of sub-region ($F(1,19) = 0.12$, $p = .73$) or interaction of sub-region with age ($F(2,19) = 1.16$, $p = .33$). *Post hoc* tests found plaque surface area increased with age for the dRSC and gRSC: 9m plaque size was larger than 6m and 3m in the dRSC (**3m:** 0 (0); **6m:** 110.68 (189.90); **9m:** 738.64 (642.17) μm^2) and larger than 3m only in the gRSC (**3m:** 0 (0); **6m:** 216.23 (306.84); **9m:** 548.71 (355.61) μm^2). In the dRSC, 3m and 6m did not differ significantly ($p = .62$), whilst in the gRSC 6m did not differ from 3m ($p = .18$) or 9m ($p = .10$). Descriptive stats display mean and SD. Boxplots display median (solid line), mean (dashed line), IQR and range. ** p < .05, ** p < .01*

To compare the development of Aβ deposition in RSC with other regions known to be involved in prodromal AD (Chetelat and Baron, 2003), coronal sections containing the CA1 region of the HPC and the EC were also stained with AmyloGlo and analysed. Again, no Aβ plaque deposition was observed in WT J20 sections in the CA1 (**Figure 4.2 A top**) or EC (**Figure 4.2 D top**). Similar to the RSC, plaques were observed from 6m in the CA1 and EC (**Figure 4.2A bottom** and **Figure 4.2 A top**) and the percentage of area covered by plaques increased from 6m to 9m (**Figure 4.2 B & E**). Additionally, the average surface

area of the deposited Aβ plaques also increased from 6m to 9m in both areas (**Figure 4.2 C & F**).

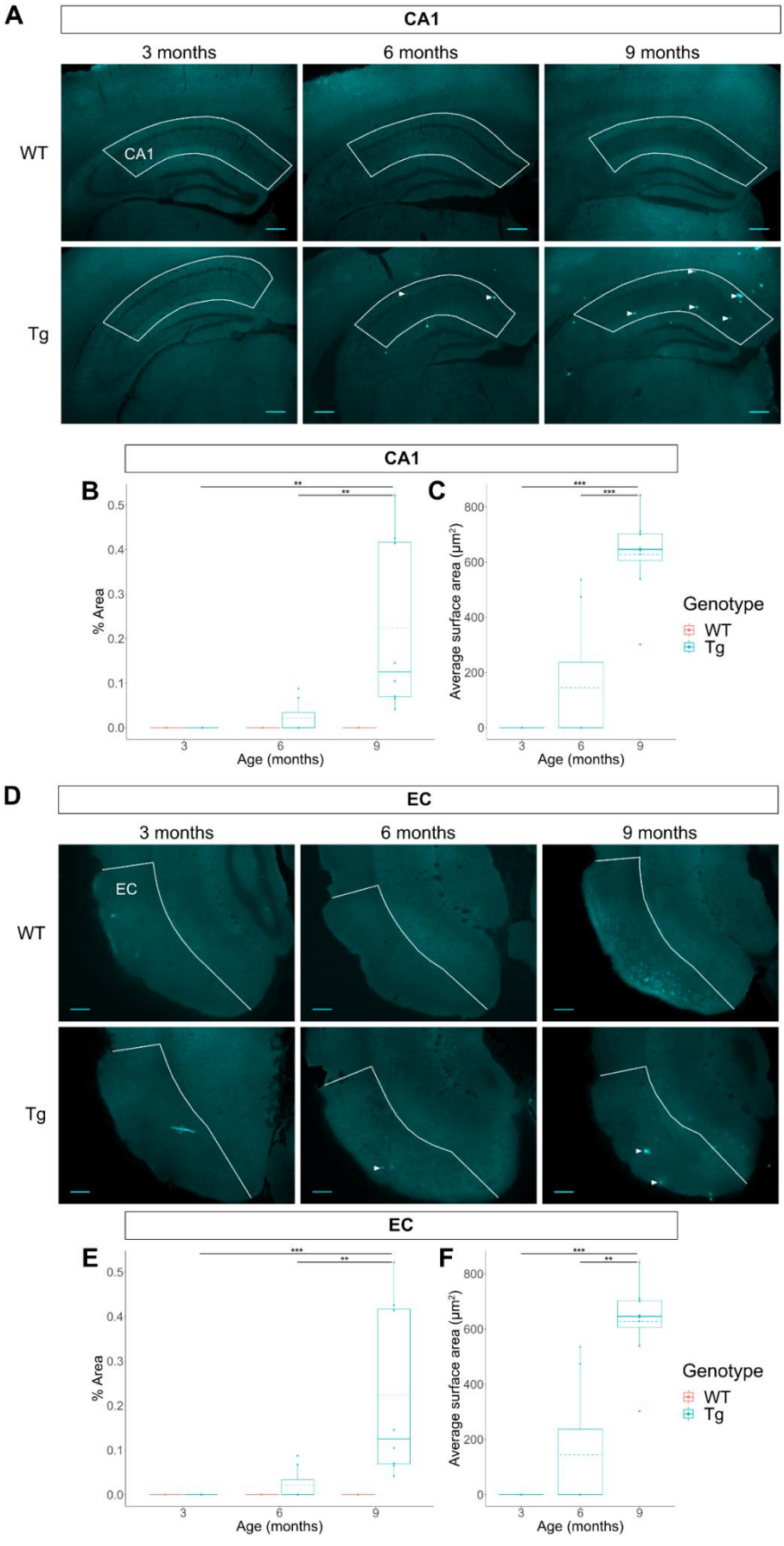

Figure 4.2 | Aβ plaque deposition in the CA1 and EC increases with age in J20 Tg mice. A Representative images (4x magnification) of Aβ plaque deposition in the CA1 in WT and Tg J20 mice at 3m, 6m and 9m. Arrows indicate plaques at 6m and 9m in Tg mice. Scale bars: 250 µm. **B** Analysis of CA1 surface area covered by plaques found significant main effects of genotype ($F(1,34) = 9.50$, $p < .01$; 2-way ANOVA) and age ($F(2,34) = 8.27$, $p < .01$), as well as a significant interaction between the two ($F(2,34) = 5.97$, $p < .01$). Tg *post hoc* tests found area covered was significantly higher at 9m as compared to both 3m and 6m (**3m:** 0 (0); **6m:** 0.02 (0.04); **9m:** 0.22 (0.20) %), while 3m and 6m did not differ significantly ($p = .74$). **C** Average plaque surface area significantly increased with age in the CA1 in Tg mice ($F(1,19) = 28.92$, $p < .001$; 1-way ANOVA). Plaque size was significantly larger at 9m than 3m and 6m (**3m:** 0 (0); **6m:** 144.28 (247.05); **9m:** 627.12 (157.12) μm^2). 3m and 6m plaque surface area did not differ ($p = .13$). **D** Representative images of Aβ plaque deposition in the EC in WT and Tg J20 mice at 3m, 6m and 9m. Arrows indicate plaques at 6m and 9m in Tg mice. Scale bars: 250 µm. **E** Analysis of EC surface area covered by plaques found significant main effects of genotype ($F(1,34) = 19.20$, $p < .001$; 2-way ANOVA) and age ($F(2,34) = 14.68$, $p < .001$), as well as a significant interaction between genotype and age ($F(2,34) = 10.82$, $p < .001$). *Post hoc* tests showed that plaques covered significantly more EC area in Tg mice at 9m than at 3m and 6m (**3m:** 0 (0); **6m:** 0.03 (0.06); **9m:** 0.21 (0.13) %). There was no significant difference between 3m and 6m ($p = .55$). **F** Average plaque surface area significantly increased with age in the EC in Tg mice ($F(2,34) = 10.62$, $p < .001$; 1-way ANOVA). Plaque size was significantly larger at 9m than 3m and 6m (**3m:** 0 (0); **6m:** 363.65; **9m:** 1202.91 (602.35) μm^2), while 3m and 6m did not differ ($p = .21$). Descriptive stats display mean and SD. Boxplots display median (solid line), mean (dashed line), IQR and range. ** $p < .01$, *** $p < .001$

Therefore, progressive RSC Aβ plaque deposition occurs in the J20 model of amyloidopathy, and follows a similar temporal pattern to other brain regions that are known to show deposition of Aβ plaques during the prodromal phase of AD – the CA1 and EC.

4.3.2 | Basal Fos expression decreases with age but is not modulated by Aβ pathology

Sections from WT and Tg J20 mice at 3, 6 and 9 month age points were immunohistochemically stained for Fos expression. Sections containing the dRSC and gRSC (**Figure 4.3 A**) were analysed to investigate whether baseline neuronal activity was disrupted in these areas. Sections containing the CA1 (**Figure 4.4 A**) and EC (**Figure 4.4 B**) were also analysed to compare against other brain regions known to be neuropathologically affected in AD. Only nuclei expressing high levels of Fos were counted (see **Section 2.5.2**), and counts were normalised to ROI area resulting in a measure of Fos positive (Fos+) cells per mm^2.

Firstly, there was a significant difference in basal Fos expression between the RSC sub-regions: the dRSC displayed significantly higher Fos expression than the gRSC (**Figure 4.3 B**). Furthermore, whilst Fos expression decreased with age – mice at the 9 month time point had the lowest expression – there was also a significant interaction between age and sub-region. The dRSC displayed a greater decrease in Fos+ cells as age increased. There was, however, no effect of genotype, or a significant interaction between age and genotype. *Post hoc* analyses found no significant differences between WT and Tg mice at any age point in the dRSC (**3m WT vs Tg:** p = .42; **6m WT *vs* Tg:** p = .63; **9m WT *vs* Tg:** p = .71) or gRSC (**3m WT *vs* Tg:** p = .39; **6m WT *vs* Tg:** p = .82; **9m WT *vs* Tg:** p = .67). This suggests that while baseline neuronal activity is significantly decreased by 9 months, amyloidopathy does not alter basal Fos expression in this region at prodromal or clinical stages.

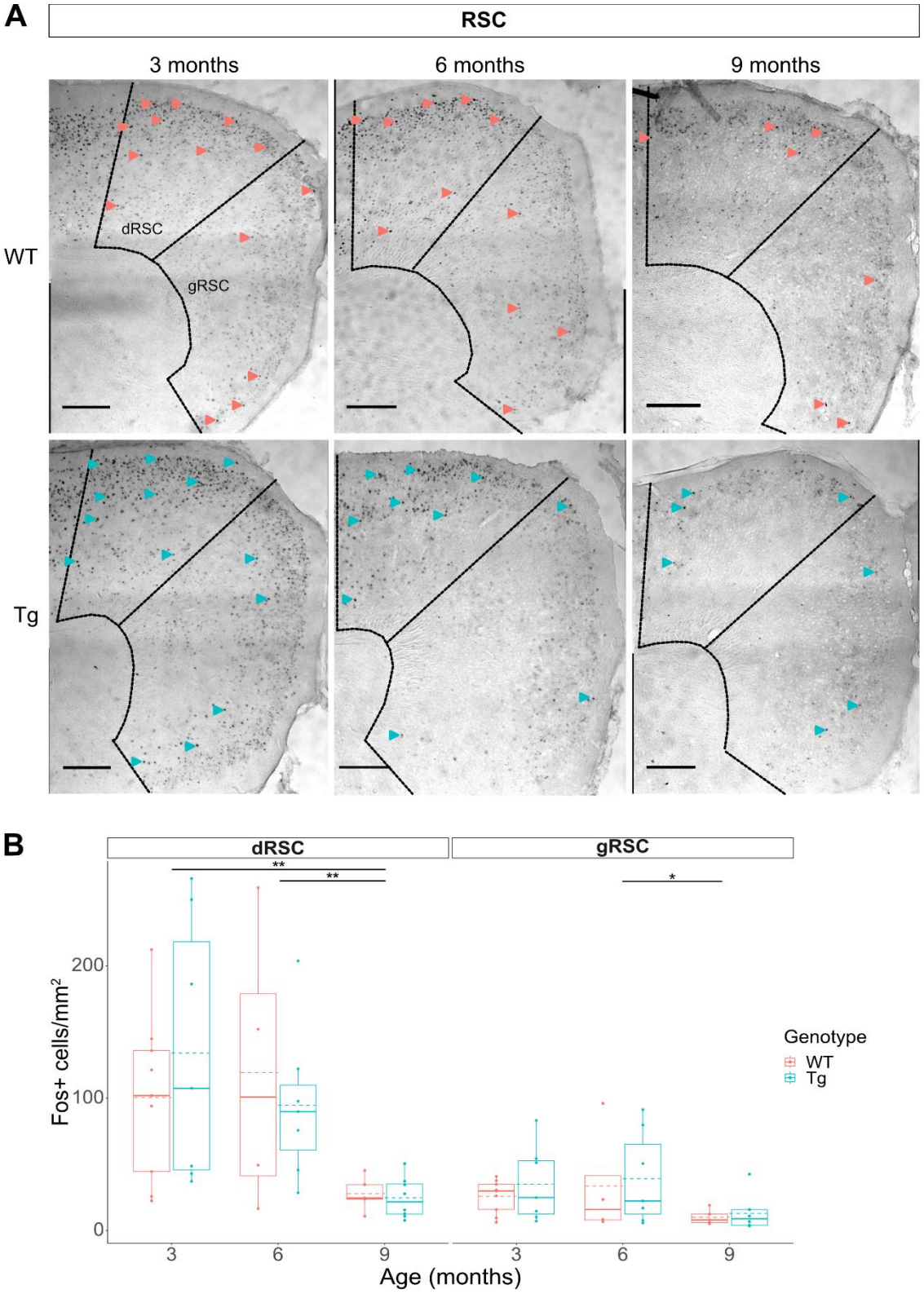

Figure 4.3 | Basal Fos expression differs between RSC sub-regions and decreases with age, but is not affected by J20 genotype. A Representative images of basal Fos expression in the RSC in WT and Tg J20 mice at 3m, 6m and 9m age points. Images of the dRSC and gRSC were taken separately (10x magnification) and stitched together. Arrows

indicate representative cells considered Fos+, but are not exhaustive of the count. Scale bars: 250 µm. **B** A three-way mixed ANOVA indicated a significant main effect of sub-region ($F(1,34) = 50.82$, $p < .001$) and age ($F(2,34) = 6.51$, $p < .01$), as well as a significant interaction between the two variables ($F(2, 34) = 7.86$, $p < .01$). *Post hoc* tests comparing age points in the dRSC found significantly fewer Fos+ cells/mm^2 at 9m than 3m and 6m, which did not differ from each other ($p = .65$) (**3m WT:** 100.44 (62.26); **3m Tg:** 134.15 (99.37); **6m WT:** 119.39 (109.6); **6m Tg:** 94.83 (57.47); **9m WT:** 27.89 (12.97); **9m Tg:** 24.69 (15.32) Fos+ cells/mm^2). In the gRSC, there were significantly fewer Fos+ cells/mm^2 at 9m than 6m, but not compared to 3m ($p = .07$). 3m and 6m also did not significantly differ in Fos expression ($p = .43$) (**3m WT:** 25.88 (12.44); **3m Tg:** 35.17 (28.49); **6m WT:** 33.73 (42.29); **6m Tg:** 39.28 (35.08); **9m WT:** 10.21 (5.73); **9m Tg:** 12.97 (13.05) Fos+ cells/mm^2). There was no significant main effect of genotype ($F(1, 34) = 0.08$, $p = .79$), or interaction between genotype and age ($F(2,34) = 0.45$, $p = .64$) or sub-region ($F(1,34) = 0.06$, $p = .81$). Finally, there was no significant interaction between all three independent variables ($F(2,34) = 0.99$, $p = .38$). Descriptive stats display mean and SD. Boxplots display median (solid line), mean (dashed line), IQR and range. *$p < .05$, **$p < .01$*

To examine whether this lack of effect of amyloidopathy on basal activity was restricted to the RSC, sections containing the CA1 and EC were also counted and analysed. Both brain regions showed a similar pattern to the dRSC and gRSC in that Fos expression decreased with age, but was not affected by genotype (**Figure 4.4 C-D**). *Post hoc* analyses in CA1 revealed no significant differences between wild-type and transgenic mice at each time point (**3m WT *vs* Tg:** $p = .56$; **6m WT *vs* Tg:** $p = .73$; **9m WT *vs* Tg:** $p = .53$), and the same was true in the EC (**3m WT *vs* Tg:** $p = .25$; **6m WT *vs* Tg:** $p = .51$; **9m WT *vs* Tg:** $p = .31$).

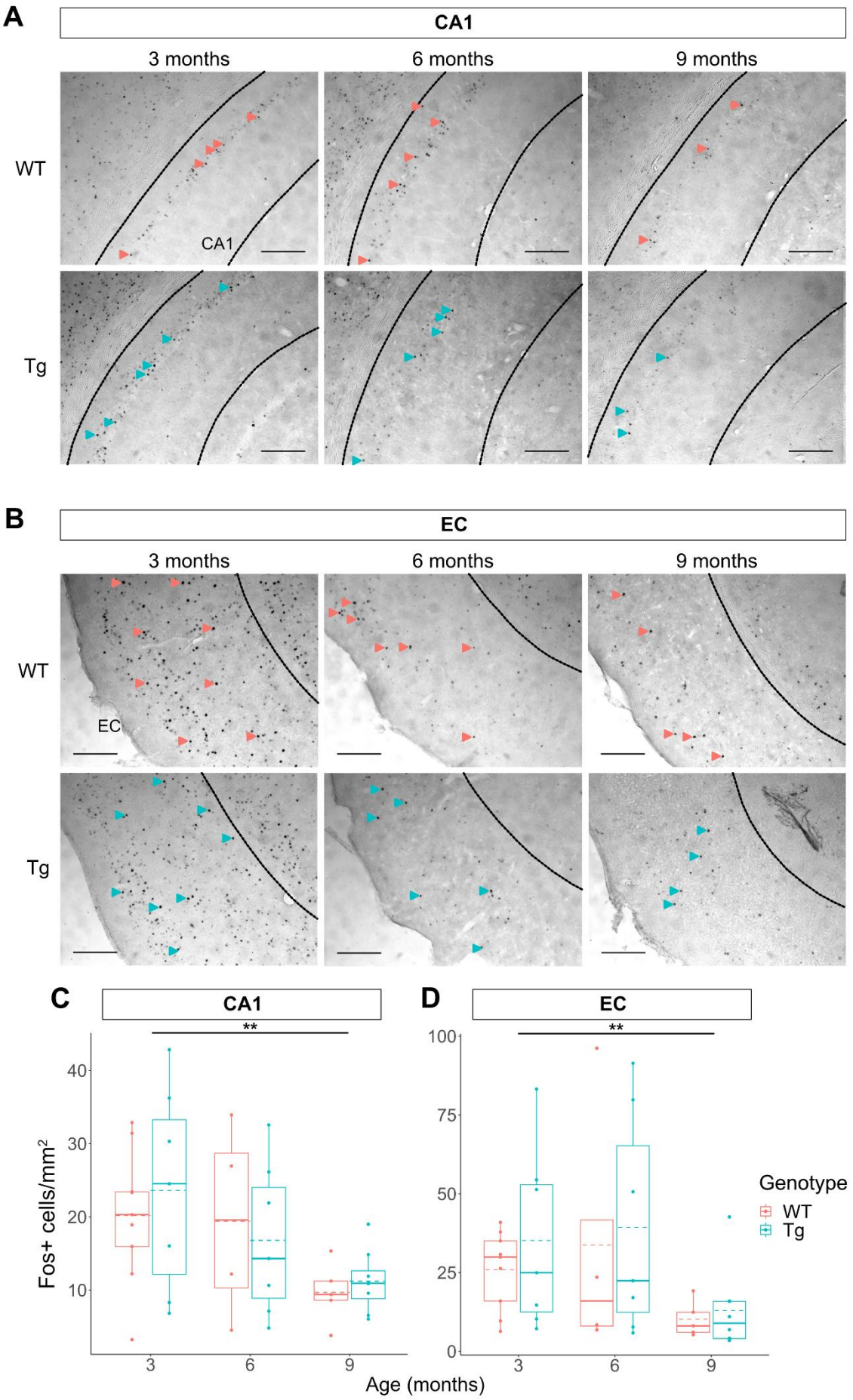
A
CA1
3 months
6 months
9 months
WT
Tg
CA1
B
EC
3 months
6 months
9 months
WT
Tg
EC
C
CA1
**
Fos+ cells/mm²
40
30
20
10
3
6
9
D
EC
**
100
75
50
25
0
3
6
9
Age (months)
Genotype
WT
Tg

Figure 4.4 | Basal Fos expression in CA1 and EC decreases with age but is not affected by J20 genotype. A-B Representative images of basal Fos expression in the CA1 (**A**) and EC (**B**) in WT and Tg J20 mice at 3m, 6m and 9m age points. Images were taken at 10x magnification, and arrows indicate representative cells considered Fos+ but are not exhaustive of the count. Scale bars: 250 µm. **C** In CA1 there was a main effect of age ($F(2,34) = 4.75$, $p < .05$; 2-way ANOVA), but no effect of genotype ($F(1,34) = 0.002$, $p = .96$) or interaction between age and genotype ($F(2,34) = 0.30$, $p = .74$). *Post hoc* tests found Fos expression was significantly lower at 9m than 3m, but there was no difference between 6m and 9m ($p = .11$) or 3m and 6m ($p = .29$) (**3m WT:** 20.18 (9.21); **3m Tg:** 23.62 (13.90); **6m WT:** 19.40 (13.43); **6m Tg:** 16.78 (10.35); **9m WT:** 9.67 (4.19); **9m Tg:** 11.22 (4.24) Fos+ cells/mm^2). **D** In the EC there was a significant main effect of age ($F(2,34) = 4.46$, $p < .05$; 2-way ANOVA), but no main effect of genotype ($F(1,34) = 0.33$, $p = .57$) or interaction between age and genotype ($F(2,34) = 0.11$, $p = .90$). *Post hoc* tests indicated that Fos expression at 3m was significantly higher than 6m or 9m, while expression did not significantly differ between those age points ($p = .89$) (**3m WT:** 36.41 (26.00); **3m Tg:** 68.76 (76.55); **6m WT:** 16.85 (12.45); **6m Tg:** 20.98 (7.67); **9m WT:** 20.77 (9.63); **9m Tg:** 15.47 (8.17) Fos+ cells/mm^2). Descriptive stats display mean and SD. Boxplots display median (solid line), mean (dashed line), IQR and range. ** *p < .01*

4.3.3 | Synaptic responses in the RSC to the ATN afferent pathway are not affected by age or genotype in J20 mice

Ex vivo whole-cell patch clamp recordings were undertaken in RSC-containing sections, and optogenetic stimulation of ATN afferent terminals was used to measure synaptic connectivity in WT and Tg J20 mice at 3, 6 and 9 months of age. Similar to the recordings in C57BL/6J mice (**Figure 3.3.3**), all putative pyramidal cells responded to stimulation of this pathway for both genotypes and all age points. Therefore probability of synaptic connectivity was not altered by age or genotype.

Other measures of synaptic response were then analysed to investigate the effect of age and/or genotype after controlling for sub-region and layer. NMDA/AMPA ratio, PPR and various EPSC measures – magnitude, time to onset and 20-80% rise time – were analysed using mixed effect models (see **Table 4.1** for cell counts for different variables).

				Count		
Age	**Genotype**	**Area**	**Layer**	**EPSC measures**	**NMDA/AMPA**	**PPR**
3m (n=189)	*WT (n=100)*	*dRSC*	*Superficial*	12	6	9
			Deep	12	3	12
		gRSC	*Superficial*	11	5	7
			Deep	12	2	9
	Tg (n=89)	*dRSC*	*Superficial*	10	5	9
			Deep	8	3	7
		gRSC	*Superficial*	11	5	10
			Deep	12	2	7
6m (n=284)	*WT (n=142)*	*dRSC*	*Superficial*	15	8	10
			Deep	15	2	13
		gRSC	*Superficial*	19	7	17
			Deep	16	6	14
	Tg (n=142)	*dRSC*	*Superficial*	20	10	16
			Deep	13	7	11
		gRSC	*Superficial*	13	7	11
			Deep	14	8	12
9m (n=208)	*WT (n=133)*	*dRSC*	*Superficial*	13	8	12
			Deep	16	6	13
		gRSC	*Superficial*	12	6	11
			Deep	15	6	15
	Tg (n=75)	*dRSC*	*Superficial*	13	7	8
			Deep	5	1	3
		gRSC	*Superficial*	12	5	9
			Deep	6	2	4
			Total	**305**	**127**	**249**

Table 4.1 | Recorded cells separated by age, genotype, RSC sub-region and cortical layer. All putative PCs recorded responded to stimulation of ATN afferent terminals. EPSC magnitude, onset time and 20-80% rise time were calculated from 305 cells total. NMDA/AMPA ratio was calculated from 127 cells, and PPR from 249 cells.

To examine EPSC magnitude, a null model (*random effect*: mouse) and three mixed effect models were created and goodness-of-fit (represented by AIC) was sequentially evaluated using χ^2 likelihood ratio comparisons. Model 1 (*random effect*: mouse; *fixed effects:* sub-region and layer*)* significantly improved upon the null model ($\chi_2(2) = 73.0$, $p < .001$; $\mathbf{AIC_{null}} = 4595.0$, $\mathbf{AIC_{M1}} = 4526.0$), and both sub-region ($F(1,280.1) = 62.2$, $p < .001$; ANOVA) and layer ($F(1,286.1) = 286.1$, $p < .001$; ANOVA) significantly affected EPSC magnitude. Fixed effect estimates (**Table 4.2**) indicate that cells in the gRSC and deep layers had a significantly lower EPSC magnitude compared to those in the dRSC and superficial layers,

respectively. Inspection of the data shows that cells in the superficial layers of the dRSC had the largest EPSC magnitude, followed by dRSC deep layer cells (**Figure 4.5**). Next, model 2 added age and genotype as fixed effects (*random effect:* mouse; *fixed effects*: sub-region, layer, age and genotype); however this model did not improve upon model 1 ($\chi_2(3) = 3.9$, $p = .27$; **AIC_{M2}** = 4528.1). Furthermore, the addition of sex as a fixed effect in model 3 (*random effect:* mouse; *fixed effects*: sub-region, layer, age, genotype and sex) did not improve upon model 2 ($\chi_2(1) = 2.8$, $p = 0.09$; **AIC_{M3}** = 4527.7), and fixed effect estimates for models 2 and 3 did not show any significant differences in EPSC magnitude for these added factors (**Table 4.2**). Therefore model 1 appears to be the best model of EPSC magnitude variability, suggesting age, genotype and sex have no effect on this measure. There was also a random effect of mouse present in model 1 – contributing 6.8% of variance to the total explained by the model – however the ICC score indicates a weak resemblance between mice (**Table 4.3** random effects).

	EPSC magnitude								
	Model 1			**Model 2**			**Model 3**		
Predictors	*Estimates*	*t*	*p*	*Estimates*	*t*	*p*	*Estimates*	*t*	*p*
Intercept	638.65 (559.64 – 717.65)	15.91	**<0.001**	724.35 (599.62 – 849.08)	11.43	**<0.001**	692.45 (564.93 – 819.96)	10.69	**<0.001**
Sub-region: gRSC	-351.77 (-439.54 – -264.01)	-7.89	**<0.001**	-353.28 (-440.75 – -265.80)	-7.95	**<0.001**	-353.87 (-441.21 – -266.52)	-7.97	**<0.001**
Layer: Deep	-206.14 (-294.39 – -117.89)	-4.6	**<0.001**	-212.49 (-300.73 – -124.24)	-4.74	**<0.001**	-214.87 (-303.07 – -126.67)	-4.79	**<0.001**
Age: 6 months				-51.06 (-175.81 – 73.69)	-0.81	0.421	-66.94 (-189.89 – 56.01)	-1.07	0.285
Age: 9 months				-67.99 (-200.39 – 64.41)	-1.01	0.313	-81.8 (-211.74 – 48.14)	-1.24	0.216
Genotype: Tg				-90.72 (-193.95 – 12.52)	-1.73	0.085	-91.67 (-192.29 – 8.95)	-1.79	0.074
Sex: Female							87.36 (-13.52 – 188.25)	1.7	0.089
Random Effects									
σ^2	146060.89			145540.38			145765.54		
τ^2_{mouse}	13750.34			11751.37			9611.95		
ICC	0.09			0.07			0.06		
N	68			68			68		
Observations	305			305			305		
Marginal R^2 / Conditional R^2	0.212 / 0.280			0.223 / 0.281			0.231 / 0.278		

Table 4.2 | Fixed and random effect results for each mixed model analysing EPSC magnitude. For fixed effects (predictors), the table displays effect size, confidence intervals, *t* statistic and significance value. For random effects, the table displays residual variance (σ^2), mouse variance (τ^2) and the ICC value. Marginal R^2 refers to variance explained by

fixed effects only, while conditional R^2 refers to variance explained by combined fixed and random effects.

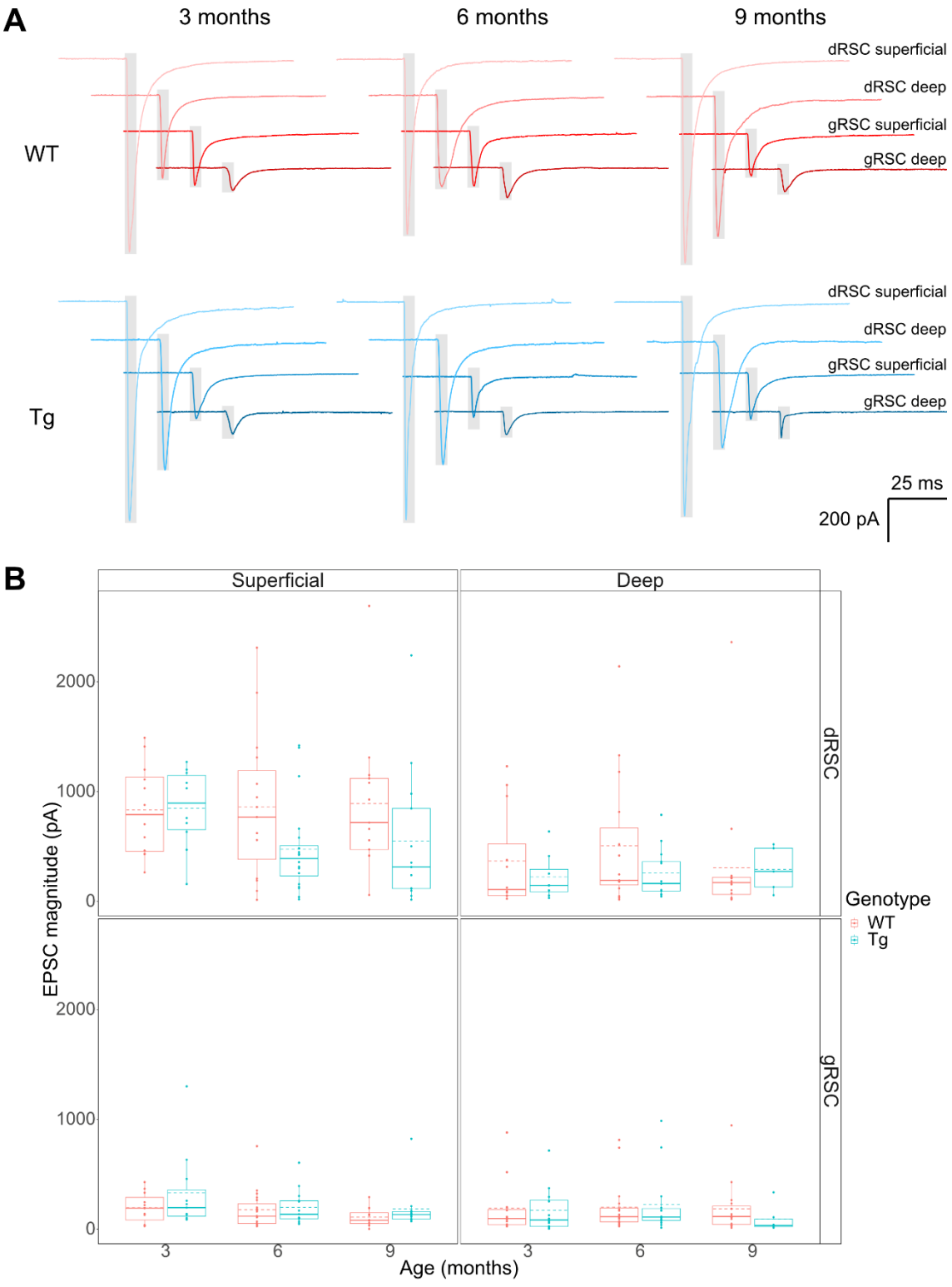

Figure 4.5 | EPSC magnitude differs between RSC sub-region and cortical layer, but is not affected by age or J20 genotype. A Representative voltage-clamp (V_H = -70 mV) traces showing the first EPSC generated from a 7 Hz stimulation protocol. Grey boxes indicate the 5 ms

optical stimulation period (470 nm wavelength). **B** EPSC magnitude differed between RSC sub-region and cortical layer: magnitude appeared largest in the superficial layers of the dRSC, followed by the deep layers dRSC whilst gRSC superficial and deep layer EPSC magnitude appeared the smallest. Neither age nor genotype significantly explained variance in EPSC magnitude, and no clear difference in these factors are observed graphically. Boxplots display median (solid line), mean (dashed line), IQR and range.

Time to onset of EPSC was then analysed, and again model 1 (*random effect*: mouse; *fixed effects:* sub-region and layer) significantly improved upon the null model (*random effect*: mouse) ($\chi_2(2) = 23.3$, $p < .001$; $\mathbf{AIC_{null}} = 620.5$, $\mathbf{AIC_{M1}} = 601.2$); with both sub-region and layer significantly affecting onset time (see **Table 4.3**). Model 2 (*random effect:* mouse; *fixed effects*: sub-region, layer, age and genotype) did not improve upon Model 1 ($\chi_2(3) = 2.7$, $p < .45$; $\mathbf{AIC_{M2}} = 604.5$) and fixed effect estimates showed no significant differences in time to onset for age or genotype. However, the addition of sex as a factor in model 3 (*random effect:* mouse; *fixed effects*: sub-region, layer, age, genotype and sex) did cause an improvement against model 2 ($\chi_2(1) = 5.1$, $p < .05$; $\mathbf{AIC_{M3}} = 601.4$), therefore a final model (model 4) was created with fixed effects of sub-region, layer and sex. This model significantly improved upon model 1 ($\chi_2(1) = 4.9$, $p < .05$; $\mathbf{AIC_{M4}} = 598.3$) and is considered the best model of time to EPSC onset. Within model 4, sub-region, layer and sex significantly affected onset time ($F(1,270.0) = 9.9$, $p < .001$; $F(1,274.4) = 15.5$, $p < .001$; $F(1,59.2) = 5.1$, $p < .05$; ANOVA). Fixed effect estimates indicate that cells in the gRSC and deep layers had significantly longer time to EPSC onset than cells in the dRSC and shallow layers (**Table 4.3**). Inspection of the data suggests this effect is driven by dRSC superficial layer cells showing the shortest onset time (**Figure 4.6**). Furthermore, cells collected from female mice showed significantly faster onset time than those collected from male mice. Finally, there was a relatively large random effect of mouse in the final model which contributed 15.3% of variance to the total variance explained (**Table 4.3** random effects), while the ICC score indicates that the correlation between mice remained low.

	Onset to EPSC											
	Model 1			**Model 2**			**Model 3**			**Model 4**		
Predictors	*Estimates*	*t*	*p*	*Estimates*	*t*	*p*	*Estimates*	*t*	*p*	*Estimates*	*t*	*p*
Intercept	0.95	13.91	**<0.001**	0.89	7.81	**<0.001**	0.98	8.43	**<0.001**	1.06	12.93	**<0.001**
	(0.82 – 1.08)			(0.67 – 1.12)			(0.75 – 1.20)			(0.90 – 1.22)		
Sub-region: gRSC	0.22	3.17	**0.002**	0.22	3.17	**0.002**	0.22	3.17	**0.002**	0.22	3.15	**0.002**
	(0.08 – 0.36)			(0.08 – 0.36)			(0.08 – 0.36)			(0.08 – 0.36)		
Layer: Deep	0.28	3.91	**<0.001**	0.28	3.99	**<0.001**	0.28	4.04	**<0.001**	0.28	3.94	**<0.001**
	(0.14 – 0.41)			(0.14 – 0.42)			(0.15 – 0.42)			(0.14 – 0.41)		
Age: 6 months				-0.05	-0.43	0.669	-0.01	-0.11	0.913			
				(-0.29 – 0.18)			(-0.24 – 0.22)					
Age: 9 months				0.07	0.53	0.598	0.1	0.78	0.434			
				(-0.18 – 0.31)			(-0.14 – 0.34)					
Genotype: Tg				0.13	1.3	0.194	0.13	1.38	0.168			
				(-0.07 – 0.32)			(-0.06 – 0.32)					
Sex: Female							-0.22	-2.3	**0.022**	-0.22	-2.25	**0.025**
							(-0.41 – -0.03)			(-0.40 – -0.03)		
Random Effects												
σ^2	0.35			0.35			0.35			0.35		
τ^2_{mouse}	0.08			0.08			0.07			0.07		
ICC	0.19			0.18			0.16			0.17		
N	68			68			68			68		
Observations	305			305			305			305		
Marginal R^2 / Conditional R^2	0.070 / 0.248			0.081 / 0.247			0.102 / 0.245			0.091 / 0.244		

Table 4.3 | Fixed and random effect results for each mixed model analysing time to onset of EPSC. For fixed effects (predictors), the table displays effect size, confidence intervals, *t* statistic and significance value. For random effects, the table displays residual variance (σ^2), mouse variance (τ^2) and the ICC value. Marginal R^2 refers to variance explained by fixed effects only, while conditional R^2 refers to variance explained by combined fixed and random effects.

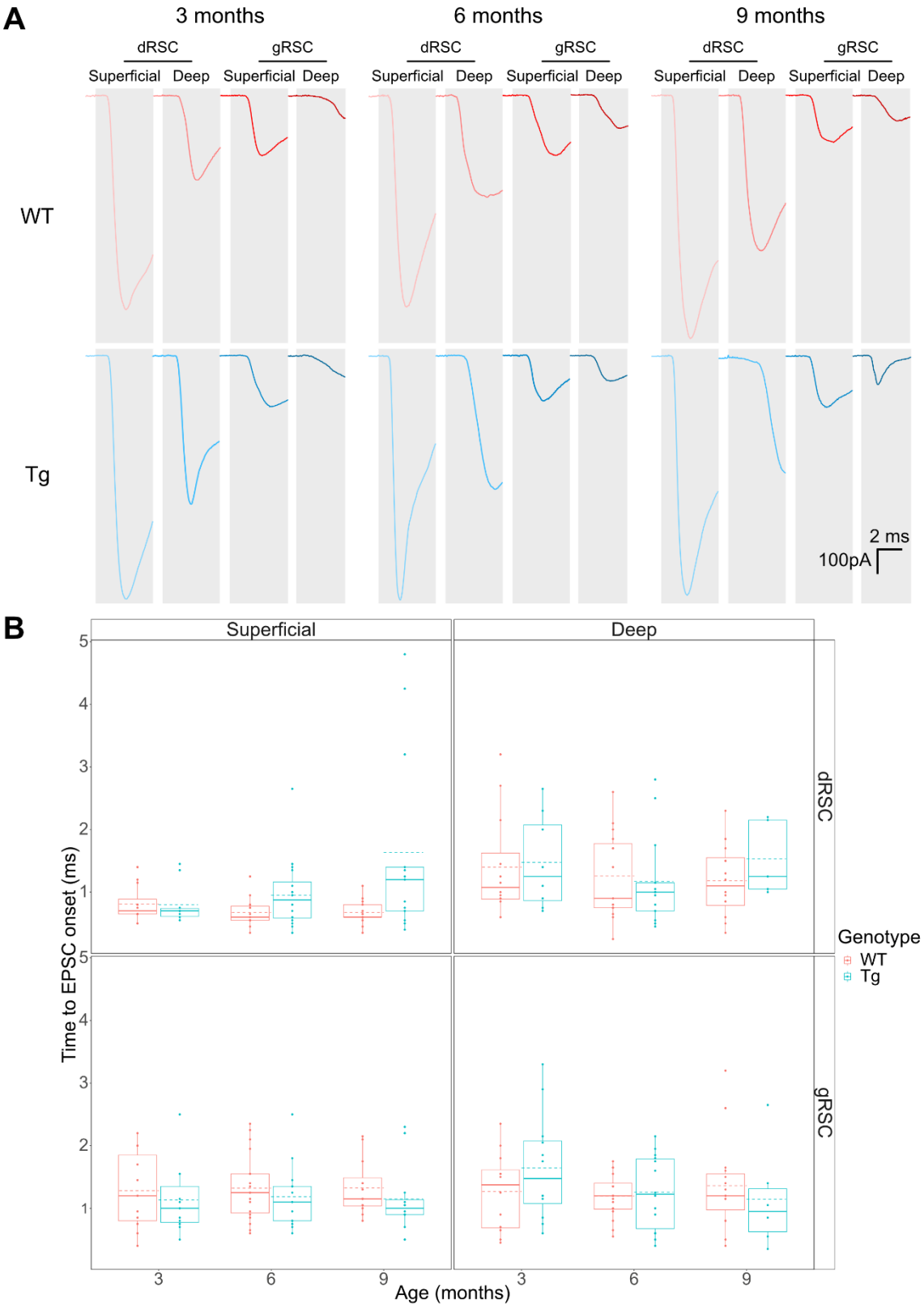

Figure 4.6 | EPSC onset differs between RSC sub-region and cortical layers, but is not affected by age or J20 genotype. A Representative voltage-clamp traces (V_H = -70 mV) showing onset of the EPSC generated by the optogenetic stimulation (grey boxes indicate optical stimulation period). **B** Time to EPSC onset differed between sub-region and layer:

dRSC superficial cells appear to show the shortest onset time. Neither age nor genotype significantly explained EPSC onset time variance, and no clear difference in these factors are observed graphically. Boxplots display median (solid line), mean (dashed line), IQR and range.

In addition to time to onset, 20-80% rise time of the first EPSC was analysed. Model 1 (*fixed effects:* sub-region and layer) did not significantly improve upon the null model ($\chi_2(2) = 6.0$, $p = .05$; $\mathbf{AIC_{null}} = 660.5$, $\mathbf{AIC_{M1}} = 658.5$), and fixed effect estimates (**Table 4.4**) indicated no differences in EPSC 20-80% rise time between cells in different RSC sub-regions or cortical layers. Model 2 (*fixed effects*: age and genotype) omitted sub-region and layer as factors due to the lack of significance in model 1, but again model 2 did not significantly improve upon the null model ($\chi_2(3) = 6.9$, $p = .08$; $\mathbf{AIC_{M2}} = 659.6$). Moreover, adding sex as a fixed effect in model 3 did not significantly improve upon model 2 ($\chi_2(1) = 1.5$, $p = .22$; $\mathbf{AIC_{M3}} = 660.0$). However, whilst model 2 did not significantly improve upon model 1, the fixed effect estimates (**Table 4.4**) displayed a lower 20-80% rise time at 6m compared to 3m, but there was no overall effect of age ($F(2,305.0) = 2.8$, $p = .06$) or a significant difference at 9m. Finally, the null model itself found a negligible random effect of mouse on variance, which was also true of models 1-3 (**Table 4.4** random effects). Therefore, EPSC 20-80% rise time was not significantly affected by sub-region, layer, age or genotype (**Figure 4.7**) and did not significantly differ between mice.

	Onset to EPSC								
	Model 1			**Model 2**			**Model 3**		
Predictors	*Estimates*	*t*	*p*	*Estimates*	*t*	*p*	*Estimates*	*t*	*p*
Intercept	0.95 (0.82 – 1.08)	13.91	**<0.001**	0.89 (0.67 – 1.12)	7.81	**<0.001**	0.98 (0.75 – 1.20)	8.43	**<0.001**
Sub-region: gRSC	0.22 (0.08 – 0.36)	3.17	**0.002**	0.22 (0.08 – 0.36)	3.17	**0.002**	0.22 (0.08 – 0.36)	3.17	**0.002**
Layer: Deep	0.28 (0.14 – 0.41)	3.91	**<0.001**	0.28 (0.14 – 0.42)	3.99	**<0.001**	0.28 (0.15 – 0.42)	4.04	**<0.001**
Age: 6 months				-0.05 (-0.29 – 0.18)	-0.43	0.669	-0.01 (-0.24 – 0.22)	-0.11	0.913
Age: 9 months				0.07 (-0.18 – 0.31)	0.53	0.598	0.1 (-0.14 – 0.34)	0.78	0.434
Genotype: Tg				0.13 (-0.07 – 0.32)	1.3	0.194	0.13 (-0.06 – 0.32)	1.38	0.168
Sex: Female							-0.22 (-0.41 – -0.03)	-2.3	**0.022**
Random Effects									
σ^2	0.35			0.35			0.35		
τ^2_{mouse}	0.08			0.08			0.07		
ICC	0.19			0.18			0.16		
N	68			68			68		
Observations	305			305			305		
Marginal R^2 */ Conditional* R^2	0.070 / 0.248			0.081 / 0.247			0.102 / 0.245		

Table 4.4 | Fixed and random effect results for each mixed model analysing EPSC 20-80% rise time. For fixed effects (predictors), the table displays effect size, confidence intervals, t statistic and significance value. For random effects, the table displays residual variance (σ2), mouse variance (τ2) and the ICC value. Marginal R^2 refers to variance explained by fixed effects only, while conditional R^2 refers to variance explained by combined fixed and random effects.

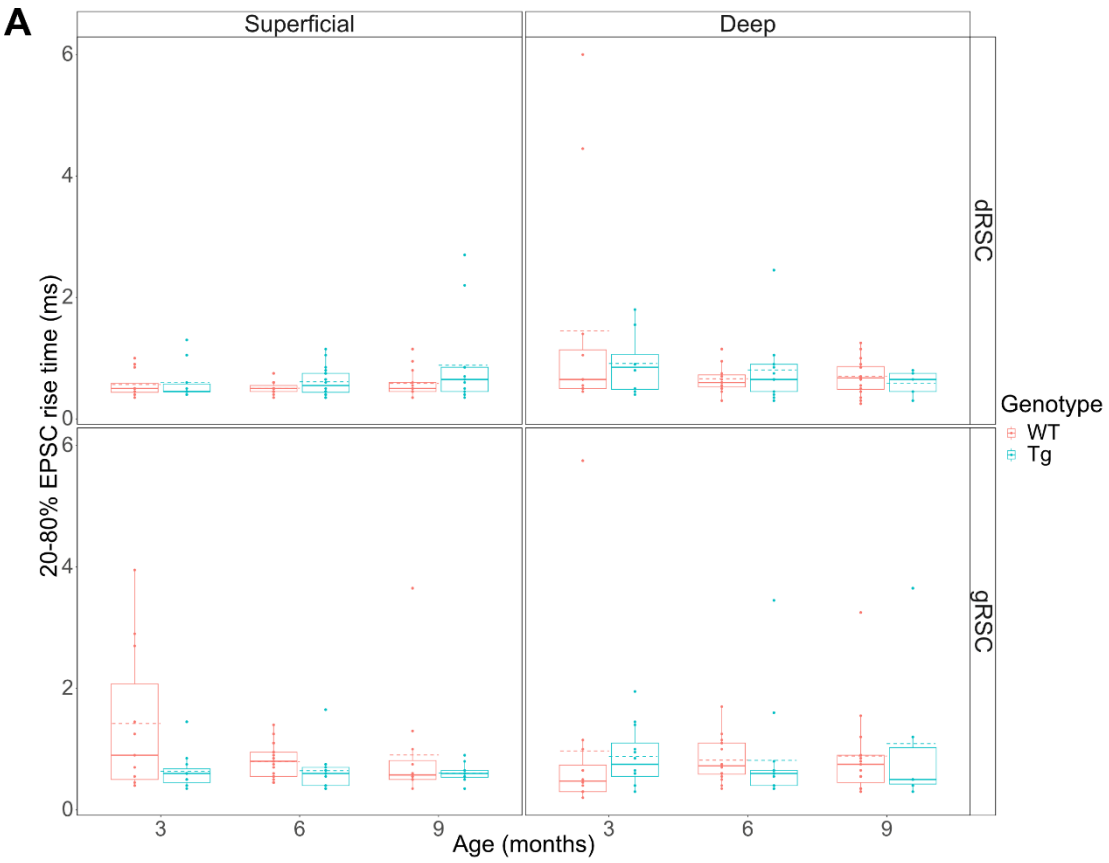

Figure 4.7 | EPSC 20-80% rise time does not differ between sub-region, cortical layer, age or J20 genotype. EPSC 20-80% rise time did not differ between sub-region, layer, age or genotype. Boxplots display median (solid line), mean (dashed line), IQR and range.

NMDA/AMPA ratio was computed from a sub-section of cells within the ATN to RSC pathway. Analysis of NMDA/AMPA ratios found that model 1 (*fixed effects:* sub-region and layer) did not significantly improve upon the null model ($\chi_2(2)$ = 2.8, p = .25; $\mathbf{AIC_{null}}$ = 28.9, $\mathbf{AIC_{M1}}$ = 30.2), and fixed effect estimates indicated

no significant differences in NMDA/AMPA ratio between sub-regions and layers (**Table 4.5**). Model 2 (*fixed effects:* age and genotype) omitted area and layer as factors due to the lack of significance in model 1, but again did improve upon the null model ($\chi_2(3) = 0.6$, $p = .89$; $\mathbf{AIC_{M2}} = 34.3$). Moreover, the addition of sex as a factor to model 3 did not significantly improve on model 2 ($\chi_2(1) = 0.9$, $p = .35$; $\mathbf{AIC_{M3}} = 35.4$). Fixed effect estimates for age, genotype and sex in models 2 and 3 found no significant differences within these factors (**Table 4.5**). Finally, the null model found a negligible random effect of mouse on variance, which was also true in models 1-3 (**Table 4.5** random effects). Therefore NMDA/AMPA ratio was not significantly affected by sub-region, layer, age or genotype (**Figure 4.8**) and did not differ significantly between mice.

	NMDA/AMPA Ratio								
	Model 1			**Model 2**			**Model 3**		
Predictors	*Estimates*	*t*	*p*	*Estimates*	*t*	*p*	*Estimates*	*t*	*p*
Intercept	0.38 (0.31 – 0.45)	10.46	**<0.001**	0.38 (0.27 – 0.48)	7.12	**<0.001**	0.36 (0.24 – 0.47)	6.24	**<0.001**
Sub-region: gRSC	0.05 (-0.04 – 0.15)	1.17	0.246						
Layer: Deep	-0.06 (-0.16 – 0.03)	-1.3	0.195						
Age: 6 months				0 (-0.12 – 0.11)	-0.06	0.948	-0.01 (-0.13 – 0.11)	-0.18	0.86
Age: 9 months				0.03 (-0.09 – 0.16)	0.52	0.602	0.03 (-0.10 – 0.15)	0.45	0.656
Genotype: Tg				-0.01 (-0.11 – 0.08)	-0.23	0.818	-0.01 (-0.10 – 0.08)	-0.22	0.827
Sex: Female							0.04 (-0.05 – 0.14)	0.94	0.347
Random Effects									
σ^2	0.07			0.07			0.07		
τ^2_{mouse}	0			0			0		
N	60			60			60		
Observations	127			127			127		
Marginal R^2 / Conditional R^2	0.022 / NA			0.005 / NA			0.012 / NA		

Table 4.5 | Fixed and random effect results for each mixed model analysing NMDA/AMPA ratio. For fixed effects (predictors), the table displays effect size, confidence intervals, *t* statistic and significance value. For random effects, the table displays residual variance (σ^2), mouse variance (τ^2) and the ICC value. Marginal R^2 refers to variance explained by fixed effects only, while conditional R^2 refers to variance explained by combined fixed and random effects.

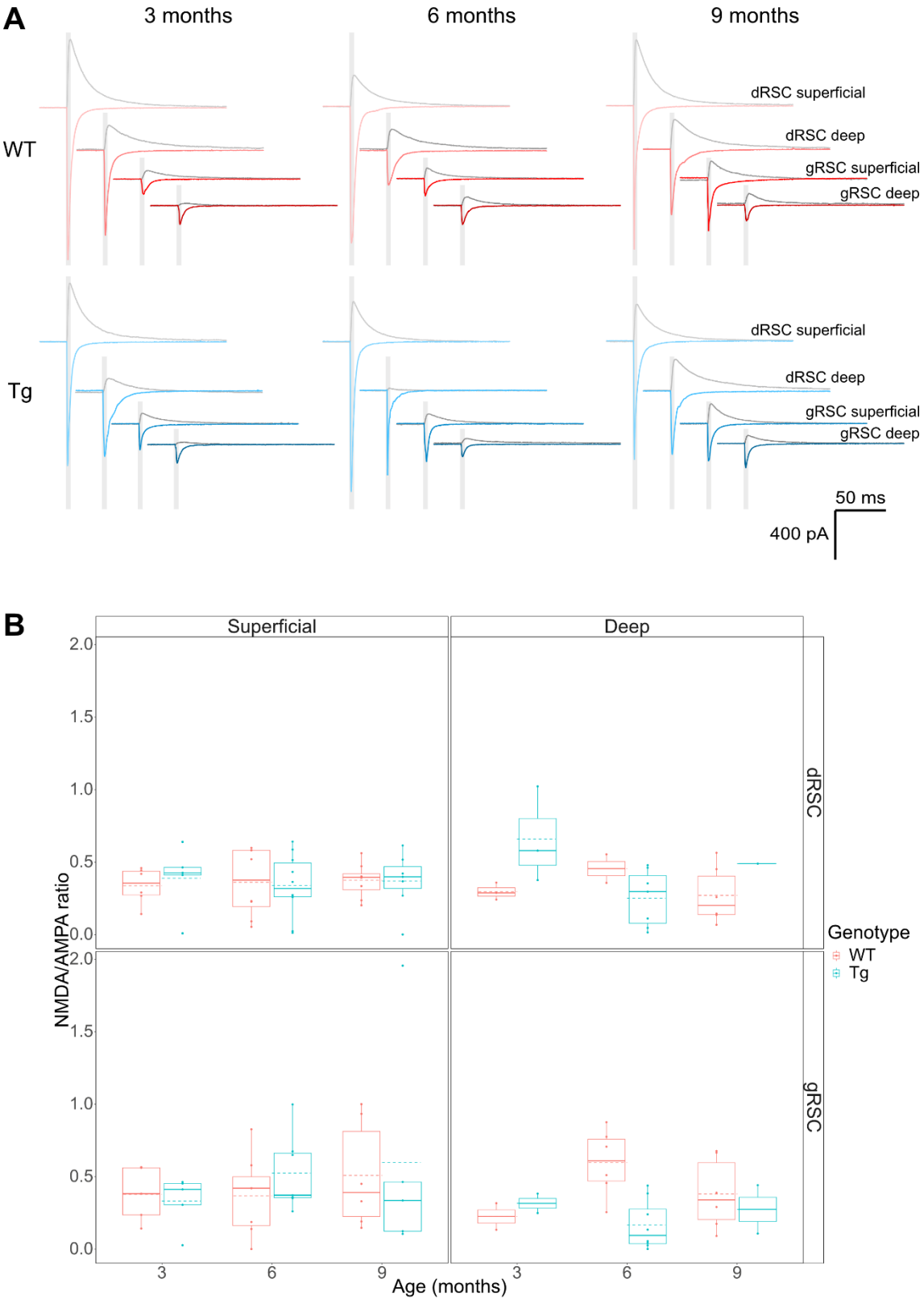

Figure 4.8 | NMDA/AMPA ratio does not differ between sub-region cortical layer, age or J20 genotype. A Representative voltage-clamp traces showing AMPAR-mediated (blue/red trace) and NMDAR-mediated EPSCs (grey trace) generated by optogenetic stimulation (grey box indicates 5 ms optical stimulation period). AMPAR responses were

recorded at V_H = -70 mV (standard aCSF) and NMDAR responses were recorded at V_H = +40 mV (standard aCSF containing (in µM): 10 DNQX, 1 CGP-55845, 10 Gabazine). **B** NMDA/AMPA ratio did not differ between sub-region, layer, age or genotype. Boxplots display median (solid line), mean (dashed line), IQR and range.

PPR from increasing interval optogenetic stimulations was computed and a null model including mouse as a random effect and a within-subjects fixed effect factor of time between first and second stimulations – i.e. increasing pulse-interval (IPI). Model 1 included sub-region and layer as additional fixed effects, and model 1 significantly improved upon the null model ($\chi_2(2) = 114.5$, $p < .001$; $\mathbf{AIC_{null}} = 650.0$, $\mathbf{AIC_{M1}} = 539.5$). Model 2 added age and genotype to model 1, but did not improve upon the model ($\chi_2(3) = 1.6$, $p = .67$; $\mathbf{AIC_{M2}} = 544.0$). Moreover, the addition of sex as a fixed effect in model 3 did not improve upon model 2 ($\chi_2(1) = 0.1$, $p = .72$; $\mathbf{AIC_{M3}} = 545.8$). Therefore, model 1 appears the best model of variance for PPR and all three fixed effect factors significantly affected PPR. IPI had a significant main effect ($F(6,1664.1) = 120.5$, $p < .001$; ANOVA), and fixed effect estimates showed a significant increase in PPR for each IPI time compared to the first 10 ms IPI sweep. Significant main effects were also found for both sub-region ($F(1,1660.9) = 107.7$, $p < .001$; ANOVA) and layer ($F(1,1656.2) = 9.8$, $p < .01$); fixed effect estimates for both factors indicate that cells in the gRSC and deep layers had significantly higher PPR ratios than those in the dRSC and superficial layers, respectively (**Table 4.6**). While PPR increased as IPI increased, examination of the data shows that median and mean values remained below 1 for all grouping factors (**Figure 4.9 B**) indicating PPD was present in this pathway across groups. Finally, there was a fairly small random effect of mouse in model 1 which contributed 4.6% of variance to the total variance explained (**Table 4.6** random effects), while the ICC score indicates that the correlation between mice remained low.

	PPR								
	Model 1			**Model 2**			**Model 3**		
Predictors	*Estimates*	*t*	*p*	*Estimates*	*t*	*p*	*Estimates*	*t*	*p*
Intercept	0.18	7.94	**<0.001**	0.19	6.05	**<0.001**	0.18	5.7	**<0.001**
	(0.13 – 0.22)			(0.13 – 0.25)			(0.12 – 0.25)		
IPI: 17 ms	0.23	9.35	**<0.001**	0.23	9.36	**<0.001**	0.23	9.36	**<0.001**
	(0.18 – 0.28)			(0.18 – 0.28)			(0.18 – 0.28)		
IPI: 51 ms	0.44	17.72	**<0.001**	0.44	17.72	**<0.001**	0.44	17.72	**<0.001**
	(0.39 – 0.49)			(0.39 – 0.49)			(0.39 – 0.49)		
IPI: 100 ms	0.41	16.57	**<0.001**	0.41	16.57	**<0.001**	0.41	16.57	**<0.001**
	(0.36 – 0.46)			(0.36 – 0.46)			(0.36 – 0.46)		
IPI: 170 ms	0.4	16.1	**<0.001**	0.4	16.1	**<0.001**	0.4	16.1	**<0.001**
	(0.35 – 0.45)			(0.35 – 0.45)			(0.35 – 0.45)		
IPI: 510 ms	0.48	19.28	**<0.001**	0.48	19.28	**<0.001**	0.48	19.29	**<0.001**
	(0.43 – 0.53)			(0.43 – 0.53)			(0.43 – 0.53)		
IPI: 1000 ms	0.59	23.71	**<0.001**	0.59	23.72	**<0.001**	0.59	23.72	**<0.001**
	(0.54 – 0.64)			(0.54 – 0.64)			(0.54 – 0.64)		
Sub-region: gRSC	0.15	10.38	**<0.001**	0.15	10.38	**<0.001**	0.15	10.36	**<0.001**
	(0.12 – 0.17)			(0.12 – 0.17)			(0.12 – 0.17)		
Layer: Deep	0.04	3.13	**0.002**	0.04	3.1	**0.002**	0.04	3.09	**0.002**
	(0.02 – 0.07)			(0.02 – 0.07)			(0.02 – 0.07)		
Age: 6 months				-0.03	-0.95	0.343	-0.03	-0.99	0.323
				(-0.08 – 0.03)			(-0.09 – 0.03)		
Age: 9 months				0	0.07	0.947	0	0.02	0.98
				(-0.06 – 0.06)			(-0.06 – 0.06)		
Genotype: Tg				-0.01	-0.23	0.816	-0.01	-0.23	0.815
				(-0.05 – 0.04)			(-0.05 – 0.04)		
Sex: Female							0.01	0.36	0.723
							(-0.04 – 0.05)		
Random Effects									
σ^2	0.08			0.08			0.08		
τ^2_{mouse}	0.01			0.01			0.01		
ICC	0.07			0.07			0.07		
N	68			68			68		
Observations	1743			1743			1743		
Marginal R^2 / Conditional R^2	0.314 / 0.360			0.315 / 0.362			0.315 / 0.363		

Table 4.6 | Fixed and random effect results for each mixed model analysing PPR. For fixed effects (predictors), the table displays effect size, confidence intervals, *t* statistic and significance value. For random effects, the table displays residual variance (σ^2), mouse variance (τ^2) and the ICC value. Marginal R^2 refers to variance explained by fixed effects only, while conditional R^2 refers to variance explained by combined fixed and random effects.

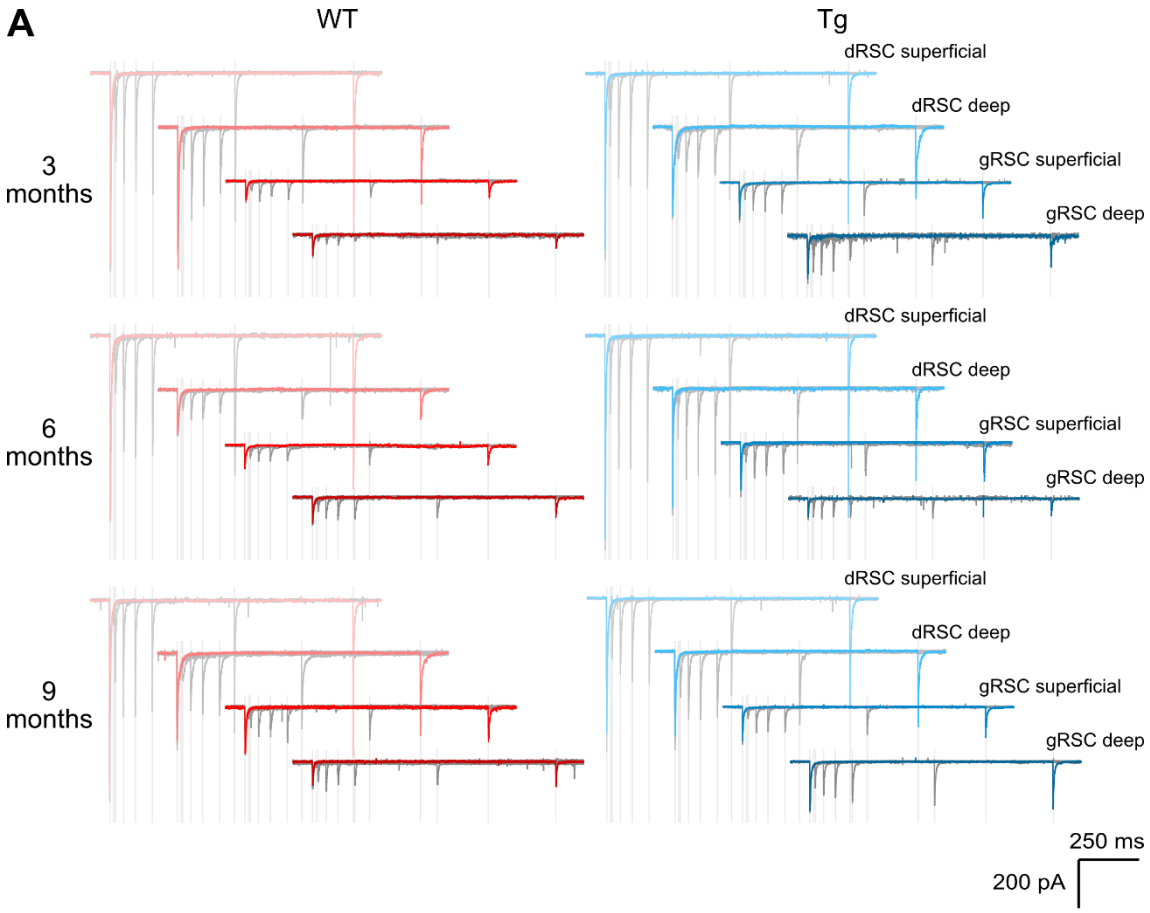
A
WT
Tg
3 months
6 months
9 months
dRSC superficial
dRSC deep
gRSC superficial
gRSC deep
250 ms
200 pA

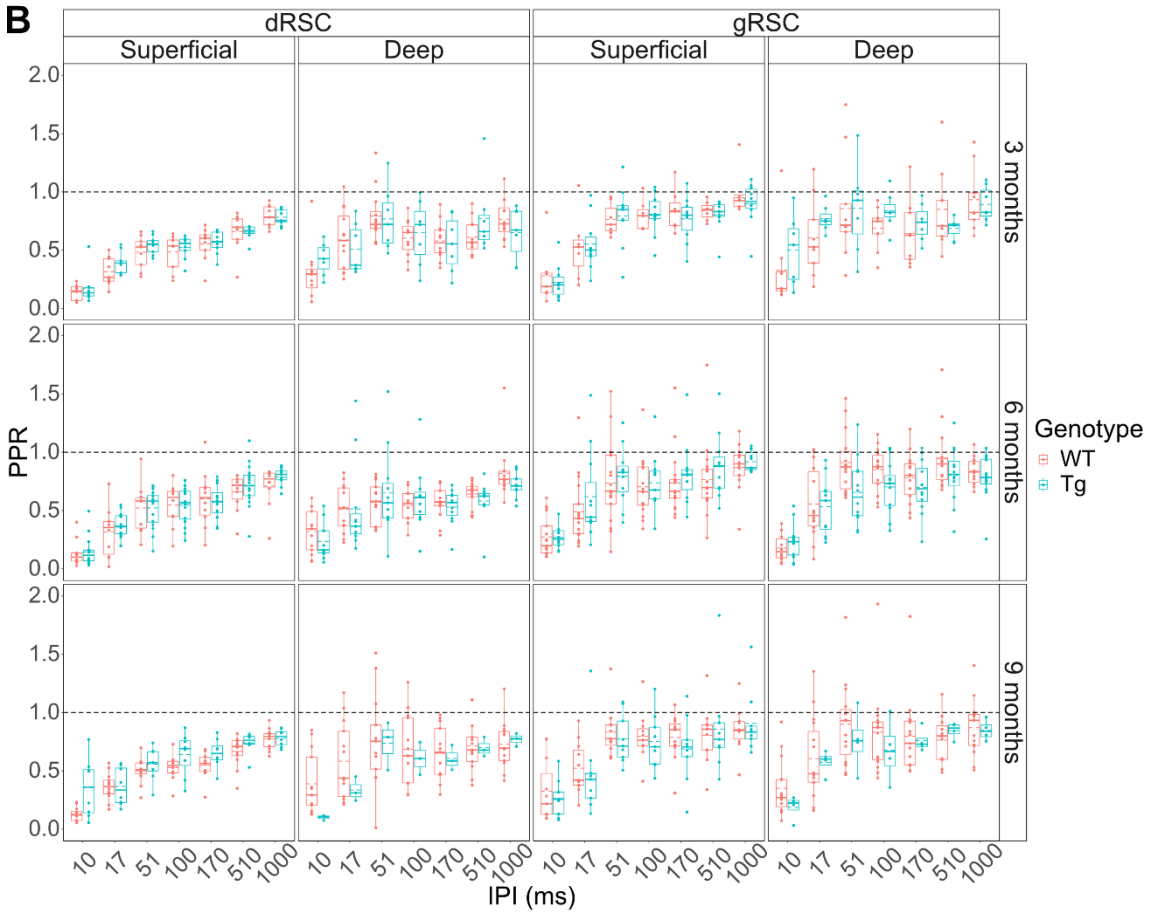
B
dRSC
gRSC
Superficial
Deep
3 months
6 months
9 months
PPR
IPI (ms)
Genotype
WT
Tg

Figure 4.9 | PPR differs between sub-region and layer, but is not affected by age or J20 genotype. A Representative voltage clamp traces (V_H = -70 mV) showing EPSCs generated by two optogenetic stimulations separated by increasing intervals. Each plot displays 7 sweeps with intervals of (grey traces) 10 ms, 17 ms, 51 ms, 100 ms, 170 ms, 510 ms and (red trace) 1000 ms. Optical stimulation periods indicated by pale grey boxes. **B** PPR increased with IPI for all cells, and mean/median PPR remained below 1 (black dashed line). PPR differed between sub-region and layer, and cells in the dRSC superficial layers appear to have a lower PPR which slowly increases. Boxplots display median (solid line), mean (dashed line), IQR and range.

4.4 | Discussion

4.4.1 | Summary

In this chapter, I aimed to investigate the RSC as a site of neuropathological change in a model of prodromal AD. Using the J20 model of amyloidopathy, I found that Aβ plaque deposition occurs in the RSC at a similar timescale to other brain areas known to show Aβ accumulations in the early stages of AD: the CA1 region of the HPC and the EC. However, plaque deposition was not associated with changes in baseline neuronal activity; while basal Fos expression decreased with age in the RSC, there was no effect of J20 genotype. Finally, I examined the ATN to RSC pathway and found no effect of age or genotype on postsynaptic responses in RSC PCs.

4.4.2 | The dRSC and gRSC show significantly different levels of basal neuronal activity

Baseline neuronal activity was compared between the RSC sub-regions, and significantly more Fos+ cells were identified per mm^2 in the dRSC. One of the main differences between the dRSC and gRSC is their structural and functional long-range connectivity. Neuroanatomical tracing studies in the rat have found that the dRSC is preferentially connected with primary and extrastriate visual cortices (Groen and Wyss, 1992). While this difference in structural connectivity

is not as pronounced in the mouse, the function of the dRSC is more equated with processing of visual information than the gRSC (Aggleton et al., 2021). Therefore, the dRSC may present with increased basal neuronal activity due to normal navigational behaviour within the home cage. Additionally, despite the dRSC showing lower anatomical connectivity with areas such as the ATN and dSub, PC synaptic responses to stimulation of these excitatory pathways were significantly higher in the dRSC compared to the gRSC (**Section 3.3.3** and **Section 4.3.3**). Therefore, the increased basal activity seen in the dRSC may be due to increased excitatory input into the dRSC from a range of presynaptic distal brain region, not just from the visual cortices. This difference in basal activity shows activity-based differentiation between the two sub-regions, and confirms that the dRSC and gRSC should be considered as distinct brain regions. Basal activity differences should also be taken into account when analysing the behavioural function of the dRSC and gRSC, and care should be taken not to directly compare neuronal activity in these areas without normalising against appropriate controls.

4.4.3 | Cortical and hippocampal basal activity decreases with age, but is not affected by Aβ pathology

The finding that Fos expression in the RSC, CA1 and EC decreased with age are consistent with prior literature that describes decreased hippocampal and cortical basal levels of Fos protein and mRNA in aged rats (Kitraki et al., 1993; Lee et al., 1998). The mechanism behind this decrease is not clear, however it may be linked to ageing-induced impairments in upstream signalling pathways such as MAPK (Zhen et al., 1999), which is the primary pathway through which Fos expression is mediated (Chung, 2015). While the number of Fos+ cells decreased with age, there were no differences in basal Fos expression between WT and Tg J20 mice at 3, 6 or 9 months of age. This was an unexpected finding, as this marker of neuronal activity has been shown to be reduced in the RSC in another model of Aβ pathology (Poirier et al., 2011). However, this reduction in Fos induction was observed following exposure to a novel environment, and reduced *Fos* mRNA expression was only observed in the CA1 when comparing AD model

Tg and WT animals following novelty-induced neuronal activity and not basal activity (Christensen et al., 2013).

The fact that basal neuronal activity was not affected by Aβ pathology in the RSC in these experiments, but prior literature has found decreases in novelty-induced Fos, suggests that the RSC (and the HPC and EC) may be very susceptible to cholinergic input dysfunction. The cholinergic system is involved in a range of cognitive processes including modulating spatial navigation, learning and memory (Solari and Hangya, 2018). Cholinergic activity is positively related to stimulus novelty in the insular cortex (Miranda et al., 2000), and environmental novelty the PFC and HPC (Giovannini et al., 2001). Identifying novelty is crucial to learning and memory as it can indicate salience and direct attention in order to create new memories or update consolidated memories. Encoding of new memories in the HPC and EC is posited to be reliant on the cholinergic modulation of theta oscillations (Barry et al., 2012). Furthermore, an important stage in the updating and reconsolidation of memory is destabilisation of the existing memory into a labile state: a process which is dependent on cholinergic action in a paradigm requiring reactivation novelty (Stiver et al., 2015).

The RSC receives cholinergic input from the basal forebrain, specifically the medial septal nucleus and diagonal band of Broca (Gonzalo-Ruiz and Morte, 2000; Nyakas et al., 1987; Woolf, 1991), similar to the HPC and EC. Indeed, the gRSC shows increased acetylcholine efflux during maze exploration that is correlated with HPC efflux (Anzalone et al., 2009). Disruption to this pathway could significantly impair behaviour, and explain the deficits in neuronal activity following exposure to a novel environment. Basal activity however was not affected in the present study as the mice were not exposed to a novel environment, or required to navigate any space other than their home cage, in the 90 minutes preceding brain collection. There is some early evidence that disruption to this pathway in AD may occur postsynaptically, as the RSC displays muscarinic receptor downregulation in the 5xFAD mouse model of amyloidopathy (Jedrasiak-Cape and Ahmed, 2020). Cholinergic input impairment following Aβ pathology does not preclude disruption to excitatory RSC inputs such as from the ATN, and in fact could help mediate glutamatergic transmission deficits, as acetylcholine is a significant modulator of many neurotransmitter systems (Picciotto et al., 2012).

4.4.4 | Aβ pathology does not disrupt input from the ATN to the RSC

Afferent projections from the ATN to the RSC exert a very large excitatory effect on the RSC (**Section 3.3.3**), and therefore are likely an important source of information for the RSC. The findings in this chapter confirmed that synaptic responses in the RSC to optogenetic stimulation of ATN axons were strongest in the dRSC and shallow layers compared to the gRSC and deep layers. However, despite the hypothesised importance of the ATN to RSC pathway in spatial navigation and subsequent disruption in AD, there was no significant change in synaptic response between WT and Tg mice at any age tested.

This lack of perturbation in the ATN to RSC projection correlates with the findings that basal neuronal activity did not differ between WT and Tg mice. As the ATN supplies substantial glutamatergic excitation onto PCs in the RSC, impaired excitatory transmission in this pathway might have similar effects to deafferentation following lesioning of the ATN (Jenkins et al., 2004). While this pathway could be affected in AD during tasks requiring high fidelity transfer of information, the evidence presented here suggests that Aβ pathology in the RSC is not sufficient to alter baseline synaptic connectivity of the ATN to RSC projections and subsequent RSC neuronal activation. Additionally, there was also no effect of increased age on synaptic responses in this pathway, suggesting that strength of this circuit does not change with age or general experience.

Deafferentation may be a key pathological change required for significant RSC disruption. While Aβ deposits do occur in the ATN in AD patients, they do not occur as early as in the RSC (Braak and Braak, 1991a, 1991b). Furthermore, the J20 model of amyloidopathy presents Aβ pathology primarily in cortical and hippocampal regions (Whitesell et al., 2019), and no plaques were detected in the ATN of the mice used in **Section 4.3.1**. It was hypothesised that Aβ oligomers present in the RSC would have synaptotoxic effects sufficient to disrupt this pathway (Hsia et al., 1999; Reiss et al., 2018). However, the results in this chapter indicate that post-synaptic Aβ pathology is not enough to impair synaptic responses and therefore suggests that disruption of the ATN to RSC pathway may not mediate cognitive deficits in pre-clinical and prodromal AD. This is supported by our recent findings that chemogenetic activation of the ATN does not improve behavioural deficits in J20 mice at 6m or 9m of age (Kohli et al., 2021).

RSC afferent disruption may still be involved in cognitive impairment in AD, but other pathways could be affected in the early stages of the disease. One possible candidate is the dSub input, which also has a fairly strong excitatory influence on the RSC (**Section 3.3.3**). The dSub also contains HD cells (Taube, 1998), and sends information on speed, trajectory and place to the RSC (Kitanishi et al., 2021). Moreover, not only does the dSub contain plaques at similar age-points to the RSC in J20 mice (Whitesell et al., 2019), lesioning this region reduces the spread of Aβ pathology into the RSC (George et al., 2014). Finally, the RSC receives input from many brain regions, but it also sends efferents to widely distributed brain regions. Therefore, as the RSC is one of the first regions to show Aβ pathology, perhaps its connectivity dysfunction lies in its efferent outputs. Spatial navigation and HD signals could still be affected in this model of dysfunction. Despite the hierarchical model of HD propagation, lesions of the RSC impair accurate HD cell orientation in the ATN (Clark et al., 2010). While top-down feedback from the RSC to the ATN appears weak (van der Goes et al., 2022), the excitatory projection from the RSC to the dorsal thalamic reticular nucleus initiates feedforward inhibition of the ATN (Vantomme et al., 2020); thereby completing the circuit.

4.4.5 | Sexual dimorphism of EPSC onset

Sexual dimorphism has been observed in a variety of synaptic and intrinsic neuronal properties across the brain. Synaptic density is higher in females than males in a variety of areas including the cortex and hippocampus, and there are differences in glutamatergic subunit distribution between the sexes (see Uhl et al., 2022 for review). Application of the sex hormone estradiol has been shown to potentiate miniature EPSC frequency and amplitude in the hippocampus (Oberlander and Woolley, 2016), and both presynaptic and postsynaptic mechanisms have been suggested.

There is little to no literature examining the effect of sex on EPSC properties following stimulation of long-range projections, however some studies have found that inhibiting estradiol synthesis almost abolishes LTP in the amygdala and HPC of female – but not male – mice (Bender et al., 2017; Vierk et al., 2012). Therefore, sex hormone signalling may play a role in the regulation of synaptic

transmission in the RSC. Furthermore, ACC-projecting cells in the claustrum show sex differences in their intrinsic properties (Chia et al., 2017). Thus, the effect of sex on EPSC onset time found here could be determined by postsynaptic factors present on RSC PCs, or by the properties of the presynaptic projection neurons. Sex had no effect on any other measures of synaptic response, including EPSC magnitude and measure of long and short term plasticity. Consequently, the importance of this sexually dimorphic effect on onset time is debatable.

Interestingly, sex was included as a fixed effect in the analysis of synaptic response as females are known to present with a higher Aβ burden (Yang et al., 2018) in some models of AD, and the effects of AD on the electrophysiological properties of neurons can be modulated by sex (Arsenault et al., 2020). However, in the experiments in this chapter, age and genotype were poor predictors of variability across the different synaptic response measures even when sex was included in the model. Furthermore, preliminary analysis of area covered by Aβ plaques and Fos expression in the RSC indicated no significant effects of sex. Therefore, no sexual dimorphic interactions with Aβ pathology were found in J20 mice.

4.4.6 | Conclusions

While the RSC displays Aβ pathology in the early stages of AD progression humans and contemporaneously with EC and HPC in the J20 mouse, this pathological marker is not associated with altered basal neuronal activity or disruption in synaptic response to stimulation of ATN to RSC excitatory projections. Therefore, while the RSC may still be a site of covert pathology in prodromal AD, the ATN to RSC pathway likely does not mediate other neuropathological or cognitive deficits in this mouse model of AD.

5 | Discussion and conclusions

5.1 | Summary of key findings

The work presented in this thesis addressed several hypotheses, proposed in **Section 1.1.4**:

1. Afferent projections to the gRSC and dRSC differ in synaptic strength and specificity.
2. RSC basal neuronal activity is altered in a mouse model of prodromal AD.
3. Synaptic responses will be disrupted in the ATN to RSC pathway in a mouse model of AD.

The work in **Chapter 3** addressed the first hypothesis. The results showed differences in the neuroanatomical targeting and synaptic responses evoked by afferent projections from the ACC, dSub and ATN to different subdivisions of the RSC.

- Neuroanatomical tracing revealed that afferent fibres from the ACC preferentially targeted the dRSC, whilst fibres from the dSub and ATN were almost exclusively found in the gRSC.
- Synaptic connectivity also differed between projections from the ACC, dSub and ATN. The probability of observing a synaptic response in RSC differed between the presynaptic regions: fewer than ½ of RSC PCs responded to ACC input, whilst around ¾ of PCs responded to dSub input and an ATN-evoked synaptic response was observed in all PCs. Synaptic strength also differed between the afferent projections: EPSCs evoked by stimulation of the ATN projection were significantly larger than those from the other presynaptic regions.
- Sub-region and laminar differences were also found for synaptic responses. ACC response probability was lowest in the gRSC superficial layers, but synaptic strength did not differ. Conversely, probability of synaptic response did not differ between sub-region and layers for dSub and ATN input, but synaptic strength was higher in the dRSC for both projections. Finally, while the ratio of AMPA to NMDA receptor-evoked synaptic currents did not differ between presynaptic regions or within the RSC, average PPR indicated significant PPD in all the afferent pathways, and PPD was larger in the dRSC and superficial layers for dSub and ATN input.

The work in **Chapter 4** investigated the second and third hypotheses. The results revealed that while Aβ pathology was present in the RSC in J20 mice, there was no change in the basal activity of RSC neurons or in the properties of synaptic responses evoked by the ATN to RSC projection.

- In J20 Tg mice, the RSC displayed Aβ aggregates from 6 months old, and both plaque size and total brain region covered increased with age from 6 to 9 months. This pathological pattern is similar to that seen in the CA1 region of the HPC and the EC in J20 mice; other brain regions known to be disrupted in the early stages of AD (Harris et al., 2010; Ying et al., 2022).
- While these areas exhibited significant increases in Aβ plaque deposition in J20 mice, this was not associated with amyloidopathy-induced changes to basal neuronal activity. Basal Fos expression decreased with age in the RSC, CA1 and EC in both WT and J20 mice, with no significant effect of J20 genotype.
- Synaptic responses in RSC PCs following stimulation of ATN afferents were not altered by age or J20 genotype. No effect of these variables was observed on EPSC magnitude, onset time, 20-80% rise time, NMDA/AMPA ratio or PPR. However, the physiological properties of ATN synaptic responses reported in **Chapter 3** were corroborated and expanded upon by experiments performed in **Chapter 4**. Specifically, EPSC magnitude and PPR were found to be significantly different between the RSC sub-regions and between superficial and deep cortical layers. EPSC magnitude remained larger in dRSC PCs than those in the gRSC, but was also significantly larger in neurons in the superficial layers. Moreover, PPD was observed in all RSC PCs, and the depressive effect of paired pulse stimulation was greater in the dRSC and in superficial cells.

5.2 | Anatomical connectivity is not a good predictor of functional connectivity in the RSC

The work presented in **Chapter 3** added to our understanding of the physiology of the RSC. The results corroborated previously described RSC PC heterogeneity (Brennan et al., 2020; Yousuf et al., 2020), and provided a

quantitative analysis of the anatomical distribution of afferent fibres across different sub-regions and laminae of the RSC (Groen and Wyss, 2003, 1992, 1990; van Groen et al., 1993; Wyss and Van Groen, 1992). Furthermore, the results replicate the finding that the ACC, dSub and ATN projections to the gRSC are excitatory (Brennan et al., 2021; Yamawaki et al., 2019b, 2019a). However, the intrinsic properties and synaptic responses of PCs in the RSC had previously only been explored in the gRSC, and only in a few recent studies. The work presented in this thesis investigated both the gRSC and dRSC, and improved our knowledge of the area by describing the connectivity differences between the two sub-regions, as well as comparing structural and functional connectivity to the RSC.

Interestingly, while both the neuroanatomical tracing and synaptic response results found differences between the gRSC and dRSC for each presynaptic region, neuroanatomical connectivity was not always associated with functional connectivity. The anatomical input from ACC was most sparse in the gRSC, which corresponded with pyramidal cells in the gRSC superficial layers displaying the lowest input probability. However, projections from the ATN and dSub showed higher fibre density and thus presumable higher anatomical connectivity with the gRSC. While input probabilities did not differ between sub-regions for either projection, stimulation of both the dSub and ATN pathways evoked larger synaptic responses in the dRSC rather than the gRSC. This demonstrates that both the dSub and ATN send strong excitatory input to the dRSC, despite a disparity in physical fibres present, and could suggest a route by which spatial information is relayed to the dRSC. Like the gRSC, the dRSC contains a variety of spatially-tuned cells, including place cells (Mao et al., 2017) and HD cells (Chen et al., 1994b), and regions such as the dSub and ATN are thought to convey the information required to form these representations to the RSC (Albo et al., 2003; Jankowski et al., 2013; Kitanishi et al., 2021). Many of these spatially-tuned neurons have been recorded in the dRSC however, providing a challenge to understand how this area received the necessary input when anatomical inputs appeared so sparse. The present results show that despite the paucity of observable structural connectivity, the dRSC receives substantial monosynaptic functional input that is likely sufficient to elicit firing in RSC pyramidal cells and thus encode spatial representations.

The anatomical tracing results also revealed significant differences in structural connectivity between different cortical layers for all inputs, but no differences in synaptic strength were seen between neurons in superficial and deep layers. Thus, our findings suggest that, at least within the RSC, it is not appropriate to equate projection density with connection strength. While one could presume that dendritic filtering of APs could result in attenuated somatic EPSC magnitude in deep PCs due to presynaptic inputs arriving in superficial layers, their apical dendrites extend to the superficial layers which contain the highest density of fibres. Furthermore, density of afferent terminals from different projections has also been shown not to predict synaptic connectivity. Research in the cat visual cortex showed that thalamocortical projections to layer 4 exhibited a sparse distribution of excitatory synapses compared to other pathways, even though these projections generate the largest synaptic response in layer 4 cells (da Costa and Martin, 2011). Similarly, thalamocortical projections to the rat sensory cortex are significantly stronger than corticocortical connections despite the latter pathway having tenfold more synaptic connections (Schoonover et al., 2014). Specifically in the RSC, anatomical colocalisation of ATN afferent fibres and dRSC L5 PC dendrites was not found to be an accurate predictor of synaptic connection (Lafourcade et al., 2022). A variety of mechanisms could underlie conflicting neuroanatomical and functional connectivity data such as the distribution of postsynaptic receptor subtypes (Pasquale and Sherman, 2011), proximity of synapses to postsynaptic cell soma (Richardson et al., 2009), convergence of inputs (Schoonover et al., 2014) and synchronicity of afferent innervation (da Costa and Martin, 2011).

Targeting of specific cell-types may also explain the discrepancy in the anatomical and synaptic results presented in **Chapter 3**. Synaptic responses were only recorded in putative PCs; however, there is evidence that some RSC afferent pathways – such as the GABAergic input from the medial septum – predominantly target INs (Unal et al., 2015). Feed-forward excitation (or inhibition) of INs is important as these cells directly inhibit neighbouring PCs (Shao and Burkhalter, 1996), thus potentially generating a net regional inhibitory effect from a glutamatergic long-range projection. Activation of different subtypes of INs can have different effects on local circuitry depending on their downstream targets (see Feldmeyer et al., 2018). Therefore, despite tremendous complexity,

understanding the properties of long-range afferent inputs onto different classes of RSC INs will be an important task, as the ability of circuits to inhibit or excite a downstream region is critical for behavioural flexibility; for example, ventral HPC regulation of the PFC promotes either approach or avoidance behaviours (Sánchez-Bellot et al., 2022). Furthermore, INs play a crucial role in generating and maintaining rhythmic patterns of neural activity, termed neuronal oscillations, which facilitate mechanisms of learning and memory such as synaptic plasticity and temporal coding (Buzsáki and Draguhn, 2004).

5.3 | Limitations of mouse models of Alzheimer's disease

While there are some non-invasive techniques available to study AD in humans, murine models of AD that express human transgenes containing EOFAD mutations enable investigation of the neuropathology and neurophysiology of this disease at cellular and synaptic resolution. While these models have provided an invaluable tool to AD researchers hoping to better understand how neuronal circuitry and cognition are affected in the disease, they are not without their limitations.

Transgenic models, such as the J20 mouse, are better considered models of a specific pathology rather than of AD. Various models exhibit amyloidopathy, tauopathy or neurodegeneration, but typically these are not expressed together (Jankowsky and Zheng, 2017). While different lines can be crossed to combine pathologies, a full recapitulation of human AD is still not possible. Moreover, the EOFAD-associated transgenes commonly expressed often lead to overexpression of the pathology and is not representative of the slow progression of LOAD (Sasaguri et al., 2017). Additionally, while APP models allow us to investigate the effects of chronic Aβ exposure and aggregation, the issue of potential developmental compensation is present in most transgenic lines. In the J20 model for example, the $APP_{Sw,Ind}$ transgene is driven by the PDGF promoter, and expression is observed from embryonic day 15 (Sasahara et al., 1991). The effects of developmental overexpression of APP are not well documented; however it is likely they will have significant effects on synaptic function, and as the brain matures compensatory mechanisms may be acquired which attenuate or mask subtler Aβ exposure effects. Some research has begun to use a mature-

onset alternative model which utilises the Tet-Off system to allow precise timing of APP expression onset (Jankowsky et al., 2005), and deficits in spatial working memory and HPC synaptic function have been characterised in these mice (Sri et al., 2019). However, while this model can avoid developmental overexpression problems it is not without caveats of its own: the effects of chronic doxycycline administration during development are currently unknown, and the anti-inflammatory properties of doxycycline have also led to it being proposed as a therapeutic option in AD treatment (Balducci and Forloni, 2019). Therefore, the mechanism by which amyloidopathy is suppressed – doxycycline administration – may fundamentally alter the model and also affect findings.

However, while murine models of AD do have many shortcomings, they are still an invaluable tool for understanding the pathogenesis of AD. Of particular importance to the experiments in this thesis is the need to investigate the neural circuitry involved in learning and memory, and murine models provide one of the best experimental options to tackle this research. While the use of cell cultures to study neural diseases is a useful tool, there are limitations which make them unsuitable for these experiments such as the fact they do not develop in their natural neuronal networks and are deprived of most physiological afferent and efferent projections (Falkenburger and Schulz, 2006). While brain-like structures have been cultivated *in vitro*, there is still significant difficulty in replicating specific brain regions such as the HPC and certain cortical layers (D'Avanzo et al., 2015). Furthermore, while other animal models such as drosophila can be used to investigate a range of brain diseases (Jeibmann and Paulus, 2009), these models often lack neural constructs directly analogous to our regions of interest in the human brain such as the thalamus and the retrosplenial cortex.

5.4 | The role of the RSC in Alzheimer's disease

The work presented in **Chapter 4** revealed that the RSC is a main site of Aβ plaque deposition in J20 mice, with Aβ pathology developing at a similar rate to other brain areas associated with prodromal AD, such as the HPC. The gRSC and dRSC did not show any differences in Aβ pathology, suggesting the two sub-regions exhibit similar pathogenesis. However, while Aβ aggregates were present from 6 months of age, the amount of soluble Aβ oligomers present was not

measured so it is unknown if soluble Aβ was present at 3 months in the RSC. However, microdialysis in the HPC has shown the presence of diffusible Aβ peptides in J20 mice from 3 months of age (Hong et al., 2011), therefore it is likely it is also present in the RSC at that age.

Although the RSC presented with Aβ pathology, there was no evidence of disruption to basal neuronal activity or synaptic responses in the ATN projection to the RSC. Previous literature has associated amyloidopathy with decreased Fos expression in the RSC and HPC, though those findings were following exposure to a novel environment (Christensen et al., 2013; Poirier et al., 2011). Therefore, whilst RSC basal neuronal activity was not altered in J20 mice in this study, behaviourally-induced neuronal activity – like that evoked by exposure to a novel environment – may still be a target for further research in this model. For example, β-bursting in the RSC has been suggested as a neurophysiological correlate of novelty, and has been shown to be disrupted in J20 mice (Walsh et al., 2022).

It was also hypothesised that synaptic input from the ATN would be disrupted in the RSC due to the synaptotoxic effects of soluble Aβ (Mucke and Selkoe, 2012), but no changes to any of the measures of synaptic response were observed in J20 mice. This pathway was chosen for investigation as it shows strong and reliable input to the RSC (**Section 3.3.3**), and lesioning of the ATN is known to disrupt cellular activity and synaptic plasticity in the RSC (Garden et al., 2009; Jenkins et al., 2004). The RSC has been suggested as a site of covert pathology in AD – defined as seemingly intact cytoarchitecture combined with functional abnormality –due to its vulnerability to deafferentation (Vann et al., 2009). However, the results presented in **Chapter 4** revealed no effects of amyloidopathy on ATN-to-RSC synaptic responses that could indicate deafferentation of this pathway. However, although the results of this study show that the presence of Aβ pathology in the RSC is not sufficient to disrupt post-synaptic responses, it remains possible that the RSC is a site of covert pathology in AD.

Unlike tauopathy models, models of amyloidopathy do not show significant neuronal atrophy (Jankowsky and Zheng, 2017). Therefore, the RSC may be susceptible to dysfunction in human AD following the physical loss of projection

neurons in presynaptic regions. Moreover, while direct synaptic response to stimulation of afferent terminals was not affected, the ability of the pathway to effectively process information could be compromised. Synaptic plasticity is critical for storing information in the brain, and altered synaptic plasticity has been found in many murine amyloidopathy models (Mango et al., 2019). While no effect of amyloidopathy was found on NMDA/AMPA ratios in **Chapter 4**, a previous study indicated that the disrupted plasticity observed of RSC synapses following ATN lesion is not associated with changes to NMDA/AMPA ratio (Garden et al., 2009). Changes to EPSC/IPSC ratios were instead proposed as the mechanism of effect, and as IPSCs were not recorded in the present experiments, this cannot be ruled out.

Another important factor in neuronal communication is neural coding: simply put, the ability of neurons to convey and process distinct information through specific patterns of activity (Johnson, 2000). At a single-cell level this includes firing rate, the temporal structure of spiking, and integration of inputs from multiple sources (Azarfar et al., 2018). Population coding requires coordinated activity of ensembles of neurons, and is impacted by network oscillatory activity in the brain (Panzeri et al., 2015). As neural coding necessitates temporally precise spiking, disruptions to the timing of neuronal activity could have substantial negative effects, especially in the RSC as it is responsible for integrating a large amount of information from multiple regions. While the present work found no evidence that the strength of the ATN to RSC pathway is affected by Aβ pathology, changes to its *in vivo* activity could disrupt behaviour and cognition. For example, thalamocortical input is reduced 1-2 seconds before hippocampal SWR events in the RSC to promote SWR-induced plasticity (Chambers et al., 2022). This brief reduction in activity “silences” PCs in the region to strengthen the comparatively weak memory-related hippocampal excitation, and failure of silencing could prevent transfer of information from the HPC. Conversely, anticipatory activity in ATN HD cells can improve speed-encoding in the RSC (Brennan et al., 2021). Inputs from other presynaptic regions also have modulatory effects on plasticity in the RSC: afferent projections from the dSub can prime PCs in the gRSC and enhance their spiking and synaptic response for a short period (Gao et al., 2021). Therefore, subtle changes to RSC afferent inputs in AD could have significant effects on cognition and warrants further investigation.

5.5 | Future directions

The work presented in this thesis has provided new insight into the RSC, including its connectivity and potential role in AD. The findings have also raised questions to be addressed in future research.

- The results show that the strength and specificity of afferent projections to RSC PCs differs dependent on presynaptic region, however there is still much we don't know about RSC circuitry. Firstly, in order to understand the influence afferent projections have on the RSC, synaptic response to long-range presynaptic inputs should be recorded in INs. Long-range excitation of INs could modulate a range of factors in the RSC including altering the gain, timing, tuning and bursting properties of PCs (Roux and Buzsáki, 2015). IN activity is also crucial to neural information processing through the generation and maintenance of neural oscillations (Buzsáki and Draguhn, 2004), and amyloidogenic mice display IN loss and dysfunction as well as impaired gamma oscillations (Pelkey et al., 2017). In addition to describing RSC afferent projections, it is imperative that we also consider its efferent projections. As well as receiving large amounts of information, the RSC also conveys information back to regions such as the ATN and dSub which could be important for updating spatial representations. In fact, lesioning of the RSC disrupts HD cells in the ATN (Clark et al., 2010). Therefore, measuring the synaptic strength and specificity of RSC efferents is also a prime candidate for future research.
- The RSC is considered an integrative hub, combining multiple information streams as part of a gain-field circuit (Bicanski and Burgess, 2018). Regions such as the ATN and dSub have distinct patterns of input in the RSC, however it is unknown if individual PCs receive stronger input from one pathway over another, or if PCs with the highest ATN synaptic response also receive the strongest dSub input. Future studies should combine optogenetic stimulation tools with disparate excitation wavelengths to examine whether a sub-population of PCs act as the conduit for the gain-field circuit. A subset of hyperexcitable PCs in the RSC – able to maintain sustained high-frequency spiking – have already been

proposed to be uniquely suited to processing sustained input and encoding information with high fidelity (Brennan et al., 2020).

- While the RSC displays Aβ pathology in early stages of AD, this work found no association between Aβ pathology and basal neuronal activity or synaptic response to ATN input. However, further exploration of this brain region during AD progression should be undertaken. In mice, disruption to neuronal activity has been reported in this area following exposure to a novel environment (Clark et al., 2010; Poirier et al., 2011), therefore examining Fos expression following tasks known to be affected in models of amyloidopathy, such as spatial navigation, should be undertaken to better understand the potential contribution of the RSC to cognitive deficits. Moreover, the RSC is one of the first areas to show hypometabolism in MCI patients (Desgranges et al., 2002), as well as disrupted functional connectivity (Dillen et al., 2017). Therefore, the evidence points to RSC disruption playing a key role in prodromal AD. Investigation of whether the RSC exhibits altered synaptic plasticity or disrupted encoding of spatial and non-spatial information are prime candidates for research into its function and connectivity. Both longitudinal *in vivo* electrophysiology and two-photon calcium imaging techniques would be suitable for exploring RSC activity during behaviour in order to correlate any neuronal dysfunction with cognitive decline over time.

5.6 | Final conclusions

Overall, the experiments presented in this thesis significantly contribute to our understanding of the RSC, its connectivity and its role in AD. This work has identified a fundamental disparity between anatomical and functional connectivity in the RSC, and has identified PCs in the dRSC as primary recipients of input from the ATN and dSub. Furthermore, work undertaken in a mouse model of AD has suggested that disruption to the RSC may be subtle and behaviourally-linked, as no effects on basal neuronal activity or synaptic response were found. In conclusion, this thesis has not only proposed and answered important research questions surrounding the RSC, but also provides a framework from which future research can investigate this under-researched brain region.

References

Aggleton, J.P., Brown, M.W., 1999. Episodic memory, amnesia, and the hippocampal–anterior thalamic axis. Behav. Brain Sci. 22, 425–444. https://doi.org/10.1017/S0140525X99002034

Aggleton, J.P., Dumont, J.R., Warburton, E.C., 2011. Unraveling the contributions of the diencephalon to recognition memory: A review. Learn. Mem. 18, 384–400. https://doi.org/10.1101/lm.1884611

Aggleton, J.P., Nelson, A.J.D., 2015. Why do lesions in the rodent anterior thalamic nuclei cause such severe spatial deficits? Neurosci. Biobehav. Rev., The Cognitive Thalamus 54, 131–144. https://doi.org/10.1016/j.neubiorev.2014.08.013

Aggleton, J.P., Nelson, A.J.D., O'Mara, S.M., 2022. Time to retire the serial Papez circuit: Implications for space, memory, and attention. Neurosci. Biobehav. Rev. 140, 104813. https://doi.org/10.1016/j.neubiorev.2022.104813

Aggleton, J.P., O'Mara, S.M., 2022. The anterior thalamic nuclei: core components of a tripartite episodic memory system. Nat. Rev. Neurosci. 1–12. https://doi.org/10.1038/s41583-022-00591-8

Aggleton, J.P., Pralus, A., Nelson, A.J.D., Hornberger, M., 2016. Thalamic pathology and memory loss in early Alzheimer's disease: moving the focus from the medial temporal lobe to Papez circuit. Brain 139, 1877–1890. https://doi.org/10.1093/brain/aww083

Aggleton, J.P., Yanakieva, S., Sengpiel, F., Nelson, A.J., 2021. The separate and combined properties of the granular (area 29) and dysgranular (area 30) retrosplenial cortex. Neurobiol. Learn. Mem. 185, 107516. https://doi.org/10.1016/j.nlm.2021.107516

Aho, K., Derryberry, D., Peterson, T., 2014. Model selection for ecologists: the worldviews of AIC and BIC. Ecology 95, 631–636. https://doi.org/10.1890/13-1452.1

Albasser, M.M., Poirier, G.L., Warburton, E.C., Aggleton, J.P., 2007. Hippocampal lesions halve immediate–early gene protein counts in retrosplenial cortex: distal dysfunctions in a spatial memory system. Eur. J. Neurosci. 26, 1254–1266. https://doi.org/10.1111/j.1460-9568.2007.05753.x

Albo, Z., Viana Di Prisco, G., Vertes, R.P., 2003. Anterior thalamic unit discharge profiles and coherence with hippocampal theta rhythm. Thalamus Relat. Syst. 2, 133–144. https://doi.org/10.1016/S1472-9288(03)00006-2

Alexander, A.S., Carstensen, L.C., Hinman, J.R., Raudies, F., Chapman, G.W., Hasselmo, M.E., 2020. Egocentric boundary vector tuning of the retrosplenial cortex. Sci. Adv. 6, eaaz2322. https://doi.org/10.1126/sciadv.aaz2322

ALZFORUM, 2022. Mutations [WWW Document]. URL https://www.alzforum.org/mutations (accessed 9.12.22).

Ameen-Ali, K.E., Simpson, J.E., Wharton, S.B., Heath, P.R., Sharp, P.S., Brezzo, G., Berwick, J., 2019. The Time Course of Recognition Memory Impairment and Glial Pathology in the hAPP-J20 Mouse Model of Alzheimer's Disease. J. Alzheimers Dis. JAD 68, 609–624. https://doi.org/10.3233/JAD-181238

Andersen, J.V., Markussen, K.H., Jakobsen, E., Schousboe, A., Waagepetersen, H.S., Rosenberg, P.A., Aldana, B.I., 2021. Glutamate metabolism and recycling at the excitatory synapse in health and neurodegeneration. Neuropharmacology 196, 108719. https://doi.org/10.1016/j.neuropharm.2021.108719

Andorfer, C., Kress, Y., Espinoza, M., de Silva, R., Tucker, K.L., Barde, Y.-A., Duff, K., Davies, P., 2003. Hyperphosphorylation and aggregation of tau in mice expressing normal human tau isoforms. J. Neurochem. 86, 582–590. https://doi.org/10.1046/j.1471-4159.2003.01879.x

Anzalone, S., Roland, J., Vogt, B., Savage, L., 2009. Acetylcholine Efflux from Retrosplenial Areas and Hippocampal Sectors During Maze Exploration. Behav. Brain Res. 201, 272–278. https://doi.org/10.1016/j.bbr.2009.02.023

Arbel-Ornath, M., Hudry, E., Boivin, J.R., Hashimoto, T., Takeda, S., Kuchibhotla, K.V., Hou, S., Lattarulo, C.R., Belcher, A.M., Shakerdge, N., Trujillo, P.B., Muzikansky, A., Betensky, R.A., Hyman, B.T., Bacskai, B.J., 2017. Soluble oligomeric amyloid-β induces calcium dyshomeostasis that precedes synapse loss in the living mouse brain. Mol. Neurodegener. 12, 27. https://doi.org/10.1186/s13024-017-0169-9

Arsenault, D., Tremblay, C., Emond, V., Calon, F., 2020. Sex-dependent alterations in the physiology of entorhinal cortex neurons in old heterozygous

3xTg-AD mice. Biol. Sex Differ. 11, 63. https://doi.org/10.1186/s13293-020-00337-0

Auger, S.D., Mullally, S.L., Maguire, E.A., 2012. Retrosplenial Cortex Codes for Permanent Landmarks. PLOS ONE 7, e43620. https://doi.org/10.1371/journal.pone.0043620

Auger, S.D., Zeidman, P., Maguire, E.A., 2017. Efficacy of navigation may be influenced by retrosplenial cortex-mediated learning of landmark stability. Neuropsychologia 104, 102–112. https://doi.org/10.1016/j.neuropsychologia.2017.08.012

Azarfar, A., Calcini, N., Huang, C., Zeldenrust, F., Celikel, T., 2018. Neural coding: A single neuron's perspective. Neurosci. Biobehav. Rev. 94, 238–247. https://doi.org/10.1016/j.neubiorev.2018.09.007

Balducci, C., Forloni, G., 2019. Doxycycline for Alzheimer's Disease: Fighting β-Amyloid Oligomers and Neuroinflammation. Front. Pharmacol. 10.

Barnett, S.C., Perry, B. a. L., Dalrymple-Alford, J.C., Parr-Brownlie, L.C., 2018. Optogenetic stimulation: Understanding memory and treating deficits. Hippocampus 28, 457–470. https://doi.org/10.1002/hipo.22960

Barros, A.C.B. de, Baruchin, L.J., Panayi, M.C., Nyberg, N., Samborska, V., Mealing, M.T., Akam, T., Kwag, J., Bannerman, D.M., Kohl, M.M., 2021. Retrosplenial cortex is necessary for spatial and non-spatial latent learning in mice. https://doi.org/10.1101/2021.07.21.453258

Barry, C., Heys, J., Hasselmo, M., 2012. Possible role of acetylcholine in regulating spatial novelty effects on theta rhythm and grid cells. Front. Neural Circuits 6.

Battaglia, F., Wang, H.-Y., Ghilardi, M.F., Gashi, E., Quartarone, A., Friedman, E., Nixon, R.A., 2007. Cortical Plasticity in Alzheimer's Disease in Humans and Rodents. Biol. Psychiatry, Neurodegenerative Disorders: Early Phenotypes, Neuroplasticity, and Progression 62, 1405–1412. https://doi.org/10.1016/j.biopsych.2007.02.027

Baudry, M., Zhu, G., Liu, Y., Wang, Y., Briz, V., Bi, X., 2015. Multiple cellular cascades participate in long-term potentiation and in hippocampus-dependent learning. Brain Res. 1621, 73–81. https://doi.org/10.1016/j.brainres.2014.11.033

Baumann, O., Mattingley, J.B., 2010. Medial Parietal Cortex Encodes Perceived Heading Direction in Humans. J. Neurosci. 30, 12897–12901. https://doi.org/10.1523/JNEUROSCI.3077-10.2010

Baumgärtel, K., Green, A., Hornberger, D., Lapira, J., Rex, C., Wheeler, D.G., Peters, M., 2018. PDE4D regulates Spine Plasticity and Memory in the Retrosplenial Cortex. Sci. Rep. 8, 3895. https://doi.org/10.1038/s41598-018-22193-0

Bazzari, A.H., Parri, H.R., 2019. Neuromodulators and Long-Term Synaptic Plasticity in Learning and Memory: A Steered-Glutamatergic Perspective. Brain Sci. 9, 300. https://doi.org/10.3390/brainsci9110300

Beggs, J.M., Moyer, J.R., McGann, J.P., Brown, T.H., 2000. Prolonged Synaptic Integration in Perirhinal Cortical Neurons. J. Neurophysiol. 83, 3294–3298. https://doi.org/10.1152/jn.2000.83.6.3294

Bekris, L.M., Yu, C.-E., Bird, T.D., Tsuang, D.W., 2010. Genetics of Alzheimer Disease. J. Geriatr. Psychiatry Neurol. 23, 213–227. https://doi.org/10.1177/0891988710383571

Bender, R.A., Zhou, L., Vierk, R., Brandt, N., Keller, A., Gee, C.E., Schäfer, M.K.E., Rune, G.M., 2017. Sex-Dependent Regulation of Aromatase-Mediated Synaptic Plasticity in the Basolateral Amygdala. J. Neurosci. 37, 1532–1545. https://doi.org/10.1523/JNEUROSCI.1532-16.2016

Benita, J.M., Guillamon, A., Deco, G., Sanchez-Vives, M., 2012. Synaptic depression and slow oscillatory activity in a biophysical network model of the cerebral cortex. Front. Comput. Neurosci. 6.

Ben-Nejma, I.R.H., Keliris, A.J., Daans, J., Ponsaerts, P., Verhoye, M., Van der Linden, A., Keliris, G.A., 2019. Increased soluble amyloid-beta causes early aberrant brain network hypersynchronisation in a mature-onset mouse model of amyloidosis. Acta Neuropathol. Commun. 7, 180. https://doi.org/10.1186/s40478-019-0810-7

Berkowitz, L.E., Harvey, R.E., Clark, B.J., 2020. Head direction cells in the TgF344-AD rat model of Alzheimer's disease. Alzheimers Dement. 16, e037822. https://doi.org/10.1002/alz.037822

Berkowitz, L.E., Harvey, R.E., Drake, E., Thompson, S.M., Clark, B.J., 2018. Progressive impairment of directional and spatially precise trajectories by TgF344-Alzheimer's disease rats in the Morris Water Task. Sci. Rep. 8, 16153. https://doi.org/10.1038/s41598-018-34368-w

Bicanski, A., Burgess, N., 2018. A neural-level model of spatial memory and imagery. eLife 7, e33752. https://doi.org/10.7554/eLife.33752

Bolte, S., Cordelières, F.P., 2006. A guided tour into subcellular colocalization analysis in light microscopy. J. Microsc. 224, 213–232. https://doi.org/10.1111/j.1365-2818.2006.01706.x

Braak, H., Braak, E., 1991a. Neuropathological stageing of Alzheimer-related changes. Acta Neuropathol. (Berl.) 82, 239–259. https://doi.org/10.1007/BF00308809

Braak, H., Braak, E., 1991b. Alzheimer's disease affects limbic nuclei of the thalamus. Acta Neuropathol. (Berl.) 81, 261–268. https://doi.org/10.1007/BF00305867

Brennan, E.K., Jedrasiak-Cape, I., Kailasa, S., Rice, S.P., Sudhakar, S.K., Ahmed, O.J., 2021. Thalamus and claustrum control parallel layer 1 circuits in retrosplenial cortex. eLife 10, e62207. https://doi.org/10.7554/eLife.62207

Brennan, E.K.W., Sudhakar, S.K., Jedrasiak-Cape, I., John, T.T., Ahmed, O.J., 2020. Hyperexcitable Neurons Enable Precise and Persistent Information Encoding in the Superficial Retrosplenial Cortex. Cell Rep. 30, 1598-1612.e8. https://doi.org/10.1016/j.celrep.2019.12.093

Brenowitz, S., Trussell, L.O., 2001. Minimizing synaptic depression by control of release probability. J. Neurosci. Off. J. Soc. Neurosci. 21, 1857–1867.

Buckingham, S.D., Jones, A.K., Brown, L.A., Sattelle, D.B., 2009. Nicotinic Acetylcholine Receptor Signalling: Roles in Alzheimer's Disease and Amyloid Neuroprotection. Pharmacol. Rev. 61, 39–61. https://doi.org/10.1124/pr.108.000562

Buckley, M.J., Mitchell, A.S., 2016. Retrosplenial Cortical Contributions to Anterograde and Retrograde Memory in the Monkey. Cereb. Cortex N. Y. NY 26, 2905–2918. https://doi.org/10.1093/cercor/bhw054

Buckner, R.L., Snyder, A.Z., Shannon, B.J., LaRossa, G., Sachs, R., Fotenos, A.F., Sheline, Y.I., Klunk, W.E., Mathis, C.A., Morris, J.C., Mintun, M.A., 2005. Molecular, Structural, and Functional Characterization of Alzheimer's Disease: Evidence for a Relationship between Default Activity, Amyloid, and Memory. J. Neurosci. 25, 7709–7717. https://doi.org/10.1523/JNEUROSCI.2177-05.2005

Buzsáki, G., 2015. Hippocampal sharp wave-ripple: A cognitive biomarker for episodic memory and planning. Hippocampus 25, 1073–1188. https://doi.org/10.1002/hipo.22488

Buzsáki, G., Draguhn, A., 2004. Neuronal Oscillations in Cortical Networks. Science 304, 1926–1929. https://doi.org/10.1126/science.1099745

Byrne, P., Becker, S., Burgess, N., 2007. Remembering the past and imagining the future. Psychol. Rev. 114, 340–375. https://doi.org/10.1037/0033-295X.114.2.340

Castellano, J.M., Kim, J., Stewart, F.R., Jiang, H., DeMattos, R.B., Patterson, B.W., Fagan, A.M., Morris, J.C., Mawuenyega, K.G., Cruchaga, C., Goate, A.M., Bales, K.R., Paul, S.M., Bateman, R.J., Holtzman, D.M., 2011. Human apoE Isoforms Differentially Regulate Brain Amyloid-β Peptide Clearance. Sci. Transl. Med. 3, 89ra57-89ra57. https://doi.org/10.1126/scitranslmed.3002156

Chagnac-Amitai, Y., Luhmann, H.J., Prince, D.A., 1990. Burst generating and regular spiking layer 5 pyramidal neurons of rat neocortex have different morphological features. J. Comp. Neurol. 296, 598–613. https://doi.org/10.1002/cne.902960407

Chambers, A.R., Berge, C.N., Vervaeke, K., 2022. Cell-type-specific silence in thalamocortical circuits precedes hippocampal sharp-wave ripples. Cell Rep. 40. https://doi.org/10.1016/j.celrep.2022.111132

Chang, Y.-M., Luebke, J.I., 2007. Electrophysiological Diversity of Layer 5 Pyramidal Cells in the Prefrontal Cortex of the Rhesus Monkey: In Vitro Slice Studies. J. Neurophysiol. 98, 2622–2632. https://doi.org/10.1152/jn.00585.2007

Chen, C., Blitz, D.M., Regehr, W.G., 2002. Contributions of receptor desensitization and saturation to plasticity at the retinogeniculate synapse. Neuron 33, 779–788. https://doi.org/10.1016/s0896-6273(02)00611-6

Chen, G., Xu, T., Yan, Y., Zhou, Y., Jiang, Y., Melcher, K., Xu, H.E., 2017. Amyloid beta: structure, biology and structure-based therapeutic development. Acta Pharmacol. Sin. 38, 1205–1235. https://doi.org/10.1038/aps.2017.28

Chen, L.L., Lin, L.H., Barnes, C.A., McNaughton, B.L., 1994a. Head-direction cells in the rat posterior cortex. II. Contributions of visual and ideothetic information to the directional firing. Exp. Brain Res. 101, 24–34. https://doi.org/10.1007/bf00243213

Chen, L.L., Lin, L.-H., Green, E.J., Barnes, C.A., McNaughton, B.L., 1994b. Head-direction cells in the rat posterior cortex. Exp. Brain Res. 101, 8–23. https://doi.org/10.1007/BF00243212

Cheng, I.H., Scearce-Levie, K., Legleiter, J., Palop, J.J., Gerstein, H., Bien-Ly, N., Puolivaöli, J., Lesné, S., Ashe, K.H., Muchowski, P.J., Mucke, L., 2007. Accelerating Amyloid-β Fibrillization Reduces Oligomer Levels and Functional Deficits in Alzheimer Disease Mouse Models*. J. Biol. Chem. 282, 23818–23828. https://doi.org/10.1074/jbc.M701078200

Chetelat, G., Baron, J.-C., 2003. Early diagnosis of Alzheimer's disease: contribution of structural neuroimaging. NeuroImage 18, 525–541. https://doi.org/10.1016/s1053-8119(02)00026-5

Chia, Z., Silberberg, G., Augustine, G.J., 2017. Functional properties, topological organization and sexual dimorphism of claustrum neurons projecting to anterior cingulate cortex. Claustrum 2, 1357412. https://doi.org/10.1080/20023294.2017.1357412

Cho, J., Sharp, P.E., 2001. Head direction, place, and movement correlates for cells in the rat retrosplenial cortex. Behav. Neurosci. 115, 3–25. https://doi.org/10.1037/0735-7044.115.1.3

Chow, V.W., Mattson, M.P., Wong, P.C., Gleichmann, M., 2010. An Overview of APP Processing Enzymes and Products. Neuromolecular Med. 12, 1–12. https://doi.org/10.1007/s12017-009-8104-z

Chrastil, E.R., 2018. Heterogeneity in human retrosplenial cortex: A review of function and connectivity. Behav. Neurosci. 132, 317–338. https://doi.org/10.1037/bne0000261

Chrastil, E.R., Sherrill, K.R., Hasselmo, M.E., Stern, C.E., 2015. There and Back Again: Hippocampus and Retrosplenial Cortex Track Homing Distance during Human Path Integration. J. Neurosci. Off. J. Soc. Neurosci. 35, 15442–15452. https://doi.org/10.1523/JNEUROSCI.1209-15.2015

Christensen, D.Z., Thomsen, M.S., Mikkelsen, J.D., 2013. Reduced basal and novelty-induced levels of activity-regulated cytoskeleton associated protein (Arc) and c-Fos mRNA in the cerebral cortex and hippocampus of APPswe/PS1ΔE9 transgenic mice. Neurochem. Int. 63, 54–60. https://doi.org/10.1016/j.neuint.2013.04.002

Christenson Wick, Z., Tetzlaff, M.R., Krook-Magnuson, E., 2019. Novel long-range inhibitory nNOS-expressing hippocampal cells. eLife 8, e46816. https://doi.org/10.7554/eLife.46816

Chung, L., 2015. A Brief Introduction to the Transduction of Neural Activity into Fos Signal. Dev. Reprod. 19, 61–67. https://doi.org/10.12717/DR.2015.19.2.061

Citri, A., Malenka, R.C., 2008. Synaptic Plasticity: Multiple Forms, Functions, and Mechanisms. Neuropsychopharmacology 33, 18–41. https://doi.org/10.1038/sj.npp.1301559

Citron, M., Oltersdorf, T., Haass, C., McConlogue, L., Hung, A.Y., Seubert, P., Vigo-Pelfrey, C., Lieberburg, I., Selkoe, D.J., 1992. Mutation of the beta-amyloid precursor protein in familial Alzheimer's disease increases beta-protein production. Nature 360, 672–674. https://doi.org/10.1038/360672a0

Clark, B.J., Bassett, J.P., Wang, S.S., Taube, J.S., 2010. Impaired Head Direction Cell Representation in the Anterodorsal Thalamus after Lesions of the Retrosplenial Cortex. J. Neurosci. 30, 5289–5302. https://doi.org/10.1523/JNEUROSCI.3380-09.2010

Cleary, J.P., Walsh, D.M., Hofmeister, J.J., Shankar, G.M., Kuskowski, M.A., Selkoe, D.J., Ashe, K.H., 2005. Natural oligomers of the amyloid-β protein

specifically disrupt cognitive function. Nat. Neurosci. 8, 79–84. https://doi.org/10.1038/nn1372

Collingridge, G.L., Kehl, S.J., McLennan, H., 1983. Excitatory amino acids in synaptic transmission in the Schaffer collateral-commissural pathway of the rat hippocampus. J. Physiol. 334, 33–46. https://doi.org/10.1113/jphysiol.1983.sp014478

Collingridge, G.L., Peineau, S., Howland, J.G., Wang, Y.T., 2010. Long-term depression in the CNS. Nat. Rev. Neurosci. 11, 459–473. https://doi.org/10.1038/nrn2867

Connors, B.W., Gutnick, M.J., 1990. Intrinsic firing patterns of diverse neocortical neurons. Trends Neurosci. 13, 99–104. https://doi.org/10.1016/0166-2236(90)90185-d

Cooper, B.G., Manka, T.F., Mizumori, S.J.Y., 2001. Finding your way in the dark: The retrosplenial cortex contributes to spatial memory and navigation without visual cues. Behav. Neurosci. 115, 1012–1028. https://doi.org/10.1037/0735-7044.115.5.1012

Cooper, B.G., Mizumori, S.J.Y., 2001. Temporary Inactivation of the Retrosplenial Cortex Causes a Transient Reorganization of Spatial Coding in the Hippocampus. J. Neurosci. 21, 3986–4001. https://doi.org/10.1523/JNEUROSCI.21-11-03986.2001

Corcoran, K.A., Donnan, M.D., Tronson, N.C., Guzmán, Y.F., Gao, C., Jovasevic, V., Guedea, A.L., Radulovic, J., 2011. NMDA Receptors in Retrosplenial Cortex Are Necessary for Retrieval of Recent and Remote Context Fear Memory. J. Neurosci. 31, 11655–11659. https://doi.org/10.1523/JNEUROSCI.2107-11.2011

Corder, E.H., Saunders, A.M., Strittmatter, W.J., Schmechel, D.E., Gaskell, P.C., Small, G.W., Roses, A.D., Haines, J.L., Pericak-Vance, M.A., 1993. Gene Dose of Apolipoprotein E Type 4 Allele and the Risk of Alzheimer's Disease in Late Onset Families. Science 261, 921–923. https://doi.org/10.1126/science.8346443

Cotman, C.W., Monaghan, D.T., Ottersen, O.P., Storm-Mathisen, J., 1987. Anatomical organization of excitatory amino acid receptors and their pathways. Trends Neurosci. 10, 273–280. https://doi.org/10.1016/0166-2236(87)90172-X

Cowansage, K.K., Shuman, T., Dillingham, B.C., Chang, A., Golshani, P., Mayford, M., 2014. Direct Reactivation of a Coherent Neocortical Memory of Context. Neuron 84, 432–441. https://doi.org/10.1016/j.neuron.2014.09.022

Cull-Candy, S.G., Leszkiewicz, D.N., 2004. Role of distinct NMDA receptor subtypes at central synapses. Sci. STKE Signal Transduct. Knowl. Environ. 2004, re16. https://doi.org/10.1126/stke.2552004re16

Czajkowski, R., Jayaprakash, B., Wiltgen, B., Rogerson, T., Guzman-Karlsson, M.C., Barth, A.L., Trachtenberg, J.T., Silva, A.J., 2014. Encoding and storage of spatial information in the retrosplenial cortex. Proc. Natl. Acad. Sci. 111, 8661–8666. https://doi.org/10.1073/pnas.1313222111

da Costa, N.M., Martin, K.A.C., 2011. How thalamus connects to spiny stellate cells in the cat's visual cortex. J. Neurosci. Off. J. Soc. Neurosci. 31, 2925–2937. https://doi.org/10.1523/JNEUROSCI.5961-10.2011

D'Avanzo, C., Aronson, J., Kim, Y.H., Choi, S.H., Tanzi, R.E., Kim, D.Y., 2015. Alzheimer's in 3D culture: Challenges and perspectives. BioEssays News Rev. Mol. Cell. Dev. Biol. 37, 1139–1148. https://doi.org/10.1002/bies.201500063

Davies, C.A., Mann, D.M., Sumpter, P.Q., Yates, P.O., 1987. A quantitative morphometric analysis of the neuronal and synaptic content of the frontal and temporal cortex in patients with Alzheimer's disease. J. Neurol. Sci. 78, 151–164. https://doi.org/10.1016/0022-510x(87)90057-8

Davis, D.G., Schmitt, F.A., Wekstein, D.R., Markesbery, W.R., 1999. Alzheimer neuropathologic alterations in aged cognitively normal subjects. J. Neuropathol. Exp. Neurol. 58, 376–388. https://doi.org/10.1097/00005072-199904000-00008

de Jong, L.W., van der Hiele, K., Veer, I.M., Houwing, J.J., Westendorp, R.G.J., Bollen, E.L.E.M., de Bruin, P.W., Middelkoop, H. a. M., van Buchem, M.A., van der Grond, J., 2008. Strongly reduced volumes of putamen and thalamus in Alzheimer's disease: an MRI study. Brain J. Neurol. 131, 3277–3285. https://doi.org/10.1093/brain/awn278

de Sousa, A.F., Cowansage, K.K., Zutshi, I., Cardozo, L.M., Yoo, E.J., Leutgeb, S., Mayford, M., 2019. Optogenetic reactivation of memory ensembles in the

retrosplenial cortex induces systems consolidation. Proc. Natl. Acad. Sci. 116, 8576. https://doi.org/10.1073/pnas.1818432116

De Strooper, B., Karran, E., 2016. The Cellular Phase of Alzheimer's Disease. Cell 164, 603–615. https://doi.org/10.1016/j.cell.2015.12.056

Decker, H., Jürgensen, S., Adrover, M.F., Brito-Moreira, J., Bomfim, T.R., Klein, W.L., Epstein, A.L., De Felice, F.G., Jerusalinsky, D., Ferreira, S.T., 2010. N-Methyl-d-aspartate receptors are required for synaptic targeting of Alzheimer's toxic amyloid-β peptide oligomers. J. Neurochem. 115, 1520–1529. https://doi.org/10.1111/j.1471-4159.2010.07058.x

DeKosky, S.T., Scheff, S.W., 1990. Synapse loss in frontal cortex biopsies in Alzheimer's disease: Correlation with cognitive severity. Ann. Neurol. 27, 457–464. https://doi.org/10.1002/ana.410270502

Deng, P.-Y., Klyachko, V.A., 2011. The diverse functions of short-term plasticity components in synaptic computations. Commun. Integr. Biol. 4, 543–548. https://doi.org/10.4161/cib.4.5.15870

Desgranges, B., Baron, J.-C., Lalevée, C., Giffard, B., Viader, F., de la Sayette, V., Eustache, F., 2002. The neural substrates of episodic memory impairment in Alzheimer's disease as revealed by FDG–PET: relationship to degree of deterioration. Brain 125, 1116–1124. https://doi.org/10.1093/brain/awf097

Dillen, K.N.H., Jacobs, H.I.L., Kukolja, J., Richter, N., von Reutern, B., Onur, Ö.A., Langen, K.-J., Fink, G.R., 2017. Functional Disintegration of the Default Mode Network in Prodromal Alzheimer's Disease. J. Alzheimers Dis. 59, 169–187. https://doi.org/10.3233/JAD-161120

Dillen, K.N.H., Jacobs, H.I.L., Kukolja, J., von Reutern, B., Richter, N., Onur, Ö.A., Dronse, J., Langen, K.-J., Fink, G.R., 2016. Aberrant functional connectivity differentiates retrosplenial cortex from posterior cingulate cortex in prodromal Alzheimer's disease. Neurobiol. Aging 44, 114–126. https://doi.org/10.1016/j.neurobiolaging.2016.04.010

Dore, K., Carrico, Z., Alfonso, S., Marino, M., Koymans, K., Kessels, H.W., Malinow, R., 2021. PSD-95 protects synapses from β-amyloid. Cell Rep. 35, 109194. https://doi.org/10.1016/j.celrep.2021.109194

Dougherty, J.J., Wu, J., Nichols, R.A., 2003. Beta-amyloid regulation of presynaptic nicotinic receptors in rat hippocampus and neocortex. J. Neurosci. Off. J. Soc. Neurosci. 23, 6740–6747.

Dudek, S.M., Bear, M.F., 1992. Homosynaptic long-term depression in area CA1 of hippocampus and effects of N-methyl-D-aspartate receptor blockade. Proc. Natl. Acad. Sci. 89, 4363–4367. https://doi.org/10.1073/pnas.89.10.4363

Duyckaerts, C., Delatour, B., Potier, M.-C., 2009. Classification and basic pathology of Alzheimer disease. Acta Neuropathol. (Berl.) 118, 5–36. https://doi.org/10.1007/s00401-009-0532-1

Edison, P., Archer, H.A., Hinz, R., Hammers, A., Pavese, N., Tai, Y.F., Hotton, G., Cutler, D., Fox, N., Kennedy, A., Rossor, M., Brooks, D.J., 2007. Amyloid, hypometabolism, and cognition in Alzheimer disease: An [11C]PIB and [18F]FDG PET study. Neurology 68, 501–508. https://doi.org/10.1212/01.wnl.0000244749.20056.d4

Edler, M.K., Sherwood, C.C., Meindl, R.S., Hopkins, W.D., Ely, J.J., Erwin, J.M., Mufson, E.J., Hof, P.R., Raghanti, M.A., 2017. Aged chimpanzees exhibit pathologic hallmarks of Alzheimer's disease. Neurobiol. Aging 59, 107–120. https://doi.org/10.1016/j.neurobiolaging.2017.07.006

Elder, G.A., Gama Sosa, M.A., De Gasperi, R., 2010. Transgenic Mouse Models of Alzheimer's Disease. Mt. Sinai J. Med. N. Y. 77, 69–81. https://doi.org/10.1002/msj.20159

Elston, G.N., 2003. Cortex, Cognition and the Cell: New Insights into the Pyramidal Neuron and Prefrontal Function. Cereb. Cortex 13, 1124–1138. https://doi.org/10.1093/cercor/bhg093

Espuny-Camacho, I., Arranz, A.M., Fiers, M., Snellinx, A., Ando, K., Munck, S., Bonnefont, J., Lambot, L., Corthout, N., Omodho, L., Vanden Eynden, E., Radaelli, E., Tesseur, I., Wray, S., Ebneth, A., Hardy, J., Leroy, K., Brion, J.-P., Vanderhaeghen, P., De Strooper, B., 2017. Hallmarks of Alzheimer's Disease in Stem-Cell-Derived Human Neurons Transplanted into Mouse Brain. Neuron 93, 1066-1081.e8. https://doi.org/10.1016/j.neuron.2017.02.001

Etter, G., van der Veldt, S., Manseau, F., Zarrinkoub, I., Trillaud-Doppia, E., Williams, S., 2019. Optogenetic gamma stimulation rescues memory impairments in an Alzheimer's disease mouse model. Nat. Commun. 10, 5322. https://doi.org/10.1038/s41467-019-13260-9

Falkenburger, B.H., Schulz, J.B., 2006. Limitations of cellular models in Parkinson's disease research, in: Riederer, P., Reichmann, H., Youdim, M.B.H., Gerlach, M. (Eds.), Parkinson's Disease and Related Disorders, Journal of Neural Transmission. Supplementa. Springer, Vienna, pp. 261–268. https://doi.org/10.1007/978-3-211-45295-0_40

Fan, X., Jin, W.Y., Wang, Y.T., 2014. The NMDA receptor complex: a multifunctional machine at the glutamatergic synapse. Front. Cell. Neurosci. 8.

Feldmeyer, D., Qi, G., Emmenegger, V., Staiger, J.F., 2018. Inhibitory Interneurons and their Circuit Motifs in the Many Layers of the Barrel Cortex. Neuroscience, Barrel Cortex Function 368, 132–151. https://doi.org/10.1016/j.neuroscience.2017.05.027

Field, A., 2013. Discovering Statistics Using IBM SPSS Statistics. SAGE.

Fischer, L.F., Mojica Soto-Albors, R., Buck, F., Harnett, M.T., 2020. Representation of visual landmarks in retrosplenial cortex. eLife 9, e51458. https://doi.org/10.7554/eLife.51458

Fournier, D.I., Eddy, M.C., DeAngeli, N.E., Huszár, R., Bucci, D.J., 2019a. Retrosplenial cortex damage produces retrograde and anterograde context amnesia using strong fear conditioning procedures. Behav. Brain Res. 369, 111920. https://doi.org/10.1016/j.bbr.2019.111920

Fournier, D.I., Monasch, R.R., Bucci, D.J., Todd, T.P., 2020. Retrosplenial Cortex Damage Impairs Unimodal Sensory Preconditioning. Behav. Neurosci. 134, 198–207. https://doi.org/10.1037/bne0000365

Fournier, D.I., Todd, T.P., Bucci, D.J., 2019b. Permanent damage or temporary silencing of retrosplenial cortex impairs the expression of a negative patterning discrimination. Neurobiol. Learn. Mem. 163, 107033. https://doi.org/10.1016/j.nlm.2019.107033

Fowler, S.W., Chiang, A.C.A., Savjani, R.R., Larson, M.E., Sherman, M.A., Schuler, D.R., Cirrito, J.R., Lesné, S.E., Jankowsky, J.L., 2014. Genetic Modulation of Soluble Aβ Rescues Cognitive and Synaptic Impairment in a Mouse Model of Alzheimer's Disease. J. Neurosci. 34, 7871–7885. https://doi.org/10.1523/JNEUROSCI.0572-14.2014

Franco, L.M., Goard, M.J., 2021. A distributed circuit for associating environmental context with motor choice in retrosplenial cortex. Sci. Adv. 7, eabf9815. https://doi.org/10.1126/sciadv.abf9815

Frizzati, A., Milczarek, M.M., Sengpiel, F., Thomas, K.L., Dillingham, C.M., Vann, S.D., 2016. Comparable reduction in Zif268 levels and cytochrome oxidase activity in the retrosplenial cortex following mammillothalamic tract lesions. Neuroscience 330, 39–49. https://doi.org/10.1016/j.neuroscience.2016.05.030

Frost, B.E., Martin, S.K., Cafalchio, M., Islam, M.N., Aggleton, J.P., O'Mara, S.M., 2021. Anterior Thalamic Inputs Are Required for Subiculum Spatial Coding, with Associated Consequences for Hippocampal Spatial Memory. J. Neurosci. 41, 6511–6525. https://doi.org/10.1523/JNEUROSCI.2868-20.2021

Gao, M., Noguchi, A., Ikegaya, Y., 2021. The subiculum sensitizes retrosplenial cortex layer 2/3 pyramidal neurons. J. Physiol. 599, 3151–3167. https://doi.org/10.1113/JP281152

Garden, D.L.F., Massey, P.V., Caruana, D.A., Johnson, B., Warburton, E.C., Aggleton, J.P., Bashir, Z.I., 2009. Anterior thalamic lesions stop synaptic plasticity in retrosplenial cortex slices: expanding the pathology of diencephalic amnesia. Brain 132, 1847–1857. https://doi.org/10.1093/brain/awp090

George, S., Rönnbäck, A., Gouras, G.K., Petit, G.H., Grueninger, F., Winblad, B., Graff, C., Brundin, P., 2014. Lesion of the subiculum reduces the spread of amyloid beta pathology to interconnected brain regions in a mouse model of Alzheimer's disease. Acta Neuropathol. Commun. 2, 17. https://doi.org/10.1186/2051-5960-2-17

Gibson, B., Butler, W.N., Taube, J.S., 2013. The head-direction signal is critical for navigation requiring a cognitive map but not for spatial learning. Curr. Biol. CB 23, 1536–1540. https://doi.org/10.1016/j.cub.2013.06.030

Gilman, J.P., Medalla, M., Luebke, J.I., 2017. Area-Specific Features of Pyramidal Neurons—a Comparative Study in Mouse and Rhesus Monkey. Cereb. Cortex 27, 2078–2094. https://doi.org/10.1093/cercor/bhw062

Giovannini, M.G., Rakovska, A., Benton, R.S., Pazzagli, M., Bianchi, L., Pepeu, G., 2001. Effects of novelty and habituation on acetylcholine, GABA, and glutamate release from the frontal cortex and hippocampus of freely moving rats. Neuroscience 106, 43–53. https://doi.org/10.1016/s0306-4522(01)00266-4

Gonzalo-Ruiz, A., Morte, L., 2000. Localization of amino acids, neuropeptides and cholinergic markers in neurons of the septum-diagonal band complex projecting to the retrosplenial granular cortex of the rat. Brain Res. Bull. 52, 499–510. https://doi.org/10.1016/s0361-9230(00)00287-2

Gottlieb, J.P., Keller, A., 1997. Intrinsic circuitry and physiological properties of pyramidal neurons in rat barrel cortex. Exp. Brain Res. 115, 47–60. https://doi.org/10.1007/PL00005684

Goulas, A., Uylings, H.B.M., Hilgetag, C.C., 2017. Principles of ipsilateral and contralateral cortico-cortical connectivity in the mouse. Brain Struct. Funct. 222, 1281–1295. https://doi.org/10.1007/s00429-016-1277-y

Gramann, K., Onton, J., Riccobon, D., Mueller, H.J., Bardins, S., Makeig, S., 2010. Human Brain Dynamics Accompanying Use of Egocentric and Allocentric Reference Frames during Navigation. J. Cogn. Neurosci. 22, 2836–2849. https://doi.org/10.1162/jocn.2009.21369

Greenhill, S.D., Ranson, A., Fox, K., 2015. Hebbian and Homeostatic Plasticity Mechanisms in Regular Spiking and Intrinsic Bursting Cells of Cortical Layer 5. Neuron 88, 539–552. https://doi.org/10.1016/j.neuron.2015.09.025

Greger, I.H., Watson, J.F., Cull-Candy, S.G., 2017. Structural and Functional Architecture of AMPA-Type Glutamate Receptors and Their Auxiliary Proteins. Neuron 94, 713–730. https://doi.org/10.1016/j.neuron.2017.04.009

Greicius, M.D., Srivastava, G., Reiss, A.L., Menon, V., 2004. Default-mode network activity distinguishes Alzheimer's disease from healthy aging: Evidence from functional MRI. Proc. Natl. Acad. Sci. U. S. A. 101, 4637–4642. https://doi.org/10.1073/pnas.0308627101

Groen, T.V., Wyss, J.M., 2003. Connections of the retrosplenial granular b cortex in the rat. J. Comp. Neurol. 463, 249–263. https://doi.org/10.1002/cne.10757

Groen, T. van, Wyss, J.M., 1992. Connections of the retrosplenial dysgranular cortex in the rat. J. Comp. Neurol. 315, 200–216. https://doi.org/10.1002/cne.903150207

Groen, T. van, Wyss, J.M., 1990. Connections of the retrosplenial granular a cortex in the rat. J. Comp. Neurol. 300, 593–606. https://doi.org/10.1002/cne.903000412

Groh, A., Meyer, H.S., Schmidt, E.F., Heintz, N., Sakmann, B., Krieger, P., 2010. Cell-type specific properties of pyramidal neurons in neocortex underlying a layout that is modifiable depending on the cortical area. Cereb. Cortex N. Y. N 1991 20, 826–836. https://doi.org/10.1093/cercor/bhp152

Gulbranson, D.R., Ho, K., Yu, G.-Q., Yu, X., Das, M., Shao, E., Kim, D., Zhang, W.J., Choudhary, K., Thomas, R., Mucke, L., 2021. Phenotypic Differences between the Alzheimer's Disease-Related hAPP-J20 Model and Heterozygous Zbtb20 Knock-Out Mice. eNeuro 8, ENEURO.0089-21.2021. https://doi.org/10.1523/ENEURO.0089-21.2021

Hampel, H., Mesulam, M.-M., Cuello, A.C., Khachaturian, A.S., Vergallo, A., Farlow, M.R., Snyder, P.J., Giacobini, E., Khachaturian, Z.S., Cholinergic System Working Group, and for the A.P.M.I. (APMI), 2019. Revisiting the Cholinergic Hypothesis in Alzheimer's Disease: Emerging Evidence from Translational and Clinical Research. J. Prev. Alzheimers Dis. 6, 2–15. https://doi.org/10.14283/jpad.2018.43

Hansen, K.B., Yi, F., Perszyk, R.E., Furukawa, H., Wollmuth, L.P., Gibb, A.J., Traynelis, S.F., 2018. Structure, function, and allosteric modulation of NMDA receptors. J. Gen. Physiol. 150, 1081–1105. https://doi.org/10.1085/jgp.201812032

Hardy, J.A., Higgins, G.A., 1992. Alzheimer's Disease: The Amyloid Cascade Hypothesis. Science 256, 184–185. https://doi.org/10.1126/science.1566067

Harris, J.A., Devidze, N., Halabisky, B., Lo, I., Thwin, M.T., Yu, G.-Q., Bredesen, D.E., Masliah, E., Mucke, L., 2010. Many Neuronal and Behavioral Impairments

in Transgenic Mouse Models of Alzheimer's Disease Are Independent of Caspase Cleavage of the Amyloid Precursor Protein. J. Neurosci. 30, 372–381. https://doi.org/10.1523/JNEUROSCI.5341-09.2010

Hashimoto, R., Tanaka, Y., Nakano, I., 2010. Heading Disorientation: A New Test and a Possible Underlying Mechanism. Eur. Neurol. 63, 87–93. https://doi.org/10.1159/000276398

He, Y., Wei, M., Wu, Y., Qin, H., Li, W., Ma, X., Cheng, J., Ren, J., Shen, Ye, Chen, Z., Sun, B., Huang, F.-D., Shen, Yi, Zhou, Y.-D., 2019. Amyloid β oligomers suppress excitatory transmitter release via presynaptic depletion of phosphatidylinositol-4,5-bisphosphate. Nat. Commun. 10, 1193. https://doi.org/10.1038/s41467-019-09114-z

He, Z., Guo, J.L., McBride, J.D., Narasimhan, S., Kim, H., Changolkar, L., Zhang, B., Gathagan, R.J., Yue, C., Dengler, C., Stieber, A., Nitla, M., Coulter, D.A., Abel, T., Brunden, K.R., Trojanowski, J.Q., Lee, V.M.-Y., 2018. Amyloid-β plaques enhance Alzheimer's brain tau-seeded pathologies by facilitating neuritic plaque tau aggregation. Nat. Med. 24, 29–38. https://doi.org/10.1038/nm.4443

Head, E., 2013. A canine model of human aging and Alzheimer's disease. Biochim. Biophys. Acta BBA - Mol. Basis Dis., Animal models of disease 1832, 1384–1389. https://doi.org/10.1016/j.bbadis.2013.03.016

Hefter, D., Ludewig, S., Draguhn, A., Korte, M., 2020. Amyloid, APP, and Electrical Activity of the Brain. The Neuroscientist 26, 231–251. https://doi.org/10.1177/1073858419882619

Heilman, K.M., Bowers, D., Watson, R.T., Day, A., Valenstein, E., Hammond, E., Duara, R., 1990. Frontal hypermetabolism and thalamic hypometabolism in a patient with abnormal orienting and retrosplenial amnesia. Neuropsychologia 28, 161–169. https://doi.org/10.1016/0028-3932(90)90098-9

Henderson, J.M., Zhu, D.C., Larson, C.L., 2011. Functions of parahippocampal place area and retrosplenial cortex in real-world scene analysis: An fMRI study. Vis. Cogn. 19, 910–927. https://doi.org/10.1080/13506285.2011.596852

Hennig, C., 2007. Cluster-wise assessment of cluster stability. Comput. Stat. Data Anal. 52, 258–271. https://doi.org/10.1016/j.csda.2006.11.025

Henry, J., Petrides, M., St-Laurent, M., Sziklas, V., 2004. Spatial conditional associative learning: effects of thalamo-hippocampal disconnection in rats. Neuroreport 15, 2427–2431. https://doi.org/10.1097/00001756-200410250-00025

Higa, K.K., Young, J.W., Geyer, M.A., 2016. Wet or dry: translatable “water mazes” for mice and humans. J. Clin. Invest. 126, 477–479. https://doi.org/10.1172/JCI86071

Hindley, E.L., Nelson, A.J.D., Aggleton, J.P., Vann, S.D., 2014. The rat retrosplenial cortex is required when visual cues are used flexibly to determine location. Behav. Brain Res. 263, 98–107. https://doi.org/10.1016/j.bbr.2014.01.028

Hong, S., Beja-Glasser, V.F., Nfonoyim, B.M., Frouin, A., Li, S., Ramakrishnan, S., Merry, K.M., Shi, Q., Rosenthal, A., Barres, B.A., Lemere, C.A., Selkoe, D.J., Stevens, B., 2016. Complement and Microglia Mediate Early Synapse Loss in Alzheimer Mouse Models. Science 352, 712–716. https://doi.org/10.1126/science.aad8373

Hong, S., Quintero-Monzon, O., Ostaszewski, B.L., Podlisny, D.R., Cavanaugh, W.T., Yang, T., Holtzman, D.M., Cirrito, J.R., Selkoe, D.J., 2011. Dynamic Analysis of Amyloid β-Protein in Behaving Mice Reveals Opposing Changes in ISF versus Parenchymal Aβ during Age-Related Plaque Formation. J. Neurosci. 31, 15861–15869. https://doi.org/10.1523/JNEUROSCI.3272-11.2011

Hsia, A.Y., Masliah, E., McConlogue, L., Yu, G.-Q., Tatsuno, G., Hu, K., Kholodenko, D., Malenka, R.C., Nicoll, R.A., Mucke, L., 1999. Plaque-independent disruption of neural circuits in Alzheimer’s disease mouse models. Proc. Natl. Acad. Sci. 96, 3228–3233. https://doi.org/10.1073/pnas.96.6.3228

Hsieh, H., Boehm, J., Sato, C., Iwatsubo, T., Tomita, T., Sisodia, S., Malinow, R., 2006. AMPAR Removal Underlies Aβ-Induced Synaptic Depression and Dendritic Spine Loss. Neuron 52, 831–843. https://doi.org/10.1016/j.neuron.2006.10.035

Huggenberger, S., Vater, M., Deisz, R.A., 2009. Interlaminar Differences of Intrinsic Properties of Pyramidal Neurons in the Auditory Cortex of Mice. Cereb. Cortex 19, 1008–1018. https://doi.org/10.1093/cercor/bhn143

Isaac, J.T.R., Ashby, M.C., McBain, C.J., 2007. The Role of the GluR2 Subunit in AMPA Receptor Function and Synaptic Plasticity. Neuron 54, 859–871. https://doi.org/10.1016/j.neuron.2007.06.001

Jack, C.R., Knopman, D.S., Jagust, W.J., Shaw, L.M., Aisen, P.S., Weiner, M.W., Petersen, R.C., Trojanowski, J.Q., 2010. Hypothetical model of dynamic biomarkers of the Alzheimer's pathological cascade. Lancet Neurol. 9, 119–128. https://doi.org/10.1016/S1474-4422(09)70299-6

Jacob, V., Petreanu, L., Wright, N., Svoboda, K., Fox, K., 2012. Regular Spiking and Intrinsic Bursting Pyramidal Cells Show Orthogonal Forms of Experience-Dependent Plasticity in Layer V of Barrel Cortex. Neuron 73, 391–404. https://doi.org/10.1016/j.neuron.2011.11.034

Jankowski, M.M., Ronnqvist, K.C., Tsanov, M., Vann, S.D., Wright, N.F., Erichsen, J.T., Aggleton, J.P., O'Mara, S.M., 2013. The anterior thalamus provides a subcortical circuit supporting memory and spatial navigation. Front. Syst. Neurosci. 7, 45. https://doi.org/10.3389/fnsys.2013.00045

Jankowsky, J.L., Slunt, H.H., Gonzales, V., Savonenko, A.V., Wen, J.C., Jenkins, N.A., Copeland, N.G., Younkin, L.H., Lester, H.A., Younkin, S.G., Borchelt, D.R., 2005. Persistent Amyloidosis following Suppression of Aβ Production in a Transgenic Model of Alzheimer Disease. PLOS Med. 2, e355. https://doi.org/10.1371/journal.pmed.0020355

Jankowsky, J.L., Zheng, H., 2017. Practical considerations for choosing a mouse model of Alzheimer's disease. Mol. Neurodegener. 12, 89. https://doi.org/10.1186/s13024-017-0231-7

Jedrasiak-Cape, I., Ahmed, O.J., 2020. Functional impact of cholinergic dysfunction on retrosplenial circuits in the 5xFAD mouse model of Alzheimer's disease. Alzheimers Dement. 16, e047611. https://doi.org/10.1002/alz.047611

Jeibmann, A., Paulus, W., 2009. Drosophila melanogaster as a Model Organism of Brain Diseases. Int. J. Mol. Sci. 10, 407–440. https://doi.org/10.3390/ijms10020407

Jellinger, K.A., Attems, J., 2007. Neurofibrillary tangle-predominant dementia: comparison with classical Alzheimer disease. Acta Neuropathol. (Berl.) 113, 107–117. https://doi.org/10.1007/s00401-006-0156-7

Jenkins, T.A., Amin, E., Brown, M.W., Aggleton, J.P., 2006. Changes in immediate early gene expression in the rat brain after unilateral lesions of the hippocampus. Neuroscience 137, 747–759. https://doi.org/10.1016/j.neuroscience.2005.09.034

Jenkins, T.A., Vann, S.D., Amin, E., Aggleton, J.P., 2004. Anterior thalamic lesions stop immediate early gene activation in selective laminae of the retrosplenial cortex: evidence of covert pathology in rats? Eur. J. Neurosci. 19, 3291–3304. https://doi.org/10.1111/j.0953-816X.2004.03421.x

Johnson, K.O., 2000. Neural Coding. Neuron 26, 563–566. https://doi.org/10.1016/S0896-6273(00)81193-9

Joo, H.R., Frank, L.M., 2018. The hippocampal sharp wave–ripple in memory retrieval for immediate use and consolidation. Nat. Rev. Neurosci. 19, 744–757. https://doi.org/10.1038/s41583-018-0077-1

Jucker, M., Walker, L.C., 2011. Pathogenic protein seeding in alzheimer disease and other neurodegenerative disorders. Ann. Neurol. 70, 532–540. https://doi.org/10.1002/ana.22615

Kaboodvand, N., Bäckman, L., Nyberg, L., Salami, A., 2018. The retrosplenial cortex: A memory gateway between the cortical default mode network and the medial temporal lobe. Hum. Brain Mapp. 39, 2020–2034. https://doi.org/10.1002/hbm.23983

Kandel, E.R., Schwartz, J.H., Jessell, T.M., 2000. Principles of neural science. McGraw-Hill, Health Professions Division, New York.

Karimi Abadchi, J., Nazari-Ahangarkolaee, M., Gattas, S., Bermudez-Contreras, E., Luczak, A., McNaughton, B.L., Mohajerani, M.H., 2020. Spatiotemporal patterns of neocortical activity around hippocampal sharp-wave ripples. eLife 9, e51972. https://doi.org/10.7554/eLife.51972

Karl, T., Bhatia, S., Cheng, D., Kim, W.S., Garner, B., 2012. Cognitive phenotyping of amyloid precursor protein transgenic J20 mice. Behav. Brain Res. 228, 392–397. https://doi.org/10.1016/j.bbr.2011.12.021

Katche, C., Bekinschtein, P., Slipczuk, L., Goldin, A., Izquierdo, I.A., Cammarota, M., Medina, J.H., 2010. Delayed wave of c-Fos expression in the dorsal hippocampus involved specifically in persistence of long-term memory storage. Proc. Natl. Acad. Sci. 107, 349–354. https://doi.org/10.1073/pnas.0912931107

Katche, C., Dorman, G., Gonzalez, C., Kramar, C.P., Slipczuk, L., Rossato, J.I., Cammarota, M., Medina, J.H., 2013. On the role of retrosplenial cortex in long-lasting memory storage. Hippocampus 23, 295–302. https://doi.org/10.1002/hipo.22092

Katche, C., Medina, J.H., 2017. Requirement of an Early Activation of BDNF/c-Fos Cascade in the Retrosplenial Cortex for the Persistence of a Long-Lasting Aversive Memory. Cereb. Cortex 27, 1060–1067. https://doi.org/10.1093/cercor/bhv284

Keene, C.S., Bucci, D.J., 2009. Damage to the retrosplenial cortex produces specific impairments in spatial working memory. Neurobiol. Learn. Mem. 91, 408–414. https://doi.org/10.1016/j.nlm.2008.10.009

Keene, C.S., Bucci, D.J., 2008a. Neurotoxic lesions of retrosplenial cortex disrupt signaled and unsignaled contextual fear conditioning. Behav. Neurosci. 122, 1070–1077. https://doi.org/10.1037/a0012895

Keene, C.S., Bucci, D.J., 2008b. Involvement of the retrosplenial cortex in processing multiple conditioned stimuli. Behav. Neurosci. 122, 651–658. https://doi.org/10.1037/0735-7044.122.3.651

Keene, C.S., Bucci, D.J., 2008c. Contributions of the retrosplenial and posterior parietal cortices to cue-specific and contextual fear conditioning. Behav. Neurosci. 122, 89–97. https://doi.org/10.1037/0735-7044.122.1.89

Khodagholy, D., Gelinas, J.N., Buzsáki, G., 2017. Learning-enhanced coupling between ripple oscillations in association cortices and hippocampus. Science 358, 369–372. https://doi.org/10.1126/science.aan6203

Kim, D.-H., Kim, H.-A., Han, Y.S., Jeon, W.K., Han, J.-S., 2020. Recognition memory impairments and amyloid-beta deposition of the retrosplenial cortex at the early stage of 5XFAD mice. Physiol. Behav. 222, 112891. https://doi.org/10.1016/j.physbeh.2020.112891

Kim, J.H., Park, K.-Y., Seo, S.W., Na, D.L., Chung, C.-S., Lee, K.H., Kim, G.-M., 2007. Reversible Verbal and Visual Memory Deficits after Left Retrosplenial Infarction. J. Clin. Neurol. 3, 62–66. https://doi.org/10.3988/jcn.2007.3.1.62

Kitamura, T., Sugimori, K., Sudo, S., Kobayashi, K., 2005. Relationship between microtubule-binding repeats and morphology of neurofibrillary tangle in Alzheimer's disease. Acta Neurol. Scand. 112, 327–334. https://doi.org/10.1111/j.1600-0404.2005.00488.x

Kitanishi, T., Umaba, R., Mizuseki, K., 2021. Robust information routing by dorsal subiculum neurons. Sci. Adv. 7, eabf1913. https://doi.org/10.1126/sciadv.abf1913

Kitraki, E., Bozas, E., Philippdis, H., Stylianopoulou, F., 1993. Aging-related changes in IGF-II and c-fos gene expression in the rat brain. Int. J. Dev. Neurosci. 11, 1–9. https://doi.org/10.1016/0736-5748(93)90029-D

Klein, W.L., 2013. Synaptotoxic Amyloid-β Oligomers: A Molecular Basis for the Cause, Diagnosis, and Treatment of Alzheimer's Disease? J. Alzheimers Dis. 33, S49–S65. https://doi.org/10.3233/JAD-2012-129039

Klementieva, O., Willén, K., Martinsson, I., Israelsson, B., Engdahl, A., Cladera, J., Uvdal, P., Gouras, G.K., 2017. Pre-plaque conformational changes in Alzheimer's disease-linked Aβ and APP. Nat. Commun. 8, 14726. https://doi.org/10.1038/ncomms14726

Kloc, M., Maffei, A., 2014. Target-Specific Properties of Thalamocortical Synapses onto Layer 4 of Mouse Primary Visual Cortex. J. Neurosci. 34, 15455–15465. https://doi.org/10.1523/JNEUROSCI.2595-14.2014

Knobloch, M., Mansuy, I.M., 2008. Dendritic Spine Loss and Synaptic Alterations in Alzheimer's Disease. Mol. Neurobiol. 37, 73–82. https://doi.org/10.1007/s12035-008-8018-z

Kobayashi, Y., Amaral, D.G., 2003. Macaque monkey retrosplenial cortex: II. Cortical afferents. J. Comp. Neurol. 466, 48–79. https://doi.org/10.1002/cne.10883

Kohli, S., Andrianova, L., Margetts-Smith, G., Brady, E., Craig, M.T., 2021. Chemogenetic activation of midline thalamic nuclei fails to ameliorate memory deficits in two mouse models of Alzheimer's disease. https://doi.org/10.1101/2021.06.30.450500

Kowalski, J., Gan, J., Jonas, P., Pernía-Andrade, A.J., 2016. Intrinsic membrane properties determine hippocampal differential firing pattern in vivo in anesthetized rats. Hippocampus 26, 668–682. https://doi.org/10.1002/hipo.22550

Kurotani, T., Miyashita, T., Wintzer, M., Konishi, T., Sakai, K., Ichinohe, N., Rockland, K.S., 2013. Pyramidal neurons in the superficial layers of rat retrosplenial cortex exhibit a late-spiking firing property. Brain Struct. Funct. 218, 239–254. https://doi.org/10.1007/s00429-012-0398-1

Lafourcade, M., van der Goes, M.-S.H., Vardalaki, D., Brown, N.J., Voigts, J., Yun, D.H., Kim, M.E., Ku, T., Harnett, M.T., 2022. Differential dendritic integration of long-range inputs in association cortex via subcellular changes in synaptic AMPA-to-NMDA receptor ratio. Neuron 110, 1532-1546.e4. https://doi.org/10.1016/j.neuron.2022.01.025

Lee, S.H., Kang, J., Ho, A., Watanabe, H., Bolshakov, V.Y., Shen, J., 2020. APP Family Regulates Neuronal Excitability and Synaptic Plasticity but Not Neuronal Survival. Neuron 108, 676-690.e8. https://doi.org/10.1016/j.neuron.2020.08.011

Lee, Y.I., Park, K.H., Baik, S.H., Cha, C.I., 1998. Attenuation of c-Fos basal expression in the cerebral cortex of aged rat. NeuroReport 9, 2733.

Lerea, L.S., McNamara, J.O., 1993. Ionotropic glutamate receptor subtypes activate c-fos transcription by distinct calcium-requiring intracellular signaling pathways. Neuron 10, 31–41. https://doi.org/10.1016/0896-6273(93)90239-N

Levin, E.D., Simon, B.B., 1998. Nicotinic acetylcholine involvement in cognitive function in animals. Psychopharmacology (Berl.) 138, 217–230. https://doi.org/10.1007/s002130050667

Li, S., Hong, S., Shepardson, N.E., Walsh, D.M., Shankar, G.M., Selkoe, D., 2009. Soluble oligomers of amyloid β-protein facilitate hippocampal long-term depression by disrupting neuronal glutamate uptake. Neuron 62, 788–801. https://doi.org/10.1016/j.neuron.2009.05.012

Lisman, J., Yasuda, R., Raghavachari, S., 2012. Mechanisms of CaMKII action in long-term potentiation. Nat. Rev. Neurosci. 13, 169–182. https://doi.org/10.1038/nrn3192

Lo, A.C., Iscru, E., Blum, D., Tesseur, I., Callaerts-Vegh, Z., Buée, L., De Strooper, B., Balschun, D., D'Hooge, R., 2013. Amyloid and Tau Neuropathology Differentially Affect Prefrontal Synaptic Plasticity and Cognitive Performance in Mouse Models of Alzheimer's Disease. J. Alzheimers Dis. 37, 109–125. https://doi.org/10.3233/JAD-122296

Long, J.M., Holtzman, D.M., 2019. Alzheimer Disease: An Update on Pathobiology and Treatment Strategies. Cell 179, 312–339. https://doi.org/10.1016/j.cell.2019.09.001

Lorenzo, A., Yankner, B.A., 1994. Beta-amyloid neurotoxicity requires fibril formation and is inhibited by congo red. Proc. Natl. Acad. Sci. U. S. A. 91, 12243–12247.

Lozano, Y.R., Page, H., Jacob, P.-Y., Lomi, E., Street, J., Jeffery, K., 2017. Retrosplenial and postsubicular head direction cells compared during visual landmark discrimination. Brain Neurosci. Adv. 1, 2398212817721859. https://doi.org/10.1177/2398212817721859

Lübke, J., Feldmeyer, D., 2007. Excitatory signal flow and connectivity in a cortical column: focus on barrel cortex. Brain Struct. Funct. 212, 3–17. https://doi.org/10.1007/s00429-007-0144-2

Lüscher, C., Malenka, R.C., 2012. NMDA Receptor-Dependent Long-Term Potentiation and Long-Term Depression (LTP/LTD). Cold Spring Harb. Perspect. Biol. 4, a005710. https://doi.org/10.1101/cshperspect.a005710

Maddock, R.J., 1999. The retrosplenial cortex and emotion: new insights from functional neuroimaging of the human brain. Trends Neurosci. 22, 310–316. https://doi.org/10.1016/S0166-2236(98)01374-5

Maguire, E.A., 2001. The retrosplenial contribution to human navigation: A review of lesion and neuroimaging findings. Scand. J. Psychol. 42, 225–238. https://doi.org/10.1111/1467-9450.00233

Malik, R., Li, Y., Schamiloglu, S., Sohal, V.S., 2022. Top-down control of hippocampal signal-to-noise by prefrontal long-range inhibition. Cell 185, 1602-1617.e17. https://doi.org/10.1016/j.cell.2022.04.001

Mango, D., Saidi, A., Cisale, G.Y., Feligioni, M., Corbo, M., Nisticò, R., 2019. Targeting Synaptic Plasticity in Experimental Models of Alzheimer's Disease. Front. Pharmacol. 10. https://doi.org/10.3389/fphar.2019.00778

Mao, D., Kandler, S., McNaughton, B.L., Bonin, V., 2017. Sparse orthogonal population representation of spatial context in the retrosplenial cortex. Nat. Commun. 8, 243. https://doi.org/10.1038/s41467-017-00180-9

Mao, D., Neumann, A.R., Sun, J., Bonin, V., Mohajerani, M.H., McNaughton, B.L., 2018. Hippocampus-dependent emergence of spatial sequence coding in retrosplenial cortex. Proc. Natl. Acad. Sci. 115, 8015–8018. https://doi.org/10.1073/pnas.1803224115

Marchette, S.A., Vass, L.K., Ryan, J., Epstein, R.A., 2014. Anchoring the neural compass: coding of local spatial reference frames in human medial parietal lobe. Nat. Neurosci. 17, 1598–1606. https://doi.org/10.1038/nn.3834

Marder, E., Abbott, L.F., Turrigiano, G.G., Liu, Z., Golowasch, J., 1996. Memory from the dynamics of intrinsic membrane currents. Proc. Natl. Acad. Sci. 93, 13481–13486. https://doi.org/10.1073/pnas.93.24.13481

Markram, H., Wang, Y., Tsodyks, M., 1998. Differential signaling via the same axon of neocortical pyramidal neurons. Proc. Natl. Acad. Sci. 95, 5323–5328. https://doi.org/10.1073/pnas.95.9.5323

Martinez-Coria, H., Green, K.N., Billings, L.M., Kitazawa, M., Albrecht, M., Rammes, G., Parsons, C.G., Gupta, S., Banerjee, P., LaFerla, F.M., 2010. Memantine Improves Cognition and Reduces Alzheimer's-Like Neuropathology in Transgenic Mice. Am. J. Pathol. 176, 870–880. https://doi.org/10.2353/ajpath.2010.090452

Maviel, T., Durkin, T.P., Menzaghi, F., Bontempi, B., 2004. Sites of Neocortical Reorganization Critical for Remote Spatial Memory. Science 305, 96–99. https://doi.org/10.1126/science.1098180

Mawuenyega, K.G., Sigurdson, W., Ovod, V., Munsell, L., Kasten, T., Morris, J.C., Yarasheski, K.E., Bateman, R.J., 2010. Decreased Clearance of CNS β-Amyloid in Alzheimer's Disease. Science 330, 1774–1774. https://doi.org/10.1126/science.1197623

McBain, C.J., Mayer, M.L., 1994. N-methyl-D-aspartic acid receptor structure and function. Physiol. Rev. 74, 723–760. https://doi.org/10.1152/physrev.1994.74.3.723

McClelland, J.L., McNaughton, B.L., O'Reilly, R.C., 1995. Why there are complementary learning systems in the hippocampus and neocortex: insights from the successes and failures of connectionist models of learning and memory. Psychol. Rev. 102, 419–457. https://doi.org/10.1037/0033-295X.102.3.419

McEntee, W.J., Crook, T.H., 1993. Glutamate: its role in learning, memory, and the aging brain. Psychopharmacology (Berl.) 111, 391–401. https://doi.org/10.1007/BF02253527

McGuinness, L., Taylor, C., Taylor, R.D.T., Yau, C., Langenhan, T., Hart, M.L., Christian, H., Tynan, P.W., Donnelly, P., Emptage, N.J., 2010. Presynaptic NMDARs in the Hippocampus Facilitate Transmitter Release at Theta Frequency. Neuron 68, 1109–1127. https://doi.org/10.1016/j.neuron.2010.11.023

McKay, B.E., Placzek, A.N., Dani, J.A., 2007. Regulation of synaptic transmission and plasticity by neuronal nicotinic acetylcholine receptors. Biochem. Pharmacol., Nicotinic Acetylcholine Receptors as Therapeutic Targets: Emerging Frontiers in Basic Research and Clinical Science 74, 1120–1133. https://doi.org/10.1016/j.bcp.2007.07.001

Milczarek, M.M., Vann, S.D., Sengpiel, F., 2018. Spatial Memory Engram in the Mouse Retrosplenial Cortex. Curr. Biol. 28, 1975-1980.e6. https://doi.org/10.1016/j.cub.2018.05.002

Minoshima, S., Giordani, B., Berent, S., Frey, K.A., Foster, N.L., Kuhl, D.E., 1997. Metabolic reduction in the posterior cingulate cortex in very early Alzheimer's disease. Ann. Neurol. 42, 85–94. https://doi.org/10.1002/ana.410420114

Miranda, M.I., Ramírez-Lugo, L., Bermúdez-Rattoni, F., 2000. Cortical cholinergic activity is related to the novelty of the stimulus. Brain Res. 882, 230–235. https://doi.org/10.1016/s0926-6410(00)00050-1

Mitchell, A.S., Czajkowski, R., Zhang, N., Jeffery, K., Nelson, A.J.D., 2018. Retrosplenial cortex and its role in spatial cognition. Brain Neurosci. Adv. 2, 2398212818757098. https://doi.org/10.1177/2398212818757098

Mockett, B.G., Richter, M., Abraham, W.C., Müller, U.C., 2017. Therapeutic Potential of Secreted Amyloid Precursor Protein APPsα. Front. Mol. Neurosci. 10.

Molnár, Z., Soós, K., Lengyel, I., Penke, B., Szegedi, V., Budai, D., 2004. Enhancement of NMDA responses by β-amyloid peptides in the hippocampus in vivo. NeuroReport 15, 1649–1652. https://doi.org/10.1097/01.wnr.0000134471.06244.d2

Molyneaux, B.J., Arlotta, P., Menezes, J.R.L., Macklis, J.D., 2007. Neuronal subtype specification in the cerebral cortex. Nat. Rev. Neurosci. 8, 427–437. https://doi.org/10.1038/nrn2151

Monyer, H., Burnashev, N., Laurie, D.J., Sakmann, B., Seeburg, P.H., 1994. Developmental and regional expression in the rat brain and functional properties of four NMDA receptors. Neuron 12, 529–540. https://doi.org/10.1016/0896-6273(94)90210-0

Moradi Chameh, H., Rich, S., Wang, L., Chen, F.-D., Zhang, L., Carlen, P.L., Tripathy, S.J., Valiante, T.A., 2021. Diversity amongst human cortical pyramidal neurons revealed via their sag currents and frequency preferences. Nat. Commun. 12, 2497. https://doi.org/10.1038/s41467-021-22741-9

Morley, J., Farr, S., Banks, W., Johnson, S., Yamada, K., Xu, L., 2008. A Physiological Role for Amyloid Beta Protein: Enhancement of Learning and Memory. Nat. Preced. 1–1. https://doi.org/10.1038/npre.2008.2119.1

Morris, R., Paxinos, G., Petrides, M., 2000. Architectonic analysis of the human retrosplenial cortex. J. Comp. Neurol. 421, 14–28. https://doi.org/10.1002/(SICI)1096-9861(20000522)421:1<14::AID-CNE2>3.0.CO;2-S

Moser, E.I., Moser, M.-B., 2008. A metric for space. Hippocampus 18, 1142–1156. https://doi.org/10.1002/hipo.20483

Mucke, L., Masliah, E., Yu, G.-Q., Mallory, M., Rockenstein, E.M., Tatsuno, G., Hu, K., Kholodenko, D., Johnson-Wood, K., McConlogue, L., 2000. High-Level Neuronal Expression of Aβ1–42 in Wild-Type Human Amyloid Protein Precursor Transgenic Mice: Synaptotoxicity without Plaque Formation. J. Neurosci. 20, 4050–4058. https://doi.org/10.1523/JNEUROSCI.20-11-04050.2000

Mucke, L., Selkoe, D.J., 2012. Neurotoxicity of Amyloid β-Protein: Synaptic and Network Dysfunction. Cold Spring Harb. Perspect. Med. 2. https://doi.org/10.1101/cshperspect.a006338

Mullan, M., Crawford, F., Axelman, K., Houlden, H., Lilius, L., Winblad, B., Lannfelt, L., 1992. A pathogenic mutation for probable Alzheimer's disease in the APP gene at the N–terminus of β–amyloid. Nat. Genet. 1, 345–347. https://doi.org/10.1038/ng0892-345

Müller, U.C., Zheng, H., 2012. Physiological Functions of APP Family Proteins. Cold Spring Harb. Perspect. Med. 2, a006288. https://doi.org/10.1101/cshperspect.a006288

Murrell, J., Farlow, M., Ghetti, B., Benson, M.D., 1991. A mutation in the amyloid precursor protein associated with hereditary Alzheimer's disease. Science 254, 97–99. https://doi.org/10.1126/science.1925564

Neave, N., Lloyd, S., Sahgal, A., Aggleton, J.P., 1994. Lack of effect of lesions in the anterior cingulate cortex and retrosplenial cortex on certain tests of spatial memory in the rat. Behav. Brain Res. 65, 89–101. https://doi.org/10.1016/0166-4328(94)90077-9

Nelson, A.J.D., Powell, A.L., Holmes, J.D., Vann, S.D., Aggleton, J.P., 2015. What does spatial alternation tell us about retrosplenial cortex function? Front. Behav. Neurosci. 9.

Nelson, P.T., Alafuzoff, I., Bigio, E.H., Bouras, C., Braak, H., Cairns, N.J., Castellani, R.J., Crain, B.J., Davies, P., Tredici, K.D., Duyckaerts, C., Frosch, M.P., Haroutunian, V., Hof, P.R., Hulette, C.M., Hyman, B.T., Iwatsubo, T., Jellinger, K.A., Jicha, G.A., Kövari, E., Kukull, W.A., Leverenz, J.B., Love, S., Mackenzie, I.R., Mann, D.M., Masliah, E., McKee, A.C., Montine, T.J., Morris, J.C., Schneider, J.A., Sonnen, J.A., Thal, D.R., Trojanowski, J.Q., Troncoso, J.C., Wisniewski, T., Woltjer, R.L., Beach, T.G., 2012. Correlation of Alzheimer Disease Neuropathologic Changes With Cognitive Status: A Review of the Literature. J. Neuropathol. Exp. Neurol. 71, 362–381. https://doi.org/10.1097/NEN.0b013e31825018f7

Nestor, P.J., Fryer, T.D., Ikeda, M., Hodges, J.R., 2003. Retrosplenial cortex (BA 29/30) hypometabolism in mild cognitive impairment (prodromal Alzheimer's disease). Eur. J. Neurosci. 18, 2663–2667. https://doi.org/10.1046/j.1460-9568.2003.02999.x

Niciu, M.J., Kelmendi, B., Sanacora, G., 2012. Overview of glutamatergic neurotransmission in the nervous system. Pharmacol. Biochem. Behav., Glutamate Receptors 100, 656–664. https://doi.org/10.1016/j.pbb.2011.08.008

Nitzan, N., McKenzie, S., Beed, P., English, D.F., Oldani, S., Tukker, J.J., Buzsáki, G., Schmitz, D., 2020. Propagation of hippocampal ripples to the neocortex by way of a subiculum-retrosplenial pathway. Nat. Commun. 11, 1947. https://doi.org/10.1038/s41467-020-15787-8

Norman, K.J., Koike, H., McCraney, S.E., Garkun, Y., Bateh, J., Falk, E.N., Im, S., Caro, K., Demars, M.P., Morishita, H., 2021. Chemogenetic suppression of anterior cingulate cortical neurons projecting to the visual cortex disrupts attentional behavior in mice. Neuropsychopharmacol. Rep. 41, 207–214. https://doi.org/10.1002/npr2.12176

Nyakas, C., Luiten, P.G., Spencer, D.G., Traber, J., 1987. Detailed projection patterns of septal and diagonal band efferents to the hippocampus in the rat with emphasis on innervation of CA1 and dentate gyrus. Brain Res. Bull. 18, 533–545. https://doi.org/10.1016/0361-9230(87)90117-1

Oberlander, J.G., Woolley, C.S., 2016. 17β-Estradiol Acutely Potentiates Glutamatergic Synaptic Transmission in the Hippocampus through Distinct

Mechanisms in Males and Females. J. Neurosci. 36, 2677–2690. https://doi.org/10.1523/JNEUROSCI.4437-15.2016

Opalka, A.N., Huang, W., Liu, J., Liang, H., Wang, D.V., 2020. Hippocampal Ripple Coordinates Retrosplenial Inhibitory Neurons during Slow-Wave Sleep. Cell Rep. 30, 432-441.e3. https://doi.org/10.1016/j.celrep.2019.12.038

Opalka, A.N., Wang, D.V., 2020. Hippocampal efferents to retrosplenial cortex and lateral septum are required for memory acquisition. bioRxiv 2020.03.23.003996. https://doi.org/10.1101/2020.03.23.003996

Orrego, F., Villanueva, S., 1993. The chemical nature of the main central excitatory transmitter: A critical appraisal based upon release studies and synaptic vesicle localization. Neuroscience 56, 539–555. https://doi.org/10.1016/0306-4522(93)90355-J

Palmqvist, S., Schöll, M., Strandberg, O., Mattsson, N., Stomrud, E., Zetterberg, H., Blennow, K., Landau, S., Jagust, W., Hansson, O., 2017. Earliest accumulation of β-amyloid occurs within the default-mode network and concurrently affects brain connectivity. Nat. Commun. 8, 1214. https://doi.org/10.1038/s41467-017-01150-x

Palop, J.J., Chin, J., Roberson, E.D., Wang, J., Thwin, M.T., Bien-Ly, N., Yoo, J., Ho, K.O., Yu, G.-Q., Kreitzer, A., Finkbeiner, S., Noebels, J.L., Mucke, L., 2007. Aberrant Excitatory Neuronal Activity and Compensatory Remodeling of Inhibitory Hippocampal Circuits in Mouse Models of Alzheimer's Disease. Neuron 55, 697–711. https://doi.org/10.1016/j.neuron.2007.07.025

Palop, J.J., Jones, B., Kekonius, L., Chin, J., Yu, G.-Q., Raber, J., Masliah, E., Mucke, L., 2003. Neuronal depletion of calcium-dependent proteins in the dentate gyrus is tightly linked to Alzheimer's disease-related cognitive deficits. Proc. Natl. Acad. Sci. U. S. A. 100, 9572–9577. https://doi.org/10.1073/pnas.1133381100

Palop, J.J., Mucke, L., 2016. Network abnormalities and interneuron dysfunction in Alzheimer disease. Nat. Rev. Neurosci. 17, 777–792. https://doi.org/10.1038/nrn.2016.141

Panzeri, S., Macke, J.H., Gross, J., Kayser, C., 2015. Neural population coding: combining insights from microscopic and mass signals. Trends Cogn. Sci. 19, 162–172. https://doi.org/10.1016/j.tics.2015.01.002

Pardilla-Delgado, E., Torrico-Teave, H., Sanchez, J.S., Ramirez-Gomez, L.A., Baena, A., Bocanegra, Y., Vila-Castelar, C., Fox-Fuller, J.T., Guzmán-Vélez, E., Martínez, J., Alvarez, S., Ochoa-Escudero, M., Lopera, F., Quiroz, Y.T., 2021. Associations between subregional thalamic volume and brain pathology in autosomal dominant Alzheimer's disease. Brain Commun. 3, fcab101. https://doi.org/10.1093/braincomms/fcab101

Parron, C., Save, E., 2004. Comparison of the effects of entorhinal and retrosplenial cortical lesions on habituation, reaction to spatial and non-spatial changes during object exploration in the rat. Neurobiol. Learn. Mem. 82, 1–11. https://doi.org/10.1016/j.nlm.2004.03.004

Pasquale, R.D., Sherman, S.M., 2011. Synaptic Properties of Corticocortical Connections between the Primary and Secondary Visual Cortical Areas in the Mouse. J. Neurosci. 31, 16494–16506. https://doi.org/10.1523/JNEUROSCI.3664-11.2011

Paxinos, G., Franklin, K.B.J., 2001. The Mouse Brain in Stereotaxic Coordinates. Academic Press.

Pelkey, K.A., Chittajallu, R., Craig, M.T., Tricoire, L., Wester, J.C., McBain, C.J., 2017. Hippocampal GABAergic Inhibitory Interneurons. Physiol. Rev. 97, 1619–1747. https://doi.org/10.1152/physrev.00007.2017

Peng, S., Zhang, Y., Zhang, J., Wang, H., Ren, B., 2011. Glutamate receptors and signal transduction in learning and memory. Mol. Biol. Rep. 38, 453–460. https://doi.org/10.1007/s11033-010-0128-9

Pengas, G., Hodges, J.R., Watson, P., Nestor, P.J., 2010. Focal posterior cingulate atrophy in incipient Alzheimer's disease. Neurobiol. Aging 31, 25–33. https://doi.org/10.1016/j.neurobiolaging.2008.03.014

Picciotto, M.R., Higley, M.J., Mineur, Y.S., 2012. Acetylcholine as a neuromodulator: cholinergic signaling shapes nervous system function and behavior. Neuron 76, 116–129. https://doi.org/10.1016/j.neuron.2012.08.036

Poirier, G.L., Amin, E., Good, M.A., Aggleton, J.P., 2011. Early-onset dysfunction of retrosplenial cortex precedes overt amyloid plaque formation in Tg2576 mice. Neuroscience 174, 71–83. https://doi.org/10.1016/j.neuroscience.2010.11.025

Poirier, G.L., Shires, K.L., Sugden, D., Amin, E., Thomas, K.L., Carter, D.A., Aggleton, J.P., 2008. Anterior thalamic lesions produce chronic and profuse transcriptional deregulation in retrosplenial cortex: a model of retrosplenial hypoactivity and covert pathology. Thalamus Relat. Syst. 4, 59–77. https://doi.org/10.1017/S1472928808000368

Pothuizen, H.H.J., Davies, M., Aggleton, J.P., Vann, S.D., 2010. Effects of selective granular retrosplenial cortex lesions on spatial working memory in rats. Behav. Brain Res. 208, 566–575. https://doi.org/10.1016/j.bbr.2010.01.001

Pothuizen, H.H.J., Davies, M., Albasser, M.M., Aggleton, J.P., Vann, S.D., 2009. Granular and dysgranular retrosplenial cortices provide qualitatively different contributions to spatial working memory: evidence from immediate-early gene imaging in rats. Eur. J. Neurosci. 30, 877–888. https://doi.org/10.1111/j.1460-9568.2009.06881.x

Powell, A., Connelly, W.M., Vasalauskaite, A., Nelson, A.J.D., Vann, S.D., Aggleton, J.P., Sengpiel, F., Ranson, A., 2020. Stable Encoding of Visual Cues in the Mouse Retrosplenial Cortex. Cereb. Cortex 30, 4424–4437. https://doi.org/10.1093/cercor/bhaa030

Pozueta, J., Lefort, R., Shelanski, M.L., 2013. Synaptic changes in Alzheimer's disease and its models. Neuroscience, Dendritic Spine Plasticity in Brain Disorders 251, 51–65. https://doi.org/10.1016/j.neuroscience.2012.05.050

Prasad, J.A., Chudasama, Y., 2013. Viral Tracing Identifies Parallel Disynaptic Pathways to the Hippocampus. J. Neurosci. 33, 8494–8503. https://doi.org/10.1523/JNEUROSCI.5072-12.2013

Puzzo, D., Privitera, L., Fa', M., Staniszewski, A., Hashimoto, G., Aziz, F., Sakurai, M., Ribe, E.M., Troy, C.M., Mercken, M., Jung, S.S., Palmeri, A., Arancio, O., 2011. Endogenous Amyloid-β is Necessary for Hippocampal Synaptic Plasticity and Memory. Ann. Neurol. 69, 819–830. https://doi.org/10.1002/ana.22313

Puzzo, D., Privitera, L., Leznik, E., Fà, M., Staniszewski, A., Palmeri, A., Arancio, O., 2008. Picomolar Amyloid-β Positively Modulates Synaptic Plasticity and Memory in Hippocampus. J. Neurosci. 28, 14537–14545. https://doi.org/10.1523/JNEUROSCI.2692-08.2008

Reilly, J.F., Games, D., Rydel, R.E., Freedman, S., Schenk, D., Young, W.G., Morrison, J.H., Bloom, F.E., 2003. Amyloid deposition in the hippocampus and entorhinal cortex: Quantitative analysis of a transgenic mouse model. Proc. Natl. Acad. Sci. 100, 4837–4842. https://doi.org/10.1073/pnas.0330745100

Reiss, A.B., Arain, H.A., Stecker, M.M., Siegart, N.M., Kasselman, L.J., 2018. Amyloid toxicity in Alzheimer's disease. Rev. Neurosci. 29, 613–627. https://doi.org/10.1515/revneuro-2017-0063

Reyes, A., Lujan, R., Rozov, A., Burnashev, N., Somogyi, P., Sakmann, B., 1998. Target-cell-specific facilitation and depression in neocortical circuits. Nat. Neurosci. 1, 279–285. https://doi.org/10.1038/1092

Richardson, R.J., Blundon, J.A., Bayazitov, I.T., Zakharenko, S.S., 2009. Connectivity Patterns Revealed by Mapping of Active Inputs on Dendrites of Thalamorecipient Neurons in the Auditory Cortex. J. Neurosci. 29, 6406–6417. https://doi.org/10.1523/JNEUROSCI.0258-09.2009

Robinson, S., Keene, C.S., Iaccarino, H.F., Duan, D., Bucci, D.J., 2011. Involvement of Retrosplenial Cortex in Forming Associations Between Multiple Sensory Stimuli. Behav. Neurosci. 125, 578–587. https://doi.org/10.1037/a0024262

Robles, R.M., Domínguez-Sala, E., Martínez, S., Geijo-Barrientos, E., 2020. Layer 2/3 Pyramidal Neurons of the Mouse Granular Retrosplenial Cortex and Their Innervation by Cortico-Cortical Axons. Front. Neural Circuits 14. https://doi.org/10.3389/fncir.2020.576504

Rogers, J., Strohmeyer, R., Kovelowski, C.J., Li, R., 2002. Microglia and inflammatory mechanisms in the clearance of amyloid beta peptide. Glia 40, 260–269. https://doi.org/10.1002/glia.10153

Roux, L., Buzsáki, G., 2015. Tasks for inhibitory interneurons in intact brain circuits. Neuropharmacology 0, 10–23. https://doi.org/10.1016/j.neuropharm.2014.09.011

RStudio Team, 2020. RStudio: Integrated Development for R. RStudio.

Ryan, T.J., Roy, D.S., Pignatelli, M., Arons, A., Tonegawa, S., 2015. Engram cells retain memory under retrograde amnesia. Science 348, 1007–1013. https://doi.org/10.1126/science.aaa5542

Saganich, M.J., Schroeder, B.E., Galvan, V., Bredesen, D.E., Koo, E.H., Heinemann, S.F., 2006. Deficits in Synaptic Transmission and Learning in Amyloid Precursor Protein (APP) Transgenic Mice Require C-Terminal Cleavage of APP. J. Neurosci. 26, 13428–13436. https://doi.org/10.1523/JNEUROSCI.4180-06.2006

Salehi, A., Ashford, J.W., Mufson, E.J., 2016. The Link between Alzheimer's Disease and Down Syndrome. A Historical Perspective. Curr. Alzheimer Res. 13, 2–6.

Salmasi, M., Loebel, A., Glasauer, S., Stemmler, M., 2019. Short-term synaptic depression can increase the rate of information transfer at a release site. PLOS Comput. Biol. 15, e1006666. https://doi.org/10.1371/journal.pcbi.1006666

Sánchez-Bellot, C., AlSubaie, R., Mishchanchuk, K., Wee, R.W.S., MacAskill, A.F., 2022. Two opposing hippocampus to prefrontal cortex pathways for the control of approach and avoidance behaviour. Nat. Commun. 13, 339. https://doi.org/10.1038/s41467-022-27977-7

Sasaguri, H., Nilsson, P., Hashimoto, S., Nagata, K., Saito, T., De Strooper, B., Hardy, J., Vassar, R., Winblad, B., Saido, T.C., 2017. APP mouse models for Alzheimer's disease preclinical studies. EMBO J. 36, 2473–2487. https://doi.org/10.15252/embj.201797397

Sasahara, M., Fries, J.W.U., Raines, E.W., Gown, A.M., Westrum, L.E., Frosch, M.P., Bonthron, D.T., Ross, R., Collins, T., 1991. PDGF B-chain in neurons of the central nervous system, posterior pituitary, and in a transgenic model. Cell 64, 217–227. https://doi.org/10.1016/0092-8674(91)90223-L

Saura, C.A., Chen, G., Malkani, S., Choi, S.-Y., Takahashi, R.H., Zhang, D., Gouras, G.K., Kirkwood, A., Morris, R.G.M., Shen, J., 2005. Conditional inactivation of presenilin 1 prevents amyloid accumulation and temporarily rescues contextual and spatial working memory impairments in amyloid precursor protein transgenic mice. J. Neurosci. 25, 6755–6764. https://doi.org/10.1523/jneurosci.1247-05.2005

Scheff, S.W., Price, D.A., Ansari, M.A., Roberts, K.N., Schmitt, F.A., Ikonomovic, M.D., Mufson, E.J., 2015. Synaptic Change in the Posterior Cingulate Gyrus in the Progression of Alzheimer's Disease. J. Alzheimers Dis. JAD 43, 1073–1090. https://doi.org/10.3233/JAD-141518

Schindelin, J., Arganda-Carreras, I., Frise, E., Kaynig, V., Longair, M., Pietzsch, T., Preibisch, S., Rueden, C., Saalfeld, S., Schmid, B., Tinevez, J.-Y., White, D.J., Hartenstein, V., Eliceiri, K., Tomancak, P., Cardona, A., 2012. Fiji: an open-source platform for biological-image analysis. Nat. Methods 9, 676–682. https://doi.org/10.1038/nmeth.2019

Schnell, E., Nicoll, R.A., 2001. Hippocampal Synaptic Transmission and Plasticity Are Preserved in Myosin Va Mutant Mice. J. Neurophysiol. 85, 1498–1501. https://doi.org/10.1152/jn.2001.85.4.1498

Schoonover, C.E., Tapia, J.-C., Schilling, V.C., Wimmer, V., Blazeski, R., Zhang, W., Mason, C.A., Bruno, R.M., 2014. Comparative strength and dendritic organization of thalamocortical and corticocortical synapses onto excitatory layer 4 neurons. J. Neurosci. Off. J. Soc. Neurosci. 34, 6746–6758. https://doi.org/10.1523/JNEUROSCI.0305-14.2014

Scimemi, A., Meabon, J.S., Woltjer, R.L., Sullivan, J.M., Diamond, J.S., Cook, D.G., 2013. Amyloid-β1–42 Slows Clearance of Synaptically Released Glutamate by Mislocalizing Astrocytic GLT-1. J. Neurosci. 33, 5312–5318. https://doi.org/10.1523/JNEUROSCI.5274-12.2013

Sempere-Ferràndez, A., Andrés-Bayón, B., Geijo-Barrientos, E., 2018. Callosal responses in a retrosplenial column. Brain Struct. Funct. 223, 1051–1069. https://doi.org/10.1007/s00429-017-1529-5

Serrano-Pozo, A., Frosch, M.P., Masliah, E., Hyman, B.T., 2011. Neuropathological Alterations in Alzheimer Disease. Cold Spring Harb. Perspect. Med. 1. https://doi.org/10.1101/cshperspect.a006189

Shah, D., Jonckers, E., Praet, J., Vanhoutte, G., Palacios, R.D. y, Bigot, C., D'Souza, D.V., Verhoye, M., Linden, A.V. der, 2013. Resting State fMRI Reveals Diminished Functional Connectivity in a Mouse Model of Amyloidosis. PLOS ONE 8, e84241. https://doi.org/10.1371/journal.pone.0084241

Shankar, G.M., Bloodgood, B.L., Townsend, M., Walsh, D.M., Selkoe, D.J., Sabatini, B.L., 2007. Natural Oligomers of the Alzheimer Amyloid-β Protein Induce Reversible Synapse Loss by Modulating an NMDA-Type Glutamate Receptor-Dependent Signaling Pathway. J. Neurosci. 27, 2866–2875. https://doi.org/10.1523/JNEUROSCI.4970-06.2007

Shankar, G.M., Li, S., Mehta, T.H., Garcia-Munoz, A., Shepardson, N.E., Smith, I., Brett, F.M., Farrell, M.A., Rowan, M.J., Lemere, C.A., Regan, C.M., Walsh, D.M., Sabatini, B.L., Selkoe, D.J., 2008. Amyloid-β protein dimers isolated directly from Alzheimer's brains impair synaptic plasticity and memory. Nat. Med. 14, 837–842. https://doi.org/10.1038/nm1782

Shao, Z., Burkhalter, A., 1996. Different Balance of Excitation and Inhibition in Forward and Feedback Circuits of Rat Visual Cortex. J. Neurosci. 16, 7353–7365. https://doi.org/10.1523/JNEUROSCI.16-22-07353.1996

Sherrill, K.R., Erdem, U.M., Ross, R.S., Brown, T.I., Hasselmo, M.E., Stern, C.E., 2013. Hippocampus and Retrosplenial Cortex Combine Path Integration Signals for Successful Navigation. J. Neurosci. 33, 19304–19313. https://doi.org/10.1523/JNEUROSCI.1825-13.2013

Shibata, H., Honda, Y., Sasaki, H., Naito, J., 2009. Organization of intrinsic connections of the retrosplenial cortex in the rat. Anat. Sci. Int. 84, 280–292. https://doi.org/10.1007/s12565-009-0035-0

Shinoe, T., Matsui, M., Taketo, M.M., Manabe, T., 2005. Modulation of synaptic plasticity by physiological activation of M1 muscarinic acetylcholine receptors in the mouse hippocampus. J. Neurosci. Off. J. Soc. Neurosci. 25, 11194–11200. https://doi.org/10.1523/JNEUROSCI.2338-05.2005

Shipton, O.A., Leitz, J.R., Dworzak, J., Acton, C.E.J., Tunbridge, E.M., Denk, F., Dawson, H.N., Vitek, M.P., Wade-Martins, R., Paulsen, O., Vargas-Caballero, M., 2011. Tau Protein Is Required for Amyloid β-Induced Impairment of Hippocampal Long-Term Potentiation. J. Neurosci. 31, 1688–1692. https://doi.org/10.1523/JNEUROSCI.2610-10.2011

Shipton, O.A., Tang, C.S., Paulsen, O., Vargas-Caballero, M., 2022. Differential vulnerability of hippocampal CA3-CA1 synapses to Aβ. Acta Neuropathol. Commun. 10, 45. https://doi.org/10.1186/s40478-022-01350-7

Sigwald, E.L., Bignante, E.A., de Olmos, S., Lorenzo, A., 2019. Fear-context association during memory retrieval requires input from granular to dysgranular retrosplenial cortex. Neurobiol. Learn. Mem. 163, 107036. https://doi.org/10.1016/j.nlm.2019.107036

Solari, N., Hangya, B., 2018. Cholinergic modulation of spatial learning, memory and navigation. Eur. J. Neurosci. 48, 2199–2230. https://doi.org/10.1111/ejn.14089

Soltesz, I., Losonczy, A., 2018. CA1 pyramidal cell diversity enabling parallel information processing in the hippocampus. Nat. Neurosci. 21, 484–493. https://doi.org/10.1038/s41593-018-0118-0

Sonnenberg, J.L., Mitchelmore, C., Macgregor-Leon, P.F., Hempstead, J., Morgan, J.I., Curran, T., 1989. Glutamate receptor agonists increase the expression of Fos, Fra, and AP-1 DNA binding activity in the mammalian brain. J. Neurosci. Res. 24, 72–80. https://doi.org/10.1002/jnr.490240111

Sordo, L., Martini, A.C., Houston, E.F., Head, E., Gunn-Moore, D., 2021. Neuropathology of Aging in Cats and its Similarities to Human Alzheimer's Disease. Front. Aging 2.

Sri, S., Pegasiou, C.-M., Cave, C.A., Hough, K., Wood, N., Gomez-Nicola, D., Deinhardt, K., Bannerman, D., Perry, V.H., Vargas-Caballero, M., 2019. Emergence of synaptic and cognitive impairment in a mature-onset APP mouse model of Alzheimer's disease. Acta Neuropathol. Commun. 7, 25. https://doi.org/10.1186/s40478-019-0670-1

Sripanidkulchai, K., Wyss, J.M., 1986. Thalamic projections to retrosplenial cortex in the rat. J. Comp. Neurol. 254, 143–165. https://doi.org/10.1002/cne.902540202

Stargardt, A., Swaab, D.F., Bossers, K., 2015. The storm before the quiet: neuronal hyperactivity and Aβ in the presymptomatic stages of Alzheimer's disease. Neurobiol. Aging 36, 1–11. https://doi.org/10.1016/j.neurobiolaging.2014.08.014

Stiver, M.L., Jacklin, D.L., Mitchnick, K.A., Vicic, N., Carlin, J., O'Hara, M., Winters, B.D., 2015. Cholinergic manipulations bidirectionally regulate object memory destabilization. Learn. Mem. 22, 203–214. https://doi.org/10.1101/lm.037713.114

Sugar, J., Witter, M.P., van Strien, N., Cappaert, N., 2011. The Retrosplenial Cortex: Intrinsic Connectivity and Connections with the (Para)Hippocampal Region in the Rat. An Interactive Connectome. Front. Neuroinformatics 5. https://doi.org/10.3389/fninf.2011.00007

Svarnik, O.E., Alexandrov, Yu.I., Gavrilov, V.V., Grinchenko, Yu.V., Anokhin, K.V., 2005. Fos expression and task-related neuronal activity in rat cerebral cortex after instrumental learning. Neuroscience 136, 33–42. https://doi.org/10.1016/j.neuroscience.2005.07.038

Svoboda, E., McKinnon, M.C., Levine, B., 2006. The functional neuroanatomy of autobiographical memory: a meta-analysis. Neuropsychologia 44, 2189–2208. https://doi.org/10.1016/j.neuropsychologia.2006.05.023

Takeuchi, T., Duszkiewicz, A.J., Morris, R.G.M., 2014. The synaptic plasticity and memory hypothesis: encoding, storage and persistence. Philos. Trans. R. Soc. B Biol. Sci. 369, 20130288. https://doi.org/10.1098/rstb.2013.0288

Talantova, M., Sanz-Blasco, S., Zhang, X., Xia, P., Akhtar, M.W., Okamoto, S., Dziewczapolski, G., Nakamura, T., Cao, G., Pratt, A.E., Kang, Y.-J., Tu, S., Molokanova, E., McKercher, S.R., Hires, S.A., Sason, H., Stouffer, D.G., Buczynski, M.W., Solomon, J.P., Michael, S., Powers, E.T., Kelly, J.W., Roberts, A., Tong, G., Fang-Newmeyer, T., Parker, J., Holland, E.A., Zhang, D., Nakanishi, N., Chen, H.-S.V., Wolosker, H., Wang, Y., Parsons, L.H., Ambasudhan, R., Masliah, E., Heinemann, S.F., Piña-Crespo, J.C., Lipton, S.A., 2013. Aβ induces

astrocytic glutamate release, extrasynaptic NMDA receptor activation, and synaptic loss. Proc. Natl. Acad. Sci. U. S. A. 110, E2518–E2527. https://doi.org/10.1073/pnas.1306832110

Tamagnini, F., Novelia, J., Kerrigan, T.L., Brown, J.T., Tsaneva-Atanasova, K., Randall, A.D., 2015. Altered intrinsic excitability of hippocampal CA1 pyramidal neurons in aged PDAPP mice. Front. Cell. Neurosci. 9.

Tamamaki, N., Tomioka, R., 2010. Long-Range GABAergic Connections Distributed throughout the Neocortex and their Possible Function. Front. Neurosci. 4.

Tamaoka, A., Odaka, A., Ishibashi, Y., Usami, M., Sahara, N., Suzuki, N., Nukina, N., Mizusawa, H., Shoji, S., Kanazawa, I., 1994. APP717 missense mutation affects the ratio of amyloid beta protein species (A beta 1-42/43 and a beta 1-40) in familial Alzheimer's disease brain. J. Biol. Chem. 269, 32721–32724.

Tasic, B., Menon, V., Nguyen, T.N., Kim, T.K., Jarsky, T., Yao, Z., Levi, B., Gray, L.T., Sorensen, S.A., Dolbeare, T., Bertagnolli, D., Goldy, J., Shapovalova, N., Parry, S., Lee, C., Smith, K., Bernard, A., Madisen, L., Sunkin, S.M., Hawrylycz, M., Koch, C., Zeng, H., 2016. Adult mouse cortical cell taxonomy revealed by single cell transcriptomics. Nat. Neurosci. 19, 335–346. https://doi.org/10.1038/nn.4216

Taube, J.S., 2007. The Head Direction Signal: Origins and Sensory-Motor Integration. Annu. Rev. Neurosci. 30, 181–207. https://doi.org/10.1146/annurev.neuro.29.051605.112854

Taube, J.S., 1998. Head direction cells and the neurophysiological basis for a sense of direction. Prog. Neurobiol. 55, 225–256. https://doi.org/10.1016/S0301-0082(98)00004-5

Taube, J.S., 1995. Head direction cells recorded in the anterior thalamic nuclei of freely moving rats. J. Neurosci. 15, 70–86. https://doi.org/10.1523/JNEUROSCI.15-01-00070.1995

Terry, R.D., Masliah, E., Salmon, D.P., Butters, N., DeTeresa, R., Hill, R., Hansen, L.A., Katzman, R., 1991. Physical basis of cognitive alterations in

alzheimer's disease: Synapse loss is the major correlate of cognitive impairment. Ann. Neurol. 30, 572–580. https://doi.org/10.1002/ana.410300410

Thal, D.R., Rüb, U., Orantes, M., Braak, H., 2002. Phases of Aβ-deposition in the human brain and its relevance for the development of AD. Neurology 58, 1791–1800. https://doi.org/10.1212/WNL.58.12.1791

Ting, J.T., Daigle, T.L., Chen, Q., Feng, G., 2014. Acute brain slice methods for adult and aging animals: application of targeted patch clampanalysis and optogenetics. Methods Mol. Biol. Clifton NJ 1183, 221–242. https://doi.org/10.1007/978-1-4939-1096-0_14

Todd, T.P., Mehlman, M.L., Keene, C.S., DeAngeli, N.E., Bucci, D.J., 2016. Retrosplenial cortex is required for the retrieval of remote memory for auditory cues. Learn. Mem. 23, 278–288. https://doi.org/10.1101/lm.041822.116

Toropova, K.A., Troshev, D.V., Ivashkina, O.I., Anokhin, K.V., 2020. Activation of c-Fos Expression in the Retrosplenial Cortex but Not the Hippocampus Accompanies Formation of an Association between the Context and the Unconditioned Stimulus and Its Subsequent Retrieval in Mice. Neurosci. Behav. Physiol. 50, 81–91. https://doi.org/10.1007/s11055-019-00872-3

Tsodyks, M.V., Markram, H., 1997. The neural code between neocortical pyramidal neurons depends on neurotransmitter release probability. Proc. Natl. Acad. Sci. 94, 719–723. https://doi.org/10.1073/pnas.94.2.719

Tu, S., Okamoto, S., Lipton, S.A., Xu, H., 2014. Oligomeric Aβ-induced synaptic dysfunction in Alzheimer's disease. Mol. Neurodegener. 9, 48. https://doi.org/10.1186/1750-1326-9-48

Turecek, R., Trussell, L.O., 2000. Control of synaptic depression by glutamate transporters. J. Neurosci. Off. J. Soc. Neurosci. 20, 2054–2063.

Uhl, M., Schmeisser, M.J., Schumann, S., 2022. The Sexual Dimorphic Synapse: From Spine Density to Molecular Composition. Front. Mol. Neurosci. 15.

Unal, G., Joshi, A., Viney, T.J., Kis, V., Somogyi, P., 2015. Synaptic Targets of Medial Septal Projections in the Hippocampus and Extrahippocampal Cortices of the Mouse. J. Neurosci. 35, 15812–15826. https://doi.org/10.1523/JNEUROSCI.2639-15.2015

Valenstein, E., Bowers, D., Verfaellie, M., Heilman, K.M., Day, A., Watson, R.T., 1987. Retrosplenial amnesia. Brain J. Neurol. 110 (Pt 6), 1631–1646. https://doi.org/10.1093/brain/110.6.1631

Valverde, F., 1986. Intrinsic neocortical organization: Some comparative aspects. Neuroscience 18, 1–23. https://doi.org/10.1016/0306-4522(86)90174-0

van der Goes, M.-S.H., Voigts, J., Newman, J.P., Toloza, E.H.S., Brown, N.J., Murugan, P., Harnett, M.T., 2022. Coordinated Head Direction Representations in Mouse Anterodorsal Thalamic Nucleus and Retrosplenial Cortex. https://doi.org/10.1101/2022.08.20.504604

Van der Werf, Y.D., Scheltens, P., Lindeboom, J., Witter, M.P., Uylings, H.B.M., Jolles, J., 2003. Deficits of memory, executive functioning and attention following infarction in the thalamus; a study of 22 cases with localised lesions. Neuropsychologia 41, 1330–1344. https://doi.org/10.1016/S0028-3932(03)00059-9

van Groen, T., Vogt, B.A., Wyss, J.M., 1993. Interconnections Between the Thalamus and Retrosplenial Cortex in the Rodent Brain, in: Vogt, B.A., Gabriel, M. (Eds.), Neurobiology of Cingulate Cortex and Limbic Thalamus: A Comprehensive Handbook. Birkhäuser Boston, Boston, MA, pp. 123–150. https://doi.org/10.1007/978-1-4899-6704-6_4

Van Welie, I., Remme, M.W.H., Van Hooft, J.A., Wadman, W.J., 2006. Different levels of Ih determine distinct temporal integration in bursting and regular-spiking neurons in rat subiculum. J. Physiol. 576, 203–214. https://doi.org/10.1113/jphysiol.2006.113944

van Wijngaarden, J.B., Babl, S.S., Ito, H.T., 2020. Entorhinal-retrosplenial circuits for allocentric-egocentric transformation of boundary coding. eLife 9, e59816. https://doi.org/10.7554/eLife.59816

Vann, S.D., Aggleton, J.P., 2005. Selective dysgranular retrosplenial cortex lesions in rats disrupt allocentric performance of the radial-arm maze task. Behav. Neurosci. 119, 1682–1686. https://doi.org/10.1037/0735-7044.119.6.1682

Vann, S.D., Aggleton, J.P., 2004. Testing the importance of the retrosplenial guidance system: effects of different sized retrosplenial cortex lesions on heading

direction and spatial working memory. Behav. Brain Res. 155, 97–108. https://doi.org/10.1016/j.bbr.2004.04.005

Vann, S.D., Aggleton, J.P., 2002. Extensive cytotoxic lesions of the rat retrosplenial cortex reveal consistent deficits on tasks that tax allocentric spatial memory. Behav. Neurosci. 116, 85–94. https://doi.org/10.1037/0735-7044.116.1.85

Vann, S.D., Aggleton, J.P., Maguire, E.A., 2009. What does the retrosplenial cortex do? Nat. Rev. Neurosci. 10, 792–802. https://doi.org/10.1038/nrn2733

Vantomme, G., Rovó, Z., Cardis, R., Béard, E., Katsioudi, G., Guadagno, A., Perrenoud, V., Fernandez, L.M.J., Lüthi, A., 2020. A Thalamic Reticular Circuit for Head Direction Cell Tuning and Spatial Navigation. Cell Rep. 31, 107747. https://doi.org/10.1016/j.celrep.2020.107747

Vedder, L.C., Miller, A.M.P., Harrison, M.B., Smith, D.M., 2017. Retrosplenial Cortical Neurons Encode Navigational Cues, Trajectories and Reward Locations During Goal Directed Navigation. Cereb. Cortex N. Y. N 1991 27, 3713–3723. https://doi.org/10.1093/cercor/bhw192

Vierk, R., Glassmeier, G., Zhou, L., Brandt, N., Fester, L., Dudzinski, D., Wilkars, W., Bender, R.A., Lewerenz, M., Gloger, S., Graser, L., Schwarz, J., Rune, G.M., 2012. Aromatase Inhibition Abolishes LTP Generation in Female But Not in Male Mice. J. Neurosci. 32, 8116–8126. https://doi.org/10.1523/JNEUROSCI.5319-11.2012

Villain, N., Desgranges, B., Viader, F., Sayette, V. de la, Mézenge, F., Landeau, B., Baron, J.-C., Eustache, F., Chételat, G., 2008. Relationships between Hippocampal Atrophy, White Matter Disruption, and Gray Matter Hypometabolism in Alzheimer's Disease. J. Neurosci. 28, 6174–6181. https://doi.org/10.1523/JNEUROSCI.1392-08.2008

Vogt, B.A., Pandya, D.N., Rosene, D.L., 1987. Cingulate cortex of the rhesus monkey: I. Cytoarchitecture and thalamic afferents. J. Comp. Neurol. 262, 256–270. https://doi.org/10.1002/cne.902620207

Vogt, B.A., Paxinos, G., 2014. Cytoarchitecture of mouse and rat cingulate cortex with human homologies. Brain Struct. Funct. 219, 185–192. https://doi.org/10.1007/s00429-012-0493-3

Vogt, B.A., Peters, A., 1981. Form and distribution of neurons in rat cingulate cortex: Areas 32, 24, and 29. J. Comp. Neurol. 195, 603–625. https://doi.org/10.1002/cne.901950406

Voronin, L.L., Cherubini, E., 2004. 'Deaf, mute and whispering' silent synapses: their role in synaptic plasticity. J. Physiol. 557, 3–12. https://doi.org/10.1113/jphysiol.2003.058966

Walsh, C., Ridler, T., Margetts-Smith, G., Garcia Garrido, M., Witton, J., Randall, A.D., Brown, J.T., 2022. β Bursting in the Retrosplenial Cortex Is a Neurophysiological Correlate of Environmental Novelty Which Is Disrupted in a Mouse Model of Alzheimer's Disease. J. Neurosci. Off. J. Soc. Neurosci. 42, 7094–7109. https://doi.org/10.1523/JNEUROSCI.0890-21.2022

Walsh, D.M., Klyubin, I., Fadeeva, J.V., Cullen, W.K., Anwyl, R., Wolfe, M.S., Rowan, M.J., Selkoe, D.J., 2002. Naturally secreted oligomers of amyloid β protein potently inhibit hippocampal long-term potentiation in vivo. Nature 416, 535–539. https://doi.org/10.1038/416535a

Wang, H.-W., Pasternak, J.F., Kuo, H., Ristic, H., Lambert, M.P., Chromy, B., Viola, K.L., Klein, W.L., Stine, W.B., Krafft, G.A., Trommer, B.L., 2002. Soluble oligomers of β amyloid (1-42) inhibit long-term potentiation but not long-term depression in rat dentate gyrus. Brain Res. 924, 133–140. https://doi.org/10.1016/S0006-8993(01)03058-X

Warburton, E.C., Baird, A., Morgan, A., Muir, J.L., Aggleton, J.P., 2001. The Conjoint Importance of the Hippocampus and Anterior Thalamic Nuclei for Allocentric Spatial Learning: Evidence from a Disconnection Study in the Rat. J. Neurosci. 21, 7323–7330. https://doi.org/10.1523/JNEUROSCI.21-18-07323.2001

Watts, J.C., Prusiner, S.B., 2018. β-Amyloid Prions and the Pathobiology of Alzheimer's Disease. Cold Spring Harb. Perspect. Med. 8, a023507. https://doi.org/10.1101/cshperspect.a023507

Wesierska, M., Adamska, I., Malinowska, M., 2009. Retrosplenial cortex lesion affected segregation of spatial information in place avoidance task in the rat. Neurobiol. Learn. Mem. 91, 41–49. https://doi.org/10.1016/j.nlm.2008.09.005

Whishaw, I.Q., Maaswinkel, H., Gonzalez, C.L.R., Kolb, B., 2001. Deficits in allothetic and idiothetic spatial behavior in rats with posterior cingulate cortex lesions. Behav. Brain Res. 118, 67–76. https://doi.org/10.1016/S0166-4328(00)00312-0

Whitesell, J.D., Buckley, A.R., Knox, J.E., Kuan, L., Graddis, N., Pelos, A., Mukora, A., Wakeman, W., Bohn, P., Ho, A., Hirokawa, K.E., Harris, J.A., 2019. Whole brain imaging reveals distinct spatial patterns of amyloid beta deposition in three mouse models of Alzheimer's disease. J. Comp. Neurol. 527, 2122–2145. https://doi.org/10.1002/cne.24555

Willem, M., Tahirovic, S., Busche, M.A., Ovsepian, S.V., Chafai, M., Kootar, S., Hornburg, D., Evans, L.D.B., Moore, S., Daria, A., Hampel, H., Müller, V., Giudici, C., Nuscher, B., Wenninger-Weinzierl, A., Kremmer, E., Heneka, M.T., Thal, D.R., Giedraitis, V., Lannfelt, L., Müller, U., Livesey, F.J., Meissner, F., Herms, J., Konnerth, A., Marie, H., Haass, C., 2015. η-Secretase processing of APP inhibits neuronal activity in the hippocampus. Nature 526, 443–447. https://doi.org/10.1038/nature14864

Wolbers, T., Büchel, C., 2005. Dissociable Retrosplenial and Hippocampal Contributions to Successful Formation of Survey Representations. J. Neurosci. 25, 3333–3340. https://doi.org/10.1523/JNEUROSCI.4705-04.2005

Wolff, M., Vann, S.D., 2019. The Cognitive Thalamus as a Gateway to Mental Representations. J. Neurosci. 39, 3–14. https://doi.org/10.1523/JNEUROSCI.0479-18.2018

Woolf, N.J., 1991. Cholinergic systems in mammalian brain and spinal cord. Prog. Neurobiol. 37, 475–524. https://doi.org/10.1016/0301-0082(91)90006-m

Wright, A.L., Zinn, R., Hohensinn, B., Konen, L.M., Beynon, S.B., Tan, R.P., Clark, I.A., Abdipranoto, A., Vissel, B., 2013. Neuroinflammation and Neuronal Loss Precede Aβ Plaque Deposition in the hAPP-J20 Mouse Model of Alzheimer's Disease. PLOS ONE 8, e59586. https://doi.org/10.1371/journal.pone.0059586

Wu, H.-Y., Hudry, E., Hashimoto, T., Kuchibhotla, K., Rozkalne, A., Fan, Z., Spires-Jones, T., Xie, H., Arbel-Ornath, M., Grosskreutz, C.L., Bacskai, B.J., Hyman, B.T., 2010. Amyloid β Induces the Morphological Neurodegenerative Triad of Spine Loss, Dendritic Simplification, and Neuritic Dystrophies through Calcineurin Activation. J. Neurosci. 30, 2636–2649. https://doi.org/10.1523/JNEUROSCI.4456-09.2010

Wu, L., Rosa-Neto, P., Hsiung, G.-Y.R., Sadovnick, A.D., Masellis, M., Black, S.E., Jia, J., Gauthier, S., 2012. Early-Onset Familial Alzheimer's Disease (EOFAD). Can. J. Neurol. Sci. 39, 436–445. https://doi.org/10.1017/S0317167100013949

Wyass, J.M., Van Groen, T., 1992. Connections between the retrosplenial cortex and the hippocampal formation in the rat: A review. Hippocampus 2, 1–11. https://doi.org/10.1002/hipo.450020102

Wyss, J.M., Van Groen, T., 1992. Connections between the retrosplenial cortex and the hippocampal formation in the rat: a review. Hippocampus 2, 1–11. https://doi.org/10.1002/hipo.450020102

Yamawaki, N., Corcoran, K.A., Guedea, A.L., Shepherd, G.M.G., Radulovic, J., 2019a. Differential Contributions of Glutamatergic Hippocampal→Retrosplenial Cortical Projections to the Formation and Persistence of Context Memories. Cereb. Cortex N. Y. N 1991 29, 2728–2736. https://doi.org/10.1093/cercor/bhy142

Yamawaki, N., Li, X., Lambot, L., Ren, L.Y., Radulovic, J., Shepherd, G.M.G., 2019b. Long-range inhibitory intersection of a retrosplenial thalamocortical circuit by apical tuft-targeting CA1 neurons. Nat. Neurosci. 22, 618. https://doi.org/10.1038/s41593-019-0355-x

Yamawaki, N., Li, X., Lambot, L., Ren, L.Y., Radulovic, J., Shepherd, G.M.G., 2019c. Long-range inhibitory intersection of a retrosplenial thalamocortical circuit by apical tuft-targeting CA1 neurons. Nat. Neurosci. 1. https://doi.org/10.1038/s41593-019-0355-x

Yamawaki, N., Radulovic, J., Shepherd, G.M.G., 2016. A Corticocortical Circuit Directly Links Retrosplenial Cortex to M2 in the Mouse. J. Neurosci. 36, 9365–9374. https://doi.org/10.1523/JNEUROSCI.1099-16.2016

Yang, J.-T., Wang, Z.-J., Cai, H.-Y., Yuan, L., Hu, M.-M., Wu, M.-N., Qi, J.-S., 2018. Sex Differences in Neuropathology and Cognitive Behavior in APP/PS1/tau Triple-Transgenic Mouse Model of Alzheimer's Disease. Neurosci. Bull. 34, 736–746. https://doi.org/10.1007/s12264-018-0268-9

Yang, S.-N., Tang, Y.-G., Zucker, R.S., 1999. Selective Induction of LTP and LTD by Postsynaptic [Ca2+]i Elevation. J. Neurophysiol. 81, 781–787. https://doi.org/10.1152/jn.1999.81.2.781

Yashiro, K., Philpot, B.D., 2008. Regulation of NMDA Receptor Subunit Expression and Its Implications for LTD, LTP, and Metaplasticity. Neuropharmacology 55, 1081–1094. https://doi.org/10.1016/j.neuropharm.2008.07.046

Yi, J.H., Whitcomb, D.J., Park, S.J., Martinez-Perez, C., Barbati, S.A., Mitchell, S.J., Cho, K., 2020. M1 muscarinic acetylcholine receptor dysfunction in moderate Alzheimer's disease pathology. Brain Commun. 2, fcaa058. https://doi.org/10.1093/braincomms/fcaa058

Ying, J., Keinath, A.T., Lavoie, R., Vigneault, E., El Mestikawy, S., Brandon, M.P., 2022. Disruption of the grid cell network in a mouse model of early Alzheimer's disease. Nat. Commun. 13, 886. https://doi.org/10.1038/s41467-022-28551-x

Yoon, S.-S., Jo, S.A., 2012. Mechanisms of Amyloid-β Peptide Clearance: Potential Therapeutic Targets for Alzheimer's Disease. Biomol. Ther. 20, 245–255. https://doi.org/10.4062/biomolther.2012.20.3.245

Yousuf, H., Nye, A.N., Moyer, J.R., 2020. Heterogeneity of neuronal firing type and morphology in retrosplenial cortex of male F344 rats. J. Neurophysiol. 123, 1849–1863. https://doi.org/10.1152/jn.00577.2019

Zaitsev, A.V., Povysheva, N.V., Gonzalez-Burgos, G., Lewis, D.A., 2012. Electrophysiological classes of layer 2/3 pyramidal cells in monkey prefrontal cortex. J. Neurophysiol. 108, 595–609. https://doi.org/10.1152/jn.00859.2011

Zeisel, A., Muñoz-Manchado, A.B., Codeluppi, S., Lönnerberg, P., La Manno, G., Juréus, A., Marques, S., Munguba, H., He, L., Betsholtz, C., Rolny, C., Castelo-Branco, G., Hjerling-Leffler, J., Linnarsson, S., 2015. Cell types in the mouse

cortex and hippocampus revealed by single-cell RNA-seq. Science 347, 1138–1142. https://doi.org/10.1126/science.aaa1934

Zhang, X.-Q., Xu, L., Yang, S.-Y., Hu, L.-B., Dong, F.-Y., Sun, B.-G., Shen, H.-W., 2021. Reduced Synaptic Transmission and Intrinsic Excitability of a Subtype of Pyramidal Neurons in the Medial Prefrontal Cortex in a Mouse Model of Alzheimer's Disease. J. Alzheimers Dis. JAD 84, 129–140. https://doi.org/10.3233/JAD-210585

Zhen, X., Uryu, K., Cai, G., Johnson, G.P., Friedman, E., 1999. Age-associated impairment in brain MAPK signal pathways and the effect of caloric restriction in Fischer 344 rats. J. Gerontol. A. Biol. Sci. Med. Sci. 54, B539-548. https://doi.org/10.1093/gerona/54.12.b539

Zhou, B., Liu, Y., Zhang, Z., An, N., Yao, H., Wang, P., Wang, L., Zhang, X., Jiang, T., 2013. Impaired functional connectivity of the thalamus in Alzheimer's disease and mild cognitive impairment: a resting-state fMRI study. Curr. Alzheimer Res. 10, 754–766. https://doi.org/10.2174/15672050113109990146

Zhurakovskaya, E., Ishchenko, I., Gureviciene, I., Aliev, R., Gröhn, O., Tanila, H., 2019. Impaired hippocampal-cortical coupling but preserved local synchrony during sleep in APP/PS1 mice modeling Alzheimer's disease. Sci. Rep. 9, 5380. https://doi.org/10.1038/s41598-019-41851-5

Ziontz, J., Adams, J.N., Harrison, T.M., Baker, S.L., Jagust, W.J., 2021. Hippocampal Connectivity with Retrosplenial Cortex is Linked to Neocortical Tau Accumulation and Memory Function. J. Neurosci. 41, 8839–8847. https://doi.org/10.1523/JNEUROSCI.0990-21.2021

Zucker, R.S., Regehr, W.G., 2002. Short-Term Synaptic Plasticity. Annu. Rev. Physiol. 64, 355–405. https://doi.org/10.1146/annurev.physiol.64.092501.114547